

# Predicting the reflectivity and colour of metals from first principles

Thèse N°9314

Présentée le 17 mai 2019

à la Faculté des sciences et techniques de l'ingénieur  
Laboratoire de théorie et simulation des matériaux  
Programme doctoral en science et génie des matériaux

pour l'obtention du grade de Docteur ès Sciences

par

**Gianluca PRANDINI**

Acceptée sur proposition du jury

Prof. D. Damjanovic, président du jury  
Prof. N. Marzari, Prof. G.-M. Rignanese, directeurs de thèse  
Prof. R. Drautz, rapporteur  
Dr A. Ferretti, rapporteur  
Prof. A. Pasquarello, rapporteur

2019



Ai miei genitori...





# Acknowledgements

This PhD thesis has been a collaborative effort and here I wish to thank all the people that have contributed to this work.

Firstly, I thank my supervisor, Prof. Nicola Marzari, for giving me the opportunity to be part of his group as a PhD candidate on a very interesting scientific project. In particular I'm grateful for the support and guidance given all along my studies, for the trust and freedom he always granted me to take my own decisions and follow my ideas, and, moreover, for the possibility I had to learn by working in an intellectually stimulating environment and by travelling to schools and conferences.

Secondly I'd like to thank my co-supervisor, Prof. Gian-Marco Rignanese, for the support and all the enjoyable and useful discussions we had in these last years. His constant help and relevant suggestions have been fundamental for the good progress of the thesis.

A special thank goes to Dr. Fanny Lalire and Dr. Frédéric Diolgent for the stimulating meetings and discussions we had periodically during my PhD, which have significantly contributed to the development of the thesis. And in general it has been a great experience for me to work with them on this project.

I also warmly thank Prof. Paolo Umari for the opportunity I had to collaborate with him and for his hospitality during my several visits to Padova. To him I'm deeply grateful for sharing with me his knowledge of coding and for the invaluable help donated in developing the code used throughout the thesis.

A sincere thank goes also to all my colleagues at THEOS I had the pleasure to meet in these four years which helped me a lot during my PhD through several discussions and shared with me many fun moments both in and out of the office. In particular I thank the colleagues that contributed to this work: Andrea, Nicolas, Ivano and my office mate Antimo who also managed to bear me for nearly four years.

Last but not least I thank with all my heart my family and friends for the constant and invaluable support over these last years; without them all of this wouldn't have been even remotely possible.

*Lausanne, 18 February 2019*

G. P.



# Abstract

Gold and copper are the only two elemental metals that show a characteristic colour, due to the presence of a drop in the reflectivity curve inside the visible range. Reflectivities of all other metals are in general high and flat for all visible frequencies, making them appear shiny and silvery white. Nowadays, with state-of-the-art theoretical methods, it is possible to calculate reflectivity and colour of a material by means of first-principles simulations and, as a consequence, predict the colour of new metal alloys. The computational approach for materials design can be, for example, useful for applications related to jewellery and the high-end watch industry, where there is the demand, due to market and fashion trends, for precious-metal alloys with specific optical properties. The simulations can therefore substitute or, at least, reduce the use of expensive and inefficient trial-and-error experiments, which is otherwise the common route followed by researchers and manufacturers in order to identify novel materials. Because of its unique properties (i.e. characteristic red-yellow colour, high corrosion resistance, high density and considerable malleability), since ancient times gold and, as a consequence, its alloys have been of particular interest for jewellery applications. In particular, gold alloys and intermetallics show a broad spectrum of colours (yellow, red, purple, white and others), which can be tuned by varying the alloying elements in the material.

In this thesis, we first discuss the physical approach used to simulate the optical properties of metals, that is the independent particle approximation for the evaluation of the dielectric function, based on the calculation of both interband and intraband contributions from the electronic structure obtained with density-functional theory simulations. We also describe in some detail the computational approach developed to perform in practice first-principles simulations in both an efficient and automatic way. For this purpose, on one hand we have developed a code, named SIMPLE, to calculate optical properties using Shirley's interpolation method, which is an efficient and robust automatic procedure. On the other hand, in order to have reliable band structures as the starting ingredients for the evaluation of the dielectric function, we have exploited the results of a protocol, named SSSP, developed by us to test the precision and performance of pseudopotentials for all elements.

Using the results above, we then show through a systematic study on elemental metals and extensive comparisons with experimental data that the chosen computational approach is able to reproduce the correct behaviour of the reflectivity curve and to capture the main differences in optical properties among several elements of the periodic table.

Finally, we perform a similar study on metal alloys by considering different types of compounds, i.e. ordered intermetallics, disordered solid solutions and heterogeneous alloys.

## Acknowledgements

---

In particular, we show through a comparison with several experimental results that, if the appropriate methods are used for the simulation of the different types of compounds, (i) the simulated colours of known coloured intermetallics are often in quantitative agreement with experiments, (ii) the main mechanisms that modify the colour of bulk gold in alloys are qualitatively captured and that (iii) we manage to reproduce the main colour trends in noble-metal-based binary alloys.

Keywords: optical properties, dielectric function, colour, independent particle approximation, first principles, density-functional theory, Drude plasma frequency, automation, metal alloys, noble metals.

## Riassunto

Oro e rame sono gli unici due metalli puri a mostrare un colore caratteristico dovuto alla presenza di un calo repentino nella curva di riflettività all'interno dell'intervallo di luce visibile. La riflettività di tutti gli altri metalli puri è generalmente alta e piatta per tutte le frequenze visibili, e ciò li fa così apparire brillanti e di colore argentato. Oggigiorno, è possibile calcolare riflettività e colore di un materiale mediante simulazioni da principi primi con metodi teorici all'avanguardia e, come conseguenza, predire il colore di nuove leghe metalliche. L'approccio computazionale per il design di materiali può essere utile, ad esempio, per applicazioni legate alla gioielleria e all'industria di orologi di alta fascia, dove c'è domanda dovuta al mercato e a tendenze di moda di leghe a base di metalli preziosi e con specifiche proprietà ottiche. Le simulazioni possono quindi sostituire o almeno ridurre l'uso di esperimenti *trial-and-error* costosi e inefficienti, i quali sono altrimenti alla base del metodo comunemente seguito da ricercatori e fabbricanti per identificare nuovi materiali.

A causa delle sue proprietà uniche (cioè caratteristico colore rosso-giallo, alta resistenza alla corrosione, alta densità e notevole malleabilità), fin dai tempi antichi l'oro e, di conseguenza, le sue leghe sono state di particolare interesse per applicazioni nel campo della gioielleria. In particolare le leghe e gli intermetallici d'oro mostrano un ampio spettro di colori (giallo, rosso, viola, bianco e altri), i quali possono essere regolati variando gli elementi aggiunti nel materiale.

In questa tesi, per prima cosa discutiamo l'approccio teorico usato per simulare le proprietà ottiche di metalli, cioè l'approssimazione di particelle indipendenti per la valutazione della funzione dielettrica, basata sul calcolo dei contributi interbanda e intrabanda a partire dalla struttura elettronica ottenuta con simulazioni di teoria del funzionale densità. Descriviamo in dettaglio anche l'approccio computazionale sviluppato per eseguire in pratica le simulazioni da principi primi in modo sia efficiente che automatico. Per questo scopo, da un lato abbiamo sviluppato un programma, chiamato SIMPLE, per calcolare le proprietà ottiche utilizzando il metodo dell'interpolazione di Shirley, che è una procedura automatica, efficiente e robusta. D'altra parte, al fine di avere delle strutture a bande affidabili come ingredienti di partenza per la valutazione della funzione dielettrica, abbiamo sfruttato i risultati di un protocollo, denominato SSSP, da noi sviluppato per testare la precisione e l'efficienza degli pseudopotenziali per tutti gli elementi.

Usando i risultati descritti sopra, mostriamo poi attraverso uno studio sistematico sui metalli semplici e un ampio confronto con dati sperimentali che l'approccio computazionale scelto è in grado di riprodurre il corretto comportamento della curva di riflettività e di trovare le

## Acknowledgements

---

principali differenze nelle proprietà ottiche tra diversi elementi della tavola periodica. Infine, eseguiamo uno studio simile anche su leghe metalliche considerando diversi tipi di composti, cioè composti intermetallici ordinati, soluzioni solide disordinate e leghe eterogenee. In particolare, mostriamo attraverso un confronto con diversi risultati sperimentali che, se vengono utilizzati i metodi appropriati per la simulazione dei diversi tipi di composti, (i) i colori simulati di noti composti intermetallici colorati sono spesso in accordo quantitativo con gli esperimenti, (ii) i principali meccanismi che modificano il colore dell'oro nelle leghe sono qualitativamente descritti e che (iii) riusciamo a riprodurre i *trends* principali del colore in leghe binarie a base di metalli nobili.

# Contents

<b>Acknowledgements</b>	<b>v</b>
<b>Abstract (English/Italiano)</b>	<b>vii</b>
<b>List of figures</b>	<b>xiii</b>
<b>List of tables</b>	<b>xxii</b>
<b>List of symbols</b>	<b>xxv</b>
<b>1 Introduction</b>	<b>1</b>
1.1 Optical properties of metals: applications . . . . .	1
1.2 Colours in metals . . . . .	2
1.2.1 Elemental metals . . . . .	2
1.2.2 Gold alloys . . . . .	3
1.3 Previous simulations . . . . .	7
1.4 Outline . . . . .	8
<b>2 Electronic-structure theory</b>	<b>13</b>
2.1 Overview of DFT and TDDFT . . . . .	13
2.1.1 DFT . . . . .	13
2.1.2 TDDFT . . . . .	14
2.2 DFT in practice . . . . .	15
2.2.1 Pseudopotential approximation . . . . .	15
2.2.2 Plane waves basis set . . . . .	16
2.3 Response function in TDDFT . . . . .	16
<b>3 Optical properties in linear response</b>	<b>19</b>
3.1 Optical measurements . . . . .	19
3.2 Maxwell's equations . . . . .	20
3.2.1 Microscopic equations . . . . .	20
3.2.2 Macroscopic equations . . . . .	21
3.2.3 Electromagnetic waves and optical constants . . . . .	22
3.3 Response function . . . . .	24
3.3.1 Linear-response theory . . . . .	24

## Contents

---

3.3.2	Microscopic-macroscopic connection . . . . .	26
3.3.3	Independent particle approximation in TDDFT . . . . .	28
3.4	Optical limit . . . . .	30
3.4.1	Interband contribution . . . . .	30
3.4.2	Intraband contribution . . . . .	31
3.4.3	Drude plasma frequency . . . . .	32
3.4.4	Non-locality . . . . .	34
3.4.5	$f$ -sum rule . . . . .	34
<b>4</b>	<b>Colour perception</b>	<b>37</b>
4.1	Trichromatic theory . . . . .	37
4.2	Photorealistic rendering . . . . .	41
<b>5</b>	<b>Computational approach</b>	<b>43</b>
5.1	SIMPLE code . . . . .	43
5.1.1	Optimal basis method . . . . .	44
5.1.2	Details of the code . . . . .	46
5.1.3	Validation and performance of the code . . . . .	47
5.2	Workflow . . . . .	51
5.3	Precision and efficiency of pseudopotential simulations . . . . .	54
5.3.1	SSSP protocol . . . . .	54
5.3.2	IPA calculations with SIMPLE . . . . .	62
<b>6</b>	<b>Reflectivity and colour of elemental metals</b>	<b>65</b>
6.1	Computational details . . . . .	65
6.2	Comparison with experiments . . . . .	70
6.2.1	Reflectivity and colour . . . . .	70
6.2.2	Plasma frequency . . . . .	73
6.2.3	Photorealistic rendering . . . . .	74
6.3	Verification of the $f$ -sum rule . . . . .	76
6.4	Validity of the Drude model . . . . .	77
6.5	Additional effects on the optical properties . . . . .	80
6.5.1	Spin-orbit coupling . . . . .	80
6.5.2	Non-local commutator . . . . .	82
<b>7</b>	<b>Reflectivity and colour of alloys</b>	<b>85</b>
7.1	Simulation of alloys . . . . .	85
7.1.1	Binary alloys . . . . .	85
7.1.2	Computational methods . . . . .	86
7.2	Optical properties in supercell simulations . . . . .	89
7.2.1	Effects of the optimal basis . . . . .	89
7.2.2	Convergence with k-points sampling and broadening . . . . .	92
7.2.3	Convergence with supercell size . . . . .	96



7.3	Comparison with experiments . . . . .	99
7.3.1	Coloured intermetallic compounds . . . . .	99
7.3.2	Binary gold alloys . . . . .	101
7.3.3	Ag-Cu . . . . .	108
7.3.4	Au-Ag-Cu . . . . .	111
7.4	Comparison among different methods . . . . .	112
7.4.1	Ag-Au . . . . .	112
7.4.2	Ag-Cu . . . . .	114
7.4.3	Au-Pd . . . . .	117
7.4.4	Trends in VCA . . . . .	119
7.5	Computational screening of gold-based intermetallics . . . . .	121
<b>8</b>	<b>Conclusions</b>	<b>125</b>
<b>A</b>	<b>Macroscopic averages in crystals</b>	<b>129</b>
<b>B</b>	<b>Derivation of the intraband contribution to the IPA dielectric function</b>	<b>131</b>
<b>C</b>	<b>Optical data</b>	<b>133</b>
C.1	Elemental metals . . . . .	134
C.2	Coloured intermetallics . . . . .	179
	<b>Bibliography</b>	<b>196</b>
	<b>Curriculum Vitae</b>	<b>197</b>



# List of Figures

1.1	Reflectance of some elemental metals as a function of the wavelength of light (in $\mu\text{m}$ ) and real samples of pure aluminum, copper and gold. . . . .	2
1.2	Ternary plots showing the range of colours of the Au-Ag-Cu (left panel) and of the Au-Pd-Ag (right panel) systems. . . . .	4
1.3	The intermetallic compound $\text{AuAl}_2$ , which has the fluorite ( $\text{CaF}_4$ ) crystal structure (right panel), shows a striking purple colour (left panel). Adapted from [1].	5
1.4	Reflectivity curves of three example systems illustrating the three main mechanisms that permit to modify the intrinsic colour of gold through alloying additions: Ag-Au [2] (shift of the reflectivity edge), Au-Pt [3] ("flattening" of the reflectivity edge) and $\text{AuX}_2$ intermetallics [4] with $X = \text{Al, Ga, In}$ (introduction of new features in the reflectivity curve). . . . .	6
1.5	Band structure of bulk gold computed at the DFT-PBE level along high-symmetry lines of the face-centered cubic (FCC) BZ. The red arrows close to the points X and L of the BZ schematically show the main $5d - 6sp$ interband transitions that give rise to the characteristic colour of gold. The Fermi level is set to the zero of energy. . . . .	8
4.1	(Left panel) The process of colour perception is the result of the interaction between a light source, an object and an observer (adapted from Ref. [5]). (Right panel) Schematic picture of a basic colour matching experiment: the three matching stimuli are adjusted until the colour of the test stimulus is undistinguishable to the observer from the colour produced by the three matching stimuli. . . . .	38
4.2	Plot of the colour matching functions (CMFs) $\bar{r}(\lambda)$ , $\bar{g}(\lambda)$ and $\bar{b}(\lambda)$ (left panel) and $\bar{x}(\lambda)$ , $\bar{y}(\lambda)$ and $\bar{z}(\lambda)$ (right panel) of the <i>CIE 1931 standard colorimetric observer</i> . From Ref. [2]. . . . .	39
4.3	CIELAB colour space. The corresponding colour coordinates $L^*$ , $a^*$ and $b^*$ are shown. . . . .	41
4.4	Example of photorealistic rendering of a metallic surface performed with the Mitsuba renderer [6]. . . . .	42

## List of Figures

---

5.1	Convergence of the interband contribution to the IPA complex dielectric function of bulk Ag with respect to the number of OB functions $N_b$ , which is controlled by the parameter $s_b$ . We show both the real (right panel) and imaginary parts (left panel) of $\epsilon^{\text{inter}}(\hat{\mathbf{q}}, \omega)$ . . . . .	48
5.2	Comparison of the interband contribution to the IPA complex dielectric function of bulk Ag calculated with the SIMPLE code and with the Yambo code. We show both the real (right panel) and imaginary parts (left panel) of $\epsilon^{\text{inter}}(\hat{\mathbf{q}}, \omega)$ . . . . .	49
5.3	Relative computational time for a IPA calculation performed with the SIMPLE code on bulk Ag, both including and not including the non-local commutator in the evaluation of the velocity matrix elements, with respect to the square of the number of OB functions $N_b$ . The reference wall time is set as the one resulting from the calculation with the smallest number of vectors. . . . .	50
5.4	Speedup of an IPA calculation performed with the SIMPLE code ( <code>simple.x</code> and <code>simple_ip.x</code> ) as a function of the number of cores for bulk Ag in a $4 \times 4 \times 4$ supercell with 64 atoms including and not including the contribution to the velocity matrix elements coming from the non-local commutator. The test is performed on Intel <sup>®</sup> Skylake <sup>®</sup> processors. . . . .	51
5.5	Schematic representation of the ColourWorkflow which is designed to simulate the reflectivity and colour of a metallic material giving as input its crystal structure. The workflow is implemented within the framework of the AiiDA infrastructure. . . . .	53
5.6	SSSP testing protocol applied to palladium. For each pseudopotential the convergence w.r.t. the wavefunction cutoff of the zone-boundary phonons ( $\delta\bar{\omega}$ ), cohesive energy ( $\delta E_{coh}$ ), pressure ( $\delta V_{press}$ ) and bands structure ( $\eta_{10}$ and $\max \eta_{10}$ ) is monitored. The horizontal dashed lines correspond to the thresholds of the SSSP selection criteria (efficiency or precision); here precision is shown. On the right-hand side we report the number of valence electrons of the pseudopotential ( $Z$ ), the $\Delta$ -factor and the $\Delta'$ -factor [7] with respect to the reference all-electron results and the converged value of the highest phonon frequency ( $\omega_{max}$ ). The circle marks the pseudopotential and wavefunction cutoff chosen for the SSSP library (version 1.1). All convergence pattern plots of the 85 elements tested are available on the Materials Cloud platform [8]. . . . .	59
5.7	Band structure of FCC Pb along a high-symmetry path, for several pseudopotential libraries (top panel). The valence bands are almost identical to each other, while some differences appear in the conduction bands: the SG15 bands deviate from the other bands around 7-10 eV over the Fermi level and a flat ghost state in the GBRV bands is clearly visible at around 8 eV. These differences between band structures can be compressed into the bands distances $\eta_v$ and $\eta_{10}$ , reported in units of meV (bottom panel). In addition, ghost states in the band interval considered can be automatically detected as peaks in the $\eta$ function, hence simplifying greatly the verification of spectral properties. . . . .	60

6.1	Dependence of the IPA Drude plasma frequency $\omega_D$ for elemental Au and Pd on the Gaussian broadening $\sigma$ for different interpolation k-points grids. . . . .	67
6.2	Dependence of $\varepsilon_2^{\text{inter}}(\omega)$ for elemental Au and Pd on the interpolation k-points grids for different values of the empirical interband broadening $\eta$ . . . . .	68
6.3	Dependence of $R(\omega)$ for elemental Au and Pd on the interpolation k-points grids for different values of $\eta$ and $\sigma$ (with $\eta = \sigma$ ). . . . .	69
6.4	Simulated (solid lines) and experimental (dot-dashed lines) reflectivities for 18 elemental metals. Experimental data are taken from Ref. [9]. The two vertical dashed lines show the limits of the visible range. . . . .	72
6.5	Comparison of simulated (green) and experimental (blue) colours for eight elemental metals in CIELAB colour space (i.e. Ag, Au, Cs, Cu, Nb, Os, Rh and Ta). Experimental colours are derived from the optical data of Ref. [9]. . . . .	73
6.6	Periodic table with the IPA Drude plasma frequency for 45 elemental metals computed in their ground-state crystal structures. The space group number of each crystal structure is also reported. . . . .	74
6.7	Comparison between the rendering of a metallic surface of pure gold (top), osmium (center) and cesium (bottom) obtained using the simulated optical constants (left panel) and real samples of the three materials (right panel). . . .	75
6.8	Verification of the valence $f$ -sum rule. $\bar{\omega}_{D,\text{eff}}$ is computed by truncating the energy integration at 20 eV. We report in parentheses the nominal number of valence electrons $Z$ used in the evaluation of $\bar{\omega}_{D,\text{val}}$ . . . . .	77
6.9	Comparison of the reflectivity obtained with IPA simulations (solid lines), Drude model (dashed lines) and from experiments [9] (dot-dashed lines) for K, Cs, Al and Au. . . . .	79
6.10	Comparison between the dielectric function and reflectivity for platinum and gold computed including ('Relativistic', solid lines) and not including ('Scalar-relativistic', dashed lines) SOC. Experimental data of the reflectivities (dot-dashed lines) are also reported [9]. . . . .	81
6.11	Comparison between the dielectric function and reflectivity for vanadium and copper computed with (solid lines) and without (dashed lines) including the non-local commutator. Experimental data of the reflectivities (dot-dashed lines) are also reported [9]. . . . .	83
7.1	Comparison of the IPA optical properties of Au and AuGa <sub>2</sub> computed with the OB method in the primitive cell (solid lines) and in a supercell (dashed lines). The total dielectric function and the reflectivity are numerically independent from the size of the simulation cell while the interband and intraband contributions, taken separately, are not. . . . .	91
7.2	Dependence of the IPA Drude plasma frequency $\omega_D$ for AgAu <sub>15</sub> and Au <sub>15</sub> Pd on the Gaussian broadening $\sigma$ for different interpolation k-points grids. . . . .	93

## List of Figures

---

7.3	Dependence of $\varepsilon_2^{\text{inter}}(\omega)$ for AgAu <sub>15</sub> and Au <sub>15</sub> Pd on the interpolation k-points grids for different values of the empirical interband broadening $\eta$ . Insets show the behaviour of $\varepsilon_2^{\text{inter}}(\omega)$ zoomed in the low-energy range, i.e. in the interval [0, 1] eV. . . . .	94
7.4	Dependence of $R(\omega)$ for AgAu <sub>15</sub> and Au <sub>15</sub> Pd on the interpolation k-points grids for different values of $\eta$ and $\sigma$ (with $\eta = \sigma$ ). . . . .	95
7.5	Dependence of $\varepsilon_2^{\text{inter}}(\omega)$ and $\omega_D$ on the size of the SQS for Ag <sub>0.25</sub> Au <sub>0.75</sub> and Au <sub>0.75</sub> Pd <sub>0.25</sub> (with $N$ being the number of atoms in the supercell). . . . .	97
7.6	Dependence of the real (dashed lines) and imaginary (solid lines) parts of the dielectric function on the size of the SQS for Ag <sub>0.25</sub> Au <sub>0.75</sub> (with $N$ being the number of atoms in the supercell). We show both $\varepsilon^{\text{inter}}(\omega)$ (left panel) and $\varepsilon(\omega)$ (right panel). . . . .	98
7.7	Dependence of the reflectivity on the size of the SQS for Ag <sub>0.25</sub> Au <sub>0.75</sub> and Au <sub>0.75</sub> Pd <sub>0.25</sub> (with $N$ being the number of atoms in the supercell). . . . .	98
7.8	Simulated (solid lines) and experimental (dashed lines) reflectivities of coloured intermetallics. Experimental data are taken from Ref. [4] for AuAl <sub>2</sub> , AuGa <sub>2</sub> and AuIn <sub>2</sub> , from Ref. [10] for PtAl <sub>2</sub> , from Ref. [11] for NiSi <sub>2</sub> and from Ref. [12] for CoSi <sub>2</sub> and PdIn. The two vertical dashed lines show the limits of the visible range. . .	100
7.9	Comparison of simulated (green) and experimental (blue) colours of known coloured intermetallics compounds in CIELAB colour colour space. . . . .	101
7.10	Comparison between the rendering of a metallic surface of the intermetallic compounds AuAl <sub>2</sub> (top), AuGa <sub>2</sub> (center) and PtAl <sub>2</sub> (bottom) obtained using the simulated optical constants (left panel) and real samples of the three materials (right panel). . . . .	102
7.11	Experimental phase diagrams of (a) Ag-Au, (b) Au-Cu, (c) Al-Au and (d) Au-Pt. Adapted from [13]. . . . .	103
7.12	Comparison of the trends in composition of the reflectivity inside the visible spectrum for Ag-Au solid solutions between SQS simulations (left panel) and experiments [2] (right panel). For reference, we also report the reflectivity curves of elemental Au and elemental Ag (dashed lines). To note that the alloy compositions of experiments and simulations are not exactly the same. . . . .	104
7.13	Comparison of the reflectivity inside the visible spectrum between supercell simulations and experiments for Au-Pt and Al-Au solid solutions. Experimental data are taken from Ref. [3] for Au <sub>0.90</sub> Pt <sub>0.10</sub> and from Ref. [14] for Al <sub>0.112</sub> Au <sub>0.888</sub> . For reference, we also report the reflectivity curve of elemental Au (dashed lines). To note that the concentrations of the alloying element in experiments are larger than those in the simulations. . . . .	105

7.14 Comparison of the trends in composition of the optical absorption inside the visible spectrum for Au-Cu solid solutions between SQS simulations (left panel) and experiments [15] (right panel). The Drude-like intraband contribution to $\varepsilon_2(\omega)$ has been subtracted from the experimental data. For reference, we also report $\varepsilon_2(\omega)$ of elemental Au and elemental Cu (dashed lines). To note that the alloy compositions of experiments and simulations are not always the same. Experimental and simulated curves have been arbitrarily shifted along the vertical axis for clarity in the comparison. . . . .	107
7.15 Comparison of $\varepsilon_2(\omega)$ for $\text{Au}_{1-x}\text{Cu}_x$ between simulations (left panel) and experiments [15] (right panel) for both the solid solution and the intermetallic phase $\text{AuCu}_3$ (at $x = 0.75$ in the simulations and at $x = 0.81$ in the experiments). For reference, we also report $\varepsilon_2(\omega)$ of elemental Cu (dashed lines). Experimental and simulated curves have been arbitrarily shifted along the vertical axis for clarity in the comparison. . . . .	107
7.16 Experimental phase diagram of Ag-Cu. Adapted from [13]. . . . .	109
7.17 Comparison of the trends in composition of the reflectivity inside the visible spectrum for Ag-Cu two-phase alloys between simulations (left panel) and experiments [16] (right panel). The results of the simulations are obtained using the Bruggeman model in which the two phases of the system are assumed to be elemental Ag and elemental Cu (dashed lines). . . . .	109
7.18 Comparison of the trends in composition of the reflectivity inside the visible spectrum for Ag-Cu two-phase alloys between experiments [16] (right panel) and results of the Bruggeman model applied to experimental data of the dielectric function of elemental Ag and elemental Cu [9] (left panel). . . . .	110
7.19 Comparison of $\varepsilon_2(\omega)$ for $\text{Ag}_{1-x}\text{Cu}_x$ between simulations (left panel) and experiments [15] (right panel) for both the solid solution and the two-phase alloy (at $x = 0.25$ in the simulations and at $x = 0.30$ in the experiments). . . . .	110
7.20 Comparison of the trends in composition of optical absorption and reflectivity for Ag-Au between SQS and VCA simulations. We report also the results for the elemental constituents, i.e. Ag and Au (dashed lines). . . . .	113
7.21 Comparison of the trends in composition of optical absorption and reflectivity for Ag-Cu between supercell and VCA simulations. We report also the results for the elemental constituents, i.e. Ag and Cu (dashed lines). . . . .	115
7.22 Comparison of the trends in composition of optical absorption and reflectivity for Ag-Cu between supercell simulations and Bruggeman model results applied on elemental Ag and elemental Cu (dashed lines). . . . .	116
7.23 Comparison of the trends in composition of optical absorption and reflectivity for Au-Pd between supercell and VCA simulations. We report also the results for the elemental constituents, i.e. Au and Pd (dashed lines). . . . .	118
7.24 Comparison of the optical absorption and reflectivity of $\text{Au}_{0.938}\text{X}_{0.062}$ , with X = Pd, Ag and Zn, between supercell and VCA simulations. For reference, we report also the results for elemental Au (dashed lines). . . . .	120

## List of Figures

---

7.25 Simulated CIELAB colour coordinates of 92 binary intermetallics of gold extracted from ICSD and COD databases of experimental crystal structures. . . .	124
C.1 Optical properties of Ag simulated at the IPA level starting from the DFT-PBE electronic structure. . . . .	134
C.2 Optical properties of Al simulated at the IPA level starting from the DFT-PBE electronic structure. . . . .	135
C.3 Optical properties of Au simulated at the IPA level starting from the DFT-PBE electronic structure. . . . .	136
C.4 Optical properties of Ba simulated at the IPA level starting from the DFT-PBE electronic structure. . . . .	137
C.5 Optical properties of Be simulated at the IPA level starting from the DFT-PBE electronic structure. . . . .	138
C.6 Optical properties of Bi simulated at the IPA level starting from the DFT-PBE electronic structure. . . . .	139
C.7 Optical properties of Ca simulated at the IPA level starting from the DFT-PBE electronic structure. . . . .	140
C.8 Optical properties of Cd simulated at the IPA level starting from the DFT-PBE electronic structure. . . . .	141
C.9 Optical properties of Co simulated at the IPA level starting from the DFT-PBE electronic structure. . . . .	142
C.10 Optical properties of Cr simulated at the IPA level starting from the DFT-PBE electronic structure. . . . .	143
C.11 Optical properties of Cs simulated at the IPA level starting from the DFT-PBE electronic structure. . . . .	144
C.12 Optical properties of Cu simulated at the IPA level starting from the DFT-PBE electronic structure. . . . .	145
C.13 Optical properties of Fe simulated at the IPA level starting from the DFT-PBE electronic structure. . . . .	146
C.14 Optical properties of Ga simulated at the IPA level starting from the DFT-PBE electronic structure. . . . .	147
C.15 Optical properties of Hf simulated at the IPA level starting from the DFT-PBE electronic structure. . . . .	148
C.16 Optical properties of Hg simulated at the IPA level starting from the DFT-PBE electronic structure. . . . .	149
C.17 Optical properties of In simulated at the IPA level starting from the DFT-PBE electronic structure. . . . .	150
C.18 Optical properties of Ir simulated at the IPA level starting from the DFT-PBE electronic structure. . . . .	151
C.19 Optical properties of K simulated at the IPA level starting from the DFT-PBE electronic structure. . . . .	152



C.20 Optical properties of Li simulated at the IPA level starting from the DFT-PBE electronic structure. . . . .	153
C.21 Optical properties of Mg simulated at the IPA level starting from the DFT-PBE electronic structure. . . . .	154
C.22 Optical properties of Mn simulated at the IPA level starting from the DFT-PBE electronic structure. . . . .	155
C.23 Optical properties of Mo simulated at the IPA level starting from the DFT-PBE electronic structure. . . . .	156
C.24 Optical properties of Na simulated at the IPA level starting from the DFT-PBE electronic structure. . . . .	157
C.25 Optical properties of Nb simulated at the IPA level starting from the DFT-PBE electronic structure. . . . .	158
C.26 Optical properties of Ni simulated at the IPA level starting from the DFT-PBE electronic structure. . . . .	159
C.27 Optical properties of Os simulated at the IPA level starting from the DFT-PBE electronic structure. . . . .	160
C.28 Optical properties of Pb simulated at the IPA level starting from the DFT-PBE electronic structure. . . . .	161
C.29 Optical properties of Pd simulated at the IPA level starting from the DFT-PBE electronic structure. . . . .	162
C.30 Optical properties of Pt simulated at the IPA level starting from the DFT-PBE electronic structure. . . . .	163
C.31 Optical properties of Rb simulated at the IPA level starting from the DFT-PBE electronic structure. . . . .	164
C.32 Optical properties of Re simulated at the IPA level starting from the DFT-PBE electronic structure. . . . .	165
C.33 Optical properties of Rh simulated at the IPA level starting from the DFT-PBE electronic structure. . . . .	166
C.34 Optical properties of Ru simulated at the IPA level starting from the DFT-PBE electronic structure. . . . .	167
C.35 Optical properties of Sc simulated at the IPA level starting from the DFT-PBE electronic structure. . . . .	168
C.36 Optical properties of Sr simulated at the IPA level starting from the DFT-PBE electronic structure. . . . .	169
C.37 Optical properties of Ta simulated at the IPA level starting from the DFT-PBE electronic structure. . . . .	170
C.38 Optical properties of Ti simulated at the IPA level starting from the DFT-PBE electronic structure. . . . .	171
C.39 Optical properties of Tc simulated at the IPA level starting from the DFT-PBE electronic structure. . . . .	172
C.40 Optical properties of Tl simulated at the IPA level starting from the DFT-PBE electronic structure. . . . .	173

## List of Figures

---

C.41 Optical properties of V simulated at the IPA level starting from the DFT-PBE electronic structure. . . . .	174
C.42 Optical properties of W simulated at the IPA level starting from the DFT-PBE electronic structure. . . . .	175
C.43 Optical properties of Y simulated at the IPA level starting from the DFT-PBE electronic structure. . . . .	176
C.44 Optical properties of Zn simulated at the IPA level starting from the DFT-PBE electronic structure. . . . .	177
C.45 Optical properties of Zr simulated at the IPA level starting from the DFT-PBE electronic structure. . . . .	178
C.46 Optical properties of PtAl <sub>2</sub> simulated at the IPA level starting from the DFT-PBE electronic structure. . . . .	179
C.47 Optical properties of CoSi <sub>2</sub> simulated at the IPA level starting from the DFT-PBE electronic structure. . . . .	180
C.48 Optical properties of PdIn simulated at the IPA level starting from the DFT-PBE electronic structure. . . . .	181
C.49 Optical properties of NiSi <sub>2</sub> simulated at the IPA level starting from the DFT-PBE electronic structure. . . . .	182
C.50 Optical properties of AuAl <sub>2</sub> simulated at the IPA level starting from the DFT-PBE electronic structure. . . . .	183
C.51 Optical properties of AuGa <sub>2</sub> simulated at the IPA level starting from the DFT-PBE electronic structure. . . . .	184
C.52 Optical properties of AuIn <sub>2</sub> simulated at the IPA level starting from the DFT-PBE electronic structure. . . . .	185

# List of Tables

5.1	Convergence of the IPA Drude plasma frequency (in eV) of bulk Ag with respect to the number of OB functions $N_b$ , computed along the three Cartesian limits (i.e. with $\hat{\mathbf{q}} = \hat{\mathbf{x}}, \hat{\mathbf{y}}, \hat{\mathbf{z}}$ ). . . . .	48
5.2	Pseudopotential libraries tested with the SSSP protocol. The short names correspond to the name used in the convergence pattern plots (see Fig. 5.6) to identify the pseudopotential libraries. . . . .	55
5.3	Selection criteria for the SSSP efficiency and SSSP precision libraries. . . . .	61
5.4	List of pseudopotentials (using the short names of Table 5.2) and corresponding wavefunction cutoffs chosen for each element considered in this work. . . . .	64
6.1	Colour differences ( $\Delta E$ ) in CIELAB colour space between simulations and experiments for 22 elemental metals. . . . .	71
6.2	Computed values of the IPA Drude plasma frequency (in eV) compared to previous simulations performed by J. Harl [17] and experiments (Exp.). The experimental values with no explicit reference are extracted from the data reported in Ref. [17], where all the original experimental references can be found. . . . .	76
6.3	Comparison of the classical Drude plasma frequency from the Drude model ( $\bar{\omega}_{D,\text{val}}$ ) and the IPA Drude plasma frequency ( $\omega_D$ ). We report in parentheses the nominal number of valence electrons $Z$ used in the evaluation of $\bar{\omega}_{D,\text{val}}$ . The error given by the Drude model with respect to the IPA results (in percentage) is also shown. . . . .	79
7.1	Different types of binary alloys and corresponding computational method used for the first-principles simulation of these systems. . . . .	89
7.2	Colour differences in CIELAB space between simulated colours and experimental colours derived from reflectivity data, $\Delta E_{\text{exp}}$ , and between simulated colours and previously published simulations, $\Delta E_{\text{sim}}$ . . . . .	100
7.3	List of binary intermetallics of gold extracted from ICSD and COD databases (part I). We report chemical formula, space group number (SG #) and database ID.122	
7.4	List of binary intermetallics of gold extracted from ICSD and COD databases (part II). We report chemical formula, space group number (SG #) and database ID.123	



# List of Symbols

<b>BSE</b>	Bethe-Salpeter equation
<b>BZ</b>	Brillouin zone
<b>CIE</b>	Commission Internationale de l'Eclairage
<b>CMF</b>	Colour matching function
<b>DFPT</b>	Density-functional perturbation theory
<b>DFT</b>	Density-functional theory
<b>EELS</b>	Electron energy loss spectroscopy
<b>GGA</b>	Generalized gradient approximation
<b>IPA</b>	Independent particle approximation
<b>KS</b>	Kohn-Sham
<b>LDA</b>	Local density approximation
<b>MBPT</b>	Many-body perturbation theory
<b>NC</b>	Norm-conserving
<b>OB</b>	Optimal basis
<b>PAW</b>	Projector-augmented wave
<b>PBE</b>	Perdew Burke Ernzerhof
<b>QE</b>	Quantum ESPRESSO
<b>SQS</b>	Special quasi random structure
<b>SSSP</b>	Standard solid state pseudopotential
<b>TDDFT</b>	Time-dependent density functional theory
<b>US</b>	Ultrasoft
<b>VCA</b>	Virtual crystal approximation



# 1 Introduction

## 1.1 Optical properties of metals: applications

The measurement of the optical constants of a material is a fundamental tool to understand and characterize its physical properties from a microscopic point of view. Knowledge of the optical properties gives insights into the electronic structure of a material and on its elementary excitations, such as excitons, plasmons and lattice vibrations. Furthermore, optical properties are an important link between theory and experiments in materials science. On one hand, optical measurements can lead to a deeper or even new understanding of the fundamental properties and interactions within a material while, on the other hand, models and/or simulations can help in interpreting these same experimental data in terms of the known elementary interactions in matter. The study of the optical properties is therefore relevant both for fundamental research in basic science and for the study and characterization of materials.

In addition, optical properties are important for novel technological applications where the optical response of a material needs to be engineered for specific purposes. Focusing only on metals, the study of optical properties is for example relevant for potential plasmonic devices (e.g. in spectrally-selective coatings [18, 19]), optoelectronics devices (e.g. in ultra thin films for transparent conductive electrodes [20, 21]), but also for microscopy and optical data storage based on the magneto-optical Kerr effect of magnetic metallic surfaces [22].

Furthermore, the optical properties of metals, and more in specific their colour (which is related to the optical properties within the visible range of the electromagnetic spectrum), play an important role in jewellery and watch industry, decoration and dentistry. For these applications, in particular for jewellery, the most interesting materials are metallic alloys based on gold [23] or other precious metals, such as silver, palladium and platinum.

The focus of this thesis is mainly on this last application of the optical properties of metals.

## 1.2 Colours in metals

### 1.2.1 Elemental metals

Reflectivities of most elemental metals are high and flat for all visible wavelengths [9]. This means that these materials effectively reflect most of the visible light impinging on their surface, making them appear shiny and whitish (see aluminum in Fig. 1.1 for an example). However, there are a few notable exceptions to this behaviour, the most notorious ones being gold and copper which show a strong characteristic colour due to the presence of a drop in the reflectivity curve inside the visible range<sup>1</sup>. As shown in Fig. 1.1, the reflectivity of gold falls abruptly from around 100% to less than 40% at a frequency corresponding roughly to 2.4 eV (or, equivalently, to a wavelength of 520 nm). Therefore it reflects almost completely red and yellow light and it absorbs all the higher frequencies of the visible spectrum. This peculiar feature is at the origin of the red-yellow colour of gold and it is due to the onset of interband electronic transitions from the occupied  $5d$  bands of gold at that particular energy. In copper the reflectivity edge is at slightly lower energies ( $\sim 2.1$  eV) so that the yellow light is also absorbed and thus the colour of copper is red. On the contrary silver appears shiny and white because the drop in the reflectivity is in the ultraviolet (close to 4 eV) and almost 100 % of the visible light is reflected.

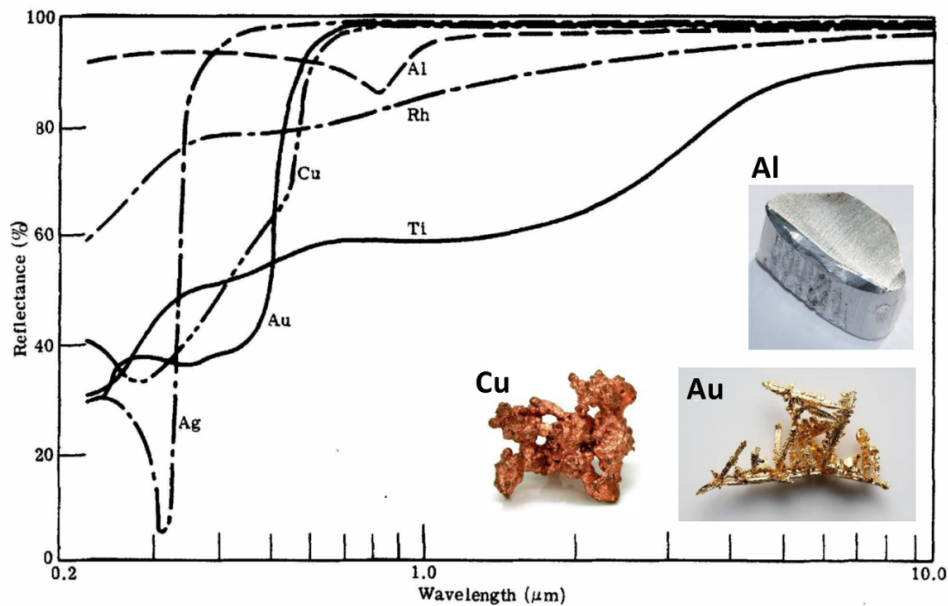


Figure 1.1 – Reflectance of some elemental metals as a function of the wavelength of light (in  $\mu\text{m}$ ) and real samples of pure aluminum, copper and gold.

<sup>1</sup>A few other elements in their pure metallic form show some degree of colouration. In particular cesium, osmium and tantalum appear yellowish, bluish and blue-gray, respectively.



### 1.2.2 Gold alloys

Gold alloys are known to assume a broad spectrum of colours (yellow, red, purple, pink, blue, white, etc.) and are of particular interest for jewellery applications [24]. Because of the characteristic behaviour of the reflectivity curve of gold inside the visible spectrum, colours of gold alloys can be tuned by varying the alloying additions and thus modifying the shape of the reflectivity curve. Different intrinsic mechanisms exist that are responsible for the modification of the reflectivity curve of gold. These mechanisms depend not only on the physical and chemical properties of the alloying element and on its concentration, but also on the atomic structure of the alloy, and, as we will show below with a few examples, these influence the final colour of the material in different ways<sup>2</sup>.

The basis of the most common jewellery and dental alloys is the ternary Au-Ag-Cu system. As can be seen in Fig. 1.2, a large variety of colours can be produced in this system by simply varying the ratios of the three constituent elements. Indeed, the drop in the reflectivity curve of gold at  $\sim 2.4$  eV is gradually shifted to lower energies if alloyed with copper and to higher energies if alloyed with silver, giving so a broad range of colours to the Au-Ag-Cu ternary system [16, 25]. As a consequence, with copper additions to gold the alloy gradually assumes reddish tints while, with silver additions, it assumes more yellow tints. The similarity in the physical and chemical properties of the three noble-metals elements allows one to qualitatively interpret the optical properties of the Au-Ag-Cu alloy as simply rising from the weighted-average of the electronic structure of the constituents elements, where the weight is given by the relative atomic concentration. In terms of the band structure, it means that the position of the occupied  $d$  bands with respect to the Fermi level, and thus the onset of interband electronic transition, is modified by varying the relative concentrations in Au-Ag-Cu.

#### White gold alloys

Silver, if used in large quantities as shown in Fig. 1.2 in weight percent (wt %), makes the Au-Ag-Cu alloy white by shifting the reflectivity edge at energies above the end of the visible spectrum. However, since for high-end jewellery applications high-carat<sup>3</sup> alloys are required, commercial white gold alloys are based on palladium and nickel as bleaching elements [26, 27] (but because of skin allergies, the use of nickel-based jewellery is restricted in Europe). Indeed, generally speaking, transition metals are more effective bleachers at smaller concentrations compared to silver, as shown in Fig. 1.2 for the case of palladium (Au-Pd-Ag system). The decolourising effect of these elements is produced in a qualitatively different way with respect to the case of silver. Indeed the reflectivity edge is not shifted but it is instead “flattened” by lowering the reflectivity in the low-energy part of the visible spectrum. In fact, transition metals introduce additional  $d$  states close to the Fermi level that give rise to new interband transitions at energies that are smaller compared to the onset of interband transitions in pure gold. In

<sup>2</sup>In this work we consider only bulk colours of alloys, i.e. that are related to the intrinsic properties of the material, and not colours due to particular surface treatments (e.g. due to surface oxide layers).

<sup>3</sup>The carat is a measure of the proportion in weight of gold inside an alloy, expressed as the number of parts of gold in 24 parts of the alloy. Therefore pure gold is 24 carat while an alloy with, for example 75 wt. % Au, is 18 carat.

particular, as confirmed both by experiments [28, 29] and first-principles simulations [30], nickel and palladium are known to introduce so-called virtual bound states [31], i.e. tightly bound states between the Fermi level and the 5*d* bands of gold, that increase the absorption processes at low energies. Instead, the position of the gold 5*d* bands is left nearly unchanged by alloying additions of Pd and Ni so that the position of the characteristic absorption edge of gold is roughly the same while the width of the virtual bound states, and therefore the optical absorption at low energies, increases as the content of the alloying element increases. For these systems, the electronic structure of the alloy cannot be simply interpreted as a mixture of the electronic structure of the constituent elements, as in the case of Au-Ag-Cu, and the effect of the impurity atoms on the optical properties of the alloy can be understood only with more complex models (i.e. Friedel [31] and Anderson [32] impurity models).

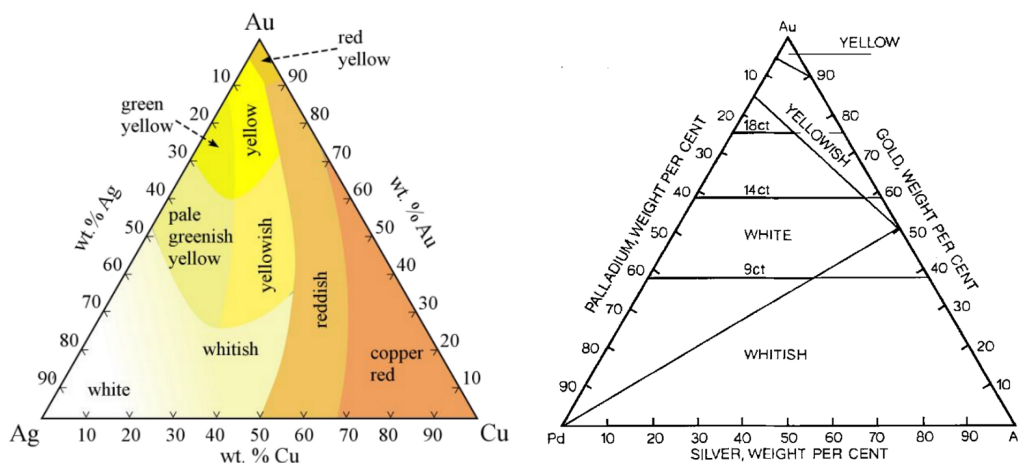


Figure 1.2 – Ternary plots showing the range of colours of the Au-Ag-Cu (left panel) and of the Au-Pd-Ag (right panel) systems.

### Intermetallic compounds

Special intrinsic colours can be sometimes observed in intermetallic compounds [12, 24, 33]. In contrast with the disordered alloys described above, intermetallic compounds have a very narrow homogeneity range and are ordered structures with a simple stoichiometric ratio among the components. Coloured intermetallic compounds usually present highly symmetric crystal structures (mostly cubic). They display particular electronic band structures that, in general, do not bear any resemblance with the band structures of their constituent elements. Because of this, they can show selective absorption of light in particular parts of the visible range while being highly reflective in the remaining parts, and hence present special intrinsic colours [12]. The most striking and known example of a coloured intermetallic compound is AuAl<sub>2</sub> which has a strong purple colour (see Fig. 1.3). Because of the presence of a pseudogap in the density of states [34], this compound strongly absorbs light in the yellow-green-blue range while it is reflective in the red and violet part of the spectrum, thus resulting in a purple

colour. The compounds  $\text{AuGa}_2$  and  $\text{AuIn}_2$ , that have the same cubic crystal structure as  $\text{AuAl}_2$ , are bluish because the dip in reflectivity is shifted to slightly lower energies and is less pronounced [4].

Since intermetallic compounds can present band structures that are qualitatively different from their constituent elements, various other intermetallic compounds other than the Cu-based and Au-based ones can be coloured. Indeed, other known examples are, to name a few, the yellow  $\text{PtAl}_2$ , blue  $\text{NiAl}$ , red  $\text{PdIn}$ , bluish gray  $\text{NiSi}_2$  and dark blue  $\text{CoSi}_2$ . However the use of intermetallic compounds in traditional jewellery is severely limited because these are typically very brittle. Alloying additions of other elements can improve their mechanical properties but at the cost of a loss in colour.

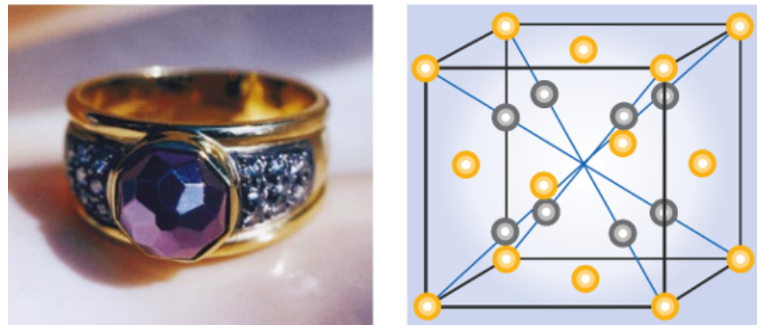


Figure 1.3 – The intermetallic compound  $\text{AuAl}_2$ , which has the fluorite ( $\text{CaF}_4$ ) crystal structure (right panel), shows a striking purple colour (left panel). Adapted from [1].

Summarizing, we can distinguish three main mechanisms that modify the intrinsic colour of gold alloys (see Fig. 1.4). In the first one, the reflectivity edge of gold is rigidly shifted so that different portions of the visible spectrum are reflected (as it happens, for example, in the Ag-Au system). In the second one, the reflectivity edge is “flattened” while the position of the edge is left roughly unchanged (Au-Ni, Au-Pd and Au-Pt are typical examples of this bleaching mechanism). In the third one, new colours are obtained by introducing completely new features in the reflectivity curve within the visible range (as it can happen in some intermetallic compounds).

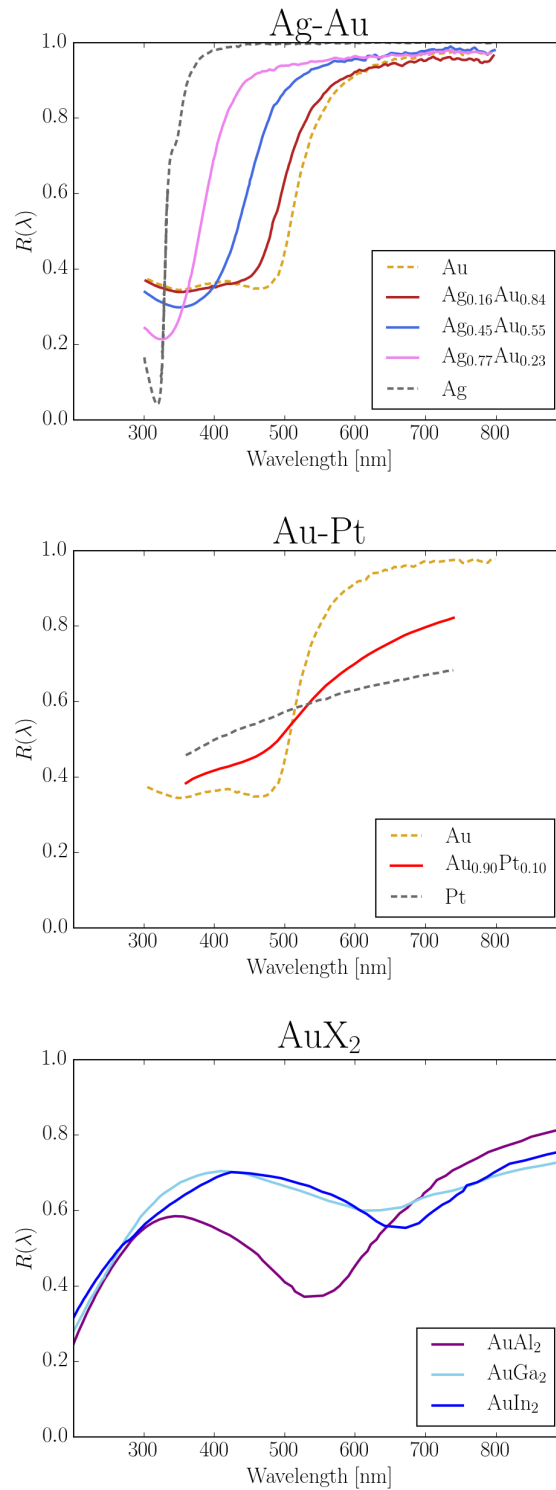


Figure 1.4 – Reflectivity curves of three example systems illustrating the three main mechanisms that permit to modify the intrinsic colour of gold through alloying additions: Ag-Au [2] (shift of the reflectivity edge), Au-Pt [3] (“flattening” of the reflectivity edge) and  $\text{AuX}_2$  intermetallics [4] with  $X = \text{Al}, \text{Ga}, \text{In}$  (introduction of new features in the reflectivity curve).

### 1.3 Previous simulations

We now want to briefly discuss some of the relevant studies found in literature about first-principles simulations of optical properties of both elemental metals and metallic alloys, with a particular focus on coloured intermetallics based on precious-metal elements (mainly on gold). If not specified otherwise, the dielectric function is always obtained within the IPA and using as input the electronic band structure computed at the DFT level with the PBE functional.

A few systematic studies of the optical properties of elemental metals have been performed. Already in 1988, Maksimov *et al.* [35] computed the optical properties, in particular dielectric function, electron energy loss function and reflectivity, of 15 elemental metals for energies ranging up to 35 eV whereas, more recently, Werner *et al.* [36] performed a similar study on 17 elemental metals extending the energy range up to 80 eV.

In the literature there are also a few systematic studies of the optical properties of intermetallic compounds. In Ref. [37] the authors calculated the optical properties of several intermetallic compounds, with a particular focus on alkali-noble intermetallics, for new possible candidates as plasmonic materials. In a similar work, Keast *et al.* [38] computed the density of states and dielectric function of gold intermetallics compounds and gold binary alloys. Regarding the simulation of specific coloured intermetallic compounds, the reflectivity and colour of the three coloured gold intermetallics AuAl<sub>2</sub>, AuGa<sub>2</sub> and AuIn<sub>2</sub> has been simulated in Ref. [34], while Keast *et al.* [10] also studied the influence of alloying elements on the reflectivity and colour of compounds with the Au<sub>1-x</sub>Pt<sub>x</sub>Al<sub>2</sub> composition, for  $x = 0, 0.5, 0.75, 1$  (similar results have been obtained by Kecik [39]). The calculated and experimental [40] reflectivity curves and colours show a good agreement for these compounds and the trends in the colour as a function of the composition are well reproduced.

First-principles studies performed on the noble-metal alloys Ag-Al [41], Al-Cu [42], Al-Au [14] and Au-Ni [30] all show an increase in the optical absorption in the infrared region, as also observed in experiments [43, 44, 14, 29, 41]. This effect produces the typical decrease of the reflectivity in the low-energy part of the spectrum in metallic alloys and gives the characteristic bleaching effect in gold alloys, as shown in Fig. 1.4 for Au-Pt.

Finally, the effect of disorder on the optical properties of Au<sub>0.5</sub>Cu<sub>0.5</sub> has been studied by comparing the dielectric function of the random solid solution, simulated using the supercell approach, with that of the ordered intermetallic compound [45].

#### Noble metals

For noble metals, the IPA approach from PBE band structures gives only qualitative agreement with respect to experiments. The general redshift of the spectra with respect to experiments is due to the failure of standard DFT approximations (e.g. LDA or GGA) to reproduce the true band structures of materials (in particular the position of the occupied *d* bands). This discrepancy can be corrected using approaches above DFT, such as the *GW* approximation from many-body perturbation theory (MBPT). IPA results show the correct features and shape

but also a redshift of the optical spectra when compared to experiments. By correcting the DFT band energies at the  $G_0W_0$  level, a quantitative agreement with respect to experiments is obtained for the optical spectra of Cu [46] and Ag [47] but not for Au, for which  $G_0W_0$  gives very similar results to the PBE ones [48]. Only within the quasi-particle self-consistent  $GW$  (QSGW) [49, 50] approach the occupied  $5d$  bands of gold are lowered in energy and the correct colour of gold is reproduced while the inclusion of spin-orbit coupling, both at the DFT and  $GW$  level, does not change significantly the optical spectra [48] (in gold the main relativistic effects are already taken into account by the scalar-relativistic contribution [51]). This discrepancy with respect to experiments is due to the deficiency of the PBE functional to describe correctly the positioning of the  $5d$  bands of gold. In particular the underestimation of the  $5d - 6sp$  interband gap is the main reason why a redshift of the drop in the reflectivity curve of  $\sim 0.4$  eV is found compared to experiments. Indeed, the onset of absorption is due to interband transitions from the  $5d$  bands to the  $6sp$  conduction bands above the Fermi level. The main transitions occur in the vicinity of the high-symmetry points X and L in the BZ [52]. The drop in the reflectivity curve of gold that gives to the material its characteristic yellow colour is due to the onset of these interband transitions.

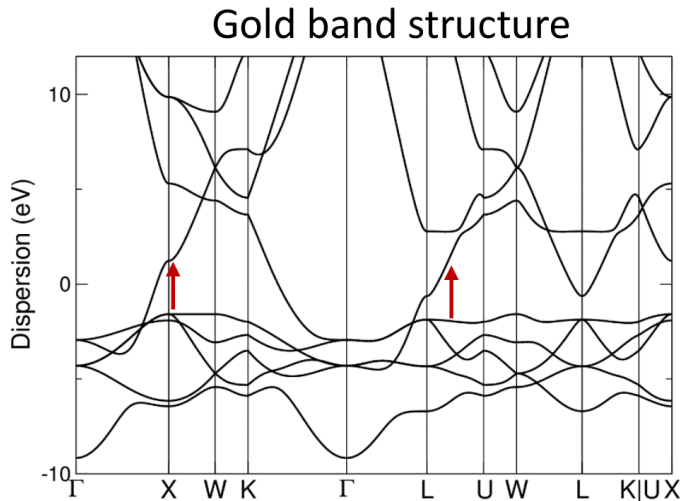


Figure 1.5 – Band structure of bulk gold computed at the DFT-PBE level along high-symmetry lines of the face-centered cubic (FCC) BZ. The red arrows close to the points X and L of the BZ schematically show the main  $5d - 6sp$  interband transitions that give rise to the characteristic colour of gold. The Fermi level is set to the zero of energy.

### 1.4 Outline

The thesis is organized as follows:

- **Chapter 2** contains a basic overview of the theoretical methods used in the thesis for the first-principles calculation of materials properties. Density-functional theory (DFT)

and time-dependent density-functional theory (TDDFT) for the study of ground-state properties and excited-states properties, respectively, are briefly reviewed, focusing on their practical implementation within the framework of the plane-wave pseudopotential method.

- **Chapter 3** contains the theory underlying the first-principles calculation of the optical properties of materials:
  - Section 3.1 and 3.2 give an overview of the macroscopic optical constants accessible in optical experiments. In particular we show the link between the macroscopic dielectric function and all the optical constants measurable in optical experiments, such as the reflectivity, by solving the Maxwell's equations for a monochromatic electromagnetic wave propagating inside a dispersive medium.
  - Section 3.3 instead shows how the macroscopic dielectric function of a material can be computed from its underlying microscopic electronic structure, by using linear response theory within the framework of TDDFT for the estimation of the linear response function. We then give the explicit expression linking the macroscopic dielectric function to the linear response function for a periodic crystal while we consider the simple independent particle approximation (IPA) for the evaluation of the linear response function.
  - Section 3.4 eventually considers the IPA macroscopic dielectric function in the optical limit. We show that in metals it can be divided in an interband contribution and an intraband (Drude-like) contribution and we discuss how the two terms are related one to the other by the  $f$ -sum rule and how the non-local part of pseudopotentials affects the calculation of optical properties.
- **Chapter 4** contains a basic description of the theoretical tools necessary in order to quantify and standardize colour measurements, focusing on trichromatic theory and CIE colour spaces. We show how the tristimulus values of the CIE- $XYZ$  colour space can be computed once the reflectivity of a material within the visible range is known and how these colour coordinates can be transformed into the more convenient uniform CIELAB colour space. We then briefly discuss photorealistic rendering, which is instead useful for the simulation of the actual appearance of real objects in 3D scenes under realistic conditions.
- **Chapter 5** describes in detail the computational approach developed in the thesis for the practical evaluation of the reflectivity and colour of metals:
  - Section 5.1 describes the SIMPLE code developed by us for the computation of the IPA dielectric function and which implements the Shirley's interpolation method for the efficient evaluation of integrals in reciprocal space.
  - Section 5.2 describes briefly the workflow designed in order to compute automatically reflectivity and colour of a material from its initial crystal structure.

- Section 5.3 instead describes the SSSP protocol developed by us in order to test pseudopotentials both in terms of precision and performance, and its application for reliable calculations of the IPA dielectric function with SIMPLE.
- **Chapter 6** contains the first-principles results obtained for the systematic study of the optical properties of 45 elemental metals:
  - Section 6.1 shows the convergence studies of the IPA dielectric function with respect to k-points sampling and spectral broadenings, and gives the relevant computational parameters used in the simulations.
  - Section 6.2 shows the main IPA results obtained for the reflectivity and colour of several elemental metals, focusing mainly on the comparison with experimental data for reflectivity and colour, but considering also the Drude plasma frequency and the actual appearance of the metals (photorealistic rendering).
  - Section 6.3 and Section 6.4 discuss the consistency of the simulations through the use of the  $f$ -sum rule and the validity of the empirical Drude model for the estimation of the optical properties of elemental metals, respectively.
  - Section 6.5 instead discusses the effect of the inclusion of the relativistic spin-orbit coupling and of the neglect of the non-local commutator deriving from the pseudopotential approximation in the estimation of the IPA optical properties.
- **Chapter 7** contains the first-principles results obtained for the study of the optical properties of binary metallic alloys, in particular focusing on gold-based compounds:
  - Section 7.1 briefly discusses the different types of alloys (i.e. intermetallics, solid solutions and heterogeneous alloys) and the main computational methods used for the first-principles simulation of these systems. In particular we describe in some detail the virtual crystal approximation (VCA) and the supercell approach based on the use of special quasi random structures (SQS) for the study of solid solutions, and the Bruggeman model for the study of heterogeneous alloys.
  - Section 7.2 focuses on the effect on the optical properties of the lowering of the symmetry in supercell calculations, both due to numerical errors related to the Shirley's interpolation method and intrinsic to supercell simulations of alloys. It contains also the convergence studies of the IPA dielectric function with respect to k-points sampling and spectral broadenings, and with respect to the supercell size for SQS simulations of alloys.
  - Section 7.3 shows the main IPA results obtained for the reflectivity and colour of binary intermetallic compounds known to be coloured and of some binary gold alloys, focusing on the comparison with experimental data available in the literature.
  - Section 7.4 instead shows the comparison of the results for binary gold alloys among the different computational methods used in the thesis to simulate the



optical properties of alloys, i.e. the supercell approach based on the use of SQS's, the VCA method and the Bruggeman model.

- **Chapter 8** contains the conclusions of the thesis.



## 2 Electronic-structure theory

Here we give a brief overview of the methods used for the first-principles calculation of the electronic structure in condensed matter. In particular, we discuss density-functional theory and time-dependent density-functional theory for the study of ground-state properties and excited-states properties, respectively. The treatment is by no means exhaustive and only the concepts most relevant for this thesis are described in some detail.

### 2.1 Overview of DFT and TDDFT

#### 2.1.1 DFT

Nowadays, the method most widely used to calculate the ground-state properties of a generic many-body system made of electrons and nuclei interacting through the Coulomb interaction is density-functional theory (DFT) which was formally developed in the two seminal works of Hohenberg and Kohn in 1964 [53] and of Kohn and Sham in 1965 [54]. In a nutshell, according to DFT a fundamental quantity describing a generic system is not only the many-body wavefunction, as in the standard formulation of quantum mechanics, but instead also the ground-state electronic density. All the difficulties related to the complex many-body interactions among electrons are confined inside the exchange-correlation contribution to the total energy. This term, that is for the time being unknown, can be approximated by models based on the homogeneous electron gas, such as the local density approximation (LDA) or the generalized gradient approximation (GGA). In fact, DFT has shown in the last three decades to be an extremely powerful theory to quantitatively predict ground-state properties of real materials.

The Hohenberg-Kohn (HK) theorem states that there is a one-to-one correspondence between ground-state electronic density  $n(\mathbf{r})$  and external potential  $V^{\text{ext}}(\mathbf{r})$ . The somehow surprising result of the HK theorem is that the ground-state density determines the external potential that gives rise to it. As a consequence, the energy of the system is a functional of the density, whose minimum is at the ground-state density and provides, in principle, the exact ground-state energy. The implementation of DFT for numerical simulations is instead based on the

Kohn-Sham (KS) approach. It consists in the use of an auxiliary system of non-interacting particles that is constructed in order to reproduce the density of the true many-body system. The basic idea of the approach is to replace the interacting many-body problem with a set of independent particle problems in presence of a self-consistent effective potential (as in mean-field methods). From the minimization with respect to the density of the total energy functional, a set of one-particle Schrödinger equations, called KS equations, is found. The interacting density can be then be computed by solving the KS equations

$$\left[ -\frac{1}{2}\nabla^2 + V^{\text{ext}}(\mathbf{r}) + V^{\text{H}}(\mathbf{r}) + V^{\text{xc}}(\mathbf{r}) \right] \psi_{\alpha}(\mathbf{r}) = E_{\alpha} \psi_{\alpha}(\mathbf{r}) \quad (2.1)$$

with eigenvalues  $E_{\alpha}$  and eigenvectors  $\psi_{\alpha}(\mathbf{r})$ , and density given by

$$n(\mathbf{r}) = \sum_{\alpha} f_{\alpha} |\psi_{\alpha}(\mathbf{r})|^2, \quad (2.2)$$

where  $f_{\alpha}$  is the occupation function of the wavefunction  $\psi_{\alpha}(\mathbf{r})$ . The KS equations have to be solved self-consistently because the effective KS potential  $V^{\text{KS}}(\mathbf{r}) = V^{\text{ext}}(\mathbf{r}) + V^{\text{H}}(\mathbf{r}) + V^{\text{xc}}(\mathbf{r})$  entering in the KS Hamiltonian  $H^{\text{KS}} = -\frac{1}{2}\nabla^2 + V^{\text{KS}}(\mathbf{r})$  depends itself on the density.

As said before,  $V^{\text{ext}}(\mathbf{r})$  is the external potential given by the Coulomb interaction between electrons and nuclei while  $V^{\text{H}}(\mathbf{r}) = \int d\mathbf{r}' \frac{n(\mathbf{r}')}{|\mathbf{r}-\mathbf{r}'|}$  is the Hartree potential and  $V^{\text{xc}}(\mathbf{r})$  is the unknown exchange-correlation potential and is defined as the functional derivative of the exchange-correlation energy with respect to the density. In the local density approximation (LDA) the exchange-correlation energy is assumed to depend locally on the electronic density and to be equal to that of an homogeneous electron gas, while in the general gradient approximation (GGA) a dependence on the gradient of the electronic density is also added.

We note here that the KS theory is constructed to reproduce only the interacting ground-state density and total energy and no other quantities are in principle correctly computed. For example, KS wavefunctions and energies do not in general correspond to the quasiparticle states and energies measured in photoemission experiments.

### 2.1.2 TDDFT

Time-dependent DFT (TDDFT) is the generalization of DFT to time-dependent problems [55]. It is an exact reformulation of the many-body time-dependent Schrödinger equation for the calculation of neutral excitations (i.e. when the number of electrons in the system is kept fixed). The Runge-Gross theorem published in 1984 [55], which plays the same role of the HK theorem for static DFT, states that there is a one-to-one correspondence between time-dependent electronic density  $n(\mathbf{r}, t)$  and time-dependent external potential  $V^{\text{ext}}(\mathbf{r}, t)$ <sup>1</sup>. As for the KS approach of static DFT, we then introduce an auxiliary system of non-interacting

---

<sup>1</sup>We assume that the time-dependent external perturbation is switched on at a time  $t = t_0$  and that the system is initially at rest in a static potential, so that  $V^{\text{ext}}(\mathbf{r}, t) = V^{\text{ext}}(\mathbf{r})$  at all times  $t < t_0$ .

particles that reproduces the time-dependent density of the true many-body system. The time-dependent density can be found by solving the time-dependent KS equations

$$\left[ -\frac{1}{2}\nabla^2 + V^{\text{ext}}(\mathbf{r}, t) + V^{\text{H}}(\mathbf{r}, t) + V^{\text{xc}}(\mathbf{r}, t) \right] \psi_{\alpha}(\mathbf{r}, t) = i\hbar \frac{\partial \psi_{\alpha}(\mathbf{r}, t)}{\partial t} \quad (2.3)$$

with density given by

$$n(\mathbf{r}, t) = \sum_{\alpha} f_{\alpha}(t) |\psi_{\alpha}(\mathbf{r}, t)|^2, \quad (2.4)$$

where  $f_{\alpha}(t)$  is the time-dependent occupation function of the wavefunction  $\psi_{\alpha}(\mathbf{r}, t)$ .  $V^{\text{H}}(\mathbf{r}, t)$  and  $V^{\text{xc}}(\mathbf{r}, t)$  are the time-dependent generalizations of the Hartree and exchange-correlation potentials defined in static DFT.

## 2.2 DFT in practice

A common approach used to numerically solve the KS equations in periodic systems is the plane-wave pseudopotential method. Since it is the method used in this work, we briefly describe it below.

### 2.2.1 Pseudopotential approximation

In the pseudopotential approximation, we replace the Coulomb potential due to the nuclei and the explicit description of the tightly bound core electrons with an effective potential  $V^{\text{PS}}$  acting only on the valence electrons. In this way, we avoid to describe the strong oscillations of the true valence wavefunctions close to the nuclei by replacing them with smooth pseudo wavefunctions. The pseudopotential approximation therefore assumes that core electrons do not contribute significantly to chemical bonding and are not substantially changed as a result of structural modifications, so that they can be safely considered frozen in the atomic nuclei (frozen core approximation). The price to pay for this computational simplification is that pseudopotentials are non-local in space, i.e.

$$V^{\text{PS}}(\mathbf{r}, \mathbf{r}') = V^{\text{loc}}(\mathbf{r}) + V^{\text{nl}}(\mathbf{r}, \mathbf{r}'), \quad (2.5)$$

where we indicate with  $V^{\text{loc}}(\mathbf{r})$  the local contribution and with  $V^{\text{nl}}(\mathbf{r}, \mathbf{r}')$  the non-local contribution. First-principles pseudopotentials are constructed from all-electron atomic calculations with the goal to reproduce as accurately as possible the scattering properties of the true atomic potential by imposing that atomic all-electron and pseudo wavefunctions are identical after a chosen core radius and that they have the same atomic eigenenergies.

These types of pseudopotentials are distinguished in three main categories: norm-conserving (NC) [56], ultrasoft (US) [57] and projector-augmented wave (PAW) [58]. In the construction of

NC pseudopotentials, the norm of each pseudo wavefunction is imposed to be identical to its corresponding all-electron wavefunction. The constraint of norm conservation is instead relaxed in the US and PAW formalisms so that smoother pseudo wavefunctions can be obtained but at the expenses of a more complex mathematical formalism.

### 2.2.2 Plane waves basis set

In periodic systems the KS wavefunctions satisfy Bloch theorem and can be written in the form  $\psi_{n\mathbf{k}}(\mathbf{r}) = e^{i\mathbf{k}\cdot\mathbf{r}} u_{n\mathbf{k}}(\mathbf{r})$ , where  $n$  and  $\mathbf{k}$  are the band index and the crystal wavevector, respectively. The function  $u_{n\mathbf{k}}(\mathbf{r})$  is periodic with the periodicity of the lattice, i.e.  $u_{n\mathbf{k}}(\mathbf{r} + \mathbf{R}) = u_{n\mathbf{k}}(\mathbf{r})$  for each Bravais lattice vector  $\mathbf{R}$  of the crystal.

The numerical solution of the KS equations in periodic systems using the pseudopotential method is efficiently obtained by expanding the wavenfunctions in a basis of plane waves as

$$\psi_{n\mathbf{k}}(\mathbf{r}) = \sum_{\mathbf{G}} e^{i(\mathbf{k}+\mathbf{G})\cdot\mathbf{r}} c_{n\mathbf{k}}(\mathbf{G}), \quad (2.6)$$

where the summation runs over the reciprocal lattice vectors  $\mathbf{G}$  and  $\{c_{n\mathbf{k}}(\mathbf{G})\}$  identifies the set of Fourier coefficients of  $\psi_{n\mathbf{k}}(\mathbf{r})$ . In practice, only a finite number of plane waves can be included in real numerical simulations and the total number of plane waves used in the expansion is specified by the condition

$$\frac{|\mathbf{k} + \mathbf{G}|^2}{2} < E_c, \quad (2.7)$$

where  $E_c$ , called wavefunction cutoff, is the parameter that controls the extension of the plane-waves basis and so the accuracy of the simulations.

When expanded in a plane-waves basis set, the KS equation  $H^{\text{KS}} |\psi_{n\mathbf{k}}\rangle = E_{n\mathbf{k}} |\psi_{n\mathbf{k}}\rangle$  is rewritten in matrix form as a secular equation and eigenvalues and eigenvectors are computed with efficient iterative diagonalization algorithms. In the non-collinear case where the spin-orbit coupling is explicitly included in the DFT calculation,  $n$  has to be understood as a spinorial band index and  $|\psi_{n\mathbf{k}}\rangle$  as a two-component spinor. Besides, for each matrix element and scalar product, this implies that we perform both an integration over the space variable  $\mathbf{r}$  and a summation over the spin variable.

## 2.3 Response function in TDDFT

A possible way to solve the time-dependent KS equations of Eq. 2.3 is with time propagation methods. In principle, this approach gives the exact (i.e. valid at all orders in perturbation theory) time-dependent density  $n(\mathbf{r}, t)$  at all times. Here we consider instead the simpler situation in which the external time-dependent perturbation is small compared to the static external potential so that linear response theory can be applied [59]. The linear response

function allows one to calculate the neutral excitations of the system in terms of the solution of the static KS problem.

The response function is defined as the functional derivative of the density with respect to the external potential

$$\chi(\mathbf{r}, \mathbf{r}', t - t') = \left. \frac{\delta n(\mathbf{r}, t)}{\delta V^{\text{ext}}(\mathbf{r}', t')} \right|_{V^{\text{ext}}(\mathbf{r}', t') = V^{\text{ext}}(\mathbf{r}')}. \quad (2.8)$$

To calculate the response function in practice, we use the chain rule

$$\chi(\mathbf{r}, \mathbf{r}', t - t') = \int dt_1 \int d\mathbf{r}_1 \frac{\delta n(\mathbf{r}, t)}{\delta V^{\text{KS}}(\mathbf{r}_1, t_1)} \frac{\delta V^{\text{KS}}(\mathbf{r}_1, t_1)}{\delta V^{\text{ext}}(\mathbf{r}', t')}. \quad (2.9)$$

We define

$$\chi^{\text{KS}}(\mathbf{r}, \mathbf{r}', t - t') = \left. \frac{\delta n(\mathbf{r}, t)}{\delta V^{\text{KS}}(\mathbf{r}', t')} \right|_{V^{\text{KS}}(\mathbf{r}', t') = V^{\text{KS}}(\mathbf{r}')}, \quad (2.10)$$

which is the response function of the non-interacting KS electrons. It can be obtained in frequency space as a straightforward exercise of time-dependent perturbation theory in terms of the solutions of the static KS equations (see Eq. 2.1)

$$\chi^{\text{KS}}(\mathbf{r}, \mathbf{r}', \omega) = \sum_{\alpha, \beta} (f_\alpha - f_\beta) \frac{n_{\alpha, \beta}(\mathbf{r}) n_{\beta, \alpha}(\mathbf{r}')}{\omega - (E_\beta - E_\alpha) + i\eta}, \quad (2.11)$$

where  $n_{\alpha, \beta}(\mathbf{r}) = \langle \psi_\alpha | \hat{n}(\mathbf{r}) | \psi_\beta \rangle = \psi_\alpha^*(\mathbf{r}) \psi_\beta(\mathbf{r})$ . Given that the Hartree and the exchange-correlation potentials are functional of the density, after applying again the chain rule and moving to frequency space we obtain a Dyson-like equation for the first-order response function in TDDFT [60]

$$\chi(\mathbf{r}, \mathbf{r}', \omega) = \chi^{\text{KS}}(\mathbf{r}, \mathbf{r}', \omega) + \int d\mathbf{r}_1 \int d\mathbf{r}_2 \chi^{\text{KS}}(\mathbf{r}, \mathbf{r}_1, \omega) \left[ \frac{1}{|\mathbf{r}_1 - \mathbf{r}_2|} + f^{\text{xc}}(\mathbf{r}_1, \mathbf{r}_2, \omega) \right] \chi(\mathbf{r}_2, \mathbf{r}', \omega), \quad (2.12)$$

where we define the exchange-correlation kernel as

$$f^{\text{xc}}(\mathbf{r}_1, \mathbf{r}_2, t_1 - t_2) = \left. \frac{\delta V^{\text{xc}}(\mathbf{r}_1, t_1)}{\delta n(\mathbf{r}_2, t_2)} \right|_{n(\mathbf{r}_2, t_2) = n(\mathbf{r}_2)}. \quad (2.13)$$

All many-body effects due to the interaction among electrons are in principle taken into account by the unknown exchange-correlation kernel.

We notice here that TDDFT is a theory valid only for longitudinal perturbations that couple scalar potentials to the density and not for transverse perturbations, such as photons, that instead couple vector potentials to the current density. Therefore, the extension of TDDFT to

## Chapter 2. Electronic-structure theory

---

currents, i.e. time-dependent current density-functional theory (TD-CDFT), should in principle be used in order to deal with transverse perturbations [61, 62]. However, the equivalence of longitudinal and transverse approach in the optical limit [63, 64, 65] makes the TDDFT treatment described up to now valid also for the study of optical properties.



## 3 Optical properties in linear response

In this Chapter, we first show the expressions that link measurable optical constants, such as the reflectivity, to the material parameters that characterize the medium, in particular to the macroscopic dielectric function. These expressions are found by solving the Maxwell's equations for electromagnetic waves propagating inside the medium. Subsequently we calculate the charge density induced in the system by the external perturbation in terms of the electronic structure of the material by using linear response theory within the framework of TDDFT. The induced charge density is then connected to the macroscopic dielectric function by performing a macroscopic average appropriate for periodic systems.

Since we are only interested in the optical properties of metals we calculate the response function within the independent particle approximation, which corresponds to neglect effects related to the electron-hole interaction (excitonic effects) as well as those related to the rapidly varying microscopic electric fields inside the material (local field effects). Since the momentum of optical photon is negligible, we can consider the optical limit, i.e. the limit of zero transferred momentum, of the expression for the macroscopic dielectric function in the independent particle approximation. In metals we show that the macroscopic dielectric function is conveniently divided in an interband and in an intraband contribution. Eventually we discuss how the two contributions are related one to the other by the  $f$ -sum rule and how the pseudopotential approximation affects the calculation of the optical properties.

The theoretical treatments discussed in this Chapter can be found in several textbooks, in particular we cite Refs. [66, 67, 68].

### 3.1 Optical measurements

Typical optical measurements give access to optical constants, such as absorption coefficient and reflectivity, as a function of the wavelength of light. These quantities can be assumed to be macroscopic (i.e. that vary on a macroscopic scale) because the spatial resolution of optical experiments is related to the wavelength of optical photons, which is of the order of hundreds of nanometers. Solids can then be approximated as continuous when studying optical experiments.

In practice, the reflectivity can be for example measured<sup>1</sup> with a spectrophotometer, where monochromatic light is shined onto a sample and the fraction of light that is reflected is then assessed. From more complex optical measurements such as ellipsometry, where the reflectivity of polarized light at oblique angles of incidence is measured, it is possible to indirectly have access also to more “fundamental” material properties, such as the full macroscopic dielectric function, which completely describe the optical properties of the material. From the point of view of colour perception, instead, it is the human eye the optical instrument that “measures” the incoming light and transforms it in bioelectrical signals that are sent to the brain and that allows us to “see” the colours.

### 3.2 Maxwell's equations

#### 3.2.1 Microscopic equations

The physical phenomenon that we have to describe in order to compute by first-principles the optical properties of a material is the interaction of light with matter from a microscopic point of view. The interaction between electromagnetic fields and matter is described by the microscopic Maxwell's equations, which are

$$\nabla \cdot \mathbf{E}^{\text{tot}}(\mathbf{r}, t) = 4\pi\rho^{\text{tot}}(\mathbf{r}, t) \quad (3.1)$$

$$\nabla \times \mathbf{E}^{\text{tot}}(\mathbf{r}, t) = -\frac{1}{c} \frac{\partial \mathbf{B}^{\text{tot}}(\mathbf{r}, t)}{\partial t} \quad (3.2)$$

$$\nabla \cdot \mathbf{B}^{\text{tot}}(\mathbf{r}, t) = 0 \quad (3.3)$$

$$\nabla \times \mathbf{B}^{\text{tot}}(\mathbf{r}, t) = \frac{4\pi}{c} \mathbf{J}^{\text{tot}}(\mathbf{r}, t) + \frac{1}{c} \frac{\partial \mathbf{E}^{\text{tot}}(\mathbf{r}, t)}{\partial t}. \quad (3.4)$$

In Maxwell's equations,  $\mathbf{E}^{\text{tot}}(\mathbf{r}, t)$  and  $\mathbf{B}^{\text{tot}}(\mathbf{r}, t)$  are the total microscopic electric and magnetic fields, respectively, while  $\mathbf{J}^{\text{tot}}(\mathbf{r}, t)$  and  $\rho^{\text{tot}}(\mathbf{r}, t)$  are the total current and charge densities, respectively. We divide current and charge densities in external and induced contributions,

$$\mathbf{J}^{\text{tot}}(\mathbf{r}, t) = \mathbf{J}^{\text{ext}}(\mathbf{r}, t) + \mathbf{J}^{\text{ind}}(\mathbf{r}, t) \quad (3.5)$$

$$\rho^{\text{tot}}(\mathbf{r}, t) = \rho^{\text{ext}}(\mathbf{r}, t) + \rho^{\text{ind}}(\mathbf{r}, t), \quad (3.6)$$

and we do the same for electric and magnetic fields. Local charge conservation follows directly from Maxwell's equations (combining Eq. 3.1 and Eq. 3.4) and is expressed as a continuity equation:

$$\nabla \cdot \mathbf{J}^{\text{tot}}(\mathbf{r}, t) + \frac{\partial \rho^{\text{tot}}(\mathbf{r}, t)}{\partial t} = 0. \quad (3.7)$$

---

<sup>1</sup>Strictly speaking it is the reflectance and not the reflectivity that is measured in experiments. However, in the limit of thick opaque materials, reflectivity and reflectance are equivalent, but the two values can be substantially different when performing optical experiments on, for example, thin films.

### 3.2.2 Macroscopic equations

As explained at the beginning of this Chapter, typical optical experiments measure quantities that vary on a macroscopic scale. A macroscopic version of the Maxwell's equations can be derived from the microscopic ones written above and that retains the same form of the microscopic version. Macroscopic quantities are obtained by an appropriate spatial average of the corresponding microscopic quantities over distances large compared to the dimension of the primitive cell but small compared to the wavelength of light (the actual average procedure used for periodic crystals will be discussed later in Section 3.3.2 and in Appendix A). To distinguish a macroscopic quantity from its microscopic counterpart, we use the notation for which we add a capital letter M as a subscript for the given quantity (e.g.  $\rho^{\text{tot}}(\mathbf{r}, t) \rightarrow \rho_{\text{M}}^{\text{tot}}(\mathbf{r}, t)$  for the total charge density).

It is common practice to write the macroscopic Maxwell's equations by introducing a polarization field that is defined by the equation

$$\mathbf{J}_{\text{M}}^{\text{ind}}(\mathbf{r}, t) = \frac{\partial \mathbf{P}(\mathbf{r}, t)}{\partial t}. \quad (3.8)$$

Because of the continuity equation (see Eq. 3.7) it also follows that  $\rho_{\text{M}}^{\text{ind}}(\mathbf{r}, t) = -\nabla \cdot \mathbf{P}(\mathbf{r}, t)$  and thus we write the external electric field<sup>2</sup> in terms of this polarization field as

$$\mathbf{E}_{\text{M}}^{\text{ext}}(\mathbf{r}, t) = \mathbf{E}_{\text{M}}^{\text{tot}}(\mathbf{r}, t) + 4\pi \mathbf{P}(\mathbf{r}, t). \quad (3.9)$$

Using Eq. 3.8 and Eq. 3.9 and neglecting any magnetic effect, the macroscopic Maxwell's equations obtained from the microscopic ones through the appropriate average procedure<sup>3</sup> are

$$\nabla \cdot \mathbf{E}_{\text{M}}^{\text{ext}}(\mathbf{r}, t) = 4\pi \rho_{\text{M}}^{\text{ext}}(\mathbf{r}, t) \quad (3.10)$$

$$\nabla \times \mathbf{E}_{\text{M}}^{\text{tot}}(\mathbf{r}, t) = -\frac{1}{c} \frac{\partial \mathbf{B}_{\text{M}}^{\text{tot}}(\mathbf{r}, t)}{\partial t} \quad (3.11)$$

$$\nabla \cdot \mathbf{B}_{\text{M}}^{\text{tot}}(\mathbf{r}, t) = 0 \quad (3.12)$$

$$\nabla \times \mathbf{B}_{\text{M}}^{\text{tot}}(\mathbf{r}, t) = \frac{4\pi}{c} \mathbf{J}_{\text{M}}^{\text{ext}}(\mathbf{r}, t) + \frac{1}{c} \frac{\partial \mathbf{E}_{\text{M}}^{\text{ext}}(\mathbf{r}, t)}{\partial t}, \quad (3.13)$$

which are written in terms of the external charge and current densities.

<sup>2</sup>In standard textbooks on electromagnetism, the external electric field is usually called displacement field and is indicated with the symbol  $\mathbf{D}(\mathbf{r}, t)$ .

<sup>3</sup>We only assume that the derivative of the macroscopic average is equal to the macroscopic average of the derivative. This property holds for the average procedure used in Section 3.3.2 for periodic crystals and described in Appendix A.

### 3.2.3 Electromagnetic waves and optical constants

In order to describe the interaction of light with matter, no external sources are present, that is  $\rho_M^{\text{ext}}(\mathbf{r}, t) = 0$  and  $\mathbf{J}_M^{\text{ext}}(\mathbf{r}, t) = \mathbf{0}$  in Maxwell's equations. For simplicity, we consider the experimental situation in which light impinging on the material is a monochromatic wave with wavevector  $\mathbf{q}$  and frequency  $\omega$  and we assume that the system responds, macroscopically, with the same behaviour as the external perturbation, so that the solution for the total electric field can be written as<sup>4</sup>

$$\mathbf{E}_M^{\text{tot}}(\mathbf{r}, t) = \mathbf{E}_M^{\text{tot}} e^{i(\tilde{q}\hat{\mathbf{q}}\cdot\mathbf{r} - \omega t)}, \quad (3.14)$$

where  $\hat{\mathbf{q}}$  is a unit vector giving the direction of propagation of the wave and  $\mathbf{E}_M^{\text{tot}}$  is the amplitude of the field. We allow the wavevector amplitude  $\tilde{q}$  to be complex in order to describe dissipation mechanisms inside the material.

In linear response, the total and external macroscopic electric fields are assumed to be proportional to each other and the linear coefficient linking the two is the complex macroscopic dielectric function. It is defined (for a monochromatic wave with wavevector  $\mathbf{q}$  and frequency  $\omega$ ) by the equation

$$\mathbf{E}_M^{\text{ext}} = \varepsilon_M \mathbf{E}_M^{\text{tot}}. \quad (3.15)$$

The macroscopic dielectric function describes the screening induced inside a material when an external perturbation is applied in order to reduce the total internal electric field and it is the principal material parameter characterizing the propagation of light inside a medium<sup>5</sup>. From Eq. 3.10 in the absence of external charges, we immediately notice that the only possible solutions are transverse plane-waves, because  $\hat{\mathbf{q}} \cdot \mathbf{E}_M^{\text{ext}} = \hat{\mathbf{q}} \cdot \mathbf{E}_M^{\text{tot}} = 0$ . Taking the rotor of Eq. 3.11 and inserting Eq. 3.13 in the resulting right-hand side, we obtain the following wave equation for light propagating inside an energy-absorbing material<sup>6</sup>

$$\nabla^2 \mathbf{E}_M^{\text{tot}}(\mathbf{r}, t) = \frac{\varepsilon_M}{c^2} \frac{\partial^2 \mathbf{E}_M^{\text{tot}}(\mathbf{r}, t)}{\partial t^2}, \quad (3.16)$$

---

<sup>4</sup>We work with complex quantities for convenience in the mathematical manipulations. It is understood that the true physical quantities are obtained by taking the real part of the corresponding complex quantities (e.g. the true total electric field is given by  $\Re[\mathbf{E}_M^{\text{tot}}(\mathbf{r}, t)]$ , where  $\Re$  indicates the real part).

<sup>5</sup>Instead of the macroscopic dielectric function we could equivalently work with the macroscopic optical conductivity, which is defined (always for a monochromatic wave with wavevector  $\mathbf{q}$  and frequency  $\omega$ ) as the linear coefficient linking the total electric field to the induced current density

$$\mathbf{J}_M^{\text{ind}} = \sigma_M \mathbf{E}_M^{\text{tot}}.$$

From Eq. 3.9 and Eq. 3.8 it follows that the macroscopic optical conductivity is related to the macroscopic dielectric function by the equation

$$\sigma_M = i \frac{\omega}{4\pi} (1 - \varepsilon_M).$$

<sup>6</sup>We have made use of the general vector relation:  $\nabla \times \nabla \times \mathbf{E}_M^{\text{tot}}(\mathbf{r}, t) = \nabla(\nabla \cdot \mathbf{E}_M^{\text{tot}}(\mathbf{r}, t)) - \nabla^2 \mathbf{E}_M^{\text{tot}}(\mathbf{r}, t)$ .

which leads to the following condition for the complex wavevector amplitude inside the material:

$$\tilde{q}^2 = \frac{\omega^2}{c^2} \varepsilon_M. \quad (3.17)$$

It is convenient to define also a complex refractive index  $\tilde{n} = n + ik$  as  $\tilde{n} \equiv c\tilde{q}/\omega$  or, equivalently,

$$\tilde{n}^2 \equiv \varepsilon_M. \quad (3.18)$$

The real part  $n$  is what it is commonly known as the refractive index while the imaginary part  $k$  is the so-called extinction coefficient. We can then write the solution for the total electric field as a damped wave for which  $n$  is related to the dispersion of the wave and  $k$  to the damping:

$$\mathbf{E}_M^{\text{tot}}(\mathbf{r}, t) = \mathbf{E}_M^{\text{tot}} e^{i(\frac{\omega}{c} n \hat{\mathbf{q}} \cdot \mathbf{r} - \omega t)} e^{-\frac{\omega}{c} k \hat{\mathbf{q}} \cdot \mathbf{r}}. \quad (3.19)$$

Having found the solution for an electromagnetic wave propagating inside a material, we can now eventually find the explicit expressions for the macroscopic quantities measurable in optical experiments in terms of the macroscopic dielectric function. The decrease in intensity of the propagating wave inside the medium is described by the absorption coefficient  $\alpha$ , which is defined as

$$\alpha = -\frac{1}{I} \frac{dI}{dr}, \quad (3.20)$$

where  $I$  is the intensity of the wave and it is simply the modulus squared of the total electric field. Because of Eq. 3.19 and Eq. 3.18 we get that<sup>7</sup>

$$\alpha = \frac{2\omega k}{c} = \frac{\omega \Im[\varepsilon_M]}{nc}. \quad (3.21)$$

Similarly we can also obtain the reflectivity  $R$ , i.e. the ratio between the reflected and incident intensities, from the Fresnel equations

$$R = \frac{(n-1)^2 + k^2}{(n+1)^2 + k^2}, \quad (3.22)$$

that is valid at normal incidence and at a vacuum-material interface (see for example Ref. [69]). As can be seen from Eqs. 3.18, 3.21 and 3.22, the knowledge of the macroscopic dielectric function gives access to all the optical constants measurable by optical experiments. The

---

<sup>7</sup>For simplicity, we assume that the absorption coefficient is measured along the direction of propagation of the wave so that  $\hat{\mathbf{q}} \parallel \mathbf{r}$ .

main purpose of the following Section is to show how to determine  $\epsilon_M$  from the underlying electronic structure of a material using linear response theory.

### 3.3 Response function

We now show how the macroscopic dielectric function of a material is linked to its underlying electronic structure. Indeed, from a theoretical point of view, the macroscopic dielectric function is the natural quantity to consider for the description of elementary excitations of a material induced by photons.

For this purpose we need to find the induced response of a material to the external electromagnetic perturbation produced by the incoming light starting from the knowledge of the electronic structure of the material. From a microscopic point of view, a solid is an ensemble of electrons and nuclei interacting through the Coulomb interaction and governed by the law of quantum mechanics. The electromagnetic perturbation is typically weak compared to the electrostatic interactions due to the atomic nuclei (e.g. valid for sunlight but not for very intense lasers) so that the response of the system can be expanded into a Taylor series with respect to the perturbation. In this work we consider only the first order response, i.e. we assume that the response is proportional to the perturbation. In this regime, called of linear response, the linear coefficient linking the response to the perturbation is called response function and it has the important property that it depends only on the unperturbed system and not on the perturbation itself.

#### 3.3.1 Linear-response theory

We consider a system of  $M$  interacting electrons at zero temperature described by the time-independent many-body Hamiltonian  $\hat{H}^{(M)}$  and satisfying the static Schrödinger equation

$$\hat{H}^{(M)} |\Psi_s\rangle = E_s^{(M)} |\Psi_s\rangle, \quad (3.23)$$

where  $E_s^{(M)}$  and  $|\Psi_s\rangle$  are the  $M$ -electron eigenvalues and eigenstates of the system, respectively. Let's then suppose to switch on a generic external time-dependent perturbation so that the complete time-dependent Hamiltonian of the system becomes  $\hat{H}^{(M)}(t) = \hat{H}^{(M)} + \hat{H}_{\text{int}}^{(M)}(t)$ . The additional term  $\hat{H}_{\text{int}}^{(M)}(t)$  is the time-dependent interaction Hamiltonian rising from the perturbation. For convenience, we consider only longitudinal perturbing fields so that we are allowed to write an external perturbing electric field as the gradient of a scalar potential

$$\mathbf{E}^{\text{ext}}(\mathbf{r}, t) = -\nabla V^{\text{ext}}(\mathbf{r}, t). \quad (3.24)$$

In this case the interaction Hamiltonian  $\hat{H}_{\text{int}}^{(M)}(t)$  is

$$\hat{H}_{\text{int}}^{(M)}(t) = \int d\mathbf{r} \hat{n}(\mathbf{r}) \delta V^{\text{ext}}(\mathbf{r}, t) \quad (3.25)$$

in which the number density operator is defined as

$$\hat{n}(\mathbf{r}) = \sum_{i=1}^M \delta(\mathbf{r} - \hat{\mathbf{r}}_i) \quad (3.26)$$

and where the external potential

$$V^{\text{ext}}(\mathbf{r}, t) = V^{\text{ext}}(\mathbf{r}) + \delta V^{\text{ext}}(\mathbf{r}, t) \quad (3.27)$$

is given by the sum of the static Coulomb electron-nucleus interaction  $V^{\text{ext}}(\mathbf{r})$  and the time-dependent external perturbation  $\delta V^{\text{ext}}(\mathbf{r}, t)$ . The fact that the external perturbation is weak with respect to the electrostatic interactions due to the atomic nuclei means that  $|\delta V^{\text{ext}}| \ll |V^{\text{ext}}|$  in every point inside the material and at every time.

As shown by Eq. 3.25, longitudinal fields have the clear advantage that they are coupled with the density of the system, which is the fundamental variable in DFT and TDDFT (see Chapter 2). Nonetheless, it is important to notice that a theoretical treatment restricted to deal only with longitudinal fields is in principle not correct for an electromagnetic perturbation because photons are a transverse perturbation (indeed the electric field is perpendicular to the direction of propagation  $\mathbf{E} \perp \hat{\mathbf{q}}$ , as shown in Section 3.2). The longitudinal approach is instead correct in the description of electron energy loss spectroscopy (EELS) where the perturbation is given by a beam of electrons which, indeed, produces longitudinal fields. However, the longitudinal and transverse approaches are equivalent in the optical limit  $\mathbf{q} \rightarrow \mathbf{0}$ . In this case the two types of perturbation give the same response [63, 64, 65] so that optical and EELS experiments furnish the same physical information. The equivalence of the two approaches follows from the gauge invariance between length gauge and velocity gauge due to the continuity equation (see Eq. 3.7).

In linear response theory, i.e. assuming that the response of the system is linear in the perturbation, the change in density  $\delta n(\mathbf{r}, t)$  due to the external perturbation is given by [68]

$$\delta n(\mathbf{r}, t) = \int_{-\infty}^{\infty} dt' \int d\mathbf{r}' \chi(\mathbf{r}, \mathbf{r}', t - t') \delta V^{\text{ext}}(\mathbf{r}', t'). \quad (3.28)$$

The function  $\chi(\mathbf{r}, \mathbf{r}', t - t')$  is called density-density response function and it is formally defined as

$$\chi(\mathbf{r}, \mathbf{r}', t - t') \equiv -\frac{i}{\hbar} \Theta(t - t') \langle \Psi_0 | [\hat{n}(\mathbf{r}, t - t'), \hat{n}(\mathbf{r}')] | \Psi_0 \rangle, \quad (3.29)$$

### Chapter 3. Optical properties in linear response

where  $\Theta(t)$  is the Heaviside step function and ensures causality (indeed  $\chi(\mathbf{r}, \mathbf{r}', t - t') = 0$  if  $t < t'$ ),  $\hat{n}(\mathbf{r}, t) \equiv e^{\frac{i}{\hbar} \hat{H}^{(M)} t} \hat{n}(\mathbf{r}) e^{-\frac{i}{\hbar} \hat{H}^{(M)} t}$  is the density operator in the Heisenberg picture and  $|\Psi_0\rangle$  is the many-body ground-state wavefunction. Within this formalism the induced charge density appearing in the microscopic Maxwell's equations is  $\rho^{\text{ind}}(\mathbf{r}, t) = (-e)\delta n(\mathbf{r}, t)$ . Because of the translational invariance of the response function with respect to time, if we use the convolution theorem for the time integration we get that in frequency space

$$\delta n(\mathbf{r}, \omega) = \int d\mathbf{r}' \chi(\mathbf{r}, \mathbf{r}', \omega) \delta V^{\text{ext}}(\mathbf{r}', \omega). \quad (3.30)$$

Starting from Eq. 3.29, the response function can be easily written in terms of the solutions of the  $M$ -electron many-body Schrödinger equation given in Eq. 3.23

$$\chi(\mathbf{r}, \mathbf{r}', \omega) = \sum_{s \neq 0} \left[ \frac{\langle \Psi_0 | \hat{n}(\mathbf{r}) | \Psi_s \rangle \langle \Psi_s | \hat{n}(\mathbf{r}') | \Psi_0 \rangle}{\omega - (E_s^{(M)} - E_0^{(M)}) + i\eta} - \frac{\langle \Psi_s | \hat{n}(\mathbf{r}) | \Psi_0 \rangle \langle \Psi_0 | \hat{n}(\mathbf{r}') | \Psi_s \rangle}{\omega + (E_s^{(M)} - E_0^{(M)}) + i\eta} \right], \quad (3.31)$$

in which  $\eta$  is a broadening introduced to perform the adiabatic switching-on of the perturbation [68]. The expression above shows that the poles of the response functions correspond to the excitation energies of the system. However it is not useful for numerical simulations because we do not know how to calculate in practice the many-body wavefunctions and their corresponding eigenenergies. As a consequence we need alternative ways to compute the response function. A possible approach, as described in Section 2.3, is to calculate the response function within the framework of TDDFT.

#### 3.3.2 Microscopic-macroscopic connection

From now on, we focus on the study of crystals which are periodic systems having the discrete periodicity of the lattice. To effectively exploit this symmetry it is convenient to perform a Fourier transform and to work in reciprocal space. We define the spatial Fourier transform of  $\chi(\mathbf{r}, \mathbf{r}', \omega)$  as

$$\chi(\mathbf{q}, \mathbf{q}', \omega) = \frac{1}{V} \int d\mathbf{r} e^{-i\mathbf{q}\cdot\mathbf{r}} \int d\mathbf{r}' e^{i\mathbf{q}'\cdot\mathbf{r}'} \chi(\mathbf{r}, \mathbf{r}', \omega) \quad (3.32)$$

where  $V$  is the volume of the crystal. In periodic crystals the density-density response function has the periodicity of the lattice, i.e.  $\chi(\mathbf{r} + \mathbf{R}, \mathbf{r}' + \mathbf{R}, \omega) = \chi(\mathbf{r}, \mathbf{r}', \omega)$  for each Bravais lattice vector  $\mathbf{R}$ . This means that the Fourier transform  $\chi(\mathbf{q}, \mathbf{q}', \omega)$  is different from zero only if  $\mathbf{q}$  and  $\mathbf{q}'$  differ by a reciprocal lattice vector [68]. For convenience we use the notation  $\chi_{\mathbf{G}, \mathbf{G}'}(\mathbf{q}, \omega) \equiv \chi(\mathbf{q} + \mathbf{G}, \mathbf{q} + \mathbf{G}', \omega)$  so that the Fourier expansion of the response function is

$$\chi(\mathbf{r}, \mathbf{r}', \omega) = \frac{1}{V} \sum_{\mathbf{q} \in \text{BZ}} \sum_{\mathbf{G}, \mathbf{G}'} e^{i(\mathbf{q} + \mathbf{G})\cdot\mathbf{r}} \chi_{\mathbf{G}, \mathbf{G}'}(\mathbf{q}, \omega) e^{-i(\mathbf{q} + \mathbf{G}')\cdot\mathbf{r}'}, \quad (3.33)$$



and we can write Eq. 3.30 in reciprocal space as

$$\delta n(\mathbf{q} + \mathbf{G}) = \sum_{\mathbf{G}'} \chi_{\mathbf{G}, \mathbf{G}'}(\mathbf{q}, \omega) \delta V^{\text{ext}}(\mathbf{q} + \mathbf{G}', \omega). \quad (3.34)$$

In terms of scalar potentials (see Eq. 3.24) the macroscopic dielectric function defined in Eq. 3.15 is given by

$$\epsilon_{\text{M}}(\mathbf{q}, \omega) \equiv \frac{\delta V_{\text{M}}^{\text{ext}}(\mathbf{q}, \omega)}{\delta V_{\text{M}}^{\text{tot}}(\mathbf{q}, \omega)}, \quad (3.35)$$

where we now explicitly write the dependence on the wavevector  $\mathbf{q}$  and the frequency  $\omega$ . To link the macroscopic dielectric function to the response function it is convenient to first introduce a microscopic (inverse) dielectric function  $\epsilon^{-1}(\mathbf{r}, \mathbf{r}', t)$  that links total and external microscopic potentials

$$\delta V^{\text{tot}}(\mathbf{r}, t) = \int_{-\infty}^{\infty} dt' \int d\mathbf{r}' \epsilon^{-1}(\mathbf{r}, \mathbf{r}', t - t') \delta V^{\text{ext}}(\mathbf{r}', t'). \quad (3.36)$$

As done in Maxwell's equations for the electric field, the total microscopic potential is divided in an external and an induced part. The induced potential seen by a test charge is the Hartree potential produced by the change in density due to the external perturbation [70] so that

$$\delta V^{\text{tot}}(\mathbf{r}, t) = \delta V^{\text{ext}}(\mathbf{r}, t) + \delta V^{\text{ind}}(\mathbf{r}, t) = \delta V^{\text{ext}}(\mathbf{r}, t) + \int d\mathbf{r}' \frac{\delta n(\mathbf{r}', t)}{|\mathbf{r} - \mathbf{r}'|}. \quad (3.37)$$

Moving to frequency space and inserting the expression of Eq. 3.30 for the change in density in Eq. 3.37, we obtain the following expression for the microscopic dielectric function defined in Eq. 3.36

$$\epsilon^{-1}(\mathbf{r}, \mathbf{r}', \omega) = \delta(\mathbf{r} - \mathbf{r}') + \int d\mathbf{r}'' \frac{\chi(\mathbf{r}'', \mathbf{r}', \omega)}{|\mathbf{r} - \mathbf{r}''|}, \quad (3.38)$$

which, in reciprocal space, becomes

$$\epsilon_{\mathbf{G}, \mathbf{G}'}^{-1}(\mathbf{q}, \omega) = \delta_{\mathbf{G}, \mathbf{G}'} + \frac{4\pi}{|\mathbf{q} + \mathbf{G}|^2} \chi_{\mathbf{G}, \mathbf{G}'}(\mathbf{q}, \omega). \quad (3.39)$$

In order to calculate the macroscopic dielectric function from the corresponding microscopic dielectric function, we need to use an appropriate average procedure, as described in Appendix A for periodic systems, that smooths out the rapidly varying fluctuations of the microscopic quantities. For monochromatic optical photons of wavevector  $\mathbf{q}$  and frequency  $\omega$ , the external perturbation is already macroscopic and  $\delta V^{\text{ext}}(\mathbf{q} + \mathbf{G}, \omega) = \delta V^{\text{ext}}(\mathbf{q} + \mathbf{0}, \omega) \delta_{\mathbf{G}, \mathbf{0}}$ .

From Eq. 3.36 we have that in reciprocal space

$$\delta V^{\text{tot}}(\mathbf{q} + \mathbf{G}, \omega) = \sum_{\mathbf{G}'} \varepsilon_{\mathbf{G}, \mathbf{G}'}^{-1}(\mathbf{q}, \omega) \delta V^{\text{ext}}(\mathbf{q} + \mathbf{G}', \omega) \quad (3.40)$$

$$= \varepsilon_{\mathbf{G}, \mathbf{0}}^{-1}(\mathbf{q}, \omega) \delta V^{\text{ext}}(\mathbf{q} + \mathbf{0}, \omega) \quad (3.41)$$

As shown in Appendix A, for small  $\mathbf{q}$  the macroscopic average of a microscopic quantity is simply given by the Fourier component  $\mathbf{G} = \mathbf{0}$  of the corresponding microscopic quantity. Thus, if we consider the  $\mathbf{G} = \mathbf{0}$  component of the total potential,  $\delta V^{\text{tot}}(\mathbf{q} + \mathbf{0}, \omega) = \varepsilon_{\mathbf{0}, \mathbf{0}}^{-1}(\mathbf{q}, \omega) \delta V^{\text{ext}}(\mathbf{q} + \mathbf{0}, \omega)$ . In conclusion, because of Eq. 3.35, the macroscopic dielectric function is linked to the microscopic dielectric function and therefore to the response function through the relation

$$\varepsilon_{\text{M}}(\mathbf{q}, \omega) = \frac{1}{\varepsilon_{\mathbf{0}, \mathbf{0}}^{-1}(\mathbf{q}, \omega)} = \frac{1}{1 + \frac{4\pi}{|\mathbf{q}|^2} \chi_{\mathbf{0}, \mathbf{0}}(\mathbf{q}, \omega)}. \quad (3.42)$$

### 3.3.3 Independent particle approximation in TDDFT

In order to evaluate  $\varepsilon_{\text{M}}(\mathbf{q}, \omega)$  the next step required is to find an expression for  $\chi_{\mathbf{0}, \mathbf{0}}(\mathbf{q}, \omega)$  that can be used for first-principles simulations. There are two main rigorous approaches to calculate the response function commonly used for the first-principles simulations of materials: TDDFT and MBPT [71]. Here we only discuss the approach based on TDDFT and linear-response theory, in particular applied to the study of periodic systems. In Section 2.3 we have shown that the response function in TDDFT satisfies a Dyson-like equation written in terms of the non-interacting KS response function (see Eq. 2.12). Since we are dealing with periodic crystals, we again move to reciprocal space so that we rewrite Eq. 2.12 in a matrix form where the basis functions are plane waves

$$\chi_{\mathbf{G}, \mathbf{G}'}(\mathbf{q}, \omega) = \chi_{\mathbf{G}, \mathbf{G}'}^{\text{KS}}(\mathbf{q}, \omega) + \sum_{\mathbf{G}_1, \mathbf{G}_2} \chi_{\mathbf{G}, \mathbf{G}'}^{\text{KS}} \left[ \frac{4\pi}{|\mathbf{q} + \mathbf{G}_1|^2} \delta_{\mathbf{G}_1, \mathbf{G}_2} + f_{\mathbf{G}_1, \mathbf{G}_2}^{\text{xc}}(\mathbf{q}, \omega) \right] \chi_{\mathbf{G}_2, \mathbf{G}'}(\mathbf{q}, \omega). \quad (3.43)$$

In the independent particle approximation (IPA) the exchange-correlation kernel  $f^{\text{xc}}$  is assumed to be zero and only the long-range contribution of the Coulomb interaction  $\mathbf{G}_1 = \mathbf{0}$  is considered in Eq. 3.43. The terms with  $\mathbf{G}_1 > \mathbf{0}$  take into account the effects due to the microscopic oscillations of the total potential (called local field effects), which in elemental metals are completely negligible (e.g. see Ref. [72] for the case of elemental copper) while in alloys they can affect the intensity of the optical absorption, especially in strongly ionic compounds (see Ref. [73] for a discussion on alkali-noble intermetallics), but in general they do not modify the main spectral features of the material (such as position of the onset of absorption and/or of the main peaks/valleys in the spectra). Furthermore, in metals we can also safely neglect static electron-hole interactions because they are screened by the conduction electrons, so that  $f^{\text{xc}} = 0$  is a reasonable approximation (only dynamical excitonic effects can possibly affect the intensity of the optical absorption spectra in metals [74]). The main inaccuracies of the IPA

approximation for the first-principles calculation of the optical properties of metals are due to the errors introduced in the evaluation of  $\chi_{\mathbf{G},\mathbf{G}'}^{\text{KS}}(\mathbf{q}, \omega)$  by the use of the PBE electronic structure. As already mentioned in Section 1.3, improvements in the accuracy of the band structures can be obtained by computing the quasi-particle corrections on top of the PBE results (typically at the *GW* level [75, 71, 76] of MBPT), albeit at a largely increased computational cost. On the other hand, in finite-gap systems, where the electron-hole interaction gives in general an important contribution to the optical properties, the exchange-correlation kernel needs to be properly included when solving Eq. 3.43<sup>8</sup>.

Within the IPA we can invert Eq. 3.43 and write explicitly the head (i.e. the matrix element  $\mathbf{G} = \mathbf{G}' = \mathbf{0}$ ) of the IPA response function, that we indicate as  $\chi_{\mathbf{G},\mathbf{G}'}^{\text{IPA}}(\mathbf{q}, \omega)$ , as

$$\chi_{\mathbf{0},\mathbf{0}}^{\text{IPA}}(\mathbf{q}, \omega) = \frac{\chi_{\mathbf{0},\mathbf{0}}^{\text{KS}}(\mathbf{q}, \omega)}{1 - \frac{4\pi}{|\mathbf{q}|^2} \chi_{\mathbf{0},\mathbf{0}}^{\text{KS}}(\mathbf{q}, \omega)}. \quad (3.44)$$

Thus, according to Eq. 3.42, the macroscopic dielectric function in the IPA is given by

$$\varepsilon_{\text{M}}^{\text{IPA}}(\mathbf{q}, \omega) = 1 - \frac{4\pi}{|\mathbf{q}|^2} \chi_{\mathbf{0},\mathbf{0}}^{\text{KS}}(\mathbf{q}, \omega). \quad (3.45)$$

From Eq. 2.11 transformed into reciprocal space we find that the KS response function for Bloch states is

$$\chi_{\mathbf{G},\mathbf{G}'}^{\text{KS}}(\mathbf{q}, \omega) = \frac{1}{V} \sum_{\mathbf{k}, \mathbf{k}'} \sum_{n, n'} (f_{n\mathbf{k}} - f_{n'\mathbf{k}'}) \frac{\langle \psi_{n\mathbf{k}} | e^{-i(\mathbf{q}+\mathbf{G})\cdot\mathbf{r}} | \psi_{n'\mathbf{k}'} \rangle \langle \psi_{n'\mathbf{k}'} | e^{i(\mathbf{q}+\mathbf{G}')\cdot\mathbf{r}} | \psi_{n\mathbf{k}} \rangle}{\omega - (E_{n'\mathbf{k}'} - E_{n\mathbf{k}}) + i\eta} \quad (3.46)$$

$$= \frac{1}{V} \sum_{\mathbf{k}} \sum_{n, n'} (f_{n\mathbf{k}} - f_{n'\mathbf{k}+\mathbf{q}}) \frac{\langle \psi_{n\mathbf{k}} | e^{-i(\mathbf{q}+\mathbf{G})\cdot\mathbf{r}} | \psi_{n'\mathbf{k}+\mathbf{q}} \rangle \langle \psi_{n'\mathbf{k}+\mathbf{q}} | e^{i(\mathbf{q}+\mathbf{G}')\cdot\mathbf{r}} | \psi_{n\mathbf{k}} \rangle}{\omega - (E_{n'\mathbf{k}+\mathbf{q}} - E_{n\mathbf{k}}) + i\eta}, \quad (3.47)$$

where the last step follows by noticing that the matrix elements entering in Eq. 3.46 are non zero only if  $\mathbf{k}' = \mathbf{k} + \mathbf{q}$  because of the conservation of crystal momentum [77]. Unless specified otherwise, the summations over the bands (with indices  $n$  and  $n'$  in Eq. 3.46) are over all occupied and unoccupied bands. Finally, we are able to write the explicit expression of the frequency- and wavevector-dependent IPA dielectric function of Eq. 3.45:

$$\varepsilon_{\text{M}}^{\text{IPA}}(\mathbf{q}, \omega) = 1 - \frac{4\pi}{|\mathbf{q}|^2} \frac{1}{V} \sum_{\mathbf{k}} \sum_{n, n'} (f_{n\mathbf{k}} - f_{n'\mathbf{k}+\mathbf{q}}) \frac{|\langle \psi_{n'\mathbf{k}+\mathbf{q}} | e^{i\mathbf{q}\cdot\mathbf{r}} | \psi_{n\mathbf{k}} \rangle|^2}{\omega - (E_{n'\mathbf{k}+\mathbf{q}} - E_{n\mathbf{k}}) + i\eta}. \quad (3.48)$$

<sup>8</sup>Alternatively, within the framework of MBPT, the electron-hole interaction is taken into account by solving the Bethe-Salpeter equation (BSE) [64], which, as of today, it is the method of choice for the calculation of the optical properties of semiconductors and insulators.

### 3.4 Optical limit

Since we are interested in the optical properties of solids, we need to study the optical limit,  $\mathbf{q} \rightarrow \mathbf{0}$ , of Eq. 3.48. Indeed, the momentum of optical photons ( $\sim 10^{-3} - 10^{-4} \text{ \AA}^{-1}$ ) can be safely assumed negligible compared to the size of a crystal BZ ( $\sim 1 \text{ \AA}^{-1}$ ). We note that  $\epsilon_M^{\text{IPA}}(\mathbf{q}, \omega)$ , as given in Eq. 3.48, is not defined for  $\mathbf{q} = \mathbf{0}$  because of the diverging term  $1/|\mathbf{q}|^2$ . Therefore, we need to explicitly study the  $\mathbf{q} \rightarrow \mathbf{0}$  limit by expanding  $\epsilon_M^{\text{IPA}}(\mathbf{q}, \omega)$  in a Taylor series around  $\mathbf{q} = \mathbf{0}$ . In general the macroscopic dielectric function depends on the direction  $\hat{\mathbf{q}} = \mathbf{q}/|\mathbf{q}|$  of the perturbing electric field, but for crystals with cubic symmetry it is the same in every direction. From this point on, we simplify the notation and drop the subscript M and superscript IPA in  $\epsilon_M^{\text{IPA}}(\mathbf{q}, \omega)$ . If not specified otherwise, in the following we always deal with the macroscopic dielectric function within the IPA.

To calculate the optical limit, we first expand the matrix elements to first order in  $\mathbf{q}$  [66]:

$$\langle \psi_{n'\mathbf{k}+\mathbf{q}} | e^{i\mathbf{q}\cdot\mathbf{r}} | \psi_{n\mathbf{k}} \rangle \stackrel{\mathbf{q} \rightarrow \mathbf{0}}{\simeq} \delta_{n',n} + (1 - \delta_{n',n}) i\mathbf{q} \cdot \langle \psi_{n'\mathbf{k}} | \mathbf{r} | \psi_{n\mathbf{k}} \rangle + O(q^2) \quad (3.49)$$

At this point it is convenient to divide the IPA dielectric function into two parts by splitting the double summation over the bands in an interband contribution coming from different bands ( $n' \neq n$ ) and in an intraband contribution coming from the same band ( $n' = n$ ):

$$\epsilon(\hat{\mathbf{q}}, \omega) = \epsilon^{\text{inter}}(\hat{\mathbf{q}}, \omega) + \epsilon^{\text{intra}}(\hat{\mathbf{q}}, \omega). \quad (3.50)$$

Because of the term  $(f_{n\mathbf{k}} - f_{n'\mathbf{k}+\mathbf{q}})$ , only transitions between occupied and unoccupied bands give non-vanishing contributions to the interband contribution. Regarding the intraband term instead, only transitions within partially-filled bands are non-vanishing. It is clear that in insulating crystals, i.e. having a finite band gap, the intraband contribution is always zero at zero temperature.

In the following we give the explicit expressions in the optical limit of the interband and intraband contributions to the IPA dielectric function that will be used in the thesis for the first-principles simulation of the optical properties of metals.

#### 3.4.1 Interband contribution

As shown in Eq. 3.49, the square modulus of the matrix element in the interband case ( $n' \neq n$ ) gives a contribution proportional to  $|\mathbf{q}|^2$  that removes the  $1/|\mathbf{q}|^2$  divergence in Eq. 3.48. However, the position operator is ill-defined in periodic boundary conditions. Hence we use the equivalent expression

$$\langle \psi_{n'\mathbf{k}} | \mathbf{r} | \psi_{n\mathbf{k}} \rangle = \frac{\langle \psi_{n'\mathbf{k}} | [\mathbf{r}, H^{\text{KS}}] | \psi_{n\mathbf{k}} \rangle}{E_{n\mathbf{k}} - E_{n'\mathbf{k}}}. \quad (3.51)$$

From Eq. 3.48, Eq. 3.49 and Eq. 3.51, it follows that the interband contribution to the dielectric function in the optical limit is

$$\varepsilon^{\text{inter}}(\hat{\mathbf{q}}, \omega) = 1 - \frac{4\pi}{V} \sum_{\mathbf{k}} \sum_{\substack{n, n' \\ n \neq n'}} \frac{|\langle \psi_{n'\mathbf{k}} | \hat{\mathbf{q}} \cdot \mathbf{v} | \psi_{n\mathbf{k}} \rangle|^2}{(E_{n'\mathbf{k}} - E_{n\mathbf{k}})^2} \frac{f_{n\mathbf{k}} - f_{n'\mathbf{k}}}{\omega - (E_{n'\mathbf{k}} - E_{n\mathbf{k}}) + i\eta}, \quad (3.52)$$

by recalling that the velocity operator is given by  $\mathbf{v} \equiv d\mathbf{r}/dt = -i[\mathbf{r}, H^{\text{KS}}]$ . The infinitesimal broadening  $\eta$  is not set to zero but it is used, in practice, as an empirical broadening with the purpose to account for scattering processes, always present in real materials, and/or finite experimental resolution.

Eq. 3.52 shows that the interband contribution to the dielectric function is a sum of independent vertical transitions between the pairs of all possible occupied and unoccupied KS states weighted by the matrix elements of the velocity operator.

### 3.4.2 Intraband contribution

The derivation of the expression for the intraband contribution to the IPA dielectric function is more tedious and it is given in Appendix B. The final result is that the intraband contribution has the same form as in the simple Drude model, that is

$$\varepsilon_1^{\text{intra}}(\hat{\mathbf{q}}, \omega) = -\frac{\omega_{\text{D}}^2(\hat{\mathbf{q}})}{\omega^2}, \quad (3.53)$$

where the IPA Drude plasma frequency is defined as

$$\omega_{\text{D}}^2(\hat{\mathbf{q}}) = \frac{4\pi}{V} \sum_{\mathbf{k}} \sum_n f_{n\mathbf{k}} \frac{\partial^2 E_{n\mathbf{k}}}{\partial k_\alpha^2} \quad (3.54)$$

$$= \frac{4\pi}{V} \sum_{\mathbf{k}} \sum_n \left( -\frac{\partial f}{\partial E_{n\mathbf{k}}} \right) \left| \frac{\partial E_{n\mathbf{k}}}{\partial k_\alpha} \right|^2 \quad (3.55)$$

Within the IPA approach  $\omega_{\text{D}}^2(\hat{\mathbf{q}})$  is not an empirical parameter as in the Drude model but it is derived from the electronic structure of the material, i.e. by first principles. To obtain Eq. 3.55 from 3.54, we have made use of the Green's theorem for periodic functions since  $E_n(\mathbf{k})$  is

### Chapter 3. Optical properties in linear response

---

periodic in reciprocal space<sup>9</sup> [78]:

$$\int d\mathbf{k} f(E_{n\mathbf{k}}) \frac{\partial^2 E_{n\mathbf{k}}}{\partial k_\alpha^2} = \int d\mathbf{k} \left( \frac{\partial E_{n\mathbf{k}}}{\partial k_\alpha} \right)^2 \left( -\frac{\partial f}{\partial E_{n\mathbf{k}}} \right). \quad (3.56)$$

Moreover, because of Hellmann-Feynman theorem, the gradient of the bands can be rewritten as the expectation value of the velocity operator, i.e.

$$\frac{\partial E_{n\mathbf{k}}}{\partial k_\alpha} = \langle \psi_{n\mathbf{k}} | v_\alpha | \psi_{n\mathbf{k}} \rangle. \quad (3.57)$$

At zero temperature,  $-\partial f / \partial E = \delta(E - E_F)$ , where  $E_F$  is the Fermi level, and the IPA Drude plasma frequency is proportional to the integral over the Fermi surface of the band velocities. No dissipation is included in this treatment (e.g. due to scattering with phonons, impurities and electrons) and therefore the imaginary part of the dielectric function, also called optical absorption, is non vanishing only at  $\omega = 0$ . Therefore, in order to include absorption also at non-zero frequencies, we reintroduce a dissipation term, given by the empirical broadening  $\gamma$ , in the same way as in the Drude model:

$$\epsilon^{\text{intra}}(\hat{\mathbf{q}}, \omega) = -\frac{\omega_D^2(\hat{\mathbf{q}})}{\omega(\omega + i\gamma)} = -\frac{\omega_D^2(\hat{\mathbf{q}})}{\omega^2 + \gamma^2} + i\frac{\omega_D^2(\hat{\mathbf{q}})\gamma}{\omega(\omega^2 + \gamma^2)}. \quad (3.58)$$

The intraband contribution to the dielectric function is actually a ground-state property because it depends only on the occupied states [79, 80] as it is evident from Eq. 3.54 and it is related to the inertia of the conduction electrons. The interband contribution is instead a linear response property and requires the knowledge of excited states (see Eq. 3.52).

#### 3.4.3 Drude plasma frequency

We show here how the IPA Drude plasma frequency, as given in Eq. 3.54, is linked to the classical Drude plasma frequency  $\bar{\omega}_D^2$  of the Drude model in which the conduction electrons are simply modelled as a classical gas of non-interacting free electrons<sup>10</sup>. From perturbation

---

<sup>9</sup> In order to apply Green's theorem we replace the discrete summation over the BZ in Eq. 3.54 with an integral. Infact, in the thermodynamic limit, discrete summations over the BZ can be transformed into integrals according to the relation

$$\frac{1}{V} \sum_{\mathbf{q}} \longrightarrow \int_{\text{BZ}} \frac{d\mathbf{q}}{(2\pi)^3}.$$

<sup>10</sup>With the term “non-interacting” we mean that the electron-electron interaction is neglected while with the term “free” we mean that the electron-ion interaction is also neglected.

theory we know that the curvature of the bands can be expanded as [81]

$$\frac{\partial^2 E_{n\mathbf{k}}}{\partial k_\alpha^2} = 1 + 2 \sum_{\substack{n' \\ n' \neq n}} \frac{|\langle \psi_{n'\mathbf{k}} | v_\alpha | \psi_{n\mathbf{k}} \rangle|^2}{E_{n\mathbf{k}} - E_{n'\mathbf{k}}}. \quad (3.59)$$

We underline here that the equation above is not exact if the potential entering in the KS Hamiltonian is non-local. It is correct only if we assume that the contribution coming from the double commutator of the non-local part of the potential with the position operator is negligible. The generalization of Eq. 3.59 for the curvature of  $E_{n\mathbf{k}}$  in presence of a non-local potential can be found in Ref. [81].

By inserting Eq. 3.59 in Eq. 3.54 we get that

$$\omega_{\text{D}}^2(\hat{\mathbf{q}}) = \frac{4\pi}{V} \sum_{\mathbf{k}} \sum_n f_{n\mathbf{k}} + \frac{8\pi}{V} \sum_{\mathbf{k}} \sum_{\substack{n, n' \\ n' \neq n}} \frac{|\langle \psi_{n'\mathbf{k}} | \hat{\mathbf{q}} \cdot \mathbf{v} | \psi_{n\mathbf{k}} \rangle|^2}{E_{n\mathbf{k}} - E_{n'\mathbf{k}}} f_{n\mathbf{k}} \quad (3.60)$$

$$= \bar{\omega}_{\text{D}}^2 - \frac{8\pi}{V} \sum_{\mathbf{k}} \sum_{\substack{n, n' \\ n < n'}} \frac{|\langle \psi_{n'\mathbf{k}} | \hat{\mathbf{q}} \cdot \mathbf{v} | \psi_{n\mathbf{k}} \rangle|^2}{E_{n'\mathbf{k}} - E_{n\mathbf{k}}} (f_{n\mathbf{k}} - f_{n'\mathbf{k}}) \quad (3.61)$$

where  $\bar{\omega}_{\text{D}}^2 = 4\pi\bar{n}$  and  $\bar{n} = 1/V \sum_{\mathbf{k}, n} f_{n\mathbf{k}}$  is the total electronic density<sup>11</sup>. Since  $n < n'$ , it is clear that the summation in the second term of the right-hand side of Eq. 3.61 gives a positive contribution and thus the IPA Drude plasma frequency is always smaller than the classical one. As we will see later, this behaviour is closely related to the  $f$ -sum rule and has practical consequences in the simulations.

It is convenient to define a classical Drude plasma frequency of the valence-conduction electrons only, as it is done in the Drude model where the electronic density is estimated from the nominal number of valence electrons  $Z$  ( $\bar{n}_{\text{val}} = Z/V$ ). Because fully occupied bands do not contribute to Eq. 3.54, the summation over all the occupied and empty bands  $n$  can be equivalently performed starting from the first valence-conduction band, i.e. excluding the low-lying bands due to the core electrons. From Eq. 3.54 we have that

$$\omega_{\text{D}}^2(\hat{\mathbf{q}}) = \bar{\omega}_{\text{D, val}}^2 - \frac{8\pi}{V} \sum_{\mathbf{k}} \sum'_{\substack{n_\nu, n' \\ n_\nu < n'}} \frac{|\langle \psi_{n'\mathbf{k}} | \hat{\mathbf{q}} \cdot \mathbf{v} | \psi_{n_\nu\mathbf{k}} \rangle|^2}{E_{n'\mathbf{k}} - E_{n_\nu\mathbf{k}}} (f_{n_\nu\mathbf{k}} - f_{n'\mathbf{k}}). \quad (3.62)$$

where, analogously to Eq. 3.61,  $\bar{\omega}_{\text{D, val}}^2 = 4\pi\bar{n}_{\text{val}}$  and  $\bar{n}_{\text{val}} = 1/V \sum'_{\mathbf{k}, n_\nu} f_{n_\nu\mathbf{k}}$  is the density of the valence-conduction electrons. With the notation  $\sum'$  it is understood that the summation over the new band index  $n_\nu$  is performed over all bands but excluding the core bands.

Eq. 3.62 gives the mathematical link between the IPA Drude plasma frequency  $\omega_{\text{D}}(\hat{\mathbf{q}})$  and the classical Drude plasma frequency  $\bar{\omega}_{\text{D, val}}$  estimated from the Drude model.

<sup>11</sup>In S.I. units  $\bar{\omega}_{\text{D}}^2 = \frac{e^2\bar{n}}{m\epsilon_0}$  where  $\epsilon_0$  is the permittivity of vacuum and  $m$  is the mass of the electron.

### 3.4.4 Non-locality

The non-locality of the pseudopotentials has some important consequences on the evaluation of the velocity matrix elements needed for the calculation of the IPA dielectric function.

The velocity operator can be written as the sum of a local contribution due to the kinetic term of the KS Hamiltonian and a non-local contribution due to the non-local part of the pseudopotential  $V^{\text{nl}}$  (see Section 2.2.1):

$$\mathbf{v} = -i[\mathbf{r}, H^{\text{KS}}] = \mathbf{p} - i[\mathbf{r}, V^{\text{nl}}]. \quad (3.63)$$

The local contribution is simply given by the momentum  $\mathbf{p} = -i\nabla$  while the non-local contribution is given by the commutator of the position operator with  $V^{\text{nl}}$ .

The inclusion of the non-local contribution to the velocity matrix elements can have a non negligible impact on the calculation of optical spectra. Generally speaking, a uniform reduction in the intensity of the spectra is typically observed by including this term but with no substantial alteration of the main spectral features. Nonetheless, the effect is strongly pseudopotential dependent (e.g. it depends from the local component  $V^{\text{loc}}$  chosen) and in some cases, as for example in copper, spectral features could also change.

Besides, we underline here that all the equations considered above for the first-principles calculation of the IPA dielectric function are valid only for NC pseudopotentials and not for US or PAW pseudopotentials. Indeed, in the US and PAW formalism, we have to deal with a generalised eigenvalue problem  $H^{\text{KS}}|\psi_\alpha\rangle = E_\alpha S|\psi_\alpha\rangle$  including the overlap operator  $S$ , such that  $\langle\psi_\alpha|S|\psi_\beta\rangle = \delta_{\alpha,\beta}$ . This modification increases substantially the complexity of the formulation and gives rise to additional terms that should be in principle included for a correct calculation of the optical properties in the US and PAW case. In particular, Eq. 3.51 and Eq. 3.57 are no longer valid and need to be corrected by taking into account the fact that the pseudo wavefunctions are not anymore orthogonal and that their norm is in general smaller than one (see e.g. Ref. [81] for the correction to Eq. 3.57 for a generalised eigenvalue problem and Ref. [82] for a detailed discussion about the evaluation of optical properties within the PAW formalism).

### 3.4.5 $f$ -sum rule

The optical constants verify multiple sum rules, of which the best known is the  $f$ -sum rule. From a practical point of view, sum rules are useful in order to test the consistency of the optical constants obtained, both in experimental and computational studies. In particular, the  $f$ -sum rule states that<sup>12</sup>

$$\int_0^{+\infty} d\omega \omega \varepsilon_2(\hat{\mathbf{q}}, \omega) = \frac{\pi}{2} \bar{\omega}_D^2. \quad (3.64)$$

---

<sup>12</sup>We use the standard notation  $\varepsilon(\hat{\mathbf{q}}, \omega) = \varepsilon_1(\hat{\mathbf{q}}, \omega) + i\varepsilon_2(\hat{\mathbf{q}}, \omega)$  to indicate the real and imaginary part of the dielectric function.



In fact, by writing explicitly the interband and intraband contributions to the imaginary part of the dielectric function, we obtain that

$$\begin{aligned} \int_0^{+\infty} d\omega \omega \varepsilon_2(\hat{\mathbf{q}}, \omega) &= \int_0^{+\infty} d\omega \omega [\varepsilon_2^{\text{intra}}(\hat{\mathbf{q}}, \omega) + \varepsilon_2^{\text{inter}}(\hat{\mathbf{q}}, \omega)] \\ &= \frac{\pi}{2} \left( \omega_D^2(\hat{\mathbf{q}}) + \frac{8\pi}{V} \sum_{\mathbf{k}} \sum_{\substack{n, n' \\ n < n'}} \frac{|\langle \psi_{n'\mathbf{k}} | \hat{\mathbf{q}} \cdot \mathbf{v} | \psi_{n\mathbf{k}} \rangle|^2}{E_{n'\mathbf{k}} - E_{n\mathbf{k}}} (f_{n\mathbf{k}} - f_{n'\mathbf{k}}) \right) \\ &= \frac{\pi}{2} \bar{\omega}_D^2. \end{aligned}$$

The last equality follows immediately from Eq. 3.61. To perform the energy integration we have made use of Eq. 3.58 and of the fact that, in the limit  $\eta \rightarrow 0$ , the imaginary part of Eq. 3.52 is given by

$$\varepsilon_2^{\text{inter}}(\hat{\mathbf{q}}, \omega) = \frac{4\pi^2}{V} \sum_{\mathbf{k}} \sum_{\substack{n, n' \\ n \neq n'}} (f_{n\mathbf{k}} - f_{n'\mathbf{k}}) \frac{|\langle \psi_{n'\mathbf{k}} | \hat{\mathbf{q}} \cdot \mathbf{v} | \psi_{n\mathbf{k}} \rangle|^2}{(E_{n'\mathbf{k}} - E_{n\mathbf{k}})^2} \delta(\omega - (E_{n'\mathbf{k}} - E_{n\mathbf{k}})). \quad (3.65)$$

The imaginary part  $\varepsilon_2^{\text{inter}}(\hat{\mathbf{q}}, \omega)$ , which gives the optical absorption due to interband transitions, is simply a sum of  $\delta$ -functions centered at the transition energies  $E_{n'\mathbf{k}} - E_{n\mathbf{k}}$  and it is positive defined for every positive frequency  $\omega$  (if  $\eta > 0$ , the  $\delta$ -function is replaced with a Lorentzian function and  $\varepsilon_2^{\text{inter}}(\hat{\mathbf{q}}, \omega)$  is still positive defined).

We underline here once again that, also in the derivation of the  $f$ -sum rule, we have assumed that the potential entering in the KS Hamiltonian is local. In presence of a non-local potential, as it is in the case of pseudopotential calculations, the  $f$ -sum rule does not hold anymore and the integral in the left-hand side of Eq. 3.64 can in principle overestimate the classical Drude plasma frequency (e.g. see Ref. [83] for a study on the alkali metals). This effect is essentially due to the fact that, in the pseudopotential formalism, the core electrons are not explicitly taken into account<sup>13</sup>.

Eq. 3.62 and Eq. 3.64 show that interband and intraband contributions are coupled together and that there is a conservation of the spectral weight between the two contributions (for a given electronic density). In particular, the presence of interband transitions (especially of transitions between bands with small energy differences close to the Fermi energy) reduces the value of the Drude plasma frequency  $\omega_D(\hat{\mathbf{q}})$  with respect to  $\bar{\omega}_{D, \text{val}}$ .

For the simple case of non-interacting free electrons, no interband transitions are allowed, i.e.  $\varepsilon_2^{\text{inter}}(\hat{\mathbf{q}}, \omega) = 0$  and therefore  $\omega_D(\hat{\mathbf{q}}) = \bar{\omega}_{D, \text{val}}$ . This explains the somewhat surprising success of

<sup>13</sup>For a discussion about the correction to the  $f$ -sum rule coming from the nonlocality of the potential see Ref. [84, 85]. For completeness, here we report the modified version of Eq. 3.64 that includes this additional correction:

$$\int_0^{+\infty} d\omega \omega \varepsilon_2(\hat{\mathbf{q}}, \omega) = \frac{\pi}{2} \left( \bar{\omega}_D^2 - \sum_{\mathbf{k}, n} f_{n\mathbf{k}} \langle \psi_{n\mathbf{k}} | [[V^{\text{nl}}, \hat{\mathbf{q}} \cdot \mathbf{r}], \hat{\mathbf{q}} \cdot \mathbf{r}] | \psi_{n\mathbf{k}} \rangle \right). \quad (3.66)$$

### Chapter 3. Optical properties in linear response

---

the classical Drude model in describing some transport and optical properties of simple metals (see Section 6.4 for further discussion on the topic). Nonetheless, when the periodic electron-ion interaction is switched on, interband transitions become possible and  $\omega_D(\hat{\mathbf{q}}) < \bar{\omega}_{D,\text{val}}$  while  $\epsilon_2^{\text{inter}}(\hat{\mathbf{q}}, \omega)$  is larger than zero at frequencies corresponding to allowed vertical transitions (i.e. when the matrix elements of the velocity operator,  $\langle \psi_{n'\mathbf{k}} | \hat{\mathbf{q}} \cdot \mathbf{v} | \psi_{n\mathbf{k}} \rangle$ , are different from zero).

## 4 Colour perception

We now want to relate the optical properties of a material to its perceived surface appearance and colour.

The process of colour vision is produced by the stimulation, through the absorption of light, of the colour-sensitive photoreceptor cells present in the retina of the human eye, called cones. There are three different types of cones that are distinguished by their sensitivity to different parts of the visible spectrum: L-cones are sensitive to short wavelengths, M-cones to medium wavelengths while S-cones to short wavelengths (corresponding approximately to red, green and blue colour, respectively). The stimulation of the cones is then converted in bioelectrical signals that are processed by the brain. Therefore, considered as a pure visual stimulus, light can be specified in terms of three parameters that are related to the three different colour-sensitive photoreceptors and that unambiguously define the character, or colour, of light.

The process of colour perception can be schematically portrayed as the interaction between a light source of visible light, i.e. electromagnetic radiation with wavelengths from 380 nm to 780 nm, an object and an observer (see Fig. 4.1, left panel). Depending on the light source, form and characteristics of the object, the angle of observation and the observer, the colour perception might be quite different. The need of standard measurements of colours brought the CIE (*Commission Internationale de l'Eclairage*) [86] to the definition of standard conditions (standard illuminants, standard observers) and to the introduction of the tristimulus values and the CIE colour spaces for a quantitative measure of colour. To simulate instead the actual appearance of an object made of a certain material with a certain colour under realistic conditions (i.e. within a scene with realistic illumination, surface properties and shape, and environment), photorealistic rendering is required.

### 4.1 Trichromatic theory

As briefly explained above, the process of colour perception is a complex and is an intrinsically subjective phenomenon. It depends not only on several external parameters but also on the individual features of the observer that perceives the colour. The goal of trichromatic

## Chapter 4. Colour perception

theory is to describe quantitatively this phenomenon by measuring the stimuli that have as a consequence the colour perception.

In the following we briefly explain the basic concepts of trichromatic theory by following the treatment of Ref. [87].

### CIE 1931

Trichromatic theory is based on the empirical laws of additive colour mixing formulated by H. G. Grassman in 1853. According to Grassman laws a colour stimulus can be matched by the additive mixture of three independent stimuli, i.e. none of the stimuli can be matched by the additive mixture of the other two stimuli. In Fig. 4.1 (right panel) we show a basic experiment of colour match. The test stimulus and the additive mixture of the three matching stimuli (e.g. monochromatic red, green and blue lights can be used) illuminate a white screen on the two side of a partition. The light flux of the three matching stimuli are then adjusted to obtain a colour appearance match between the test and the three matching stimuli<sup>1</sup>.

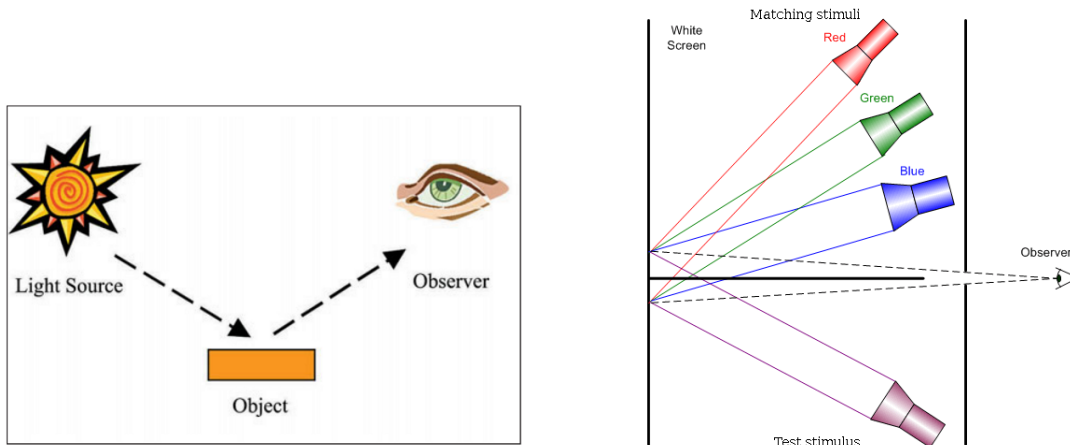


Figure 4.1 – (Left panel) The process of colour perception is the result of the interaction between a light source, an object and an observer (adapted from Ref. [5]). (Right panel) Schematic picture of a basic colour matching experiment: the three matching stimuli are adjusted until the colour of the test stimulus is undistinguishable to the observer from the colour produced by the three matching stimuli.

For a generic non-monochromatic colour stimulus defined by a spectral power distribution (SPD),  $\phi(\lambda)$ , we can describe the colour match between the unknown stimulus, [C], and the three matching stimuli through the relation

$$[C] = \int_{380\text{nm}}^{780\text{nm}} d\lambda \bar{r}(\lambda) \phi(\lambda) \cdot [R] + \int_{380\text{nm}}^{780\text{nm}} d\lambda \bar{g}(\lambda) \phi(\lambda) \cdot [G] + \int_{380\text{nm}}^{780\text{nm}} d\lambda \bar{b}(\lambda) \phi(\lambda) \cdot [B], \quad (4.1)$$

<sup>1</sup>In general, two matched colour stimuli that look indistinguishable to a human observer can have different spectral power distributions (SPDs).

where [R], [G] and [B] are the units of the three monochromatic matching stimuli red, green and blue. The three functions  $\bar{r}(\lambda)$ ,  $\bar{g}(\lambda)$  and  $\bar{b}(\lambda)$  are called colour-matching functions (CMFs) and describe the chromatic response of the observer and are related to the sensitivity of the three types of cones in the human retina.

The need of reproducibility for additive colour match experiments led in 1931 to the introduction of the *CIE 1931 standard colorimetric observer* for which the observation conditions were standardized choosing a 2° foveal field of observation with a dark surround. The disadvantage of using monochromatic red, green and blue lights as matching stimuli is that the curves contain negative values, which refer to the fact that in some part of the spectrum a match can be obtained only if one of the matching stimuli is added to the test stimulus. To solve the problem the CIE decided to transform from the real [R], [G] and [B] primary set to a set of imaginary primaries [X], [Y] and [Z] where the corresponding CMFs, indicated as  $\bar{x}(\lambda)$ ,  $\bar{y}(\lambda)$  and  $\bar{z}(\lambda)$ , have no negative values (see Fig. 4.2).

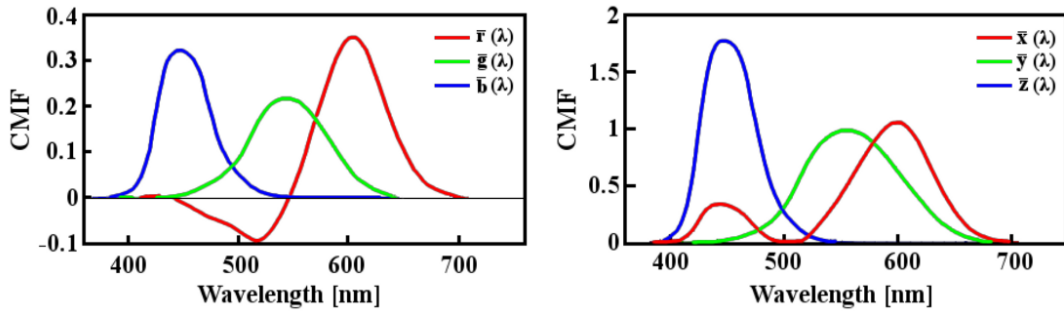


Figure 4.2 – Plot of the colour matching functions (CMFs)  $\bar{r}(\lambda)$ ,  $\bar{g}(\lambda)$  and  $\bar{b}(\lambda)$  (left panel) and  $\bar{x}(\lambda)$ ,  $\bar{y}(\lambda)$  and  $\bar{z}(\lambda)$  (right panel) of the *CIE 1931 standard colorimetric observer*. From Ref. [2].

The amounts of the primaries needed to achieve a match with the test stimulus are called tristimulus values and, in analogy with Eq. 4.1, are defined as

$$X = k \int_{380\text{nm}}^{780\text{nm}} d\lambda \bar{x}(\lambda) \phi(\lambda), \quad Y = k \int_{380\text{nm}}^{780\text{nm}} d\lambda \bar{y}(\lambda) \phi(\lambda), \quad Z = k \int_{380\text{nm}}^{780\text{nm}} d\lambda \bar{z}(\lambda) \phi(\lambda), \quad (4.2)$$

where  $k$  is a constant. The tristimulus values ( $X, Y, Z$ ) completely describe a colour stimulus and define the so called CIE- $XYZ$  colour space. Because we are mostly interested in the colour of metals, which are non self-luminous reflecting materials, the SPD  $\phi(\lambda)$  entering in Eq. 4.2 is given by  $\phi(\lambda) = R(\lambda) S(\lambda)$ , where  $R(\lambda)$  is the reflectivity of the object and  $S(\lambda)$  is the SPD of the illuminant<sup>2</sup>. The constant  $k$  is chosen so that  $Y = 100$  for objects for which  $R(\lambda) = 1$  for all visible wavelengths.

<sup>2</sup>For the calculation of the tristimulus values of precious-metal alloys, the most commonly used illuminant is the D65 illuminant which corresponds to average daylight as defined by CIE standards. Other illuminants still in use today are the B and C illuminants.

### CIELAB

The CIE- $XYZ$  colour space is not suitable to describe colour differences because it is not uniform, that is colour differences depend on the position within the colour space. Several attempts have been made to find uniform colour spaces, so that a given colour difference is independent from the position in the colour space. One of the most used colour spaces, which is nearly uniform, is the CIE 1976 ( $L^* a^* b^*$ ), or CIELAB colour space. It is defined by the following equations

$$L^* = 116 f(Y/Y_n) - 16 \quad (4.3)$$

$$a^* = 500 [f(X/X_n) - f(Y/Y_n)] \quad (4.4)$$

$$b^* = 200 [f(Y/Y_n) - f(Z/Z_n)] \quad (4.5)$$

where  $X_n$ ,  $Y_n$  and  $Z_n$  are the tristimulus values of a specified white object. The function  $f$  is defined as

$$f(t) = t^{\frac{1}{3}} \quad \text{if } t > (24/116)^3 \quad (4.6)$$

$$f(t) = \frac{841}{108}t + \frac{16}{116} \quad \text{if } t \leq (24/116)^3. \quad (4.7)$$

In this colour space (see Fig. 4.3) the three coordinates represent:

- $L^*$ : brightness (black if the value is 0, white if the value is 100)
- $a^*$ : red colouring if the value is positive, green if the value is negative
- $b^*$ : yellow colouring if the value is positive, blue if the value is negative

Since the CIELAB colour space is nearly uniform, euclidean distances can be used to approximately represent the perceived magnitude of colour differences between two objects in the same external conditions. Therefore, if  $(L_1^*, a_1^*, b_1^*)$  and  $(L_2^*, a_2^*, b_2^*)$  are the CIELAB coordinates of two objects, their colour difference is simply given by

$$\Delta E = \sqrt{(L_1^* - L_2^*)^2 + (a_1^* - a_2^*)^2 + (b_1^* - b_2^*)^2}. \quad (4.8)$$

In order to be perceivable by the human eye,  $\Delta E > 1 - 2$ .

Trichromatic theory gives a rigorous framework that permits to estimate the colouration of a material by knowing the optical constants of the material (in particular  $R(\lambda)$ ) and to condense this information in three numbers, i.e. the colour coordinates. In this section we have summarized the principal systems of colour coordinates developed by CIE in order to quantify and standardize colour measurements. These tools permit the quantitative measurement of

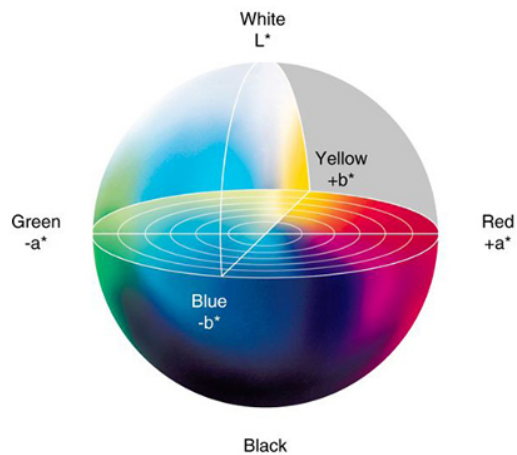


Figure 4.3 – CIELAB colour space. The corresponding colour coordinates  $L^*$ ,  $a^*$  and  $b^*$  are shown.

colour of metallic alloys and the comparison of the colour of different alloys (e.g. to compare different compositions or to compare experimental and simulated results).

## 4.2 Photorealistic rendering

The goal of photorealistic, or physically-based, rendering is to create a simulated image that is as similar as possible to a photograph of a real 3D scene. For physically-based rendering we mean that general and reasonable physical models are used to simulate the propagation of light in a scene and its interaction with objects inside the scene. The basic physical model adopted in photorealistic rendering is geometrical optics, where light is approximated as a particle travelling in straight lines. Geometrical optics is an approximation of wave optics, in which light is described as an electromagnetic wave, that is valid when the wavelength of light is much smaller than the size of the objects in the scene being rendered. Ray tracing is the principal algorithm used in photorealistic rendering and consists in following the path of rays of light through a scene as they propagate and bounce off objects within an environment. In mathematical terms this has been formalised in the framework of the light transport equation (also called rendering equation [88]) whose solution gives the light entering in the camera (observer eye). For the rendering of an object made of a particular material, we need to specify its main wavelength-dependent optical constants (e.g. refractive index and extinction coefficient in the visible spectrum) and a model that describes the characteristics of the surface of the material under investigation (e.g. conductor, dielectric, plastic, etc.). By also specifying the light source(s), the environment of the scene, and the camera we can then render the scene using a photorealistic rendering software (e.g. the Mitsuba renderer [6]), as shown in Fig 4.4.

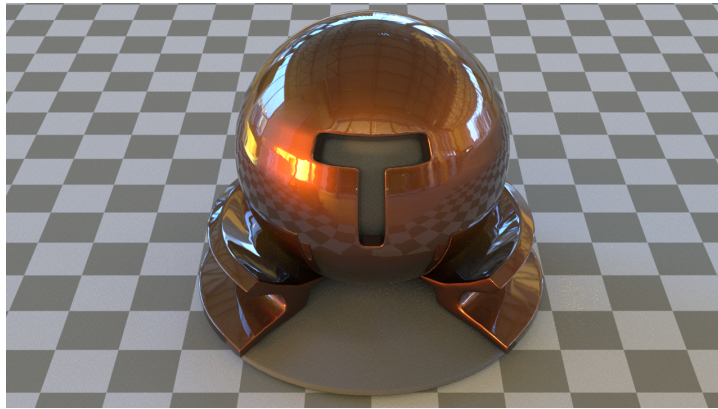


Figure 4.4 – Example of photorealistic rendering of a metallic surface performed with the Mitsuba renderer [6].



# 5 Computational approach

In this Chapter we describe the computational approach developed and used in the thesis for the first-principles simulation of the reflectivity and colour of metals. In particular, we describe in detail the code developed in order to compute the IPA dielectric function (Section 5.1), the workflow developed in order to perform automatic simulations (Section 5.2) and the protocol developed in order to test the precision and performance of pseudopotentials (Section 5.3). Part of the results discussed here have been already described in Ref. [89] and published in Ref. [90].

## 5.1 SIMPLE code

Eq. 3.52 and Eq. 3.55 for the calculation of the IPA dielectric function require a dense sampling of the BZ in order to obtain converged optical spectra for metals. Therefore we choose to use an interpolation method to calculate optical properties that is both efficient and straightforward to use, having as complementary goal also the automation of the simulations.

For this purpose we exploit the method originally developed by E. L. Shirley in 1996 [91], which is based on the use of an optimal basis (OB) set to represent the periodic part of the Bloch wavefunctions. Since, notably, the OB set is systematically improvable, accurate results can be obtained at a strongly reduced computational cost.

It is worth mentioning here that an alternative powerful approach for the interpolation of band-structure properties is the interpolation method based on the use of maximally localized Wannier functions (MLWF) as basis [92]. Wannier functions are physically appealing since they are localized in real space and can be used as an exact tight-binding basis. Moreover, Wannier interpolation is both an efficient and precise method for the evaluation of quantities that require a fine sampling of the BZ; in particular, in the Wannier representation the k-dependent KS Hamiltonian does not need to be explicitly constructed and the matrix elements of the velocity operator are analytic if written in terms of Wannier functions [93]. On the other hand, the method has the drawback that the construction of the MLWF's is not an easily automatizable procedure, especially for metals, for which an additional disentanglement step of the empty bands is required [94]. However, in recent years there have been promising

advances towards the development of an automatic procedure for the “Wannierization” of periodic systems [95], including also the more complex case of metals [96]. Once these new approaches will be interfaced with DFT engines, it would be interesting to systematically assess and compare performance and precision of Shirley’s and Wannier’s interpolations. We now briefly describe the OB method and its implementation in the SIMPLE code<sup>1</sup>.

### 5.1.1 Optimal basis method

The basic idea of the OB method [91] is to obtain a reduced set of basis functions, indicated with the notation  $\{b_i\}$ , for representing the periodic part  $u_{n\mathbf{k}}(\mathbf{r})$  of the Bloch wavefunctions  $\psi_{n\mathbf{k}}(\mathbf{r}) = e^{i\mathbf{k}\cdot\mathbf{r}} u_{n\mathbf{k}}(\mathbf{r})$  at any  $\mathbf{k}$ -point inside the BZ. The OB  $\{b_i\}$  are constructed starting from the periodic KS states  $\{u_{n\mathbf{k}}\}$  calculated on an initial coarse  $\mathbf{k}$ -grid, and then using a Gram-Schmidt orthonormalization algorithm with a threshold  $s_b$ , which proceeds  $\mathbf{k}$ -point by  $\mathbf{k}$ -point. With this approach we disregard basis vectors which would contribute only marginally (i.e. below the threshold) to the periodic KS states and the dimension  $N_b$  of the OB is directly governed by the threshold  $s_b$ .

Using this basis we can approximate a generic periodic KS state with wavevector  $\mathbf{k}$  and band index  $n$  as

$$u_{n\mathbf{k}}(\mathbf{x}) \simeq \sum_{i=1}^{N_b} \tilde{b}_i^{n\mathbf{k}} b_i(\mathbf{x}). \quad (5.1)$$

Once the OB is constructed it is possible to obtain the periodic part of the Bloch wavefunctions at a generic  $\mathbf{k}$ -point by following the interpolation procedure described in Ref. [97]. For this purpose, we need to construct the matrix elements of the  $\mathbf{k}$ -dependent KS Hamiltonian  $H^{\text{KS}}(\mathbf{k}) \equiv e^{-i\mathbf{k}\cdot\mathbf{r}} H^{\text{KS}} e^{i\mathbf{k}\cdot\mathbf{r}}$  in terms of the OB. By diagonalizing this matrix we can then obtain the coefficients  $\tilde{b}_i^{n\mathbf{k}}$  and the band energies  $E_{n\mathbf{k}}$  for each point  $\mathbf{k}$  in the dense interpolation  $\mathbf{k}$ -grid.

### Band interpolation

The operator  $H^{\text{KS}}(\mathbf{k})$  is divided into three separate contributions (kinetic energy, local potential and non-local potential):

$$H^{\text{KS}}(\mathbf{k}) = \frac{(-i\nabla + \mathbf{k})^2}{2} + V^{\text{loc}} + V^{\text{nl}}(\mathbf{k}). \quad (5.2)$$

---

<sup>1</sup>In SIMPLE a generalization of the OB method is also implemented, which allows the calculation of the dielectric function at the BSE level for finite-gap systems. This part of the code is not relevant for the thesis and it is not discussed in further detail here (see Ref. [89] for additional informations).

In our implementation the OB functions are expanded in a plane-wave basis as

$$b_i(\mathbf{x}) = \sum_{\mathbf{G}} e^{i\mathbf{G}\cdot\mathbf{r}} b_i(\mathbf{G}), \quad (5.3)$$

where the sum is over the reciprocal lattice vectors  $\mathbf{G}$  and  $\{b_i(\mathbf{G})\}$  is the set of Fourier coefficients of  $b_i(\mathbf{r})$ . By using the expression above we obtain the matrix elements of the KS Hamiltonian

$$H_{ij}^{\text{KS}}(\mathbf{k}) = \langle b_i | H^{\text{KS}}(\mathbf{k}) | b_j \rangle = \frac{1}{2} [k^2 \delta_{ij} + \mathbf{k} \cdot \mathbf{K}_{ij}^{(1)} + K_{ij}^{(0)}] + V_{ij}^{\text{loc}} + V_{ij}^{\text{nl}}(\mathbf{k}). \quad (5.4)$$

The terms inside the square brackets in Eq. 5.4 refer to the matrix elements of the  $\mathbf{k}$ -dependent kinetic energy that have a simple quadratic polynomial dependence on  $\mathbf{k}$ . For convenience, we define two additional quantities,  $\mathbf{K}_{ij}^{(1)}$  and  $K_{ij}^{(0)}$ , in terms of the Fourier coefficients  $b_i(\mathbf{G})$ :

$$\mathbf{K}_{ij}^{(1)} = 2 \sum_{\mathbf{G}} b_i^*(\mathbf{G}) \mathbf{G} b_j(\mathbf{G}), \quad (5.5)$$

$$K_{ij}^{(0)} = \sum_{\mathbf{G}} b_i^*(\mathbf{G}) \mathbf{G}^2 b_j(\mathbf{G}). \quad (5.6)$$

The matrix elements of the local potential do not depend on  $\mathbf{k}$  and are easily obtained in real space using fast-Fourier transforms:

$$V_{ij}^{\text{loc}} = \int d\mathbf{r} b_i^*(\mathbf{x}) V^{\text{loc}}(\mathbf{r}) b_j(\mathbf{x}). \quad (5.7)$$

For the non-local potential, we only consider NC pseudopotentials so that the non-local part of the pseudopotential can be written as

$$V_{ij}^{\text{nl}}(\mathbf{k}) = \sum_{\lambda} \beta_{\lambda i}^*(\mathbf{k}) D_{\lambda} \beta_{\lambda j}(\mathbf{k}), \quad (5.8)$$

where the index  $\lambda = (I, n, m, l)$  refers to the sites  $I$  of the ions in the cell together with the associated atomic quantum numbers  $(n, m, l)$  and  $D_{\lambda}$  are the coefficients of the pseudopotential. In the expression above  $\beta_{\lambda i}(\mathbf{k}) = \langle \beta_{\lambda} | e^{i\mathbf{k}\cdot\mathbf{r}} | b_i \rangle$ , where  $|\beta_{\lambda}\rangle$  are the pseudopotential projector functions centered on each ionic site  $I$ .

Since  $\mathbf{K}_{ij}^{(1)}$ ,  $K_{ij}^{(0)}$  and  $V_{ij}^{\text{loc}}$  do not depend on  $\mathbf{k}$ , they need to be calculated only once after the OB is built. The matrix elements  $V_{ij}^{\text{nl}}(\mathbf{k})$  of the non-local part of the pseudopotential instead have a non-analytic dependence over  $\mathbf{k}$  and thus they should be calculated for every  $\mathbf{k}$ . The calculation of the matrix elements  $H_{ij}^{\text{KS}}(\mathbf{k})$  and the subsequent diagonalization of the matrix for each point  $\mathbf{k}$  give the coefficients  $\tilde{b}_i^{n\mathbf{k}}$  and the band energies  $E_{n\mathbf{k}}$  for all the bands  $n \leq N_b$ .

### Dielectric function

Once the coefficients and the band energies at all the needed  $\mathbf{k}$ -points are known, we have almost all the elements necessary to calculate the IPA dielectric function through Eq. 3.52 and Eq. 3.58. For this purpose we also need the matrix elements of the  $\mathbf{k}$ -dependent velocity operator

$$\mathbf{v}(\mathbf{k}) = -i[\mathbf{r}, H^{\text{KS}}(\mathbf{k})] = -i\nabla + \mathbf{k} - i[\mathbf{r}, V^{\text{nl}}(\mathbf{k})]. \quad (5.9)$$

In terms of the OB these are given by

$$\begin{aligned} \langle u_{n\mathbf{k}} | \mathbf{v}(\mathbf{k}) | u_{n'\mathbf{k}} \rangle &= \frac{1}{2} \sum_{i,j=1}^{N_b} (\tilde{b}_i^{n\mathbf{k}})^* \tilde{b}_j^{n'\mathbf{k}} \mathbf{K}_{ij}^{(1)} + \mathbf{k} \langle u_{n\mathbf{k}} | u_{n'\mathbf{k}} \rangle + \\ &+ (-i) \sum_{i,j=1}^{N_b} (\tilde{b}_i^{n\mathbf{k}})^* \tilde{b}_j^{n'\mathbf{k}} \langle b_i | [\mathbf{r}, V^{\text{nl}}(\mathbf{k})] | b_j \rangle. \end{aligned} \quad (5.10)$$

The local contribution to the velocity matrix elements (first two terms in the right-hand side of Eq. 5.10) are easily obtained once the KS Hamiltonian matrix in Eq. 5.4 is diagonalized. On the other hand the matrix elements  $\langle b_i | [\mathbf{r}, V^{\text{nl}}(\mathbf{k})] | b_j \rangle$  of the commutator of the non-local part of the pseudopotential need to be computed and, having a non-analytic dependence over  $\mathbf{k}$ , they should be calculated for each  $\mathbf{k}$ .

#### 5.1.2 Details of the code

The OB method described above is implemented in the SIMPLE code, which is included as a package within the Quantum ESPRESSO (QE) distribution [98]. It is divided into two different executables: `simple.x` and `simple_ip.x`. The executable `simple.x` builds the OB and saves to disk all the relevant matrix elements needed for the calculation of the optical properties. The actual IPA calculation is then performed by `simple_ip.x`.

Throughout the SIMPLE code, MPI parallelization is exploited and linear algebra operations are efficiently performed through calls to BLAS and LAPACK libraries. Spin-orbit interaction is implemented and the code works only with NC pseudopotentials.

More in detail, `simple.x` relies, as starting point, on the results of a *nscf* calculation of QE performed on a uniform grid of  $\mathbf{k}$ -points without the use of symmetry. The  $\mathbf{k}$ -grid should include also the seven periodic images of  $\Gamma$  in order to better preserve the periodicity in reciprocal space of the  $\mathbf{k}$ -dependent Hamiltonian (see Ref. [97] for a more detailed discussion on the topic). After the construction of the OB functions, the  $\mathbf{k}$ -independent matrix elements  $\mathbf{K}_{ij}^{(1)}$ ,  $K_{ij}^{(0)}$  and  $V_{ij}^{\text{loc}}$  (see Eq. 5.5, Eq. 5.6 and Eq. 5.7 respectively) of the KS Hamiltonian in the OB are computed. For the non-local part of the pseudopotential we store the  $\mathbf{k}$ -dependent projectors  $\beta_{\lambda_j}(\mathbf{k})$  of Eq. 5.8, as originally proposed in Ref. [97], at each  $\mathbf{k}$ -point  $\mathbf{k}$  on a uniform interpolation  $\mathbf{k}$ -grid in the BZ, as well as the matrix elements  $\langle b_i | [\mathbf{r}, V^{\text{nl}}(\mathbf{k})] | b_j \rangle$  giving the

non-local contribution to the velocity operator (see last term of Eq. 5.10).

The IPA dielectric function is then computed by `simple_ip.x` on the uniform interpolation k-grid, proceeding k-point by k-point. The empirical interband and intraband broadenings, i.e.  $\eta$  of Eq. 3.52 and  $\gamma$  of Eq. 3.58, are specified in input. Besides, in order to ease the convergence of the value of the IPA Drude plasma frequency, the Fermi-Dirac derivative in Eq. 3.55 is replaced with a Gaussian function centered at the Fermi level and having a user-defined broadening  $\sigma$ .

The code then writes in standard output the Drude plasma frequency  $\omega_D(\hat{\mathbf{q}})$ , computed in the limit  $\mathbf{q} \rightarrow \mathbf{0}$  along the three Cartesian limits (i.e. with  $\hat{\mathbf{q}} = \hat{\mathbf{x}}, \hat{\mathbf{y}}, \hat{\mathbf{z}}$ ), and provides two data files with the real and imaginary parts of the interband contribution to the IPA dielectric function,  $\varepsilon_1^{\text{inter}}(\hat{\mathbf{q}}, \omega)$  and  $\varepsilon_2^{\text{inter}}(\hat{\mathbf{q}}, \omega)$ , also computed along the three Cartesian directions. The code writes to disk also the real and imaginary part of the total IPA dielectric function (see Eq. 3.50) and the EELS spectrum, which is given by  $-\Im[\varepsilon^{-1}(\hat{\mathbf{q}}, \omega)]$  (i.e. by the imaginary part of the inverse dielectric function).

### 5.1.3 Validation and performance of the code

We consider, as test system, bulk silver in the FCC primitive cell with lattice parameter  $a = 7.869$  bohr. The DFT calculations with the `pw.x` code of QE are performed with the PBE approximation [99] for the exchange-correlation functional at a wavefunction cutoff of 55 Ry and using the scalar-relativistic NC pseudopotential for Ag from the SG15 library [100]. For the ground-state calculation (*scf* calculation in `pw.x`) we use a  $24 \times 24 \times 24$  Monkhorst-Pack [101] k-grid while the periodic functions  $\{u_{n\mathbf{k}}\}$  needed for the construction of the OB are obtained on a  $2 \times 2 \times 2$  uniform k-grid including the seven periodic images of  $\Gamma$  and considering 11 conduction bands<sup>2</sup> (*nscf* calculation in `pw.x`). The IPA optical properties are calculated on a  $44 \times 44 \times 44$  uniform k-grid with the inclusion of the non-local contribution to the velocity matrix elements and broadening parameters (i.e.  $\eta$ ,  $\gamma$  and  $\sigma$ ) of 0.1 eV. Because we are considering a FCC cubic crystal, the dielectric function is isotropic and is simply a scalar (i.e. independent from the direction  $\hat{\mathbf{q}}$ ).

#### Convergence with the optimal basis

First, we investigate the convergence of the IPA dielectric function with respect to the threshold  $s_b$  which controls the quality of the OB used for representing the periodic part of the Bloch wavefunctions. In Fig. 5.1 we show how both  $\varepsilon_1^{\text{inter}}(\hat{\mathbf{q}}, \omega)$  and  $\varepsilon_2^{\text{inter}}(\hat{\mathbf{q}}, \omega)$  of Ag are fully converged at  $s_b = 0.01$  a.u., or equivalently with  $N_b = 103$  basis functions (to be compared with the value  $N_b = 315$  corresponding to the complete basis, i.e. to  $s_b = 0.0$  a.u.). Similar results are found for the convergence of  $\omega_D(\hat{\mathbf{q}})$ , and are shown in Table 5.1, where we also notice that in poorly converged calculations the cubic symmetry of bulk Ag is not preserved.

<sup>2</sup>Convergence of the optical spectra with respect to the *nscf* k-grid was also studied. In a primitive cell a  $2 \times 2 \times 2$  k-grid is more than sufficient to reach convergence while in a supercell the sole  $\Gamma$  point is already sufficient (in both cases including the periodic images of  $\Gamma$ ).

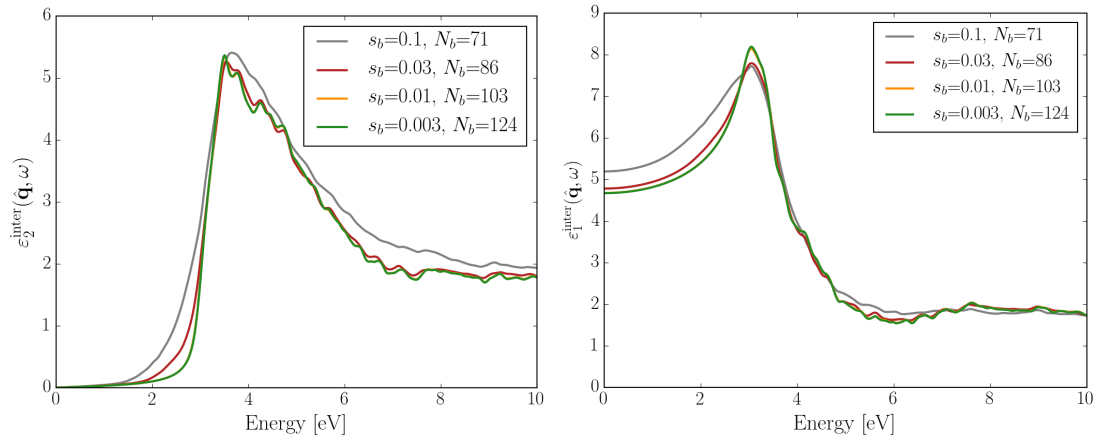


Figure 5.1 – Convergence of the interband contribution to the IPA complex dielectric function of bulk Ag with respect to the number of OB functions  $N_b$ , which is controlled by the parameter  $s_b$ . We show both the real (right panel) and imaginary parts (left panel) of  $\epsilon^{\text{inter}}(\hat{\mathbf{q}}, \omega)$ .

$N_b$	$\omega_D(\hat{\mathbf{x}})$	$\omega_D(\hat{\mathbf{y}})$	$\omega_D(\hat{\mathbf{z}})$
71	8.70	8.50	8.59
86	8.85	8.83	8.83
103	8.97	8.97	8.97
124	8.98	8.98	8.98

Table 5.1 – Convergence of the IPA Drude plasma frequency (in eV) of bulk Ag with respect to the number of OB functions  $N_b$ , computed along the three Cartesian limits (i.e. with  $\hat{\mathbf{q}} = \hat{\mathbf{x}}, \hat{\mathbf{y}}, \hat{\mathbf{z}}$ ).

### Validation with respect to other codes

We validate the IPA implementation of the SIMPLE code by comparing the results obtained for Ag with respect to equivalent simulations performed with the Yambo code [102] for the interband contribution to  $\varepsilon(\hat{\mathbf{q}}, \omega)$ , and with the BoltzWann module [103] of the Wannier90 code [104] for the intraband contribution to  $\varepsilon(\hat{\mathbf{q}}, \omega)$ . As both codes are interfaced with the QE distribution we can perform a straightforward comparison starting from the same DFT ground-state density used for the SIMPLE calculation using all the same relevant computational parameters (k-grid, number of bands, broadenings, etc.). To note that, in order to calculate the optical properties, Yambo does not use any interpolation method in k-space while BoltzWann, instead, uses the Wannier's interpolation method [105]. For the SIMPLE calculation we use an OB constructed setting  $s_b = 0.01$  a.u. that, as shown above, gives well converged spectra. Fig. 5.2 shows that SIMPLE and Yambo give almost identical results for  $\varepsilon^{\text{inter}}(\hat{\mathbf{q}}, \omega)$ . For the intraband contribution we find that the Drude plasma frequency of Ag is  $\omega_D(\hat{\mathbf{q}}) = 8.93$  eV with the SIMPLE code while it is  $\omega_D(\hat{\mathbf{q}}) = 8.96$  eV with the BoltzWann code. Therefore we conclude that for both the interband and intraband contributions the agreement between SIMPLE and the other codes is excellent.

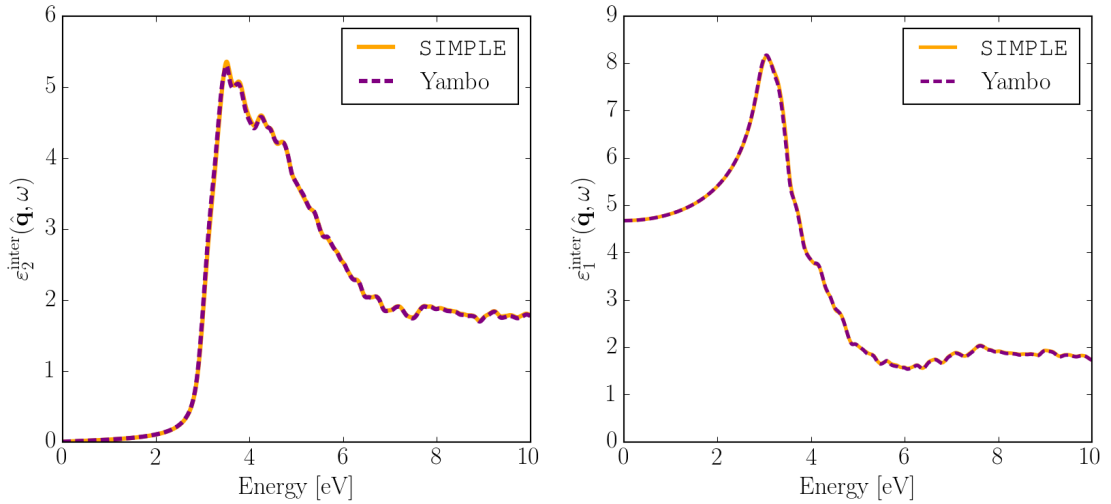


Figure 5.2 – Comparison of the interband contribution to the IPA complex dielectric function of bulk Ag calculated with the SIMPLE code and with the Yambo code. We show both the real (right panel) and imaginary parts (left panel) of  $\varepsilon^{\text{inter}}(\hat{\mathbf{q}}, \omega)$ .

### Scaling with the optimal basis

As the core of the present approach is the reduction of the basis sets for representing wavefunctions, we are compelled to assess how such reduction improves the computational performance. In the calculations we have to deal with matrices of dimension  $N_b \times N_b$  (i.e. the k-dependent Hamiltonian  $H_{ij}^{\text{KS}}(\mathbf{k})$  of Eq. 5.4) and the computational cost is dictated by the construction (or “filling”) of this matrix through the computation of the k-dependent contribu-

tions coming from the non-local part of the pseudopotentials rather than by its diagonalization. For this reason the wall time of a IPA calculation is expected to scale quadratically with respect to  $N_b$ .

We study the computational cost of the IPA approach performed with the SIMPLE code as the number of OB functions  $N_b$  is varied, as shown in Fig. 5.3 for bulk silver. We set as reference time the computer time (or wall time) of the calculation with the smallest number of OB functions. As expected, the time of computation scales with the square of  $N_b$ . In Fig. 5.3 we also show how the inclusion of the non-local commutator in the computation of the velocity matrix elements significantly slows down the calculation.

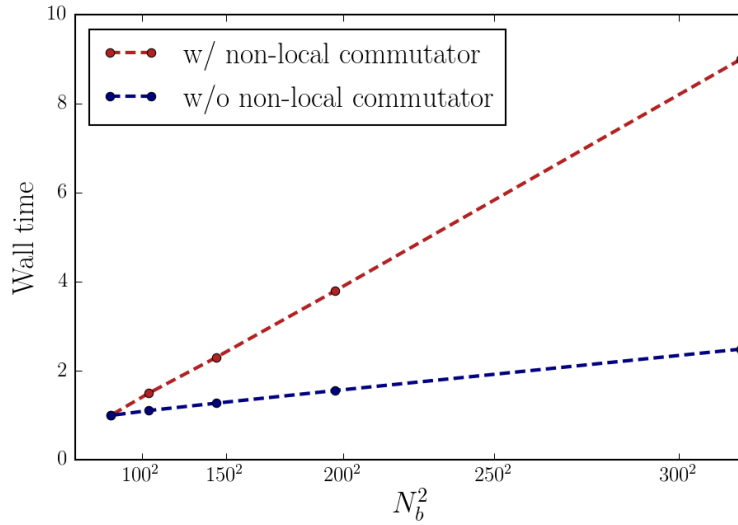


Figure 5.3 – Relative computational time for a IPA calculation performed with the SIMPLE code on bulk Ag, both including and not including the non-local commutator in the evaluation of the velocity matrix elements, with respect to the square of the number of OB functions  $N_b$ . The reference wall time is set as the one resulting from the calculation with the smallest number of vectors.

**Core scaling**

In order to assess the performances of the SIMPLE code for its use in parallel architectures, we investigate the speedup of the code as a function of the number of single processing units. We consider Ag in a  $4 \times 4 \times 4$  FCC supercell with 64 atoms and 1216 electrons. The total number of OB functions considered in the simulations is 2687, corresponding to  $s_b = 0.01$  a.u. In general, a significant part of the total computational cost is due to the `simple.x` run. Therefore the speedup is calculated by summing the wall times of the `simple.x` and `simple_ip.x` runs performed with the same number of cores. In Fig. 5.4 we show the results for the case in which the number of cores corresponds to the number of MPI tasks and we compare simulations performed including and not including the computation of the non-local commutator entering in the estimation of the velocity matrix elements. In order to obtain similar wall times for



a given number of cores, we use an interpolation k-grid of  $8 \times 8 \times 8$  and  $16 \times 16 \times 16$  when including and not including the non-local commutator, respectively. Although the scaling of `simple_ip.x` alone is close to a linear behaviour, the total scaling of the combined simulations deviates from the ideal linear scaling, mainly because of the computations of the k-dependent matrix elements due to the non-local part of the pseudopotentials (see Eq. 5.8 and Eq. 5.10) performed by `simple.x`. Indeed, if the calculation of the non-local commutator of Eq. 5.10 is avoided, the scaling is significantly improved, as shown in Fig. 5.4.

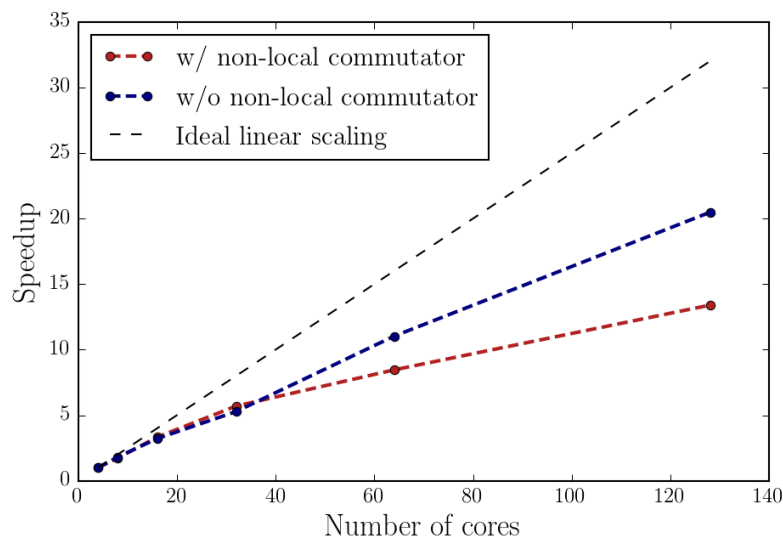


Figure 5.4 – Speedup of an IPA calculation performed with the SIMPLE code (`simple.x` and `simple_ip.x`) as a function of the number of cores for bulk Ag in a  $4 \times 4 \times 4$  supercell with 64 atoms including and not including the contribution to the velocity matrix elements coming from the non-local commutator. The test is performed on Intel<sup>®</sup> Skylake<sup>®</sup> processors.

The systematic improvement of the OB set and, as a consequence, of the accuracy of the results by simply increasing the number of included basis functions, gives the notable advantage that our code can be used to perform efficient computations in a straightforward way from the user point of view (the accuracy is controlled simply by a single input parameter, i.e.  $s_b$ ). Moreover, the simplicity of the method and the fact that all the calculations needed to obtain the optical properties from a generic initial crystal structure can be run within a single open-source software, i.e. the QE distribution, makes easier the automation of the required sequence of computational steps and thus the systematic evaluation of the dielectric function for a large number of materials.

## 5.2 Workflow

Most of the calculations needed for this thesis are performed using AiiDA [106], an open-source Python infrastructure for computational science that can track the provenance of data and calculations and that allows one to implement workflows that can run automatically complex

sequences of calculations. AiiDA prepares and submits calculations and then retrieves and stores the results inside a database, all automatically, thus ensuring the reproducibility of all results obtained. The database can be subsequently queried to extract the necessary data and informations. AiiDA is particularly useful for high-throughput computational studies for which a large number of simulations needs to be performed for many different materials and a high-degree of automation of the computational procedure is desirable and often necessary. As described below, the steps of calculations required by our computational approach in order to simulate the reflectivity and colour of a material from the initial crystal structure are fully implemented as an AiiDA workflow, named `ColourWorkflow`, and schematically depicted in Fig. 5.5. Thanks to the `ColourWorkflow` it is possible, giving as input a generic crystal structure, to obtain directly as output the reflectivity and colour of a given material.

Our procedure to obtain the reflectivity and colour of a metal at the IPA level from an initial crystal structure (e.g. extracted from experimental databases such as ICSD [107], COD [108] or Pauling file [109]) can be divided into three main steps.

In the first step we compute the ground-state electronic density of the system by solving the KS equations and, if needed, by also relaxing the internal atomic positions and/or the external coordinates of the simulation cell representing the initial crystal structure. Afterwards, starting from the computed ground-state density, we obtain the KS energies and wavefunctions for the number of empty bands and k-points necessary for the subsequent calculation of the optical properties with the OB method. The DFT simulations are performed with the QE distribution and are in practice handled by the `PwWorkflow`, a robust lower-level AiiDA workflow called by the `ColourWorkflow`, that can restart QE calculations in case the user-specified wall time is reached before the simulation is completed or in case of common QE errors for which a small adjustment of the input parameters allows the simulation to end successfully [90].

In the second step we compute the dielectric function at the IPA level using the OB method as implemented in the `SIMPLE` code. As described in Section 5.1.2, `SIMPLE` first builds the OB and computes the relevant matrix elements on a dense uniform k-points grid (performed by the `simple.x` executable), and then it computes the IPA dielectric function, including both interband and intraband contributions, and other derived optical constants such as the reflectivity (performed by the `simple_ip.x` executable).

In the last step the colour is obtained from the reflectivity through a python module. The integral involved in the calculation of the tristimulus values (see Eq. 4.2) is estimated by discretizing the wavelengths inside the visible range in steps of 1 nm and using the *CIE 1931 standard colorimetric observer* and the spectral power distribution of the D65 illuminant. The tristimulus values are then converted to other standard systems of colour coordinates such as CIELAB and sRGB colour spaces. If needed, photorealistic rendering of a surface with the simulated optical constants is then performed with the Mitsuba renderer [6].

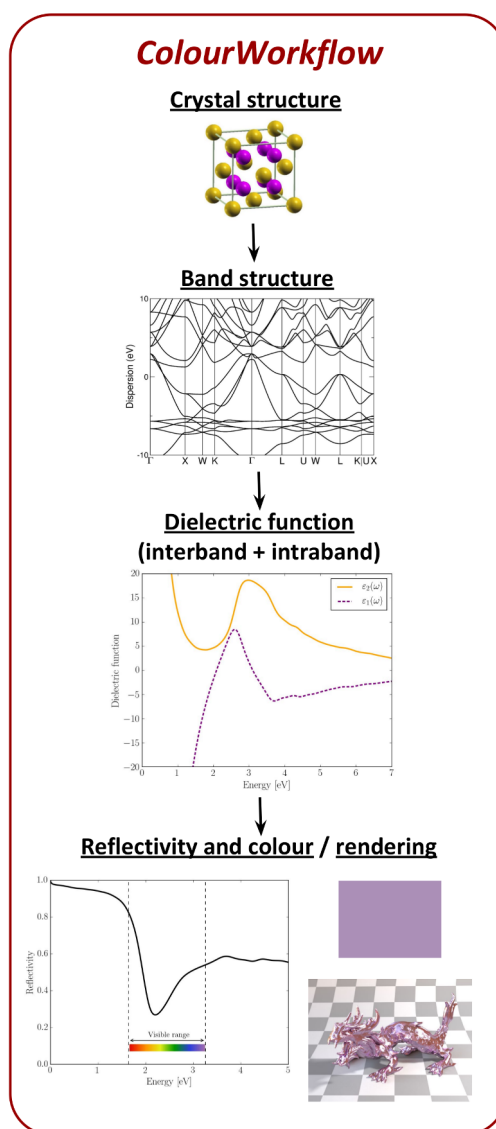


Figure 5.5 – Schematic representation of the ColourWorkflow which is designed to simulate the reflectivity and colour of a metallic material giving as input its crystal structure. The workflow is implemented within the framework of the AiiDA infrastructure.

### 5.3 Precision and efficiency of pseudopotential simulations

Our goal is to perform a systematic study of the reflectivity and colour of several metallic systems and we ideally want to have reliable results at the lowest possible computational cost for the precision required by our application. In DFT calculations performed with the plane-wave pseudopotential method, this means that we would like to always employ pseudopotentials that reproduce the true all-electron results at the smallest possible wavefunction cutoff (see Eq. 2.7) for all elements of the periodic table considered.

For this purpose we exploit the results of the SSSP protocol developed by us [90] to test pseudopotentials. Pseudopotential and corresponding wavefunction cutoff for each element of the periodic table relevant for this thesis are selected according to the SSSP results in order to perform efficient and reliable IPA calculations with SIMPLE.

#### 5.3.1 SSSP protocol

Here we discuss a pseudopotential testing protocol, named SSSP (standard solid-state pseudopotential) testing protocol, which is based on several independent criteria in order to assess both the precision and the efficiency of pseudopotentials for solid-state pseudopotential calculations. The SSSP protocol is made of a verification part, based on the  $\Delta$ -factor test [110, 111], and an extensive performance-oriented part based on plane-wave convergence tests for phonon frequencies, band structures, cohesive energies and stress tensors. Adopting these criteria we identify two curated pseudopotential libraries for 85 elements of the periodic table that we target for high-throughput materials screening (called “SSSP efficiency” library) and high-precision materials modelling (called “SSSP precision” library).

In practice, we investigate the precision and performance of several pseudopotential libraries publicly available for the QE distribution. All the tested pseudopotential libraries are based on the generalized gradient approximation (GGA) for the PBE exchange-correlation functional [99] at the scalar-relativistic level, and they include the three main pseudization approaches: NC, US and PAW (see Table 5.2 for a list of all the pseudopotential libraries tested).

#### Verification and convergence tests

**Equation of state.** In order to assess the precision of pseudopotentials, we compute the  $\Delta$ -factor, i.e. the integral of the difference between the equations of state calculated with pseudopotential simulations and with reference all-electron results for elemental crystals. For this purpose we use the protocol introduced in 2014 by Lejaeghere *et al.* [110]. This protocol was exploited to compare 15 different DFT codes, including both all-electron and pseudopotential codes, in order to verify the reproducibility of the PBE equations of state of elemental crystals across different methods and implementations [111]. The protocol consists in calculating the energy-versus-volume at 7 equidistant points centred around the reference equilibrium volume and then performing a Birch-Murnaghan fit. From the parameters of the fit some important physical quantities related to the structural and elastic properties of the system are

### 5.3. Precision and efficiency of pseudopotential simulations

Full name	Short name	Method	Reference
pslibrary.0.3.1 US	031US	US	[112]
pslibrary.0.3.1 PAW	031PAW	PAW	[112]
pslibrary.1.0.0 US (high acc.)	100US	US	[113]
pslibrary.1.0.0 PAW (high acc.)	100PAW	PAW	[113]
GBRV-1.2 (US)	GBRV-1.2	US	[114]
GBRV-1.4 (US)	GBRV-1.4	US	[114]
GBRV-1.5 (US)	GBRV-1.5	US	[114]
SG15 (NC)	SG15	NC	[100]
SG15-1.1 (NC)	SG15-1.1	NC	[100]
RE Wentzcovitch (PAW)	Wentzcovitch	PAW	[115]
Goedecker (NC)	Goedecker	NC	[116]
PseudoDojo (NC)	Dojo	NC	[117]
THEOS (US)	THEOS	US	

Table 5.2 – Pseudopotential libraries tested with the SSSP protocol. The short names correspond to the name used in the convergence pattern plots (see Fig. 5.6) to identify the pseudopotential libraries.

extracted: the equilibrium volume  $V_0$ , the bulk modulus  $B_0$  and the first derivative of the bulk modulus  $B_1$ . The  $\Delta$ -factor, that is reported in units of meV/atom, gives an overall estimate of the discrepancy between pseudopotentials and all-electron results in terms of these structural properties.

The reference all-electron results of the equation of states are the ones of the WIEN2k code [118] reported in Ref. [111], with the exception of the rare-earth nitrides for which we use the WIEN2k results reported in Ref. [115]. All pseudopotential calculations needed for the  $\Delta$ -factor estimation are performed at the reference wavefunction cutoff of 200 Ry using a dense Monkhorst-Pack [101] k-grid of  $20 \times 20 \times 20$  and a Marzari-Vanderbilt smearing [119] of 2 mRy. Magnetism is included for the equations of state of oxygen and chromium (antiferromagnetism), manganese (antiferromagnetism) and iron, cobalt, nickel and the rare-earth nitrides (ferromagnetism).

For the efficiency of pseudopotentials instead, within the SSSP testing protocol we study the convergence of four different quantities as a function of the wavefunction cutoff  $E_c$ , i.e. of the number of plane-waves used in the expansion of the KS states. The tested quantities are phonons frequencies at the zone-border, cohesive energies, pressure, and band structures. All the calculations are performed on the ground-state structures of elemental crystals at 0 K, as provided in Ref. [120], with the exception of fluorine for which the  $\text{SiF}_4$  structure is used because of convergence issues of the elemental fluorine structure and of lanthanides that are not included in the test set of Ref. [120] and for which the nitride structures of Ref. [115] are used. In total we test 85 different elements of the periodic table.

In all pseudopotential frameworks, a plane-wave representation of the charge density requires a cutoff,  $E_\rho$ , higher than the wavefunction cutoff,  $E_c$ . Typically, convergence tests are

performed by varying  $E_c$  and keeping the dual, i.e. the ratio  $E_\rho/E_c$ , fixed. Also the SSSP convergence patterns are obtained at fixed duals (equal to 4 for NC pseudopotentials and to 8 for US and PAW pseudopotentials) and taking  $E_c^{\text{ref}} = 200$  Ry as the reference wavefunction cutoff. All the quantities are considered as differences with respect to the corresponding reference value calculated at  $E_c^{\text{ref}}$ . An example of the calculated convergence pattern plot is shown in Fig. 5.6 for the case of palladium. We perform all the tests on the elemental crystals using a relatively coarse  $6 \times 6 \times 6$  Monkhorst-Pack k-grid (except for oxygen and all the lanthanides where a  $10 \times 10 \times 10$  k-grid is used instead) because in our protocol for convergence we are not directly interested in the absolute values of the tested quantities but rather on their difference with respect to the reference values computed at  $E_c^{\text{ref}}$ . We also disregard spin-polarization in all the convergence tests but we have verified for the magnetic structures that the convergence patterns are not substantially altered by the inclusion of magnetism.

**Phonon frequencies.** The convergence of vibrational properties of elemental crystals is performed by calculating, within the framework of density-functional perturbation theory (DFPT), the phonon frequencies at the zone-border of the BZ, i.e. at the point  $\mathbf{Q} = (\frac{1}{2}, \frac{1}{2}, \frac{1}{2})$  in relative coordinates of the reciprocal lattice vectors. While the  $\Delta$ -factor test is related to the structural and elastic properties of the system, by considering phonon frequencies at the border of the BZ we have access to information related to both acoustic and optical modes.

The number of phonon frequencies depends on the number of atoms in the unit cell, and so on the element under investigation. In the convergence pattern plots of the SSSP testing protocol we condense the information related to the several phonon frequencies into a single number  $\delta\bar{\omega}$ . It is defined as a relative average deviation (in percentage) among all the phonon frequencies  $\omega_i$  calculated at  $\mathbf{Q}$  for each wavefunction cutoff  $E_c$

$$\delta\bar{\omega} = \sqrt{\frac{1}{N} \sum_{i=1}^N \left| \frac{\omega_i(E_c) - \omega_i(E_c^{\text{ref}})}{\omega_i(E_c^{\text{ref}})} \right|^2}, \quad (5.11)$$

where  $N$  is the total number of phonon frequencies. The maximum relative deviation is similarly defined as

$$\delta\bar{\omega}_{\text{error}} = \max_i \left| \frac{\omega_i(E_c) - \omega_i(E_c^{\text{ref}})}{\omega_i(E_c^{\text{ref}})} \right|, \quad (5.12)$$

and it is represented as an half error bar in the convergence pattern plots.

If the highest phonon frequency  $\omega_{\text{max}}$  of an elemental crystal at  $\mathbf{Q}$  is smaller than  $100 \text{ cm}^{-1}$  at  $E_c^{\text{ref}}$ , the absolute average deviation and the corresponding maximum deviation are computed instead of the relative ones, since a precision of a few  $\text{cm}^{-1}$  is often the reasonable target for a DFPT calculation.

**Cohesive energy.** We investigate the convergence of the energy difference between the crystalline solid and the corresponding individually isolated atoms, i.e. the cohesive energy of the

### 5.3. Precision and efficiency of pseudopotential simulations

elemental crystals. The quantity  $\delta E_{coh}$  considered in the SSSP testing protocol is defined as the absolute difference between the cohesive energy at a given wavefunction cutoff  $E_c$  and the one at the reference wavefunction cutoff  $E_c^{ref}$ , i.e. 200 Ry (in units of meV per atom).

**Pressure.** We evaluate the convergence of the stress by computing the hydrostatic pressure, which is defined as  $P = 1/3 \text{Tr}(\sigma)$ , where  $\sigma$  is the stress tensor. Rather than checking convergence directly on the pressure itself (the magnitude of which depends strongly on the stiffness of the material) we evaluate it through its conversion into an equivalent volume. This allows the definition of a stiffness-agnostic and hence material's independent convergence criterion. Starting from the Birch-Murnaghan equation of state for the pressure fitted on the reference all-electron calculations

$$P_{\text{BM}}(V) = \frac{3B_0}{2} \left[ \left( \frac{V_0}{V} \right)^{\frac{7}{3}} - \left( \frac{V_0}{V} \right)^{\frac{5}{3}} \right] \times \left\{ 1 + \frac{3}{4} (B'_0 - 4) \left[ \left( \frac{V_0}{V} \right)^{\frac{2}{3}} - 1 \right] \right\}, \quad (5.13)$$

we define the deviation volume  $V'$  as the one closest to the equilibrium volume  $V_0$  such that  $P_{\text{BM}}(V') = \delta P$ , where  $\delta P = P(E_c) - P(E_c^{ref})$  is the residual pressure of a calculation performed at the cutoff  $E_c$ . With this definition, fully converged values of pressure give  $\delta P = 0$  and therefore  $V' = V_0$ . Once  $V'$  is known we can eventually find the relative volume deviation (in percentage) due to the residual pressure:  $\delta V_{press} = (V' - V_0)/V_0$ , which is the quantity considered in the SSSP testing protocol.

**Band structure.** The tests discussed so far deal with ground-state quantities only, computed either using DFT or DFPT. However, pseudopotential calculations are often employed to study optical, transport and other properties that involve charged or neutral excitations. The majority of excited-states calculations are based on MBPT, e.g.  $G_0W_0$  and self-consistent  $GW$  [75, 71, 76], the Bethe-Salpeter equation (BSE) [64], or dynamical mean field theory (DMFT) [121], and are performed on-top of a DFT calculation, which provides the starting point for both self-consistent and one-shot approaches. Hence, we include band structures in our testing protocol, taking into account both the occupied bands and some of the lower lying unoccupied bands. Here, we outline a protocol for performing both convergence tests and verification of band structures by defining a bands distance (a similar idea has been proposed independently in Ref. [122]). The aim is to quantify how much two band structures “differ” by introducing a simple and computationally inexpensive metric in the band structures space. We call our bands distance  $\eta$  and consider two cases that are distinguished solely by the number of bands taken into account. The  $\eta_v$  (or “eta valence”) considers the occupied bands only, while in the  $\eta_{10}$  (or “eta conduction 10”) all the bands up to 10 eV above the Fermi level are considered. We choose a uniform Monkhorst-Pack mesh, in the full BZ and with no symmetry reduction. Choosing a high-symmetry path could result in an unsatisfactory arbitrary choice, as different recipes for the standardization of paths have been introduced in the recent literature [123, 124] and interesting features of the band structure may occur

## Chapter 5. Computational approach

---

far from the high-symmetry lines (such as Weyl points) [125, 126]. A uniform mesh is also more appropriate from the point of view of electron's nearsightedness [127]: if the energy eigenvalues are known on a sufficiently fine uniform k-points mesh, it is possible to get an *exact* real-space representation of the Hamiltonian in a Wannier function basis [105] and then interpolate to an arbitrary fine mesh.

Let us suppose we have two sets of bands  $E_{n\mathbf{k}}^A$  and  $E_{n\mathbf{k}}^B$ ; we define the distance between the two sets of (valence) bands as

$$\eta_v(A, B) = \min_{\omega} \sqrt{\frac{\sum_{n\mathbf{k}} \tilde{f}_{n\mathbf{k}} (E_{n\mathbf{k}}^A - E_{n\mathbf{k}}^B + \omega)^2}{\sum_{n\mathbf{k}} \tilde{f}_{n\mathbf{k}}}}, \quad (5.14)$$

where

$$\tilde{f}_{n\mathbf{k}} = \sqrt{f_{n\mathbf{k}}(E_F^A, \sigma) f_{n\mathbf{k}}(E_F^B, \sigma)}, \quad (5.15)$$

$f_{n\mathbf{k}}(E, \sigma)$  being the Fermi-Dirac distribution and  $\sigma$  the smearing width. The Fermi energies,  $E_F^{(A,B)}$ , for the two band structures  $A$  and  $B$  are obtained from the relation  $N_{el}^{(A,B)} = \sum_{n\mathbf{k}} f_{n\mathbf{k}}^{(A,B)}(E_F^{(A,B)}, \sigma)$ , where  $N_{el}$  is the number of electrons. In order to properly align the two sets of bands,  $\eta_v$  is defined as the minimum with respect to a rigid energy shift  $\omega$ .

We now consider also the low-lying conduction bands by introducing  $\eta_{10}$ , defined as in Eq. 5.14 but with a Fermi level up shift of 10 eV. In this way,  $\eta_{10}$  measures the bands distance of the valence bands plus the conduction bands up to 10 eV above the Fermi energy.

Finally, we also take into account the possibility that significant differences between band structures may occur only in subregions of the BZ or in small energy ranges. After computing the  $\eta$ , we check the slowest converging band by computing  $\max \eta$ , defined as

$$\max \eta = \max_{n\mathbf{k}} |E_{n\mathbf{k}}^A - E_{n\mathbf{k}}^B + \omega|, \quad (5.16)$$

and request that it has to be converged with a slightly higher threshold than  $\eta$  itself.

In the SSSP testing protocol we use  $\eta_{10}$  and  $\max \eta_{10}$  (in units of meV) as criteria to quantitatively study the convergence of band structures.

### Selection criteria

The selection criteria used to build our two optimal pseudopotential libraries, namely the SSSP efficiency and SSSP precision libraries (version 1.1), are listed in Table 5.3. The main idea behind the SSSP precision library is to provide the pseudopotentials that are the closest to all-electron calculations in terms of  $\Delta$ -factor computed at the reference wavefunction cutoff  $E_c^{\text{ref}}$ , without much consideration on the computational cost and the wavefunction cutoffs actually needed to converge all relevant quantities. On the other hand, the SSSP efficiency library is designed for practical applications that should remain affordable, and therefore



### 5.3. Precision and efficiency of pseudopotential simulations

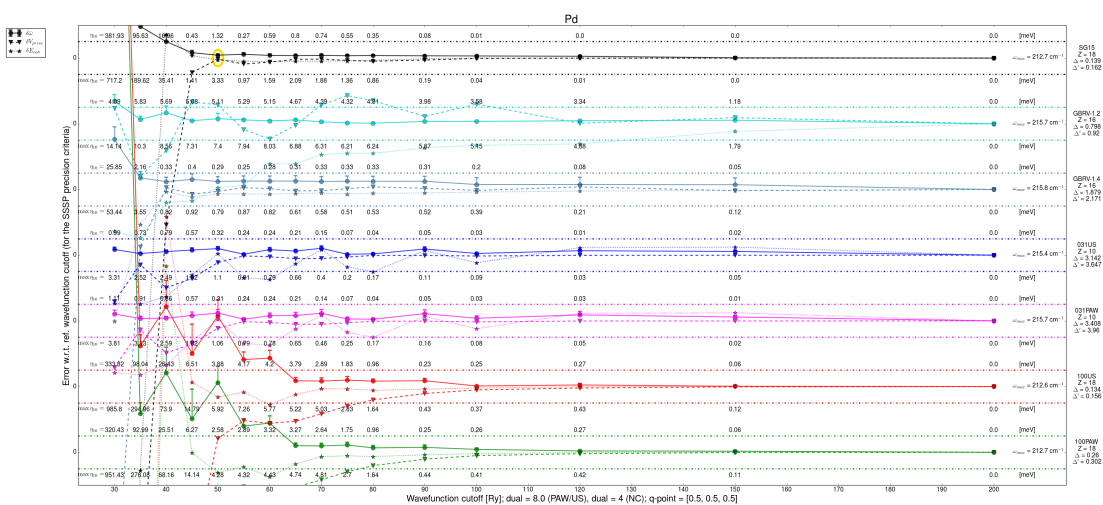


Figure 5.6 – SSSP testing protocol applied to palladium. For each pseudopotential the convergence w.r.t. the wavefunction cutoff of the zone-boundary phonons ( $\delta\bar{\omega}$ ), cohesive energy ( $\delta E_{coh}$ ), pressure ( $\delta V_{press}$ ) and bands structure ( $\eta_{10}$  and  $\max \eta_{10}$ ) is monitored. The horizontal dashed lines correspond to the thresholds of the SSSP selection criteria (efficiency or precision); here precision is shown. On the right-hand side we report the number of valence electrons of the pseudopotential ( $Z$ ), the  $\Delta$ -factor and the  $\Delta'$ -factor [7] with respect to the reference all-electron results and the converged value of the highest phonon frequency ( $\omega_{max}$ ). The circle marks the pseudopotential and wavefunction cutoff chosen for the SSSP library (version 1.1).

All convergence pattern plots of the 85 elements tested are available on the Materials Cloud platform [8].

## Chapter 5. Computational approach

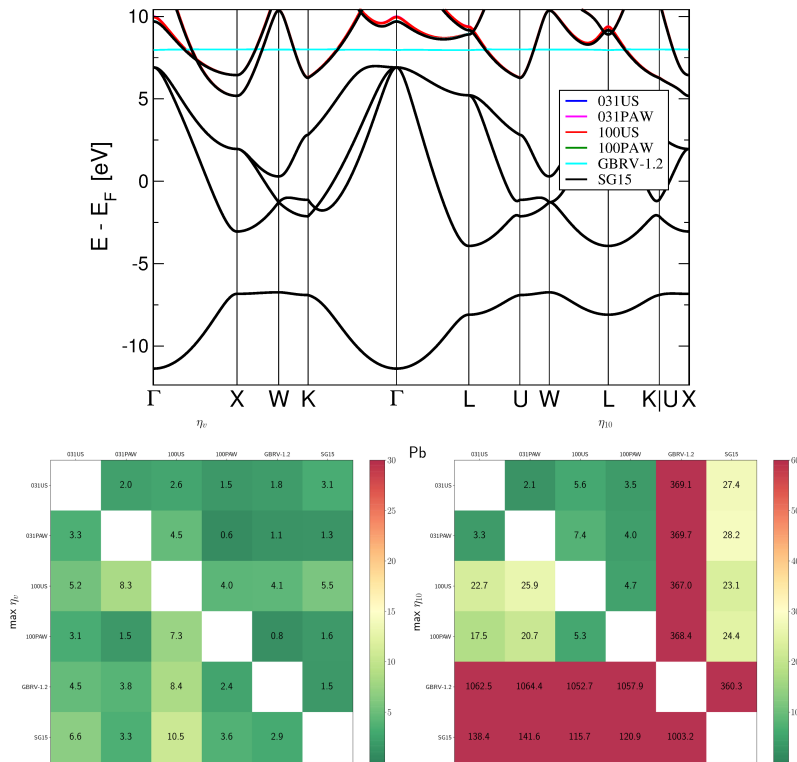


Figure 5.7 – Band structure of FCC Pb along a high-symmetry path, for several pseudopotential libraries (top panel). The valence bands are almost identical to each other, while some differences appear in the conduction bands: the SG15 bands deviate from the other bands around 7-10 eV over the Fermi level and a flat ghost state in the GBRV bands is clearly visible at around 8 eV. These differences between band structures can be compressed into the band distances  $\eta_v$  and  $\eta_{10}$ , reported in units of meV (bottom panel). In addition, ghost states in the band interval considered can be automatically detected as peaks in the  $\eta$  function, hence simplifying greatly the verification of spectral properties.

### 5.3. Precision and efficiency of pseudopotential simulations

pseudopotentials are chosen such that wavefunction cutoffs are as low as possible while keeping the precision reasonable.

For SSSP efficiency, when possible we select pseudopotentials with a rather small  $\Delta$ -factor (below 1 meV/atom). The phonons  $\delta\bar{\omega}$  should be converged within 2% (or within  $2\text{ cm}^{-1}$  if the highest phonon frequency is smaller than  $100\text{ cm}^{-1}$ ), the cohesive energy  $\delta E_{coh}$  within 2 meV/atom, the pressure within 1% for  $\delta V_{press}$  (i.e. 0.33% on the lattice parameter of a cubic crystal) and the band structure within 10 meV for  $\eta_{10}$  and within 20 meV for  $\max\eta_{10}$ . For the SSSP precision, the criteria are slightly stricter (see Table 5.3) and we systematically opt for the pseudopotential with the smallest  $\Delta$ -factor. Therefore the wavefunction cutoffs of the SSSP precision are typically higher than the ones proposed for the SSSP efficiency.

	SSSP efficiency	SSSP precision	notes
Phonon frequencies ( $\delta\bar{\omega}$ )	< 2%	< 1%	< $1\text{ cm}^{-1}$ if $\omega_{max} < 100\text{ cm}^{-1}$
Cohesive energy ( $\delta E_{coh}$ )	< 2 meV/atom	< 2 meV/atom	
Pressure ( $\delta V_{press}$ )	< 1%	< 0.5%	in terms of volume differences
Band structure ( $\eta_{10}$ )	< 10 meV	< 10 meV	
Band structure ( $\max\eta_{10}$ )	< 20 meV	< 20 meV	
Equation of state ( $\Delta$ -factor)	< 1 meV/atom (if possible)	smallest	

Table 5.3 – Selection criteria for the SSSP efficiency and SSSP precision libraries.

**Ghost states.** We use the bands distance  $\eta_{10}$  defined above not only for the convergence tests but also to compare the band structures of the tested pseudopotentials for all the elemental crystals considered. However different pseudopotentials are often generated with different combinations of semi-core states in the valence band. Hence, we compare only the bands they have in common, by taking the minimum number of electrons of all the sets and removing the exceeding low-energy bands accordingly. By means of this additional criterion it is possible to automatically detect ghost states [128] in a pseudopotential in the valence and in the conduction up to the chosen threshold (here 10 eV above the Fermi energy), as they are signalled by extremely large values (of the order of eV or more) of the band distances when computed with respect to other ghost-free pseudopotentials (see Fig. 5.7 for an example).

We refer to Ref. [90] for additional information and discussions on the SSSP protocol, and for the list of pseudopotentials and corresponding suggested wavefunction cutoffs of the two SSSP libraries (version 1.1) selected according to the selection criteria given in Table 5.3. On a more general level, apart from the SSSP testing protocol and libraries, all the data obtained through the application of the SSSP protocol to the tested pseudopotential libraries provides a database of verification data and convergence tests that facilitates the optimal choice of pseudopotentials and wavefunction cutoffs for custom applications. For example, some physical properties may be implemented only for some pseudopotential types (typically only NC) or some applications may require convergence of just a subset of the quantities that we consider in the SSSP testing protocol. By a look at our plots and data, see for instance the condensed plot for palladium shown in Fig. 5.6, a user can quickly select the optimal pseudopotential and wavefunction cutoff tailored for the specific application.

In fact, this is what we do for IPA calculations performed with SIMPLE.

### 5.3.2 IPA calculations with SIMPLE

In IPA calculations performed with SIMPLE, we cannot simply use the two pseudopotential libraries proposed in the SSSP with the corresponding suggested wavefunction cutoffs chosen according to the SSSP selection criteria because the SSSP libraries are a mixture of NC, US and PAW pseudopotentials. The SIMPLE code, instead, supports only NC pseudopotentials and so we are restricted to use exclusively this type of pseudopotentials. For the selection of the NC pseudopotentials and corresponding converged wavefunction cutoffs to be used in our work, we focus our attention only on the plane-wave convergence of band structure and pressure, and on the precision of structural properties estimated through the  $\Delta$ -factor test. In particular, the electronic band structures are a fundamental ingredient in the determination of the IPA dielectric function and thus, for our work, it is important to have reliable and well-converged band structures. Differences between two sets of band structures are quantitatively measured through the  $\eta$  function, as defined within the SSSP protocol (see Section 5.3.1), that can be used to compare both band structures obtained at two different wavefunction cutoffs for the same pseudopotential and band structures obtained with two different pseudopotentials.

We check the precision of pseudopotentials in the estimation of the equilibrium volume by means of the equation of state and we disregard those that have a  $\Delta$ -factor that is too large compared to all-electron results. Because we often want to relax both cell-internal and cell-external degrees of freedoms of the considered crystal structures, it is necessary to have converged stresses and forces. For our purposes, we are less interested in having fully converged phonon frequencies and cohesive energies and thus we do not consider their convergence, as it is instead performed in the SSSP protocol for the selection of pseudopotentials.

Moreover, we also check the comparison of band structures of a given elemental crystal among different pseudopotentials (see chessboard plots in Fig. 5.7). If a single pseudopotential shows discrepancies with respect to all the other pseudopotentials considered in the SSSP (which are generated with different codes and by different authors), it is likely the sign of inaccuracies related to that particular pseudopotential and its use should therefore be avoided. However, because of the absence of reference all-electron band structures data, we cannot be sure that the pseudopotential we choose has the true PBE band structure. Finally, with the help of chessboard plots and band structure diagrams, we check for the presence in the pseudopotentials of ghost states in empty bands up to 10 eV above the Fermi energy and, if any ghost state is found, avoid to employ those pseudopotentials.

By inspecting all these data from the SSSP database of tests, we decide to use the SG15 [100] (version 1.0 and 1.1) NC pseudopotential library for most of the elements of the periodic table because it is, in most of the cases, both precise and efficient. We select the converged wavefunction cutoffs to be used in our simulations such that each KS energy  $E_{n\mathbf{k}}$  in the valence and in the conduction up to 10 eV above the Fermi level<sup>3</sup> is converged at least within 20 meV

---

<sup>3</sup>For our work, we are mainly interested in the calculation of the optical properties within the visible range. Therefore the convergence of the band structure up to 10 eV above the Fermi level is a safe choice for a reliable

### 5.3. Precision and efficiency of pseudopotential simulations

---

( $\max \eta_{10}$ ) and that the pressure gives discrepancies in the equilibrium volume of less than 0.5 % ( $\delta V_{press}$ ). The average  $\Delta$ -factor is 0.8 meV/atom and the average wavefunction cutoff is 64 Ry for all the elements considered. For a few elements, i.e. Mn, Cr and Fe, the SG15 pseudopotentials do not give a satisfactory equilibrium volume. For these elements we use the Pseudo Dojo [117] (version 0.4) pseudopotentials with the wavefunction cutoff suggested by the authors for accurate simulations. Moreover, we use the Pseudo Dojo pseudopotentials instead of the SG15 ones also for Hf, due to a very large number of electrons in the valence of the SG15 pseudopotential, and for Zn, due to convergence problems in the self-consistent solution of the KS equations for some DFT simulations. No ghost states up to 10 eV above the Fermi energy are present in the pseudopotentials selected.

The list of all pseudopotentials and corresponding wavefunction cutoffs used for all the elements of the periodic table considered in this work is shown in Table 5.4.

---

estimation of the reflectivity at the IPA level within this range.

## Chapter 5. Computational approach

---

Element	Pseudopotential	Cutoff [Ry]	Element	Pseudopotential	Cutoff [Ry]
Li	SG15	70	Y	SG15	55
Be	SG15	60	Zr	SG15	55
B	SG15	55	Nb	SG15	90
C	SG15	80	Mo	SG15	50
N	SG15	80	Tc	SG15	55
Na	SG15	100	Ru	SG15	50
Mg	SG15	90	Rh	SG15	55
Al	SG15	80	Pd	SG15	55
Si	SG15-1.1	50	Ag	SG15	55
P	SG15-1.1	65	Cd	SG15	55
K	SG15	55	In	SG15-1.1	80
Ca	SG15	55	Sn	SG15-1.1	65
Sc	SG15	55	Sb	SG15-1.1	60
Ti	SG15	60	Te	SG15-1.1	55
V	SG15	70	Cs	SG15-1.1	60
Cr	Dojo	100	Ba	SG15	60
Mn	Dojo	100	Hf	Dojo	65
Fe	Dojo	100	Ta	SG15	65
Co	SG15	70	W	SG15	55
Ni	SG15	80	Re	SG15	90
Cu	SG15	90	Os	SG15	70
Zn	Dojo	90	Ir	SG15	50
Ga	SG15	90	Pt	SG15	65
Ge	SG15	70	Au	SG15	55
As	SG15-1.1	50	Hg	SG15	65
Rb	SG15	50	Tl	SG15	60
Sr	SG15	55	Pb	SG15	50
			Bi	SG15	50

Table 5.4 – List of pseudopotentials (using the short names of Table 5.2) and corresponding wavefunction cutoffs chosen for each element considered in this work.

# 6 Reflectivity and colour of elemental metals

In this Chapter we discuss the results of the simulations of the reflectivity and colour of all 45 elemental solids up to atomic number 83 (i.e. up to the element bismuth) that are metallic in their ground-state crystal structures, with the exclusion of lanthanides<sup>1</sup>. All the simulations are performed following the computational approach described in Chapter 5.

## 6.1 Computational details

As discussed in Section 5.3.2, we always use the PBE scalar-relativistic pseudopotentials and wavefunction cutoffs reported in Table 5.4, that have been selected for both precise and efficient DFT calculations and with a particular focus on the convergence of band structures. All calculations on elemental metals are performed on the ground-state crystal structures at zero temperature, as provided in Ref. [110] (and available online [120]). The equilibrium volume of each structure corresponds to the reference PBE value obtained by extensively tested all-electron calculations for the equation of state [111]. If needed, the crystal structures are reduced to the primitive cell using the spglib library [129]. Spin-polarization is not included in our calculations, so that the effect of magnetism on the optical properties of the magnetic crystals Cr, Mn, Fe, Co and Ni is neglected.

When considering anisotropic crystals, we always deal with the dielectric function  $\varepsilon(\omega)$  averaged over the three Cartesian directions:

$$\varepsilon(\omega) = \frac{\varepsilon(\hat{\mathbf{x}}, \omega) + \varepsilon(\hat{\mathbf{y}}, \omega) + \varepsilon(\hat{\mathbf{z}}, \omega)}{3}. \quad (6.1)$$

We define a corresponding average IPA Drude plasma frequency as  $\omega_D^2 = [\omega_D^2(\hat{\mathbf{x}}) + \omega_D^2(\hat{\mathbf{y}}) + \omega_D^2(\hat{\mathbf{z}})]/3$ . In fact, the most typical experimental situation is to have polycrystalline materials in which grains have random orientations, and the average procedure described before is justified.

The dielectric function is evaluated by always including the non-local commutator in the

---

<sup>1</sup>Lanthanides are disregarded because DFT-PBE calculations are known to fail in correctly describing, even qualitatively,  $f$  electrons due to strong correlation effects.

computation of the velocity matrix elements. The effect of the inclusion of spin-orbit coupling and of the neglect of the non-local commutator in the estimation of the IPA optical properties is discussed in more detail in Section 6.5.

The convergence of the IPA dielectric function with respect to all the relevant computational parameters has been studied. In Fig. 6.1 we show the dependence of the IPA Drude plasma frequency of Au and Pd with respect to the Gaussian broadening, named  $\sigma$ , used for the evaluation of the Fermi-surface integral in Eq. 3.55. The calculations are performed with different uniform interpolation k-grids for the summations over the BZ entering in the estimation of the interband and intraband contributions to the IPA dielectric function. We choose Au and Pd as test examples because they are representative of the two limiting cases in which a single free-electron-like band crosses the Fermi energy (*sp* metals) and in which are instead the flat *d* bands that cross the Fermi energy (transition metals), respectively. For large values of  $\sigma$ , the different k-grids give all very similar results but the discrepancies increase by decreasing  $\sigma$ . In Au a large  $\sigma$  and a relatively coarse k-grid (i.e. 0.4 eV and  $30 \times 30 \times 30$ , respectively) give already a good estimate of the value of  $\omega_D$  extrapolated for vanishingly small  $\sigma$  but in Pd the increase of the broadening introduces a significant error with respect to the value at the limit  $\sigma \rightarrow 0$ . Similarly, we also study the convergence of  $\epsilon_2^{\text{inter}}(\omega)$  with respect to k-points grids at different values of the empirical interband broadening  $\eta$ . As shown in Fig. 6.2, coarse k-grids and small values of  $\eta$  give rise to spurious oscillations in the spectra. Clearly, by increasing  $\eta$  we observe a faster convergence of  $\epsilon_2^{\text{inter}}(\omega)$  with k-points sampling and a corresponding broadening of all the spectral features<sup>2</sup>. We then calculate the reflectivity  $R(\omega)$  from  $\epsilon^{\text{inter}}(\omega)$  and  $\epsilon^{\text{intra}}(\omega)$  obtained using the same value for the respective broadenings, i.e.  $\eta = \sigma$  (see Fig. 6.3). The spurious oscillations observed in  $\epsilon_2^{\text{inter}}(\omega)$  are, to some degree, attenuated in  $R(\omega)$ . Most importantly, if a dense enough interpolation k-grid is used (e.g.  $64 \times 64 \times 64$ ), we note that  $R(\omega)$  is nearly independent from the values of  $\eta$  and  $\sigma$  chosen.

As a compromise between accuracy of the results and computational cost, we make the choice to employ an interpolation k-grid of  $64 \times 64 \times 64$  and  $\eta = \sigma = 0.1$  eV for each elemental metal considered, if not specified otherwise. An exception is elemental aluminium for which, because of a very slow convergence of  $\epsilon^{\text{inter}}(\omega)$  with respect to k-points sampling, the interpolation k-grid used is  $80 \times 80 \times 80$  and  $\eta$  is set to 0.2 eV.

The additional computational parameters reported below are used for all the elemental metals studied. In the *scf* calculation of QE for the evaluation of the ground-state density we use a Monkhorst-Pack k-grid of  $24 \times 24 \times 24$  and a Marzari-Vanderbilt smearing of 0.02 Ry. In the *nscf* calculation of QE needed for the construction of the Shirley's OB we use a uniform k-grid of  $2 \times 2 \times 2$  including the seven periodic images of  $\Gamma$ . We make the safe choice to use  $s_b = 0.0075$  a.u. for the construction of the OB in SIMPLE. We compute the dielectric function  $\epsilon(\omega)$  for frequencies in the range [0, 20] eV using at least 30 empty conduction bands<sup>3</sup>. The

<sup>2</sup>The convergence behaviour of  $\epsilon_1^{\text{inter}}(\omega)$  is very similar to the one of  $\epsilon_2^{\text{inter}}(\omega)$  and it is not shown here.

<sup>3</sup>If the number of valence bands  $N_v$  is larger than 30, we consider  $N_v$  empty conduction bands rather than 30. Although  $\epsilon_2^{\text{inter}}(\omega)$  converges fast with respect to the number of empty bands since only the conduction bands up to 20 eV above the Fermi energy give a non-negligible contribution in the range of frequencies [0, 20] eV, the convergence of  $\epsilon_1^{\text{inter}}(\omega)$  is slower and requires a larger number of bands.



occupations  $f_{n\mathbf{k}}$  of the KS states are computed according to the Fermi-Dirac distribution at room temperature (i.e. 0.025 eV) whereas the empirical dissipation  $\gamma$  entering in Eq. 3.58 for the evaluation of  $\epsilon^{\text{intra}}(\omega)$  is set equal to 0.1 eV, which is of the order of typical experimental values for metals [130, 131]. The effect of using a larger value of  $\gamma$  on the dielectric function is to increase the optical absorption (see imaginary part of Eq. 3.58). In terms of the reflectivity of simple elemental metals such as potassium, for which the Drude model of Eq. 3.58 is a good approximation to the true optical properties (see Section 6.4 and Fig. 6.9 therein), an increase of the dissipation  $\gamma$  translates in a reduction of the intensity of the reflectivity below the classical Drude plasma frequency  $\bar{\omega}_{\text{D, val}}$  and to a smoothening of the reflectivity edge appearing at the frequency  $\bar{\omega}_{\text{D, val}}$ .

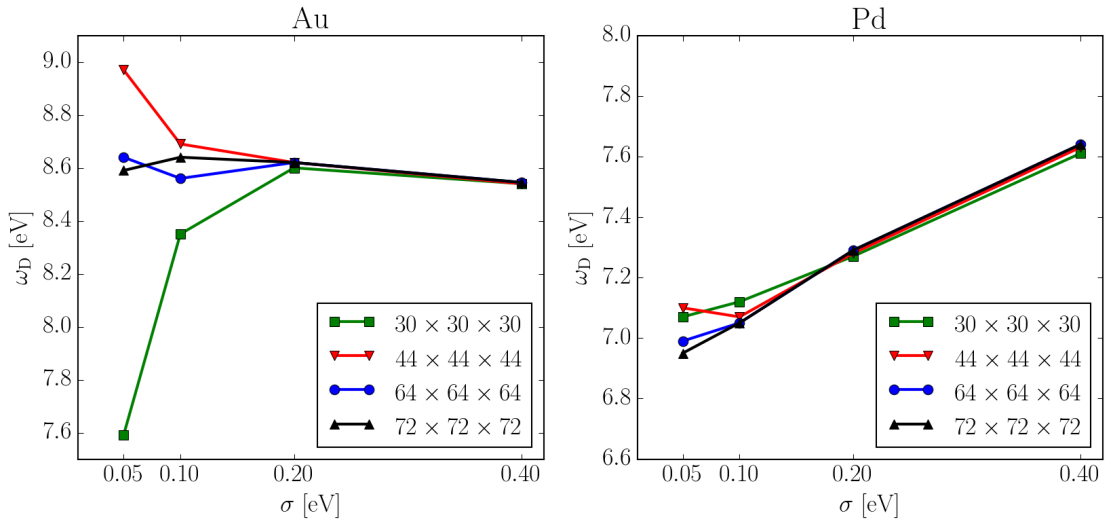


Figure 6.1 – Dependence of the IPA Drude plasma frequency  $\omega_{\text{D}}$  for elemental Au and Pd on the Gaussian broadening  $\sigma$  for different interpolation k-points grids.

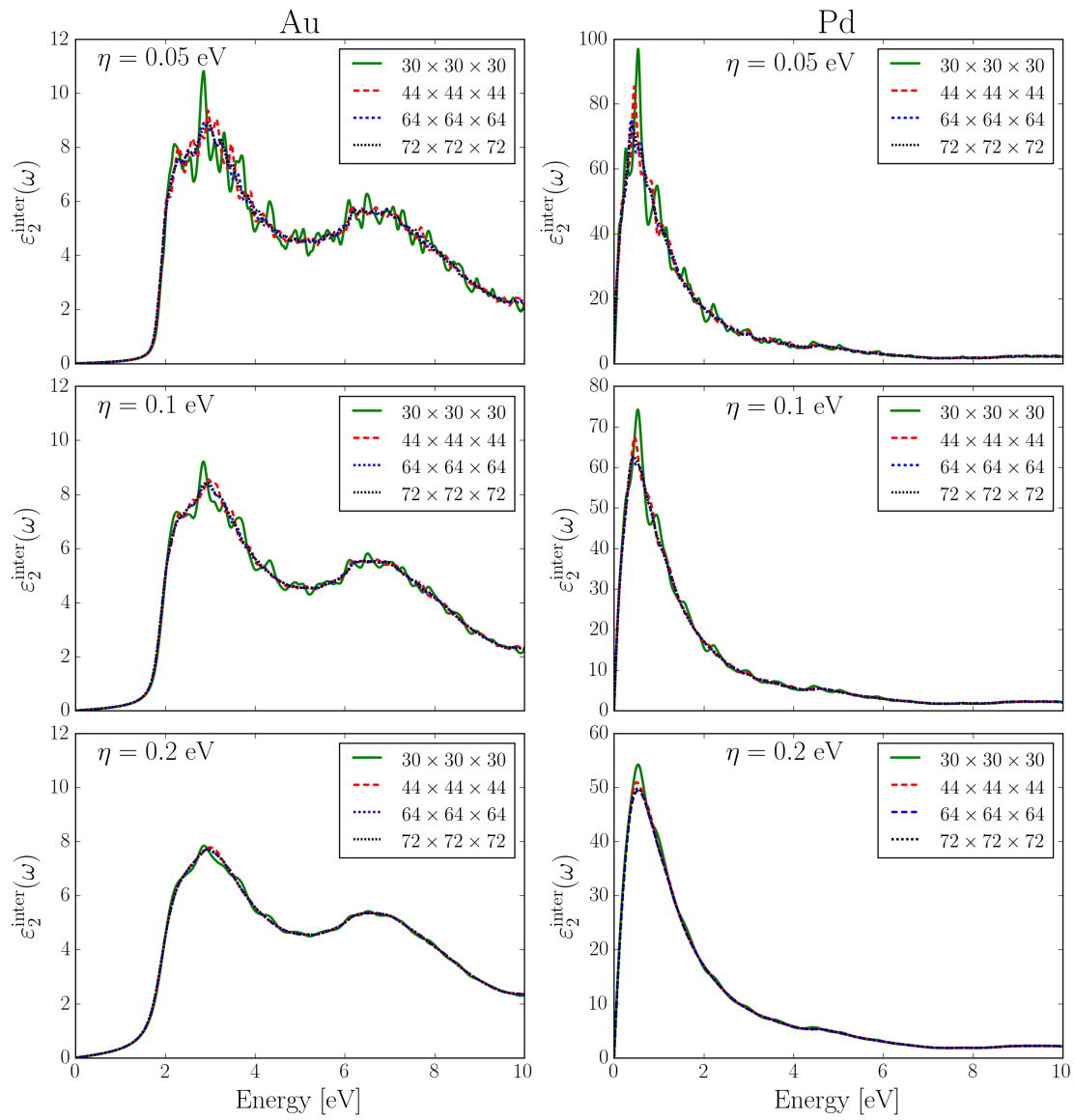


Figure 6.2 – Dependence of  $\epsilon_2^{\text{inter}}(\omega)$  for elemental Au and Pd on the interpolation k-points grids for different values of the empirical interband broadening  $\eta$ .

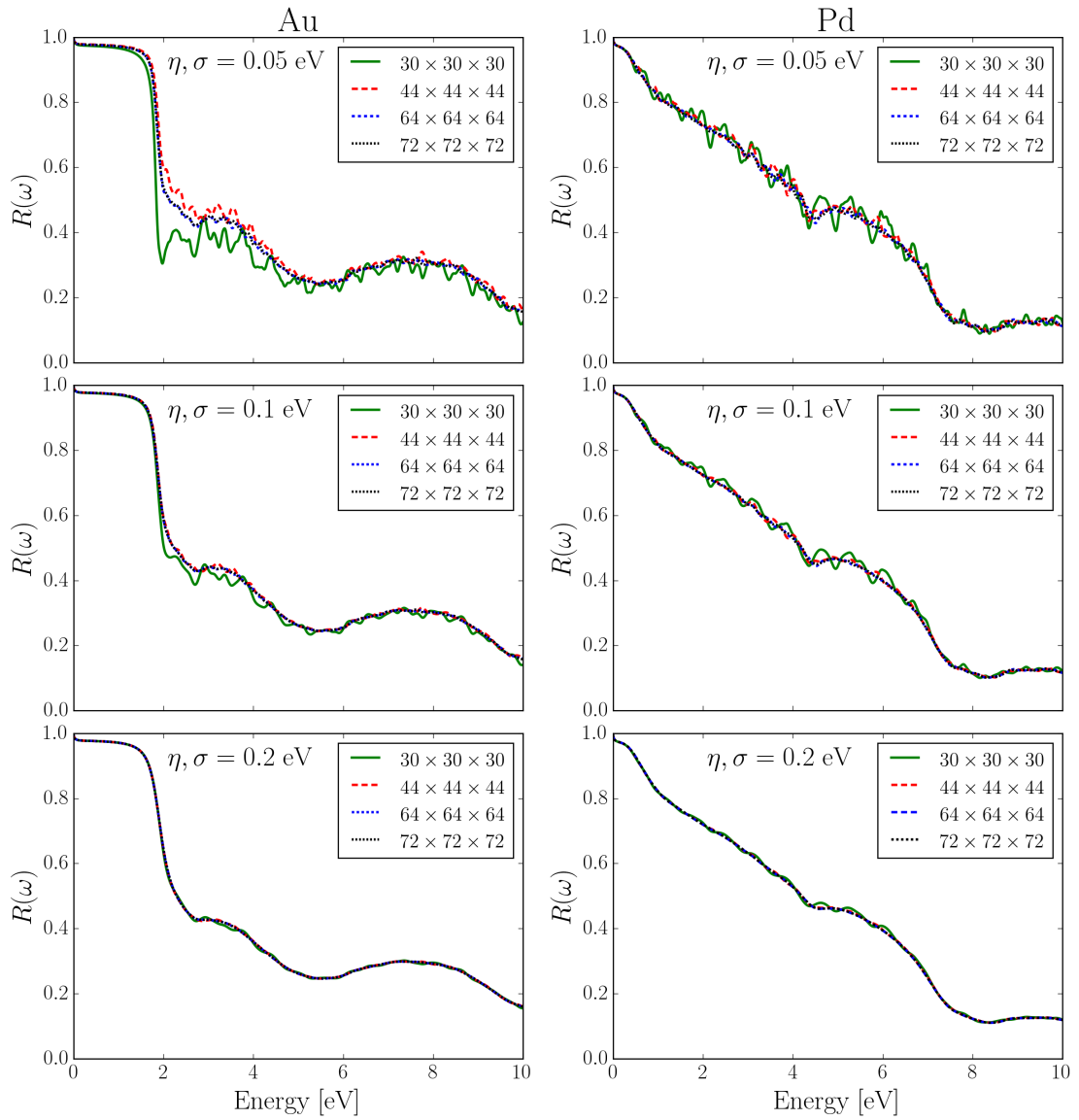


Figure 6.3 – Dependence of  $R(\omega)$  for elemental Au and Pd on the interpolation k-points grids for different values of  $\eta$  and  $\sigma$  (with  $\eta = \sigma$ ).

## 6.2 Comparison with experiments

### 6.2.1 Reflectivity and colour

We show in Fig. 6.4 the comparison between IPA results and experimental data for the reflectivity curve of 18 elemental metals, and focusing in a range of frequencies centered around the visible range (i.e. [1.65, 3.26] eV). Experimentally, we observe high and flat reflectivities along the visible spectrum for the “precious” transition metals (i.e. Rh, Ir and Pd) while we observe flat but less high reflectivities for the other transition metals considered (i.e. V, Nb, Ta, Cr, Mo and W). As a consequence, in terms of CIELAB colour coordinates, the first have large CIELAB brightness  $L^*$  and thus whitish colour while the others have smaller brightness and thus a more greyish colour. An interesting exception among the transition metals is osmium, that shows a reflectivity curve that is low in the low-energy part of the visible spectrum but then suddenly rises in the blue-violet part, thus giving a bluish tint to pure osmium. A similar behaviour is found also in tantalum but the rise of the reflectivity curve in the blue-violet region is significantly smaller and, consequently, also the bluish tint of the material. Instead, the simple *sp* metals lithium, potassium and aluminium all have very high and nearly flat reflectivity curves in the visible range (and therefore whitish colour) while in beryllium the intensity of the reflectivity is lower, and comparable to that of the transition metals (and thus having a greyish colour). Interestingly, the reflectivity curve of cesium decreases significantly within the visible range, so that red and yellow light are strongly reflected while the other visible frequencies are absorbed, giving a yellow tint to the material. As clearly shown in Fig. 6.4, the IPA simulations reproduce these different features of the elemental metals. For noble metals instead, the characteristic drop in the reflectivity curve in the visible range (for Cu and Au) or in the ultraviolet (for Ag) is also reproduced by the simulations, but at smaller energies compared to experiments due to the well-known underestimation of the interband gap of DFT-PBE band structures (see Chapter 1 and discussion therein).

We can quantitatively compare experiments and simulations in terms of colour coordinates by converting the reflectivity curves in the visible range to CIE colour spaces. In Fig. 6.5 we show the comparison between simulated colours and experimental colours in CIELAB space for some elemental metals. The colour differences between simulations and experiments for 22 elemental metals are summarized in Table 6.1. The average colour difference is  $\langle \Delta E \rangle = 6.0$  over these 22 elements ( $\langle \Delta E \rangle = 3.8$  if not including the three noble metals).

The IPA approach applied on top of PBE band structures predicts the reflectivity and colour of elemental metals surprisingly well. Although the colour is not always in quantitative agreement with experiments (see Table 6.1 and Fig. 6.5), we conclude that the shape and the main features of the experimental reflectivity curve are reproduced in elemental metals.

These results are somewhat surprisingly because we know that quasiparticle corrections modify significantly the DFT-PBE band structure in metals and the corrections are known to be *k*-dependent [46, 47] (i.e. they do not act as a simple scissor operator). Nonetheless, our approximated simulations manage to capture the correct features of the optical constants, intuitively because the dielectric function is given by the sum of all possible vertical transi-

tions over all the BZ and small differences in the positions and features of the bands (like gradient and curvature) are averaged out in the spectra. In the special case of noble metals the position of the occupied  $d$  bands in PBE is not correct and, since there are no other allowed interband transitions in that energy range, the onset of absorption in PBE is also not at the correct position (similar to the case of semiconductors for which the DFT-PBE band gap is systematically underestimated). On the other hand, the shape of  $\epsilon_2(\omega)$  for noble metals is reasonably well reproduced. This points to the fact that the PBE KS states, although giving an inaccurate description of the energy of the  $d$  bands, are a reasonable approximation of the true quasiparticle states.

Element	$\Delta E$
Li	5.1
Na	1.2
K	2.9
Cs	12.5
Be	3.6
V	3.7
Nb	3.4
Ta	2.4
Cr	4.0
Mo	2.4
W	3.4
Os	6.5
Co	5.5
Rh	1.8
Ir	2.9
Ni	4.6
Pd	0.5
Pt	5.2
Cu	11.8
Ag	12.4
Au	33.9
Al	1.4

Table 6.1 – Colour differences ( $\Delta E$ ) in CIELAB colour space between simulations and experiments for 22 elemental metals.

## Chapter 6. Reflectivity and colour of elemental metals

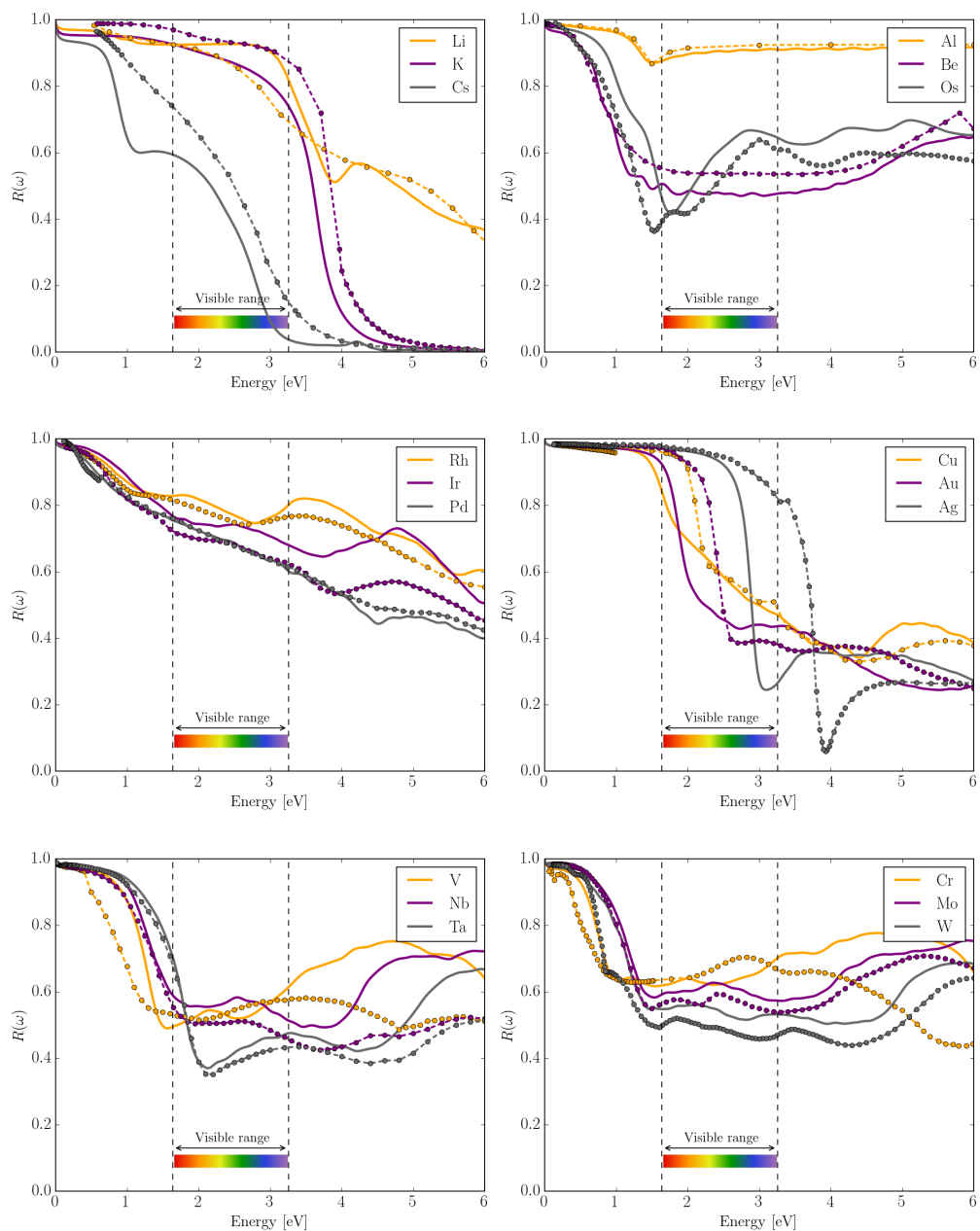


Figure 6.4 – Simulated (solid lines) and experimental (dot-dashed lines) reflectivities for 18 elemental metals. Experimental data are taken from Ref. [9]. The two vertical dashed lines show the limits of the visible range.

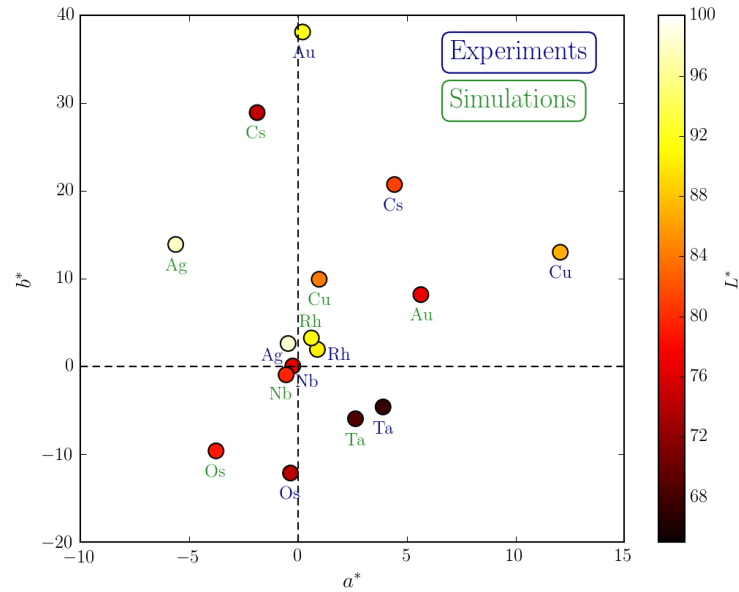


Figure 6.5 – Comparison of simulated (green) and experimental (blue) colours for eight elemental metals in CIELAB colour space (i.e. Ag, Au, Cs, Cu, Nb, Os, Rh and Ta). Experimental colours are derived from the optical data of Ref. [9].

### 6.2.2 Plasma frequency

We report in Fig. 6.6 the IPA Drude plasma frequency for all the 45 elemental metals studied. For anisotropic crystals, the average value  $\omega_D$  is shown. We observe the trend that for the alkali metals (Na, K, Rb, Cs) the IPA Drude plasma frequency decreases moving down in the column of the periodic table. This is explained by the fact that the volume of the primitive cell increases going down the column and that, for these simple metals,  $\omega_D \simeq \bar{\omega}_{D,\text{val}} \propto 1/\sqrt{V}$ . In lithium the situation is not so simple due to stronger interband transitions (see Table 6.3). Moreover, as a foreseeable general rule, elements in the same column of the periodic table and sharing the same crystal structures typically have similar values of  $\omega_D$ .

## Chapter 6. Reflectivity and colour of elemental metals

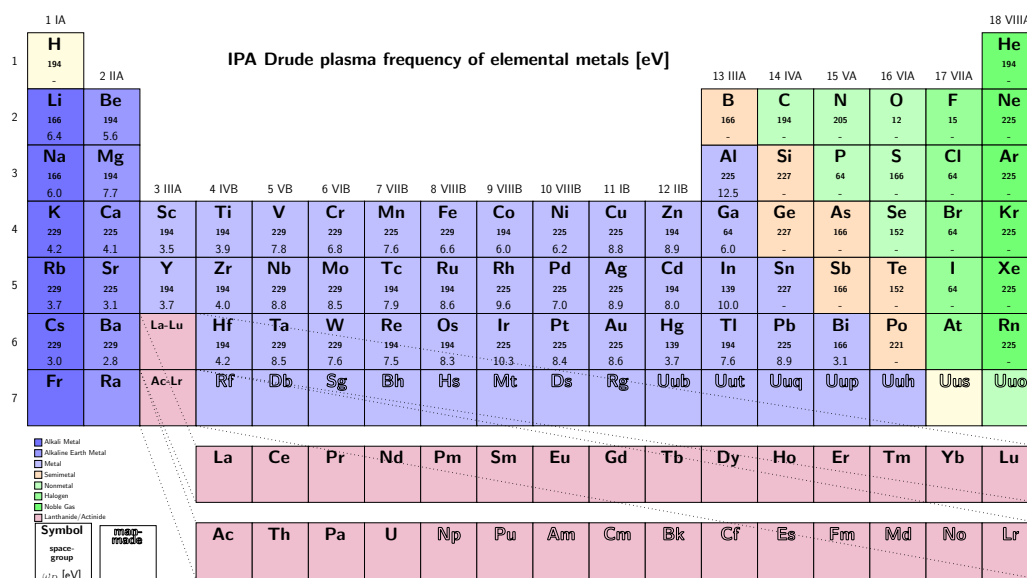


Figure 6.6 – Periodic table with the IPA Drude plasma frequency for 45 elemental metals computed in their ground-state crystal structures. The space group number of each crystal structure is also reported.

As shown in Table 6.2, our IPA results are in good agreement both with experiments and with the simulations performed by J. Harl [17] at the same level of theory for several elemental metals<sup>4</sup>. The small discrepancies found between the simulations most likely originate from the fact that in Ref. [17] the IPA Drude plasma frequency is evaluated at the experimental lattice parameter while we instead use the PBE lattice parameter. Indeed our values are systematically smaller than the ones in Ref. [17]. The remaining discrepancies are probably due to small differences in the details of the two implementations.

### 6.2.3 Photorealistic rendering

Photorealistic rendering is performed with the software Mitsuba [6]. In Fig. 6.7 we show the rendering of a metallic surface of elemental gold, osmium and cesium using the IPA optical constants and the comparison with the appearance of experimental samples of the same materials.

In gold, the shift of the reflectivity edge in the simulations with respect to experiments makes the rendered colour more reddish than the true colour of pure gold. On the other hand the bluish colour of osmium and the yellow colour of cesium are reasonably well reproduced by the IPA simulations.

<sup>4</sup>For transition metals there are no experimental data available because, due to the presence of interband transitions even at vanishingly small frequencies, the Drude plasma frequency cannot be extracted by fitting experimental optical data to the Drude model, even at very low energies.



## 6.2. Comparison with experiments

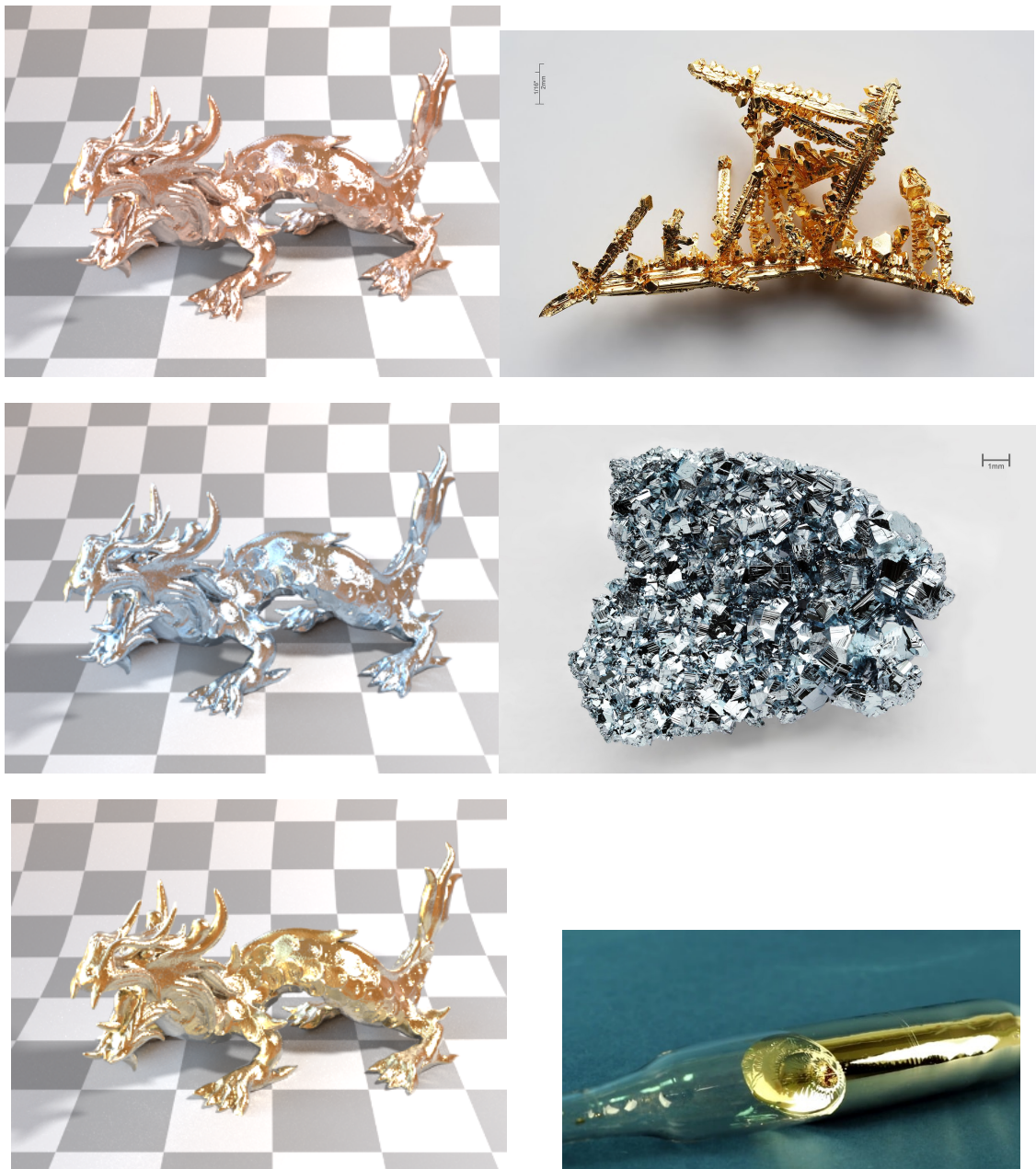


Figure 6.7 – Comparison between the rendering of a metallic surface of pure gold (top), osmium (center) and cesium (bottom) obtained using the simulated optical constants (left panel) and real samples of the three materials (right panel).

Element	This work	J. Harl [17]	Exp.
Cu	8.8	9.1	8.8, 8.9
Ag	8.9	9.2	8.9 ± 0.2 [130], 8.9
Au	8.6	9.0	8.45 [131], 8.7
Li	6.4	6.5	6.4
Na	6.0	5.9	5.7
Ca	4.1	4.3	5.7
Al	12.5	12.6	12.3 , 12.5
Rh	9.6	10.1	
Pd	7.0	7.4	
Pt	8.4	8.8	

Table 6.2 – Computed values of the IPA Drude plasma frequency (in eV) compared to previous simulations performed by J. Harl [17] and experiments (Exp.). The experimental values with no explicit reference are extracted from the data reported in Ref. [17], where all the original experimental references can be found.

### 6.3 Verification of the $f$ -sum rule

We perform a check *a posteriori* of the consistency of our simulations by verifying the  $f$ -sum rule. In real simulations we can calculate the dielectric function in an finite energy range and not up to infinity, so that the numerical integration required in Eq. 3.64 is in practice truncated at a cutoff energy  $\omega_c$ . We can define an energy-dependent effective classical Drude plasma frequency  $\bar{\omega}_{D,\text{eff}}^2(\omega_c)$  as:

$$\bar{\omega}_{D,\text{eff}}^2(\omega_c) = \frac{2}{\pi} \int_0^{\omega_c} d\omega \omega \varepsilon_2(\omega). \quad (6.2)$$

In case the transitions coming from the valence electrons can be considered essentially exhausted above the cutoff energy  $\omega_c$ , such that  $\varepsilon_2(\omega > \omega_c) \simeq 0$ , we can do the approximation  $\bar{\omega}_{D,\text{eff}}(\omega_c) \simeq \bar{\omega}_{D,\text{val}}$ . For a given elemental metal, the number of valence electrons per atom is assumed to be equal to the nominal valence  $Z$  of the element. However, if the pseudopotential contains also semi-core states in its valence the cutoff energy should be lower than the energy of the onset of absorption for the included semi-core electrons. If not, the electrons in the semi-core states should also be included in the valence  $Z$  in order to satisfy the  $f$ -sum rule for the valence electrons.

As already discussed in Section 3.4.5, the  $f$ -sum rule is valid for the total number of electrons and does not exactly hold for the valence-conduction electrons only. Indeed, in the pseudopotential formalism, the core electrons are frozen inside the nucleus and the  $f$ -sum rule can be slightly violated due to the non-locality of the pseudopotentials (see Section 3.4.5). The truncation of the integral always gives an underestimation of  $\bar{\omega}_{D,\text{val}}^2$  while the effect of the non-local potential can instead bring to an overestimation of  $\bar{\omega}_{D,\text{val}}^2$ . In practice, it has been verified both in experimental [132] and computational studies [83, 35] on elemental metals that the  $f$ -sum rule is nearly verified also for the valence-conduction electrons only.

Our calculations of  $\varepsilon(\omega)$  in elemental metals are performed up to 20 eV. Therefore we check the consistency of our calculations through the valence  $f$ -sum rule for elements in which we can assume that the transitions from the valence are exhausted above 20 eV and that eventual semicore states of the pseudopotential are more than 20 eV below the Fermi level. In most of the transition metals and in the noble metals as well, the interband transitions from the valence  $d$  electrons are not yet exhausted at 20 eV and these elements are not considered. Instead, for K, Rb, Cs, Sr and Ba, transitions from the semicore  $p$  states starts below 20 eV and so they are also not included<sup>5</sup>. In Fig. 6.8 we show the comparison between  $\bar{\omega}_{D,\text{val}}$  and  $\bar{\omega}_{D,\text{eff}}(\omega_c)$  with  $\omega_c = 20$  eV for thirteen elemental metals that satisfy the aforementioned conditions. The values of the classical Drude plasma frequency are extracted from Ref. [78] in which the experimental volume is used together with the nominal valence  $Z$  of the element. As it is clear from Fig. 6.8 the valence  $f$ -sum rule holds reasonably well.

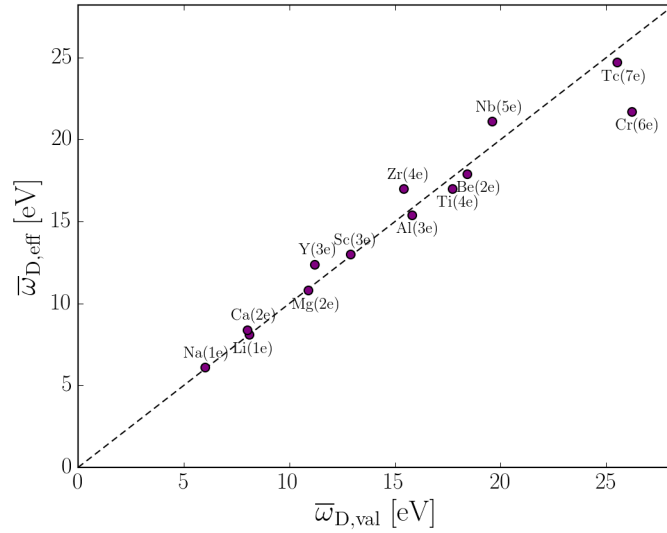


Figure 6.8 – Verification of the valence  $f$ -sum rule.  $\bar{\omega}_{D,\text{eff}}$  is computed by truncating the energy integration at 20 eV. We report in parentheses the nominal number of valence electrons  $Z$  used in the evaluation of  $\bar{\omega}_{D,\text{val}}$ .

## 6.4 Validity of the Drude model

In the empirical Drude model, developed by Paul Drude in 1900, the valence electrons in a metal are assumed to be a gas of free and charged classical particles. The application of the kinetic theory of gases to this system allows one to estimate the optical properties of a metal once the density of valence electrons in the material is known. The Drude model can furnish a reasonable estimation of the IPA Drude plasma frequency, i.e.  $\omega_D \simeq \bar{\omega}_{D,\text{val}}$ , in simple metals for which the conduction electrons can be assumed to be nearly free. Indeed, Table 6.3 shows that the Drude model gives reliable results for elemental metals with only

<sup>5</sup>However, for these elements, we have checked that the valence  $f$ -sum rule holds if the integral is truncated before the onset of the transitions from the  $p$  semicore states.

one valence electron per atom, such as the alkali metals. Because of the free-electron-like behaviour of these metals, interband transitions from the partially-filled conduction band are very weak, with the exception of Li, and the second term in the right-hand side of Eq. 3.62 can be neglected. Indeed we notice that the error of the Drude model has a clear trend and increases by moving down in the periodic table from Na to Cs due to a corresponding increase of the interband absorption processes (see Appendix C.1). A behaviour similar to alkali metals is shown by the noble metals. The  $s$  electrons in the partially-filled conduction band can still be assumed nearly free and are not substantially perturbed by the occupied  $d$  states lying lower in energy so that the Drude model is again in good agreement with IPA results.

In Fig. 6.9 we compare the reflectivity obtained from the Drude model using the values for  $\bar{\omega}_{D, \text{val}}$  reported in Table 6.3 and the reflectivity from IPA simulations. Interband transitions in potassium are very weak up to 15 eV and IPA simulations and Drude model give similar results and both reproduce the experimental behaviour. Infact the material is highly reflective for energies below the plasma frequency while it is roughly transparent for higher energies<sup>6</sup>. On the other hand, for cesium, interband transitions in the visible range are stronger and IPA simulations and Drude model differ. In aluminum, IPA simulations and Drude model give similar results but, of course, the Drude model does not reproduce the dip in the experimental reflectivity curve at around 1.5 eV that is due to interband transitions. In gold the reflectivity curve in the visible range is dominated by interband transitions involving the  $5d$  electrons that strongly reduce the reflectivity at energies smaller than the Drude plasma frequency. Therefore the Drude model, although giving the correct Drude plasma frequency, does not reproduce the experimental behaviour of the reflectivity of gold (and, similarly, of copper and silver) which is instead captured by the IPA simulations.

Summarizing, in order to be predictive in the estimation of the optical properties of metals, both interband and intraband contributions need to be computed *ab initio*.

---

<sup>6</sup>To notice that, in general, the Drude plasma frequency does not coincide with the plasma frequency corresponding to the true plasmon resonance of the material, which is defined as the frequency  $\omega_p$  for which  $\epsilon_1(\omega_p) = 0$ . But in the case of elemental potassium, for which interband transitions are negligible, the two values are nearly equal.

Element	$\omega_D$	$\bar{\omega}_{D,\text{val}}$	Error (%)
Li	6.4	8.1 (1e)	27
Na	6.0	6.0 (1e)	0.0
K	4.2	4.4 (1e)	4.8
Rb	3.7	4.0 (1e)	8.1
Cs	3.0	3.5 (1e)	17
Cu	8.8	10.8 (1e)	23
Ag	8.9	9.0 (1e)	1.1
Au	8.6	9.0 (1e)	4.6
Mg	7.7	10.9 (2e)	42
Al	12.5	15.8 (3e)	26

Table 6.3 – Comparison of the classical Drude plasma frequency from the Drude model ( $\bar{\omega}_{D,\text{val}}$ ) and the IPA Drude plasma frequency ( $\omega_D$ ). We report in parentheses the nominal number of valence electrons  $Z$  used in the evaluation of  $\bar{\omega}_{D,\text{val}}$ . The error given by the Drude model with respect to the IPA results (in percentage) is also shown.

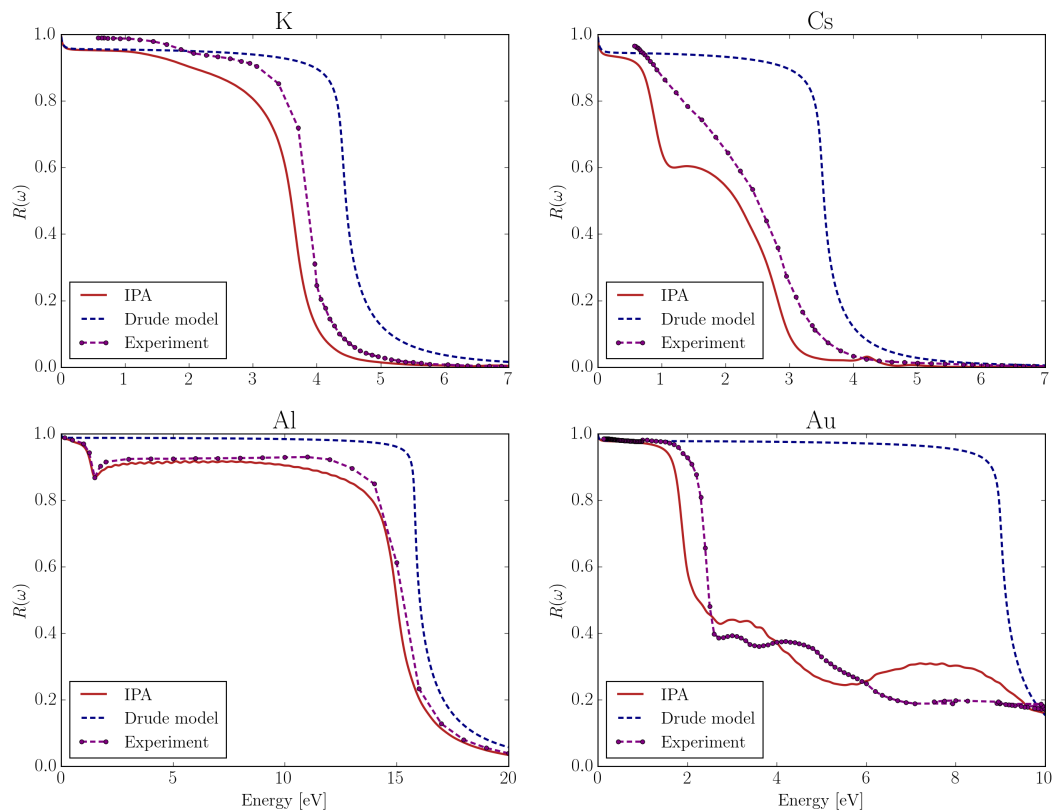


Figure 6.9 – Comparison of the reflectivity obtained with IPA simulations (solid lines), Drude model (dashed lines) and from experiments [9] (dot-dashed lines) for K, Cs, Al and Au.

### 6.5 Additional effects on the optical properties

We now study the effect of the inclusion of SOC and of the neglect of the non-local commutator in the evaluation of the IPA optical properties.

#### 6.5.1 Spin-orbit coupling

All the calculations in this work are performed at the scalar-relativistic level. Here we want to study the effect of the inclusion of an additional relativistic correction, namely the spin-orbit coupling (SOC).

The Schrödinger equation is a non-relativistic approximation of the more general relativistic Dirac equation in the limit in which relativistic corrections can be neglected. Relativistic corrections are typically added to the Schrödinger equation as a perturbation and are divided into three terms: the mass-velocity and Darwin terms, that are included at the scalar-relativistic level, and the SOC. The mass-velocity and Darwin terms usually give the largest relativistic contributions but for heavy-elements SOC can be relevant too.

Here we study the effect of SOC on the optical properties of two heavy elements relevant for our work, i.e. gold and platinum (see Fig. 6.10). In gold the largest relativistic effects come from the mass-velocity and the Darwin terms while SOC gives only a small correction [51]. In particular, the splitting of the bands induced by the SOC reduces the interband gap so that the absorption edge appears at a slightly lower energy. However, the shape of the reflectivity curve is not changed and the shift of the absorption edge leads, as a consequence, to a drop in the reflectivity curve a bit redshifted with respect to the scalar-relativistic calculation. Similarly, the SOC only reduces the IPA Drude plasma frequency by 0.2 eV (from 8.6 eV to 8.4 eV), given that the conduction band crossing the Fermi level is almost left unmodified by the inclusion of SOC [52]. However, because of the shift of the reflectivity edge, there is a perceivable change in colour between scalar-relativistic and fully relativistic simulations ( $\Delta E = 3.6$ ). We notice that the correction in  $R(\omega)$  due to the SOC is in the wrong direction compared to experiments and the simulated colour moves further away from the yellow part of the colour space (in terms of CIELAB colour space it means that  $b^*$  decreases).

In platinum the effect of SOC is more dramatic. The low-energy peak in  $\epsilon_2^{\text{inter}}(\omega)$  at 0.2 eV in the scalar-relativistic simulation due to  $d$ - $d$  interband transitions is shifted by 0.6 eV to higher energies by including the SOC. This gives rise to a reduction in the reflectivity curve at around 0.8 eV that well reproduces the experimental data and that is absent in the scalar-relativistic case. The inclusion of SOC also reduces the Drude plasma frequency by nearly 20 %. Besides, we note in passing that our results are in very good agreement with previous all-electron calculations [51].

For platinum the effect of SOC is large but it modifies the optical properties in the infrared region of the spectrum and not in the visible so that the colour remains almost unchanged ( $\Delta E = 1.0$ )<sup>7</sup>.

---

<sup>7</sup>We computed also the optical properties of the heavy element tungsten including SOC. However, for this material, no significant differences with respect to the scalar-relativistic case are found in the reflectivity curves for

## 6.5. Additional effects on the optical properties

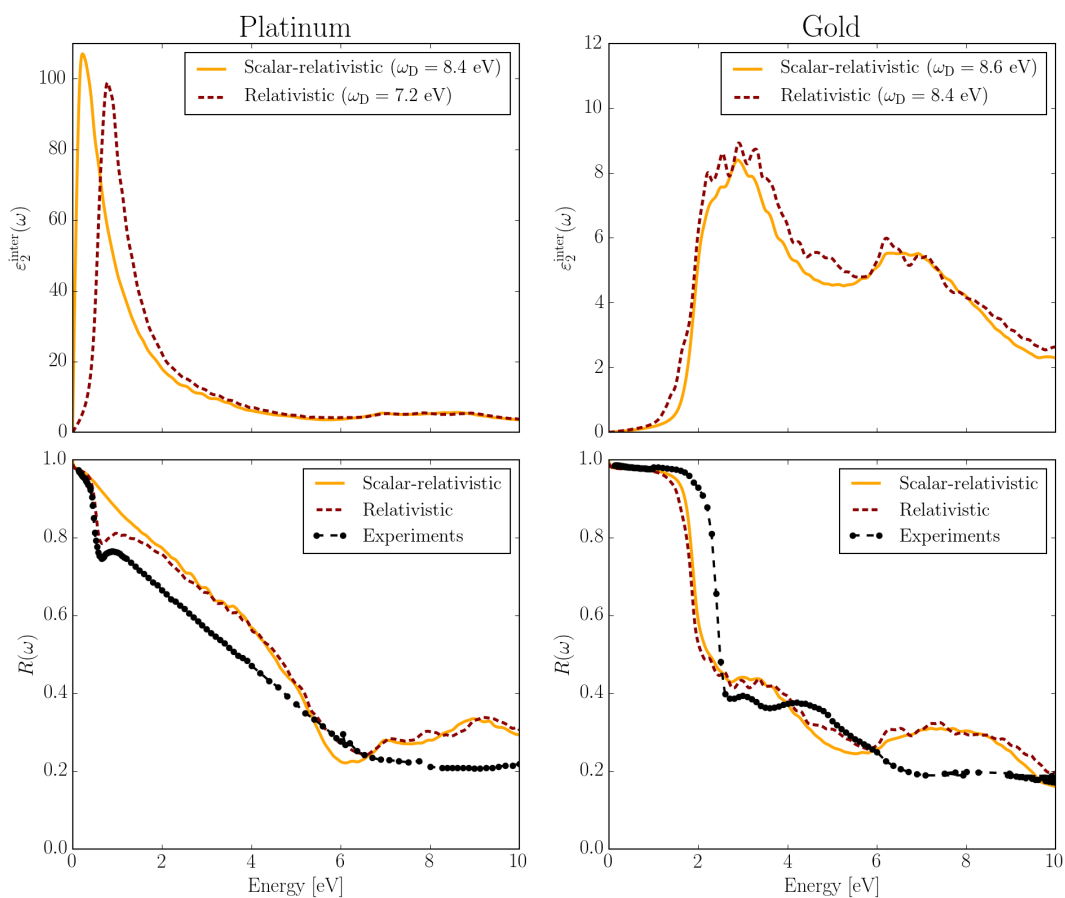


Figure 6.10 – Comparison between the dielectric function and reflectivity for platinum and gold computed including ('Relativistic', solid lines) and not including ('Scalar-relativistic', dashed lines) SOC. Experimental data of the reflectivities (dot-dashed lines) are also reported [9].

### 6.5.2 Non-local commutator

The neglect of the non-local commutator gives a systematic overestimation of the velocity matrix elements, both of the diagonal (intraband) and off-diagonal (interband) terms. As a consequence, the reflectivity curve  $R(\omega)$  is also overestimated by neglecting this contribution. However the absorption edge and the position of the peaks in the spectra, that are given by the energy differences between unoccupied and occupied bands, are not modified by this contribution. In Fig. 6.11 we study the effect of the non-local commutator on the optical properties of vanadium and copper for which this correction is particularly large. The IPA Drude plasma frequency is overestimated by 33 % for vanadium and by 35 % for copper. We perform the same test also for other elements, for which the effect is less pronounced but still noticeable. In silver, palladium and rhodium the overestimation is of 7-9 %, while in gold it is negligible. The interband optical absorption, given by  $\varepsilon_2^{\text{inter}}(\omega)$ , is also overestimated and the discrepancies are, in general, energy dependent. However, for all the materials tested, the main spectral features of  $\varepsilon_2^{\text{inter}}(\omega)$  are not modified by the neglect of the non-local commutator, as explained before, with the notable exception of copper. In copper, as already noted by Marini *et al.* [72], the shape of  $\varepsilon_2^{\text{inter}}(\omega)$  is significantly altered, and at the absorption edge, the overestimation is more than 100 %. In the case of copper, the non-local commutator is actually needed to reproduce the experimental data.

The effect on the colour of the inclusion of the non-local commutator for vanadium and copper is small but perceivable:  $\Delta E = 2.2$  for vanadium and  $\Delta E = 6.2$  for copper.

---

energies up to 10 eV, and thus the data are not shown here.



## 6.5. Additional effects on the optical properties

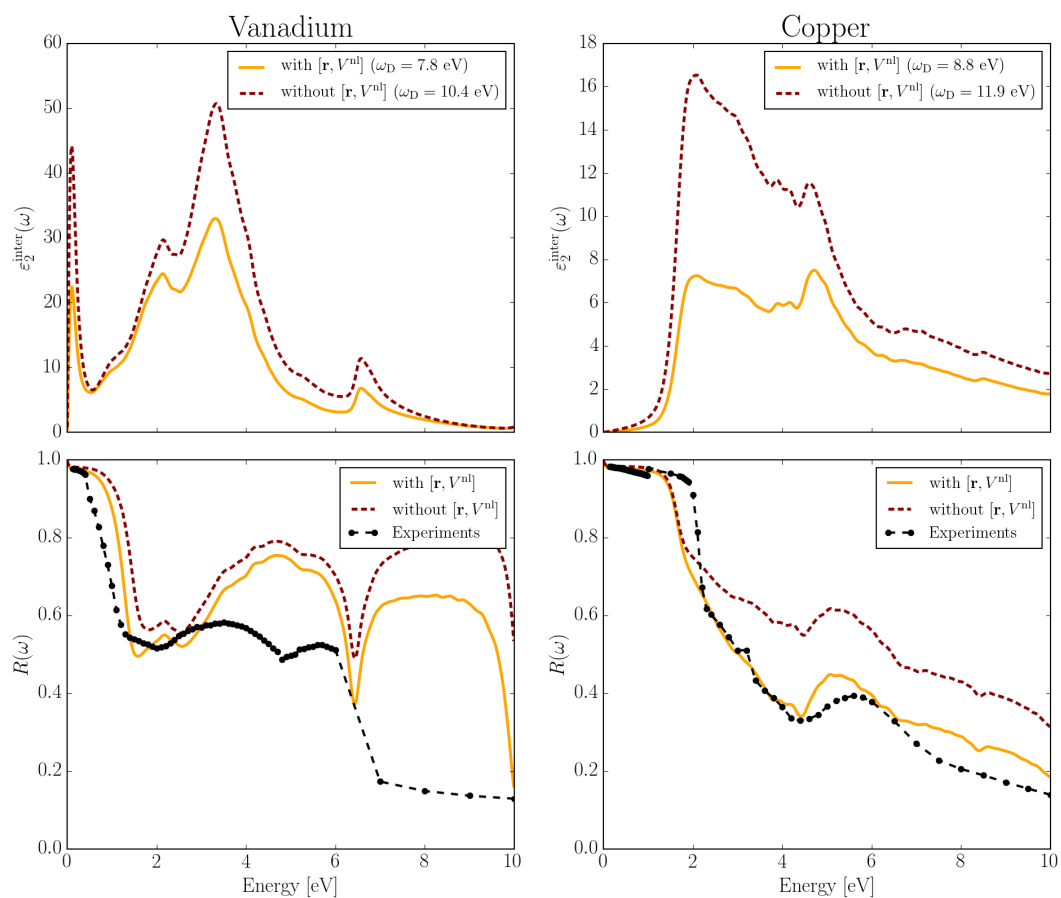


Figure 6.11 – Comparison between the dielectric function and reflectivity for vanadium and copper computed with (solid lines) and without (dashed lines) including the non-local commutator. Experimental data of the reflectivities (dot-dashed lines) are also reported [9].



# 7 Reflectivity and colour of alloys

In Chapter 6 we have discussed the results of the simulations of the reflectivity and colour of elemental metals and we have compared the simulated optical data with experiments. In this Chapter we perform a similar study on metallic alloys, focusing mainly on noble-metal binary compounds, and considering different types, i.e. intermetallics, solid solutions and heterogeneous alloys.

## 7.1 Simulation of alloys

### 7.1.1 Binary alloys

We consider binary alloys, that we indicate with the nomenclature  $A_{1-x}B_x$ , where A and B are the two constituent elements and  $x$  is the atomic concentration of element B. According to the atomic configuration and microstructure, these can be schematically divided into three main categories: solid solutions, intermetallic compounds and heterogeneous alloys. In solid solutions the atoms of the two constituent elements are randomly distributed over the sites of the lattice and with a probability of occupation given by the concentration of the element in the alloy<sup>1</sup>. Intermetallic compounds are ordered structures that have a defined crystal structure and simple stoichiometric ratios (or, more correctly, a narrow homogeneity range). Heterogeneous binary alloys instead consist of a mixture of two phases due to the presence of a solubility gap in the phase diagram. Pure solid solutions and intermetallic compounds are single-phase alloys while heterogeneous alloys are two-phase alloys, and the single phases coexisting in a heterogeneous alloy can be either solid solutions or intermetallic compounds.

---

<sup>1</sup>There is also a fourth category that is not considered in this work, the so-called metallic glasses. As in solid solutions, atoms of the constituent elements in metallic glasses are randomly distributed but, in this case, the solid is amorphous, i.e. there is no underlying periodic lattice. These could be studied with the methods described here, but would require large supercells and realistic, microscopic atomistic models.

### 7.1.2 Computational methods

#### Intermetallic compounds

In first-principles simulations, intermetallic compounds can be treated as elemental crystals because they have a defined crystal structure and simple stoichiometric ratios. They are truly periodic systems and can be simply simulated in their primitive cell in the same way as it is done for elemental crystals.

#### Solid solutions

The first-principles simulation of disordered solid solutions is not as straightforward as the simulation of ordered intermetallic compounds. Indeed, from a practical point of view, the random occupation of the lattice sites and thus the lack of a truly periodic potential in these systems does not allow for the definition of a primitive cell that can be periodically repeated in order to build an infinite crystal. From a conceptual point of view, this actually means that Bloch theorem and thus the reciprocal space formalism underlying band theory is not in principle applicable to solid solutions. If we consider the disorder introduced by the addition of alloying elements in the periodic lattice as a perturbation with respect to the pure elemental crystal, Bloch states are no longer eigenstates of the Hamiltonian of the system but they scatter into other states with a certain finite lifetime. However, Bloch states can still be considered as approximate eigenstates if the broadening of the state is much smaller than the width of the corresponding electronic band.

Several methods exist to model the properties of disordered alloys. We distinguish between effective-medium approaches and supercell approaches. In effective-medium methods, all the possible microscopic configurations of the random system are averaged into an effective-medium having the same crystal structure of the constituent elements. In the supercell approach instead, the basic idea is to simulate the effect of disorder by building large enough simulation cells that are able to reproduce the properties of the true random alloy. Here we briefly describe the virtual crystal approximation (VCA) and the method of the so-called special quasi random structure (SQS) [133, 134] for the effective-medium and supercell approaches, respectively; these are the two main computational methods considered in this work for the simulation of solid solutions.

The VCA method assumes that each atomic site of the parent crystal structure is composed by "virtual" atoms. The potential generated by these virtual atoms,  $V_{VCA}$ , is given by a composition-weighted average of the potentials  $V_A$  and  $V_B$  of the two constituent elements A and B:

$$V_{VCA} = (1 - x)V_A + xV_B. \quad (7.1)$$

The VCA is valid in the weak-scattering limit, i.e. when the difference in potential of the two constituents is small compared to their bandwidth. Depending on the application, it can sometimes be an adequate approximation mainly for isoelectronic alloys, i.e. when the

constituent elements belong to the same column of the periodic table, and their potentials are similar. However the VCA approach does not take into account effects related to structural relaxation. Indeed, it is a model that assumes the alloy has the same symmetry of the parent crystal structure and does not include effects related to local symmetry lowering. However, in a real solid solution, an A atom may be coordinated locally by varying numbers of A and B neighbours. This modifies the local environment of each site and, in general, lowers the local symmetry with respect to that of the parent lattice.

An even simpler model that it is worth to briefly describe, is the rigid band model. According to this model, the potentials  $V_A$  and  $V_B$  of the two constituent elements A and B are approximated as equal, i.e.  $V_A = V_B$ . This means that the band structures of the two elemental crystals of A and B are assumed to be the same while the position of the Fermi energy is allowed to change according to the number of electrons per atom, which depends on the concentrations of the two constituent elements in the alloy.

For completeness, we also mention that more sophisticated methods that go beyond the VCA approximation and that do not require the use of supercells exist: the coherent potential approximation (CPA) [135] and the so-called "computational alchemy" method [136] are two notable examples. However, due to their significant additional complexity, these methods are not considered in this work and therefore are not discussed in further detail here.

Contrary to the effective-medium techniques, the supercell approach does not rely on any mean-field model and the effect of disorder is simulated in a "brute-force" way by employing large simulation cells (supercells). The supercell representing the random alloy  $A_{1-x}B_x$  is occupied by an appropriate number of atoms of elements A and B corresponding to the atomic concentration  $x$ . However, in practice, supercells always have a spurious periodicity because of the periodic boundary conditions imposed in the simulations. Therefore, convergence of the properties under investigation with respect to the supercell size must always be carefully performed. The naive construction of supercells by randomly occupying the lattice sites with atoms of element A or B (with the probability of occupation given by the atomic concentration of the alloy) is not the most efficient solution. A systematic improvement, both in terms of accuracy and computational cost, can be obtained through the use of SQSs. A SQS can be seen as the supercell that best represents the true random alloy for a given number of atoms per supercell. The theory underlying the construction of SQSs is based on the cluster expansion (CE) [137] method, which is a rigorous approach for the first-principles simulation of both ordered and disordered alloys. Without going into details, the main idea of the SQS method is to build "special" finite supercells that reproduce the structural correlation functions of the perfectly random alloy. The goal is therefore to build structures that locally resemble the true random alloy. However, it is worth mentioning that for SQSs of relatively small size ( $N \sim O(10)$ , where  $N$  is the number of atoms in the supercell), only the first pair correlation functions of the random alloy can be exactly reproduced. Hence this approach is appropriate if the physical properties under investigation depend only on the local environment and are not influenced by long-range interactions.

The SQS method, since it is based on the CE method, can be used in principle for any property

that is defined on a fixed lattice. Nonetheless, for each alloy property computed, one should always study the convergence of the given property with respect to the number of correlation functions of the random alloy that are reproduced by the SQS (to give a practical example, convergence of the total energy does not necessarily imply convergence of the optical properties or viceversa). In practice, SQSs with only 16 atoms or less have been successfully applied to calculate, for instance, thermodynamic and magnetic properties of metallic alloys [138] and also the band gap of semiconductor alloys [134].

When dealing with the simulation of optical properties within the framework of the supercell approach, the effect of alloying additions on a pure elemental crystal is to give rise to new electronic interband transitions due to zone folding effects (pseudodirect transitions), degeneracy breaking of electronic states (crystal-field splittings due to symmetry lowering) and localised impurity states (sublattice localisation), which cannot be found in simple VCA calculations [134]. Moreover, since SQSs electronic states have lower symmetry than VCA ones and can correspond to a combination of VCA states of different character, also the oscillator strengths of optical transitions are modified if compared to VCA calculations<sup>2</sup>. In general, these effects could lead to substantial differences between SQS and VCA optical spectra.

In this work we use the supercell approach, based mainly on the use of SQSs, to simulate the reflectivity and colour of solid solutions. As we will show below, the SQS approach is able to qualitatively capture the main trends in the reflectivity curve, and thus in the colour, of gold-based solid solutions. In our opinion, it is the method that gives the best compromise between accuracy and computational cost and, at the same time, allows one to perform systematic first-principles studies in a relatively straightforward way.

### Heterogeneous alloys

We assume that the grain sizes within the heterogeneous alloy are macroscopic so that we can define a macroscopic dielectric function of the phase within a grain. We use the Bruggeman model (e.g. see Ref. [140]) to estimate the dielectric function, that we indicate as  $\epsilon_{\text{Br}}$ , of the alloy made of the two phases  $\alpha$  and  $\beta$ . If the total concentration  $x$  of the alloy is known, we can calculate the amounts of the two phases present,  $x_\alpha$  and  $x_\beta$  ( $x_\alpha + x_\beta = 1$ ), by applying the lever rule to the phase diagram of the system. The dielectric function of the mixture within the Bruggeman model is given, in terms of the dielectric functions  $\epsilon_\alpha$  and  $\epsilon_\beta$  of the single phases, by the following expression:

$$(1 - x_\beta) \frac{\epsilon_\alpha - \epsilon_{\text{Br}}}{\epsilon_\alpha + 2\epsilon_{\text{Br}}} + x_\beta \frac{\epsilon_\beta - \epsilon_{\text{Br}}}{\epsilon_\beta + 2\epsilon_{\text{Br}}} = 0. \quad (7.2)$$

The dielectric function of the single phases can be obtained with the methods described above

---

<sup>2</sup>As formalized in Ref. [139], the new features appearing in the band structure of alloys simulated with the supercell approach can be described in terms of an effective alloy band structure of a fictitious primitive cell having the symmetry of the parent lattice, and these lead, in practice, to bands with a finite broadening.

for intermetallic compounds and solid solutions.

In Table 7.1 we summarize the computational methods used in this work in order to simulate the reflectivity and colour of different types of binary alloys.

Binary alloys	Computational method
Intermetallic compounds	Primitive cell
Solid solutions	Supercell (SQS)
Heterogeneous alloys	Bruggeman model

Table 7.1 – Different types of binary alloys and corresponding computational method used for the first-principles simulation of these systems.

## 7.2 Optical properties in supercell simulations

We discuss the effects on the optical properties of the lowering of symmetry in supercells with respect to the case of primitive cells. Indeed, supercells of alloys have lower symmetry compared to the corresponding pure crystals. Furthermore, the approximated Shirley's OB method reduces the symmetry even in supercells that are in principle equivalent to the primitive cell.

### 7.2.1 Effects of the optimal basis

According to the equations shown in Section 3.4, the computed IPA optical properties should not depend on the size of the simulation cell. In other words, the dielectric function of, e.g. pure gold, should be identical if computed in a primitive cell or in an equivalent supercell. In fact, if the cubic symmetry of pure Au is preserved in supercell calculations, pseudodirect transitions would be forbidden by symmetry (they would correspond to indirect transitions between different k-points in the BZ of the primitive cell, which are not allowed because of crystal momentum conservation [77]). However, the introduction of some amount of disorder in the supercell, e.g. by internal displacement of the atomic positions, would break the symmetry of the system and the matrix elements of the velocity operator would not be exactly zero anymore. Moreover, because of the presence of the squared difference of band energies in the denominator of Eq. 3.65, weak transitions between states just below and just above the Fermi level would give a large contribution to  $\epsilon_2^{\text{inter}}(\omega)$  for small energies<sup>3</sup>. This is what actually happens in the OB method, where a tiny amount of disorder is always inevitably present. Indeed, the OB method is an approximate interpolation method that does not preserve the symmetry of the system, even if the supercell has the full symmetry of the primitive cell. Interpolated bands have always some small numerical errors so that band degeneracies are not exactly preserved as well as the equivalence due to crystal symmetry of k-points in the BZ. In practice, as shown below, this numerical error affects only the low-energy

<sup>3</sup>Unless specified otherwise, in this Chapter we always deal with the dielectric function averaged over the three Cartesian directions as defined in Eq. 6.1.

part of  $\epsilon^{\text{inter}}(\omega)$ .

To numerically assess these effects we consider two test examples: elemental gold and the intermetallic compound AuGa<sub>2</sub>. In particular, we study elemental gold in the primitive FCC cell and in an equivalent  $2 \times 2 \times 4$  FCC supercell with 16 atoms. Similarly, for the intermetallic compound AuGa<sub>2</sub>, we consider both the primitive cell containing 3 atoms and a  $2 \times 2 \times 2$  supercell containing 24 atoms. For a meaningful comparison we use same broadenings (i.e.  $\eta$ ,  $\sigma$  and  $\gamma$ ) and equivalent k-points grids and number of empty bands between primitive cells and supercells calculations. In Fig. 7.1 we notice for both examples the presence of a spurious peak centered at around 0.1-0.2 eV in  $\epsilon_2^{\text{inter}}(\omega)$  for supercell calculations. The effect is dramatic in Au while in AuGa<sub>2</sub>, where real low-energy interband transitions exist, it is less pronounced (for Pd, where a strong low-energy peak is present in the primitive cell, as shown in Fig. 6.2, primitive cell and supercell results are basically identical). Moreover, as we can see in Fig. 7.1, this spurious effect does not modify significantly the total dielectric function and, as a consequence, the reflectivity curve. Quantitatively, we verify this with the help of the  $f$ -sum rule. Indeed, if the results obtained for the total dielectric function in the primitive cell and in the supercell can be considered consistent, the integral entering in the evaluation of the  $f$ -sum rule should give nearly the same number in the two cases. In fact, the numerical evaluation of the integral in the primitive cell and in the supercell gives values that differ by less than 0.2 % for both Au and AuGa<sub>2</sub>. Therefore we can state that the true physical quantities, i.e. the total dielectric function and the reflectivity, are numerically independent from the size of the supercell. Instead the interband and intraband contributions, if considered separately, can show some differences due to the intrinsic amount of disorder introduced by the OB method. Nonetheless, depending on the system studied and on the amount of disorder introduced (i.e., for our simulations, on the size of the OB as discussed in Section 5.1), the spurious peak could in principle have a small impact in the low-energy part of the spectrum and thus to result in a small reduction of the reflectivity.

As we will see in the following, the absorption peak in  $\epsilon_2^{\text{inter}}(\omega)$  at low energies is present also in supercell simulations of alloys where the symmetry lowering of the system with respect to the pure crystal is intrinsically related to the alloying additions inside the simulation cell, and not just due to the disorder introduced by the OB method<sup>4</sup>. Computing the optical properties of a perfect crystal with the OB method can therefore be seen as equivalent to the simulation of a perfect crystal perturbed with a small amount of disorder<sup>5</sup>.

---

<sup>4</sup>Similar results have been found in first-principles studies on Au [141] and Al [142] thin films performed with the supercell approach, in which case the intensity and position of the low-energy peak depend on the number of layers considered.

<sup>5</sup>From this point of view we can say that the peak at low energies is not spurious but it is a real effect due to the introduction in the system of an "artificial" (because given by numerical errors) disorder.



## 7.2. Optical properties in supercell simulations

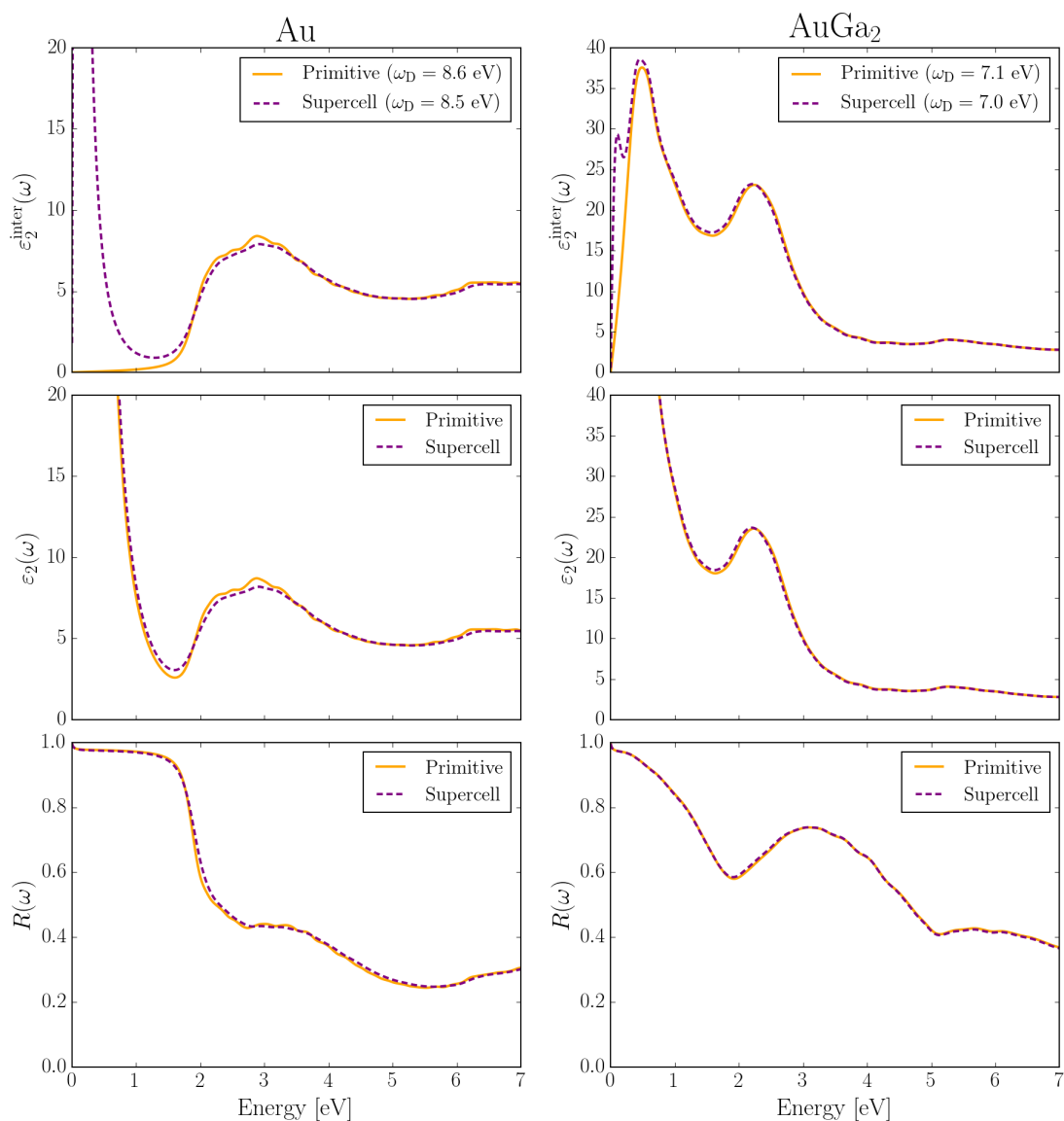


Figure 7.1 – Comparison of the IPA optical properties of Au and AuGa<sub>2</sub> computed with the OB method in the primitive cell (solid lines) and in a supercell (dashed lines). The total dielectric function and the reflectivity are numerically independent from the size of the simulation cell while the interband and intraband contributions, taken separately, are not.

### 7.2.2 Convergence with k-points sampling and broadening

Similarly to Section 6.1 for elemental metals, we now study the convergence of the dielectric function and of the reflectivity for supercells with respect to k-points sampling and broadening, i.e.  $\eta$  and  $\sigma$ . As test examples for supercell simulations of gold-based alloys, we perform the convergence studies on two  $2 \times 2 \times 4$  FCC supercells of gold with 16 atoms, AgAu<sub>15</sub> and Au<sub>15</sub>Pd, in which an atom of Au is replaced with an atom of Ag and an atom of Pd, respectively. Fig. 7.2 shows that the convergence of the IPA Drude plasma frequency in supercells is less straightforward compared to the case of elemental metals. The value of  $\omega_D$  depends more strongly on the interpolation k-grid and converges slowly to a common value, even for large  $\sigma$ . This behaviour can be explained by the fact that in supercells there are several bands that cross the Fermi level due to zone folding. Therefore the complex shape of the Fermi surface requires denser k-grids to be accurately sampled. Moving to the interband contribution, we observe in Fig. 7.3 a general blurring of all the features of  $\epsilon_2^{\text{inter}}(\omega)$  by increasing  $\eta$ , as for elemental metals (see Fig. 6.2), and an increase of the optical absorption in the low-energy range (roughly up to 2 eV). Similarly to the supercell calculations of elemental Au and of the AuGa<sub>2</sub> intermetallic shown in Section 7.2.1, we observe the presence of a peak at low energies in the optical absorption of AgAu<sub>15</sub> and AuPd<sub>15</sub>. However, in contrast with the case described before, the appearance of the peak is not only due to the disorder introduced by the numerical inaccuracies of the OB method but it is due to allowed interband transitions. Indeed, when considering supercells for the simulation of alloys, the symmetry of the system is truly reduced if compared to the symmetry of the pure crystal (e.g. of elemental gold when considering gold alloys) and thus new interband transitions become possible, as explained in Section 7.1.2<sup>6</sup>. The effect of  $\eta$  on the optical spectra in supercell calculations of gold alloys is similar to the effect of  $\gamma$  in elemental metals. We also notice that the low-energy optical absorption in Au<sub>15</sub>Pd is significantly stronger and extends to higher energies compared to AgAu<sub>15</sub>. Indeed Pd impurities in the Au matrix give rise to virtual bound states below the Fermi level that increase the absorption at frequencies below the interband gap of elemental gold and makes the absorption edge characteristic of elemental gold smoother. The features of  $\epsilon_2^{\text{inter}}(\omega)$  within the visible range or at higher energies converge fast with respect to k-points (already a  $16 \times 16 \times 11$  k-grid gives reasonably converged results), but not the low-energy peak whose intensity is strongly k-points dependent (see insets in Fig. 7.3). At a fixed value of the broadenings (for simplicity we consider  $\eta = \sigma$  given that  $\omega_D$  changes by less than 5 % in both systems by varying  $\sigma$ ), we observe that the reduction of the intensity of the peak by increasing the density of the k-points grid is compensated by a corresponding increase of the value of  $\omega_D$ . This explains why the reflectivity curves shown in Fig. 7.4 converge significantly faster than the single interband and intraband contributions with k-points sampling. On the other hand the reflectivity is

---

<sup>6</sup>These considerations, resulting from simulations performed with the SIMPLE code, have been verified by performing the same supercell calculations also with Yambo. In a  $2 \times 2 \times 2$  supercell of elemental Au, no low-energy peak is present in  $\epsilon_2^{\text{inter}}(\omega)$  calculated by Yambo because the symmetry of the primitive cell is preserved (contrarily to SIMPLE, no interpolation methods are used in Yambo). Instead, in supercells calculations of alloys (e.g. for Ag-Au) where the symmetry is lower than the primitive cell, the same low-energy peak appears also in the interband optical absorption computed with Yambo.

## 7.2. Optical properties in supercell simulations

more sensitive to the value of  $\eta$  chosen. A larger value of  $\eta$  produces a stronger smoothing of the reflectivity edge of elemental gold in  $\text{AgAu}_{15}$  and  $\text{Au}_{15}\text{Pd}$  (similar to the effect that  $\gamma$  has on the reflectivity). And the reflectivity edge of elemental gold is more strongly flattened in  $\text{AuPd}_{15}$  compared to  $\text{AgAu}_{15}$  due to the stronger interband optical absorption below the interband gap of pure gold.

Unless specified otherwise, for the simulation of all binary compounds shown below, we always use as wavefunction cutoff the largest value between the wavefunction cutoffs of the two constituent elements, as taken from Table 5.4. We choose the interpolation k-grid to be used in the evaluation of the dielectric function in terms of a k-point density, which is defined as the maximum distance between adjacent k-points along the reciprocal axes (in  $\text{\AA}^{-1}$ ). In order to calculate the dielectric function in the frequency range  $[0, 10]$  eV, we always make the over-conservative choice to consider a number of empty bands equal to  $N_v$ , i.e. to the number of valence bands. For the simulation of gold solid solutions with the supercell approach, we fix  $\gamma = 0.001$  eV given that the low-energy absorption is controlled by  $\eta$ . In the case of intermetallic compounds we instead set  $\gamma = 0.1$  eV as done in Chapter 6 for elemental metals. Other relevant computational parameters used in all intermetallics and supercell simulations are:  $s_b = 0.01$  a.u.,  $\eta = 0.15$  eV,  $\sigma = 0.1$  eV.

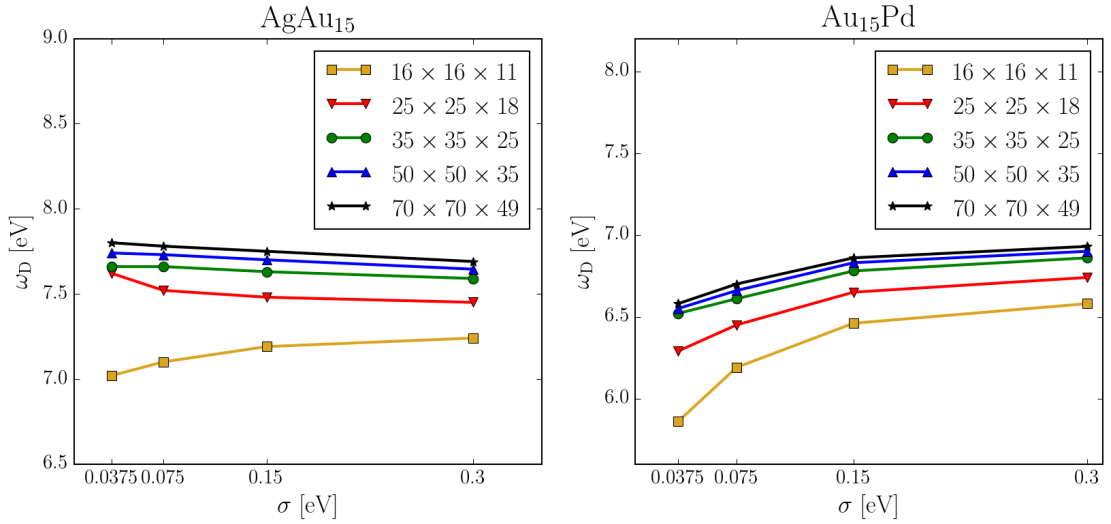


Figure 7.2 – Dependence of the IPA Drude plasma frequency  $\omega_D$  for  $\text{AgAu}_{15}$  and  $\text{Au}_{15}\text{Pd}$  on the Gaussian broadening  $\sigma$  for different interpolation k-points grids.

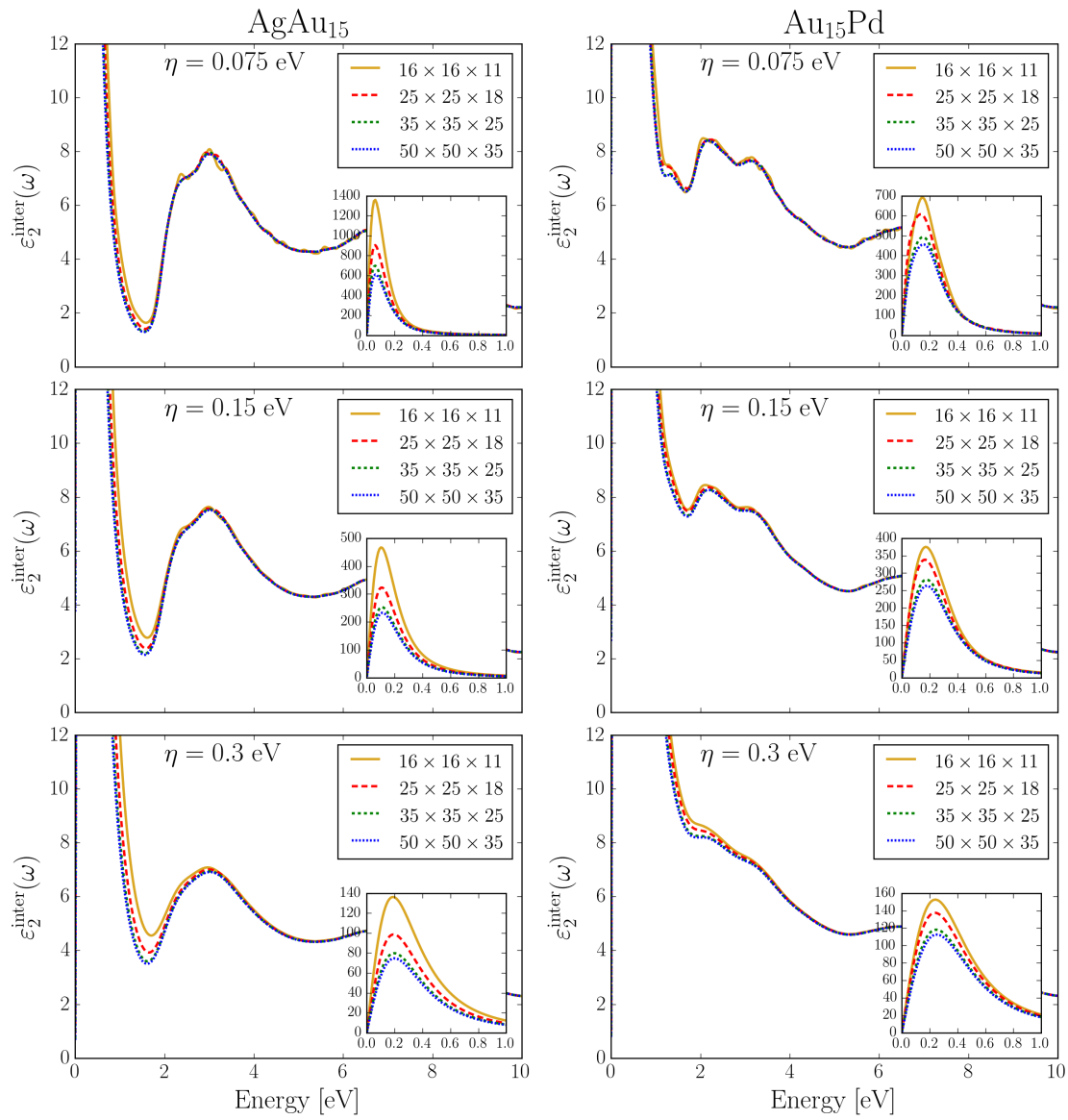


Figure 7.3 – Dependence of  $\varepsilon_2^{\text{inter}}(\omega)$  for  $\text{AgAu}_{15}$  and  $\text{Au}_{15}\text{Pd}$  on the interpolation k-points grids for different values of the empirical interband broadening  $\eta$ . Insets show the behaviour of  $\varepsilon_2^{\text{inter}}(\omega)$  zoomed in the low-energy range, i.e. in the interval  $[0, 1]$  eV.

## 7.2. Optical properties in supercell simulations

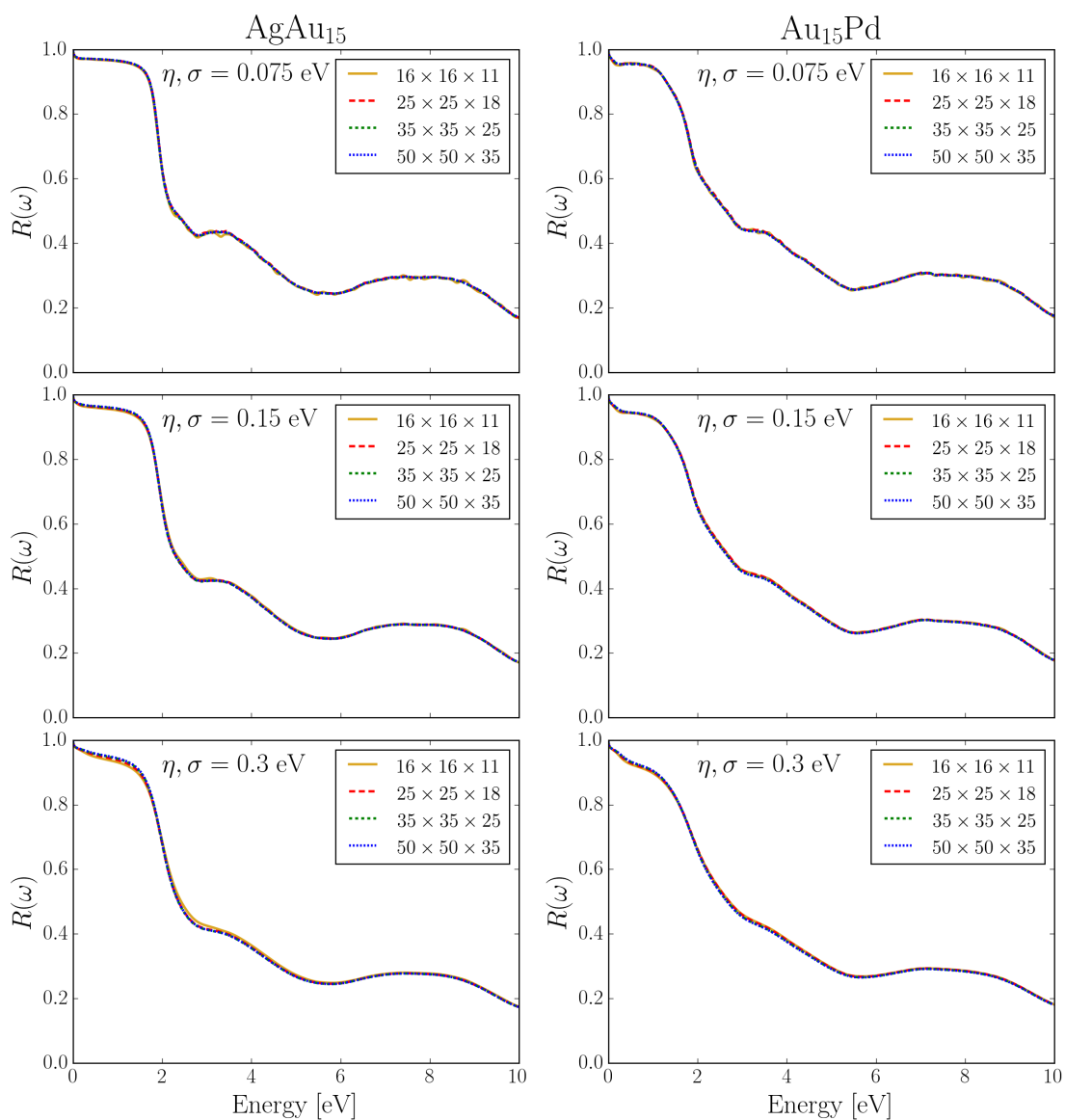


Figure 7.4 – Dependence of  $R(\omega)$  for  $\text{AgAu}_{15}$  and  $\text{Au}_{15}\text{Pd}$  on the interpolation k-points grids for different values of  $\eta$  and  $\sigma$  (with  $\eta = \sigma$ ).

### 7.2.3 Convergence with supercell size

We simulate the effect of disorder in the optical properties of solid solutions by employing the supercell approach, and using in particular the SQS approach for the simulation of simple stoichiometric ratios. We now study the convergence of the reflectivity with the size of the supercell and, as a consequence, with the number of structural correlation functions of the random alloy that are exactly reproduced by the SQS.

We perform this study by considering  $\text{Ag}_{0.25}\text{Au}_{0.75}$  and  $\text{Au}_{0.75}\text{Pd}_{0.25}$  in SQSs with  $N = 8, 16$  and  $32$ . All the SQSs considered in this work are generated with the ATAT package [143, 144]. We relax both cell-internal and cell-external degrees of freedom and, in order to perform a consistent convergence study of the SQSs sizes, we use equivalent k-points grids for the different supercells (always defined in terms of k-point density). As shown in Fig. 7.5 for  $\varepsilon_2^{\text{inter}}(\omega)$  and  $\omega_D$ , the interband and intraband contributions, taken separately, depend on the size of the simulation cell. Similarly to the supercell calculations for  $\text{AgAu}_{15}$  and  $\text{Au}_{15}\text{Pd}$  shown in Section 7.2.2, we observe the presence of a peak at low energies in the interband optical absorption of the SQS simulations for  $\text{Ag}_{0.25}\text{Au}_{0.75}$  and  $\text{Au}_{0.75}\text{Pd}_{0.25}$ . In particular, the increase of the size of the supercell moves the spectral weight from the intraband to the interband contribution by introducing more interband transitions at low energies. This is the reason why the intensity of the low-energy peak in  $\varepsilon_2^{\text{inter}}(\omega)$  increases by increasing  $N$  while, on the other hand, the IPA Drude plasma frequency decreases. Nonetheless the total spectral weight does not significantly depend on the size of the supercell, as can be verified through the  $f$ -sum rule. Indeed, the integral in Eq. 3.64 provides the same number for the different supercell sizes within 0.1% for  $\text{Ag}_{0.25}\text{Au}_{0.75}$  and within 0.4% for  $\text{Au}_{0.75}\text{Pd}_{0.25}$ .

Although the low-energy peak in the interband optical absorption is centred well below 1 eV and thus  $\varepsilon_2^{\text{inter}}(\omega)$  in the visible range is nearly independent from  $N$ , it has a stronger effect on  $\varepsilon_1^{\text{inter}}(\omega)$ , which instead shows a slow  $-1/\omega^2$  decay [17] that extends inside the visible range (see Fig. 7.6, left panel). However, the features of the total dielectric function inside the visible range or in the ultraviolet are not sensitive to the different sizes and atomic configurations of the SQSs and converge quickly with  $N$ . For example, in  $\text{Ag}_{0.25}\text{Au}_{0.75}$  the total dielectric function can be considered fully converged already at  $N = 16$  (see Fig. 7.6, right panel). Hence, also the reflectivity converges fast with the size of the SQS both for  $\text{Ag}_{0.25}\text{Au}_{0.75}$  and  $\text{Au}_{0.75}\text{Pd}_{0.25}$ , as Fig. 7.7 clearly shows. For  $\text{Au}_{0.75}\text{Pd}_{0.25}$  instead, the convergence of the low-energy part (up to 1.5 eV) of the total dielectric function and of the reflectivity is slower; nonetheless all the different simulation cells give the same results for larger energies. As already noticed in Chapter 7.2.2 for  $\text{AgAu}_{15}$  and  $\text{AgAu}_{15}$ , the interband optical absorption in  $\text{Au}_{0.75}\text{Pd}_{0.25}$  below the visible range is stronger compared to  $\text{Ag}_{0.25}\text{Au}_{0.75}$  because of additional interband transitions due to tightly bound Pd impurity states (i.e. virtual bound states).

Similarly to the convergence study on the size of the supercells shown above, we have also verified that SQSs with a fixed number of atoms (i.e.  $N = 16$ ) but with different atomic configurations and/or cell shapes give very similar optical properties among them, as it would be expected from the previous results on the fast convergence with the cell size. Similarly the effect of the relaxation of the atomic positions inside the cell is also negligible.

## 7.2. Optical properties in supercell simulations

Indeed, only very symmetric crystal structures, as in the case of cubic intermetallic phases, can have a significant effect on the optical properties since the high symmetry of the structure could give rise to characteristic features in the band structure and density of states. For example, the presence of pseudo gaps in the density of states, as it happens for the AuAl<sub>2</sub> intermetallic compound, can introduce absorption peaks and valleys in specific regions of the visible spectrum.

At this point, we would like to highlight that the division of the IPA dielectric function in interband and intraband contributions is more a theoretical construction than a real physical distinction. In supercell calculations of alloys, as shown by the preceding analysis, it is the sum of the two contributions that is physically meaningful and can be compared with experimental data and not the single contributions. This effect, relevant for the first-principles simulation of optical properties in supercells, has been already noticed and discussed by J. Harl *et al.* [145] in the study of Cu surfaces.

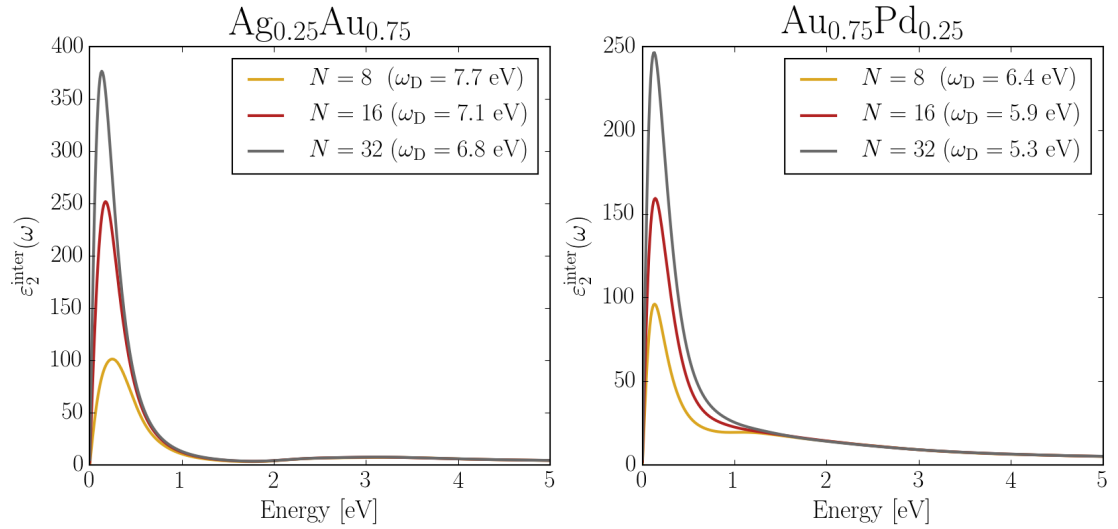


Figure 7.5 – Dependence of  $\epsilon_2^{\text{inter}}(\omega)$  and  $\omega_D$  on the size of the SQS for  $\text{Ag}_{0.25}\text{Au}_{0.75}$  and  $\text{Au}_{0.75}\text{Pd}_{0.25}$  (with  $N$  being the number of atoms in the supercell).

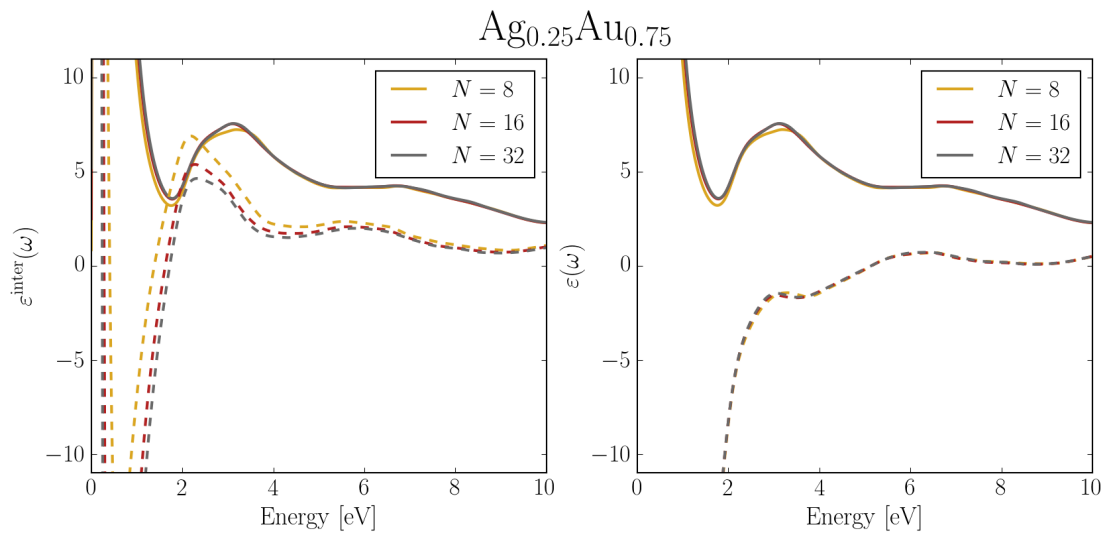


Figure 7.6 – Dependence of the real (dashed lines) and imaginary (solid lines) parts of the dielectric function on the size of the SQS for  $\text{Ag}_{0.25}\text{Au}_{0.75}$  (with  $N$  being the number of atoms in the supercell). We show both  $\epsilon^{\text{inter}}(\omega)$  (left panel) and  $\epsilon(\omega)$  (right panel).

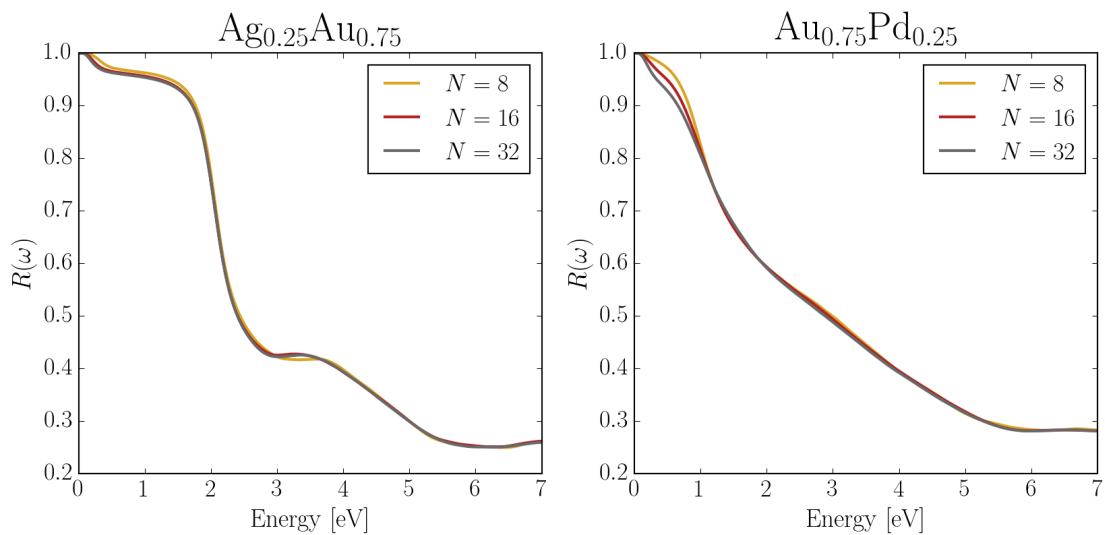


Figure 7.7 – Dependence of the reflectivity on the size of the SQS for  $\text{Ag}_{0.25}\text{Au}_{0.75}$  and  $\text{Au}_{0.75}\text{Pd}_{0.25}$  (with  $N$  being the number of atoms in the supercell).



## 7.3 Comparison with experiments

We show that the computational approach described in Chapter 5 applied to the methods of Table 7.1 for the simulation of different types of alloys is able to reproduce the correct trends in the optical properties of metallic alloys. In particular, we show through a comparison with several experimental results that the three main mechanisms that modify the colour of gold in alloys (see Fig. 1.4 and discussion therein) are captured by our simulations and that we manage to reproduce the main colour trends in the Au-Ag-Cu ternary system.

Although, due to the approximations used, we often do not have quantitative agreement with experiments (with the notable exception of the coloured intermetallic compounds for which the simulations are often accurate), we instead find the correct qualitative trends with respect to composition and alloying elements.

### 7.3.1 Coloured intermetallic compounds

We simulate the reflectivity and colour of intermetallic compounds that are experimentally known to be coloured. The compounds studied are the purple AuAl<sub>2</sub>, blue AuIn<sub>2</sub>, bluish AuGa<sub>2</sub>, yellow PtAl<sub>2</sub>, red PdIn, blue-grey NiSi<sub>2</sub> and dark blue CoSi<sub>2</sub>. All these intermetallic compounds have cubic symmetry: AuAl<sub>2</sub>, AuGa<sub>2</sub>, AuIn<sub>2</sub>, PtAl<sub>2</sub>, CoSi<sub>2</sub> and NiSi<sub>2</sub> crystallize in the FCC CaF<sub>2</sub> prototype structure (space group Fm $\bar{3}$ m) while PdIn crystallizes in the BCC CsCl prototype structure (space group Pm $\bar{3}$ m). To compare our results with previous computational results, we perform the simulations at the experimental lattice parameter<sup>7</sup>.

The interpolation k-grid to be used in the evaluation of the dielectric function is defined by using a k-points density equal to 0.04 Å<sup>-1</sup>. With this choice the number of k-points included in the uniform k-grids is of the order  $O(10^5)$  for all the cubic intermetallic compounds considered (corresponding to uniform k-grids in the range from 46 × 46 × 46 up to 56 × 56 × 56). Other computational parameters used in the simulations are given in Section 7.2.2.

As shown in Fig. 7.8, the experimental shape of the reflectivity curve for the coloured intermetallics is well reproduced by the simulations. In Fig. 7.9 we show the corresponding comparison between simulated and experimental colours in CIELAB colour space for the seven intermetallics studied. The colour differences between our simulations and experiments are summarized in Table 7.2, where the comparison with previous first-principles simulations [34, 10] is also reported. The agreement with previous simulations is satisfactory and, moreover, we reproduce the true colour of the intermetallic compounds studied. For example, the comparison between photorealistic rendering and real material samples clearly shows that the simulations predict the correct colours of purple AuAl<sub>2</sub>, bluish AuGa<sub>2</sub> and yellow PtAl<sub>2</sub> (see Fig. 7.10). The agreement is worse only for PdIn because, although experimental and simulated reflectivity curves are very similar, the experimental reflectivity edge is at the border of the visible spectrum (i.e. in the red region) and the small redshift shown by the simulations

<sup>7</sup>The effect of the variation of the lattice parameter on the optical properties of these intermetallics is relatively small. However, in some cases there can be a shift in the spectra: in AuAl<sub>2</sub>, for example, the shift of the dip in the reflectivity between the curve obtained at the PBE lattice parameter and at the experimental one is ~ 0.1 eV.

has a strong impact on the resulting colour.

The characteristic colours of these intermetallic compounds is due to selective optical absorption in confined regions of the visible spectrum [12] (see Appendix C.2 where the simulated  $\varepsilon_2(\omega)$  and other relevant optical constants for these intermetallics are reported). For the gold compounds, the optical absorption inside the visible range is given by transitions from  $sp$  conduction states below the Fermi level to unoccupied states above the Fermi level. The bands originating from the  $5d$  states of gold, that are problematic in the study of elemental noble metals, are at around 5 eV below the Fermi level and these do not contribute to the characteristic colours of these compounds [146]. This explains the better agreement with experiments found for the gold intermetallics compounds compared to the case of elemental gold (see Section 6.2).

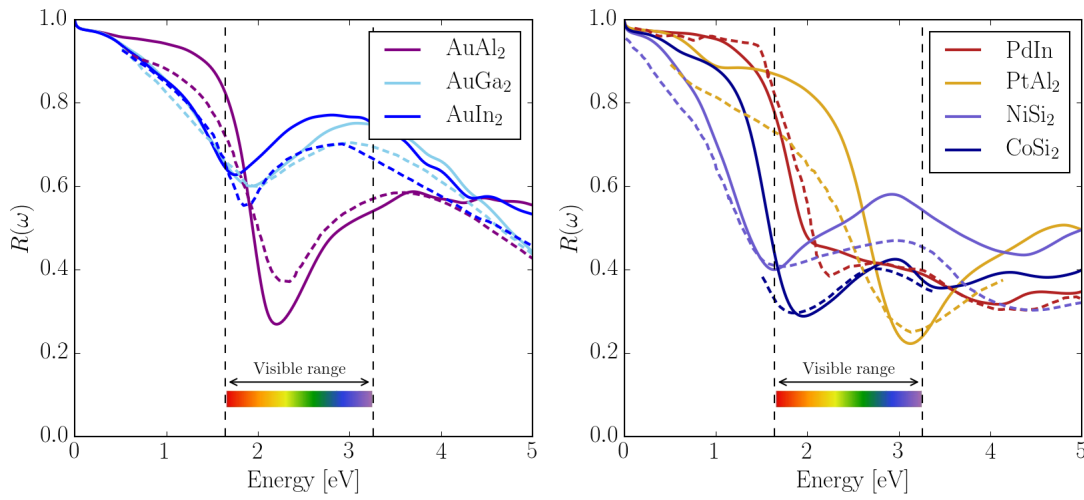


Figure 7.8 – Simulated (solid lines) and experimental (dashed lines) reflectivities of coloured intermetallics. Experimental data are taken from Ref. [4] for  $\text{AuAl}_2$ ,  $\text{AuGa}_2$  and  $\text{AuIn}_2$ , from Ref. [10] for  $\text{PtAl}_2$ , from Ref. [11] for  $\text{NiSi}_2$  and from Ref. [12] for  $\text{CoSi}_2$  and  $\text{PdIn}$ . The two vertical dashed lines show the limits of the visible range.

Compound	$\Delta E_{\text{exp}}$	$\Delta E_{\text{sim}}$
$\text{AuAl}_2$	11 [4]	8 [10], 4 [34]
$\text{AuGa}_2$	2 [4]	1 [34]
$\text{AuIn}_2$	4 [4]	1 [34]
$\text{PtAl}_2$	12 [10]	2 [10]
$\text{CoSi}_2$	3 [12]	
$\text{NiSi}_2$	5 [11]	
$\text{PdIn}$	10 [12]	

Table 7.2 – Colour differences in CIELAB space between simulated colours and experimental colours derived from reflectivity data,  $\Delta E_{\text{exp}}$ , and between simulated colours and previously published simulations,  $\Delta E_{\text{sim}}$ .

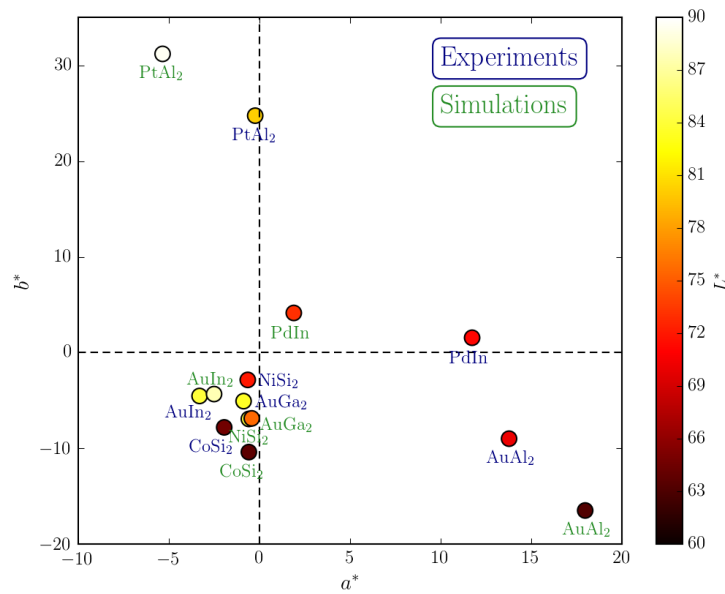


Figure 7.9 – Comparison of simulated (green) and experimental (blue) colours of known coloured intermetallics compounds in CIELAB colour space.

### 7.3.2 Binary gold alloys

We now simulate the reflectivity of binary gold alloys for different alloying elements and at different compositions, and compare our results with experimental data. We consider four gold-based alloy systems that show different behaviours of the optical properties in the visible range and for which there are available in the literature experimental data on the reflectivity and/or on the optical absorption. The systems studied are Ag-Au, Al-Au, Au-Pt and Au-Cu. Concerning the phase stability of these systems [13] (see Fig. 7.11 for the corresponding phase diagrams), Ag is completely soluble in Au thus Au and Ag form solid solutions for each composition and no long-range order is observed at low temperatures. Also Au and Cu form solid solutions over all concentrations at high temperatures but, for certain composition ranges, ordered intermetallic phases can be obtained at lower temperatures. In particular the known intermetallic compounds are the cubic  $\text{AuCu}_3$  and  $\text{Au}_3\text{Cu}$  (space group  $\text{Pm}\bar{3}\text{m}$ ), the low-temperature phase  $\text{AuCu(I)}$  (space group  $\text{P4/mmm}$ ) and the high-temperature phase  $\text{AuCu(II)}$  (space group  $\text{Imma}$ ). Au-Pt also forms a complete series of solid solutions at high temperatures but a miscibility gap appears with decreasing temperature. Al is instead soluble in Au up to about 14 at. % and several intermetallic compounds occur in the phase diagram, such as the already mentioned purple  $\text{AuAl}_2$ .

The experimental reflectivity data reported below for Ag-Au [2], Au-Pt [3] and Al-Au [14] are all measured on samples made of solid solutions. The measurements of optical absorption for different concentrations of Au-Cu are also performed on solid solutions but, for the composition  $x = 0.81$ , there are available measurements for both the solid solution and the intermetallic compound  $\text{AuCu}_3$  [15].

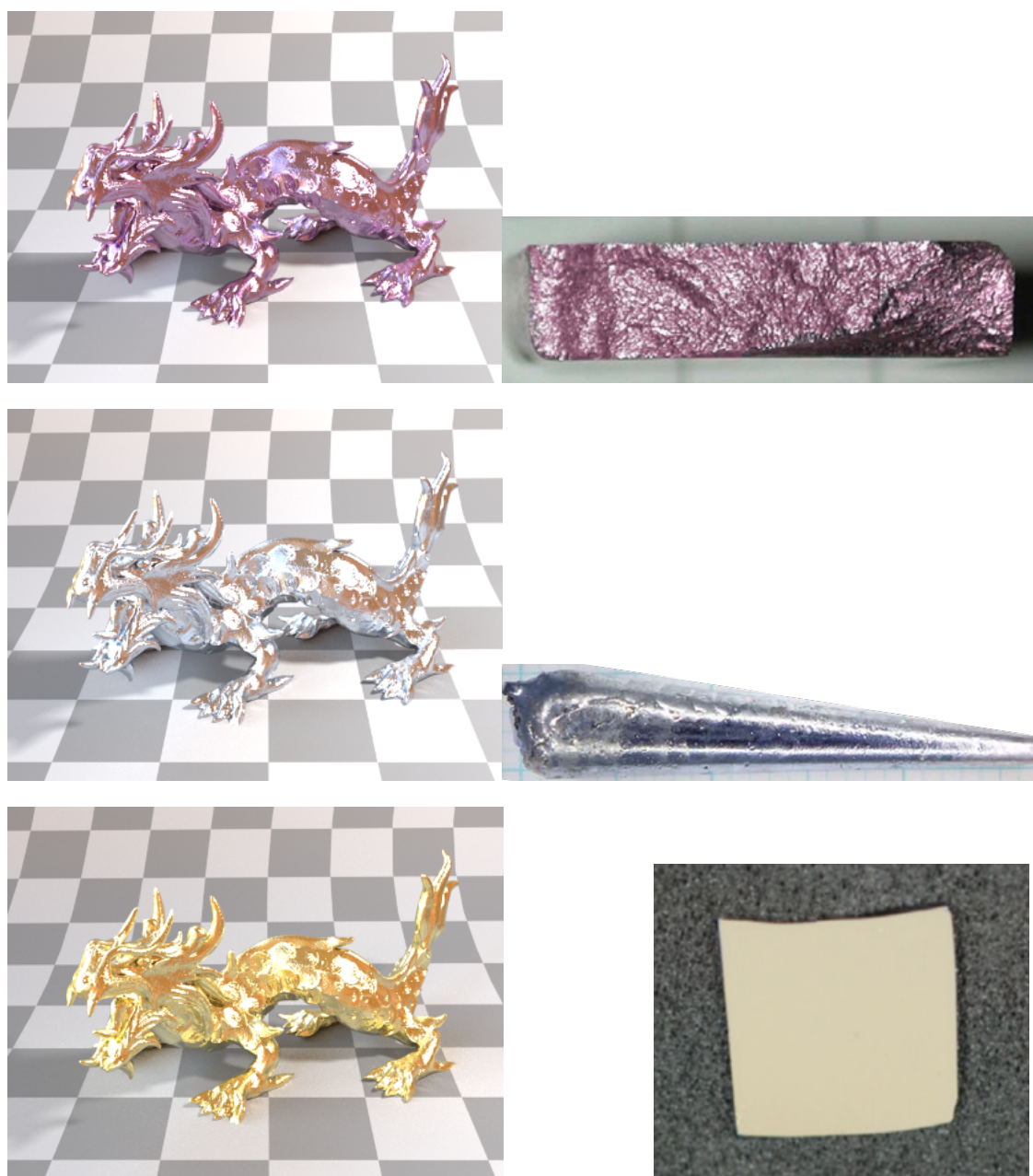


Figure 7.10 – Comparison between the rendering of a metallic surface of the intermetallic compounds  $\text{AuAl}_2$  (top),  $\text{AuGa}_2$  (center) and  $\text{PtAl}_2$  (bottom) obtained using the simulated optical constants (left panel) and real samples of the three materials (right panel).

### 7.3. Comparison with experiments

As discussed before, we use the supercell approach to simulate the optical properties of solid solutions. It is an approximate method to study random alloys and we expect less good agreement with respect to experiments if compared to the case of intermetallic compounds. In the following, we use FCC SQSs with 16 atoms per cell for the simple stoichiometric ratios  $x = 0.25, 0.5, 0.75$  (for Ag-Au and Au-Cu). As explicitly shown in Section 7.2.3 for  $\text{Ag}_{0.25}\text{Au}_{0.75}$ , the total dielectric function and thus the reflectivity are both well converged with respect to the size of the SQS at  $N = 16$ . To simulate the effect of small concentrations of the alloying element on gold we use instead, as done for the convergence study in Section 7.2.2, a simple FCC supercell with 16 atoms in which an Au atom is replaced with an atom of the alloying element, i.e. having an atomic concentration  $x = 0.0625$  of the alloying element<sup>8</sup> (for Al-Au and Au-Pt). The interpolation k-grid is set according to a k-point density of  $0.04 \text{ \AA}^{-1}$  (corresponding roughly to 11'000 points) while other relevant computational parameters used in the simulations are given in Section 7.2.2.

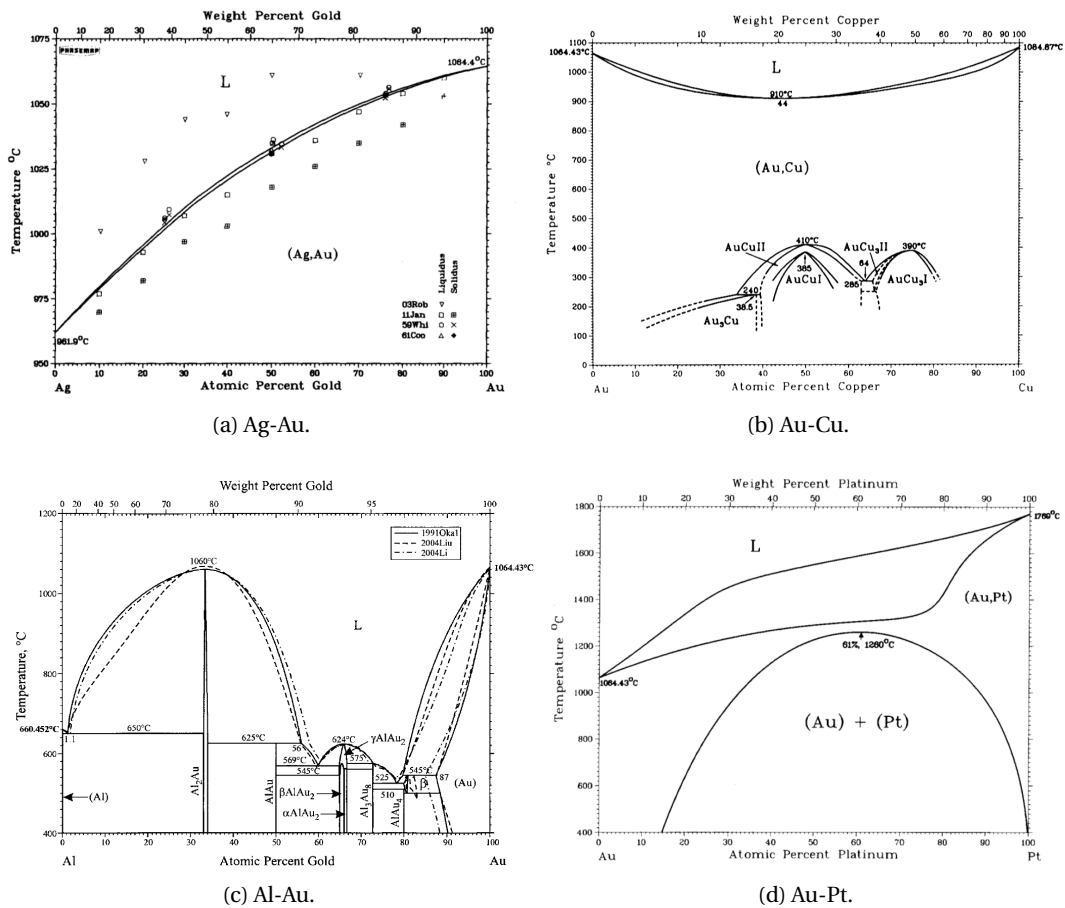


Figure 7.11 – Experimental phase diagrams of (a) Ag-Au, (b) Au-Cu, (c) Al-Au and (d) Au-Pt. Adapted from [13].

<sup>8</sup>We have verified that supercells with 32 atoms and same composition yield very similar results to the supercells with 16 atoms used.

**Ag-Au**

We study the effect of composition on the reflectivity of the Ag-Au system and compare experimental data of solid solutions with SQS simulations. The Ag-Au system is the prototypical example of the first mechanism discussed in Section 1.2.2 by which it is possible to modify the colour of gold in alloys. Fig. 7.12 shows that the gradual shift to lower wavelengths of the reflectivity edge of gold by increasing the Ag content is reproduced by the simulations. However, as already discussed in Section 6.2 for the case of elemental noble metals, the position of the reflectivity edge in IPA simulations based on DFT-PBE band structures does not correspond to the experimental one, but it is instead systematically shifted to longer wavelengths for each concentration  $x$  considered.

Although the simulations are not in quantitative agreement with experiments, the qualitative trends in reflectivity, and thus in colour, with respect to the alloy composition of Ag-Au are reproduced.

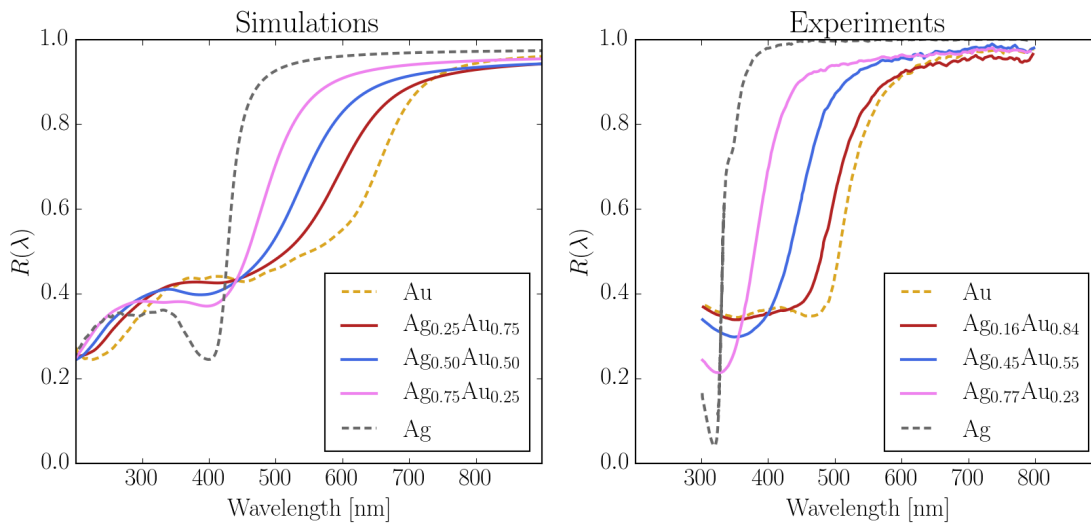


Figure 7.12 – Comparison of the trends in composition of the reflectivity inside the visible spectrum for Ag-Au solid solutions between SQS simulations (left panel) and experiments [2] (right panel). For reference, we also report the reflectivity curves of elemental Au and elemental Ag (dashed lines). To note that the alloy compositions of experiments and simulations are not exactly the same.

**Al-Au and Au-Pt**

After having investigated the effect of the composition on the reflectivity of the Ag-Au system, we now study how different alloying elements, in particular we consider Pt and Al, affect the reflectivity of gold for small alloying concentrations. As explained before, we simulate the effect of small alloying additions of Al (resp. Pt) on the reflectivity of Au by employing supercells with 16 atoms in which an Au atom is replaced with an Al (resp. Pt) atom.

The Au-Pt system is an example of the second mechanism discussed in Section 1.2.2 by which

it is possible to modify the colour of gold in alloys, and that produces a bleaching effect by reducing the reflectivity in the long-wavelength region of the visible spectrum. A similar bleaching effect is observed also alloying gold with elements that are in the same column as Pt in the periodic table, i.e. in the Au-Pd and Au-Ni systems, and which are the alloys traditionally used in the jewellery industry for the production of white gold alloys [24]. The Al-Au system shows instead a combination of the first (as in Ag-Au) and second mechanisms.

As shown in Fig. 7.13, Pt additions in Au strongly smoothen the reflectivity curve but the position of the edge is not substantially modified<sup>9</sup>. Al additions in Au produce both a reduction of the reflectivity in the long-wavelength region (similar to the effect of Pt additions, although the reduction in intensity is less strong) and a small but clear shift to lower wavelengths of the reflectivity edge (similar to the effect of Ag additions). The supercell simulations qualitatively capture these two different effects and the qualitative differences between the two alloying elements.

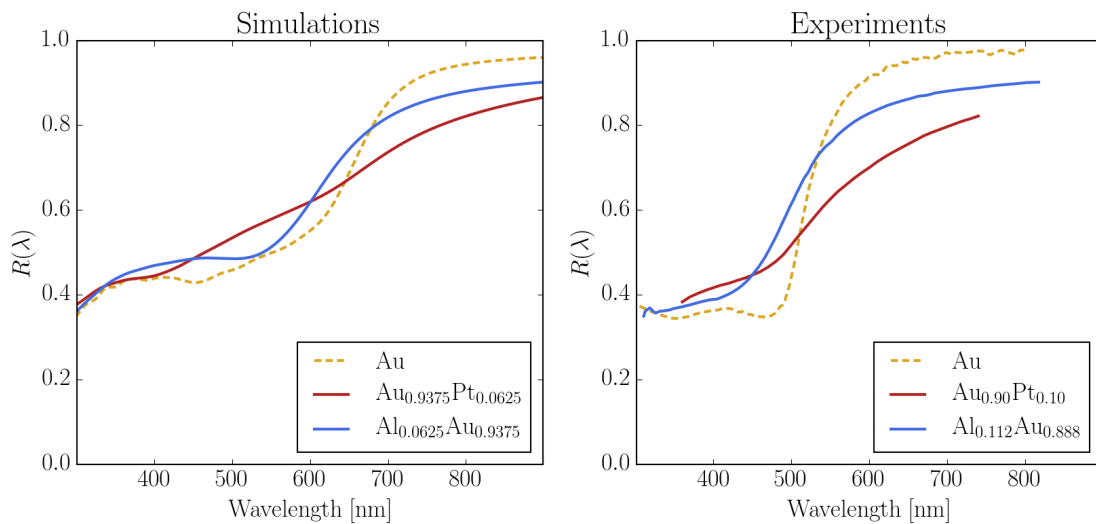


Figure 7.13 – Comparison of the reflectivity inside the visible spectrum between supercell simulations and experiments for Au-Pt and Al-Au solid solutions. Experimental data are taken from Ref. [3] for  $\text{Au}_{0.90}\text{Pt}_{0.10}$  and from Ref. [14] for  $\text{Al}_{0.112}\text{Au}_{0.888}$ . For reference, we also report the reflectivity curve of elemental Au (dashed lines). To note that the concentrations of the alloying element in experiments are larger than those in the simulations.

We notice that, for a given alloy composition, the smoothening of the reflectivity edge in the simulations is stronger than in experiments (in Fig. 7.13, concentrations of the alloying element in experiments are larger than those in simulations). For this reason we use a slightly smaller concentration with respect to experiments in order to compare the colour trends in gold alloys with respect to the alloying element. The addition of alloying elements gives a too strong bleaching effect by attenuating the onset of interband absorption of elemental gold more than in experiments. The strong low-energy optical absorption can be marginally reduced and tuned by decreasing  $\eta$  but not eliminated because intrinsic to supercell simulations. The

<sup>9</sup>Pd and Ni additions to gold give the same qualitative behaviour [29, 30].

increase of optical absorption in metallic alloys is actually observed experimentally [43, 44, 14, 29, 41] but to a smaller degree compared to supercell simulations.

### Au-Cu

Similarly to what we have previously done for the reflectivity of Ag-Au, we now study the effect of composition on the optical absorption of Au-Cu. We observe in Fig. 7.14 a gradual deformation of the features in the optical absorption by varying the alloy composition from one elemental metal to the other. In particular, we notice a shift to lower energies of the onset of absorption in Au-Cu by varying the composition from elemental Au to elemental Cu. But, since the absorption edge of Cu is nearly at the same energy of the absorption edge of Au (roughly 0.3 eV lower in energy), the effect is less evident compared to Ag-Au, where the absorption edges of the two constituent elements are instead separated by roughly 1.5 eV. Nonetheless, the small shift to lower energies of the onset of absorption by increasing the Cu content in Au gives rise to a corresponding shift of the reflectivity edge that changes the colour of the Au-Cu alloy from the red-yellow colour of pure gold to the red colour of pure copper, and which corresponds to the first mechanism by which it is possible to modify the colour of gold in alloys. In the simulations, this effect is reproduced but it is partially attenuated by a stronger absorption in the infrared region and, similarly to Ag-Au, for a given composition the onset of absorption is systematically shifted by  $\sim 0.4$  eV compared to experiments.

Therefore we conclude that the noble-metal elements Ag and Cu behave in a similar way as alloying elements on the reflectivity and colour of gold. The gradual shift of the reflectivity edge, as measured in experiments and qualitatively reproduced by our simulations, gives rise to the broad range of colours of the Au-Ag-Cu system shown in Fig. 1.2. In the Ag-Cu binary system the behaviour of the reflectivity curve is instead different and it is discussed in more detail below.

We then compare also the optical absorption of the  $\text{Au}_{1-x}\text{Cu}_x$  solid solution, at  $x = 0.81$  for experiments and at  $x = 0.75$  for simulations, with the optical absorption of the intermetallic compound appearing around the composition  $x = 0.75$ , i.e. the cubic  $\text{AuCu}_3$  phase. The purpose of this comparison is to study the differences in optical properties between ordered and disordered phases<sup>10</sup>. As shown in Fig. 7.15, the optical absorption of the intermetallic compound is very similar to the one of the random alloy with the notable exception of the presence of an additional peak at around 3.6 eV, which is missing in  $\epsilon_2(\omega)$  for the solid solution. The comparison of the SQS results for the disordered alloy with the simulated results of the intermetallic compound shows that the simulations clearly capture this small difference. Nonetheless we underline that there is no significant change in the resulting colour between ordered and disordered alloy for this system because the position of the onset of absorption is not modified by the presence of long-range order, and thus neither is the colour.

---

<sup>10</sup>A similar study has been already performed on Au-Cu at the intermediate composition  $x = 0.5$  [45].



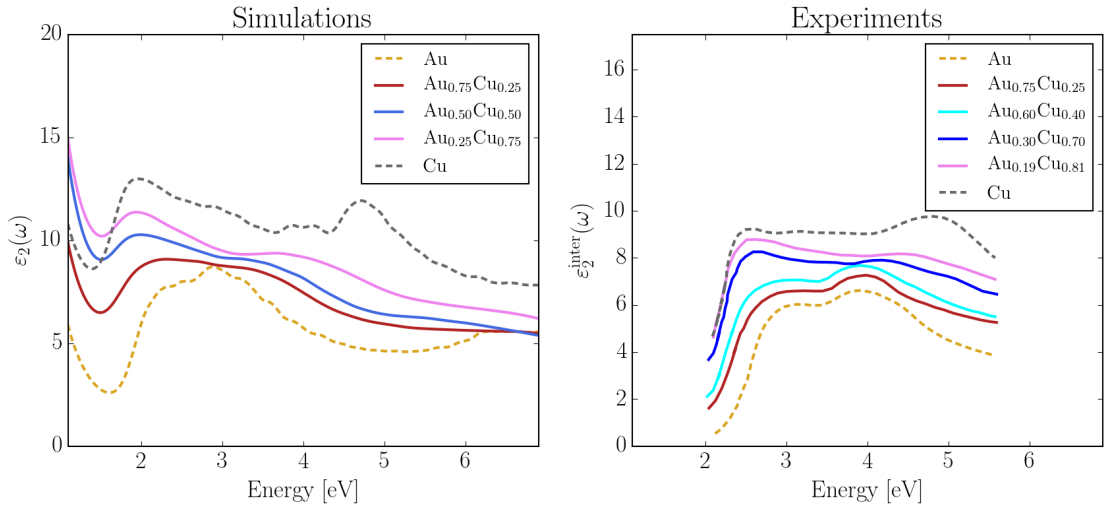


Figure 7.14 – Comparison of the trends in composition of the optical absorption inside the visible spectrum for Au-Cu solid solutions between SQS simulations (left panel) and experiments [15] (right panel). The Drude-like intraband contribution to  $\varepsilon_2(\omega)$  has been subtracted from the experimental data. For reference, we also report  $\varepsilon_2(\omega)$  of elemental Au and elemental Cu (dashed lines). To note that the alloy compositions of experiments and simulations are not always the same. Experimental and simulated curves have been arbitrarily shifted along the vertical axis for clarity in the comparison.

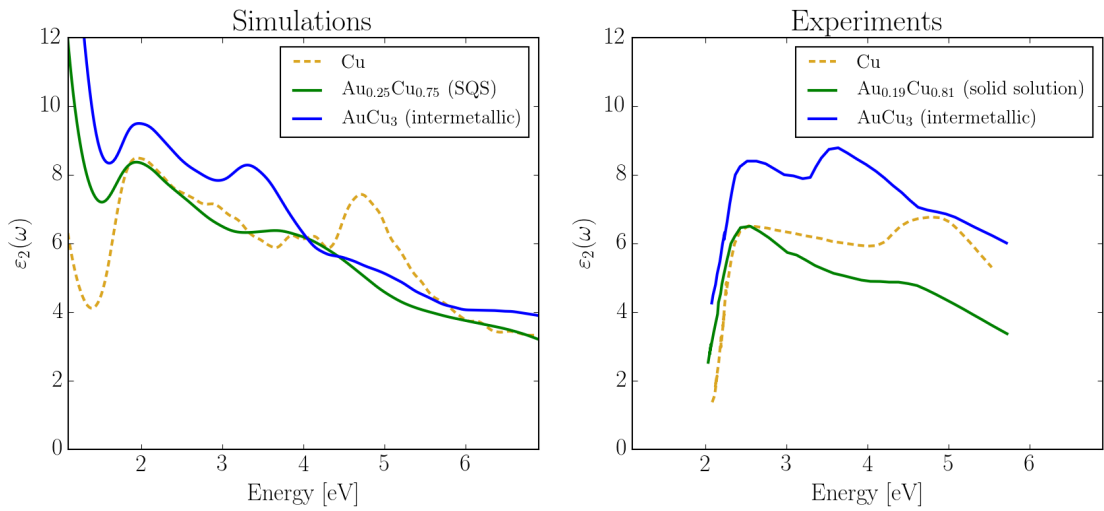


Figure 7.15 – Comparison of  $\varepsilon_2(\omega)$  for  $\text{Au}_{1-x}\text{Cu}_x$  between simulations (left panel) and experiments [15] (right panel) for both the solid solution and the intermetallic phase  $\text{AuCu}_3$  (at  $x = 0.75$  in the simulations and at  $x = 0.81$  in the experiments). For reference, we also report  $\varepsilon_2(\omega)$  of elemental Cu (dashed lines). Experimental and simulated curves have been arbitrarily shifted along the vertical axis for clarity in the comparison.

### 7.3.3 Ag-Cu

Up to now we have dealt only with solid solutions and intermetallic compounds. In order to treat also the case of heterogeneous alloys, we consider the Ag-Cu system. In fact, as shown in Fig. 7.16, the phase diagram of Ag-Cu exhibits eutectic behaviour with a wide miscibility gap and the system tends to segregate in phases of nearly pure Ag and pure Cu at room temperature [13].

The experimental reflectivity data reported below for Ag-Cu are measured on two-phase alloys made of nearly pure Cu and Ag phases [16]. However, for the composition  $x = 0.30$ , there are also available experimental data of optical absorption obtained from measurements performed on both a segregated two-phase sample made of a pure Cu phase and a pure Ag phase, and on a metastable solid solution obtained by vapor quenching [15].

We simulate the optical properties of  $\text{Ag}_{1-x}\text{Cu}_x$  two-phase alloys by employing the Bruggeman model described in Section 7.1.2. The  $\alpha$  and  $\beta$  phases entering in the expression for the alloy dielectric function  $\epsilon_{\text{Br}}$  of Eq. 7.2 are assumed to be elemental Ag and elemental Cu, respectively. And the dielectric functions of the two constituent elements are taken from the simulations of elemental metals reported in Chapter 6. As shown in Fig. 7.16, Ag additions in Cu increase the reflectivity at wavelengths shorter than the reflectivity edge of elemental Cu but do not shift the position of the edge. The Bruggeman model provides the correct trend with composition but the effect on the drop in the reflectivity is less evident because the reflectivity edge of elemental Cu in the IPA simulations is less steep than the experimental one. As a verification of the validity of the Bruggeman model to describe the optical properties of Ag-Cu two-phase alloys, we apply the model using experimental data of the dielectric function of elemental Ag and elemental Cu [9] for the two-phase alloy instead of the data from IPA simulations, and we find very good agreement with the experimental reflectivity data of the Ag-Cu samples [16] (see Fig. 7.18).

We then compare in Fig. 7.19 also the optical absorption of the  $\text{Ag}_{1-x}\text{Cu}_x$  two-phase alloy, at  $x = 0.70$  for the experiments and at  $x = 0.75$  for the simulations, with respect to the metastable solid solution having the same composition. In the two-phase alloy, where the alloy optical properties are well approximated by a combination of those of pure Cu and pure Ag (Bruggeman model), we observe two onset of absorption: the first one at  $\sim 2.1$  eV corresponding to the absorption edge of pure Cu and the second one at  $\sim 4.0$  eV corresponding to the absorption edge of pure Ag. The optical absorption of the solid solution instead is very similar to the one of pure Ag but, in addition, we observe the presence of a supplementary broad peak at energies below the onset of absorption of pure Ag due to Cu impurity states. The SQS results for the solid solution and the results of the Bruggeman model applied on the IPA dielectric function of elemental Ag and Cu reproduce the two different trends, although the SQS shows a small blueshift of the peak that follows the absorption edge of pure Ag which is not observed experimentally.

### 7.3. Comparison with experiments

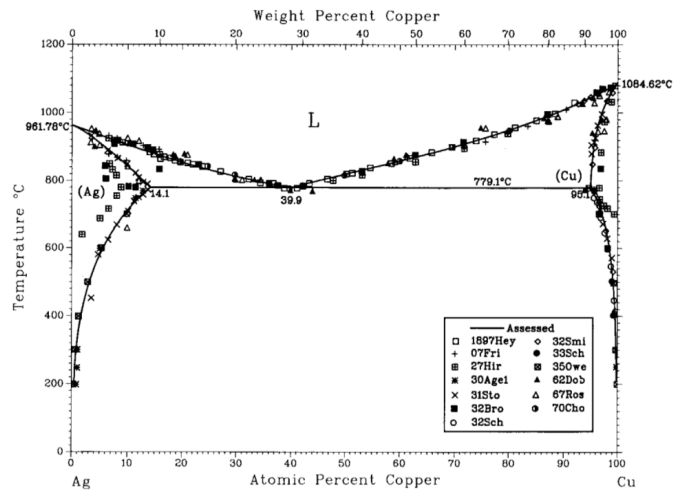


Figure 7.16 – Experimental phase diagram of Ag-Cu. Adapted from [13].

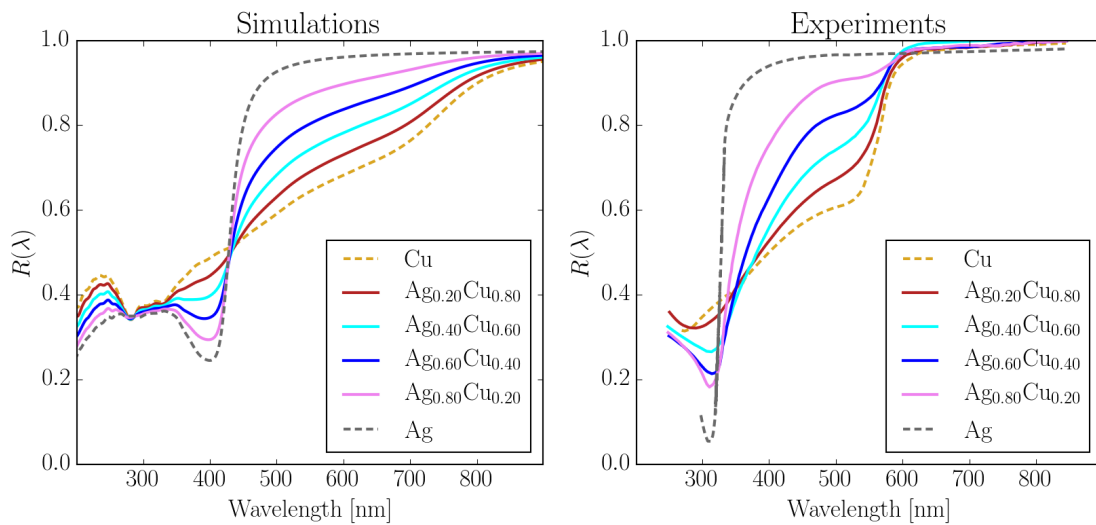


Figure 7.17 – Comparison of the trends in composition of the reflectivity inside the visible spectrum for Ag-Cu two-phase alloys between simulations (left panel) and experiments [16] (right panel). The results of the simulations are obtained using the Bruggeman model in which the two phases of the system are assumed to be elemental Ag and elemental Cu (dashed lines).

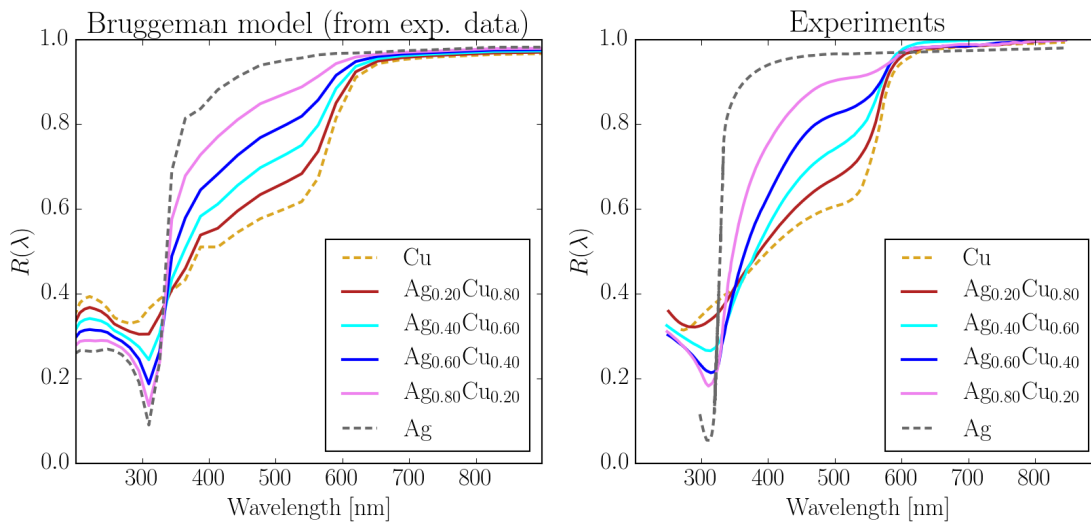


Figure 7.18 – Comparison of the trends in composition of the reflectivity inside the visible spectrum for Ag-Cu two-phase alloys between experiments [16] (right panel) and results of the Bruggeman model applied to experimental data of the dielectric function of elemental Ag and elemental Cu [9] (left panel).

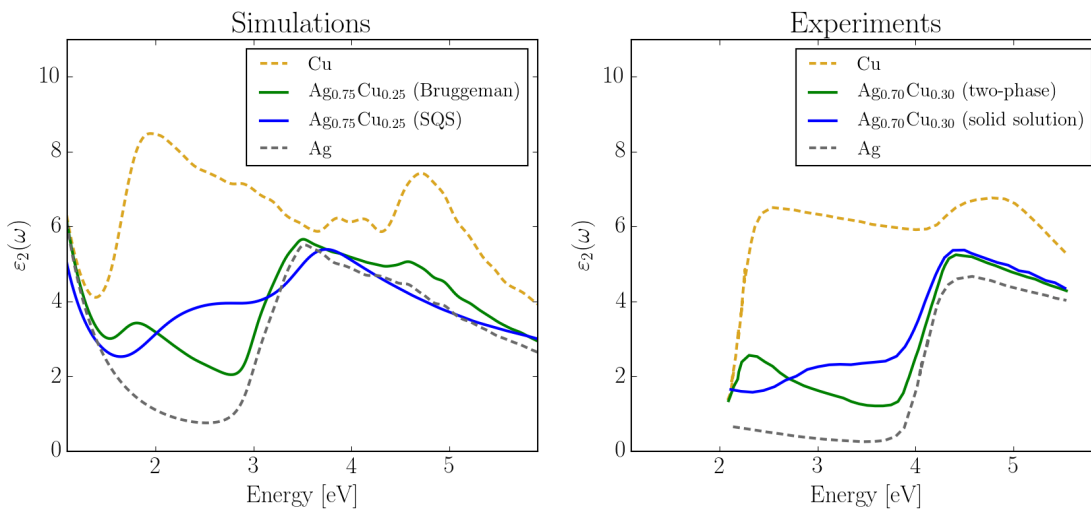


Figure 7.19 – Comparison of  $\epsilon_2(\omega)$  for  $\text{Ag}_{1-x}\text{Cu}_x$  between simulations (left panel) and experiments [15] (right panel) for both the solid solution and the two-phase alloy (at  $x = 0.25$  in the simulations and at  $x = 0.30$  in the experiments).

### 7.3.4 Au-Ag-Cu

Based on the comparison performed above between experimental data and first-principles simulations, we can now give a more complete interpretation of the different colour trends observed in the Au-Ag-Cu ternary system and shown in Fig. 1.2. Indeed, we have studied how the different trends in reflectivity (and thus in colour) of the constituent binary systems, i.e. Ag-Au, Au-Cu and Ag-Cu, can be interpreted in terms of the different phases (ordered phases, disordered phases and mixture of phases) present in the three systems. The combination of these data related to the constituent binaries thus furnishes an overview of the colour trends in Au-Ag-Cu.

Summarizing, for Ag-Au solid solutions, where we have a gradual shift of the reflectivity edge by varying alloying additions from elemental Au to elemental Ag, the colour of the alloy changes from red-yellow to yellow, pale greenish-yellow and eventually white of pure Ag. Au-Cu solid solutions show a similar behaviour and the colour of the alloy changes from red-yellow to reddish and eventually red of pure Cu. Instead, in Ag-Cu two-phase alloys there is no shift of the reflectivity edge but, for all wavelengths in the visible range below the reflectivity edge of elemental Cu, the reflectivity curve rises roughly uniformly so that the colour of Ag-Cu changes from the red of pure Cu to reddish and then directly to whitish and white [24].

The extensive comparison between experimental data and first-principles simulations has shown that the computational approach of Chapter 5 applied to the methods of Table 7.1 for the simulation of different types of alloys qualitatively reproduces all the main colour trends of the Au-Ag-Cu ternary system.

### 7.4 Comparison among different methods

We compare the results on the optical properties of alloys computed with different methods and show the main differences among them, with a particular focus on the effect in the resulting colour of the alloy. We consider the supercell approach, principally based on the use of SQSs, an effective-medium approach, i.e the VCA method, and the Bruggeman model. We discuss in more detail the physical effects that give rise to the different features of the optical properties. We show that it is important to use the appropriate computational method in order to predict the correct trends in the optical properties of metallic alloys.

VCA simulations are performed by following the implementation described in Ref. [147]. VCA pseudopotentials are generated from the NC pseudopotentials of the SG15 or Pseudo Dojo libraries and convergence of the VCA results with respect to the wavefunction cutoff has been inspected. From the convergence studies performed we opt to use the SG15 pseudopotentials and wavefunction cutoff of 70 Ry for both Ag-Au and Au-Pd alloys while, for Ag-Cu, we use the Pseudo Dojo pseudopotentials and wavefunction cutoff of 100 Ry (see Section 6.1 for the other computational parameters used). The IPA dielectric function is always computed at the equilibrium volume of the VCA alloy<sup>11</sup>.

We have seen that, for the systems considered above, the supercell approach reproduces the correct experimental trends in reflectivity of noble-metal-based solid solutions. As discussed in Section 7.1.2, the VCA method is a simple effective-medium approach for the simulation of solid solutions which is significantly less expensive than the SQS approach in terms of computational resources, so it is worth to assess its predictive power.

We compare the results obtained with the SQS method and with the VCA approach for the simulation of the optical properties of Ag-Au, Ag-Cu and Au-Pd solid solutions, by considering different alloy concentrations  $x$ .

#### 7.4.1 Ag-Au

In Ag-Au the qualitative behaviour and trends of the VCA and SQS optical absorption and reflectivity are very similar for all compositions considered (see Fig. 7.20). In both methods we observe a gradual shift of the onset of absorption in  $\epsilon_2(\omega)$  to higher energies by increasing the Ag content in Au, to which corresponds a gradual shift of the reflectivity edge. The  $d$ -bands lower gradually with respect to the Fermi level by increasing the concentration of Ag. Indeed, a band structure analysis performed on the VCA results for Ag-Au shows that the interband transition energy at the high-symmetry point X of the BZ between the top valence  $d$ -band and the conduction band above the Fermi level (see Fig. 1.5) increases gradually by increasing the Ag content from 2.77 eV for elemental Au to 4.44 eV for elemental Ag. The good agreement between SQS and VCA results is explained by the fact that the weak-scattering limit

---

<sup>11</sup>The VCA equilibrium lattice parameters of Au-Pd and Ag-Cu follow the ideal Vegard's law while in Ag-Au there are small deviations from the ideal behaviour. However, Ag and Au have almost the same PBE equilibrium lattice parameter and the relative deviations at intermediate compositions are less than 0.5% with respect to the two end points.

is a reasonable approximation for the isoelectronic Ag-Au system (and similarly for Au-Cu) and the electronic structure of the alloy can be considered as a mixture of the electronic structure of the single constituents. There is however a small discrepancy between the two approaches, given that a small lowering of the reflectivity in the low-energy part of the spectrum with respect to the pure elements is observed in the SQS simulations but not in the VCA simulations. This behaviour is experimentally measured in Ag-Au [44, 148] and it is actually a general effect observed in metallic alloys. It is due to the fact that the scattering of the conduction electrons in alloys is increased with respect to pure elemental crystals because of disorder. A similar effect is observed also in the electrical resistivity of metals since the resistivity in metallic alloys is larger than in elemental metals (Matthiessen's rule).

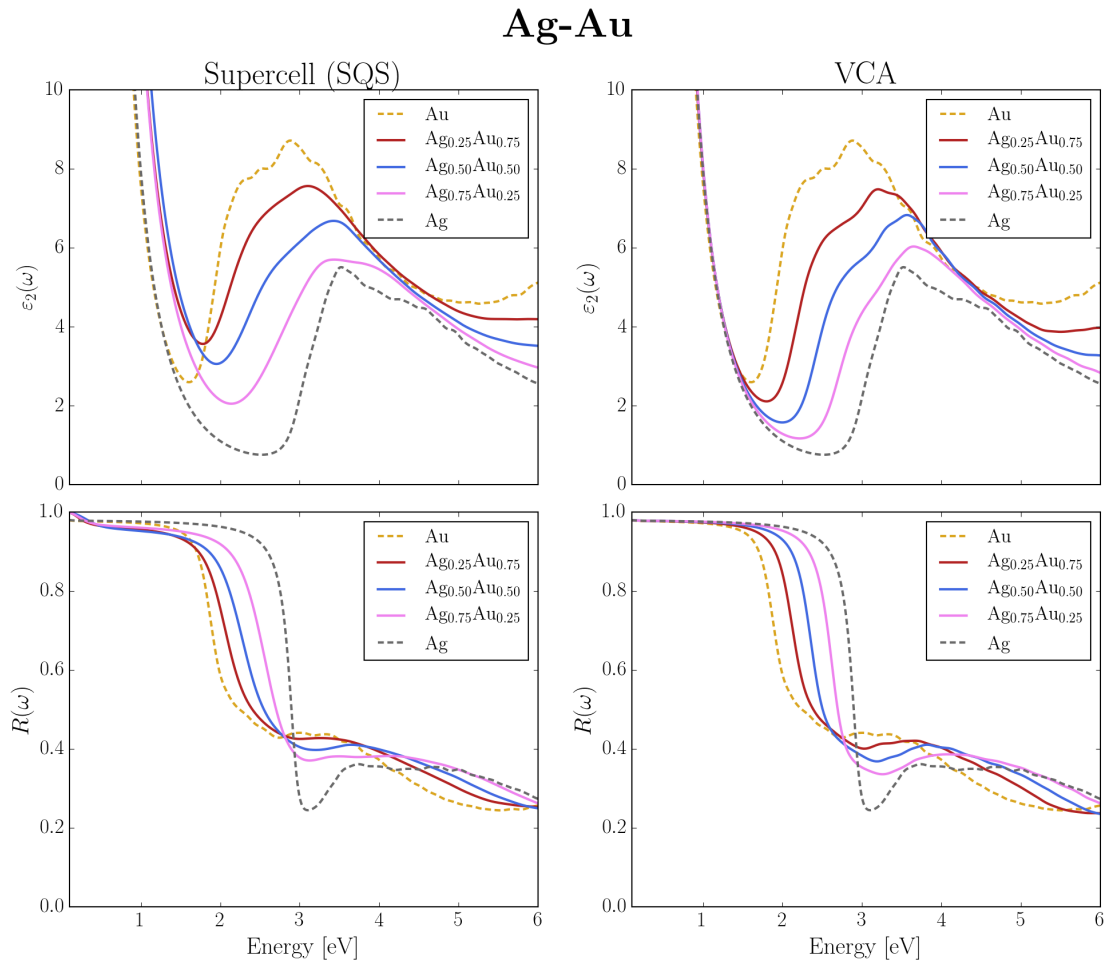


Figure 7.20 – Comparison of the trends in composition of optical absorption and reflectivity for Ag-Au between SQS and VCA simulations. We report also the results for the elemental constituents, i.e. Ag and Au (dashed lines).

### 7.4.2 Ag-Cu

In Fig. 7.21 we compare supercell and VCA simulations for the Ag-Cu system at different compositions. Supercell results for Ag-Cu at relatively small Cu concentrations ( $x = 0.0625$  and  $x = 0.25$ ) show a broad absorption peak centred at around 2.4 eV, i.e. below the absorption edge of elemental Ag, that is due to Cu impurity states and that is found also in the experimental data for Ag-Cu solid solutions (see Fig. 7.19). For higher Cu concentrations ( $x = 0.50$  and  $x = 0.75$ ) the broad peak moves to lower energies and gradually deforms into the absorption edge of elemental Cu. However, in terms of reflectivity, this trend roughly corresponds to a shift of the reflectivity edge to lower frequencies by increasing the Cu content in Ag. On the other hand, in VCA simulations, we observe a simple gradual shift of the onset of absorption to lower energies by varying the concentration of the alloy from elemental Ag to elemental Cu, which is very similar to the situation encountered in VCA simulations for the Ag-Au system. Because of this behaviour of the optical absorption, there is a corresponding gradual shift of the reflectivity edge to lower energies by increasing the Cu content in Ag. The broad absorption peak centered at around 2.4 eV is instead not observed in VCA simulations.

Since the  $d$ -bands of elemental Cu and Ag are more separated in energy, in Ag-Cu the weak-scattering limit is not as good as an approximation compared to Ag-Au and Au-Cu and thus the VCA method does not give the correct trend in optical absorption with respect to composition for solid solutions. Nonetheless, despite supercell and VCA optical absorptions show some differences, the two methods give similar trends in terms of the reflectivity curve (i.e. a similar simple shift of the reflectivity edge).

As discussed in Section 7.3, the Ag-Cu system is a two-phase alloy at normal experimental conditions and the Bruggeman model correctly describes the optical properties of the heterogeneous system. Therefore, for completeness, we compare also the results of the Bruggeman model with the SQS results (see Fig. 7.22). In the Bruggeman model the alloy optical absorption is given by a mixture of the dielectric functions of the two constituents elements<sup>12</sup>, as given by Eq. 7.2. Cu additions to Ag gradually increase the optical absorption at around 1.8 eV, which corresponds to the onset of absorption in elemental Cu. This gives rise to the “shoulder” in the reflectivity curve at around that energy, which is the feature observed in the experiments performed on two-phase samples of Ag-Cu. In contrast with supercell and VCA simulations, no shift of the reflectivity edge is observed in the results for the Bruggeman model.

In Ag-Cu the three methods considered, i.e. SQS, VCA and Bruggeman model, all give qualitatively different results for the optical absorption.

---

<sup>12</sup>In practice, the simple composition-weighted average,  $\epsilon_{\text{Avg}}$ , of the dielectric functions of the two constituent elements A and B, i.e.

$$\epsilon_{\text{Avg}} = (1 - x)\epsilon_A + x\epsilon_B, \quad (7.3)$$

gives very similar results to the dielectric function  $\epsilon_{\text{Br}}$  obtained from the Bruggeman model for the same concentration  $x$  of the alloy.



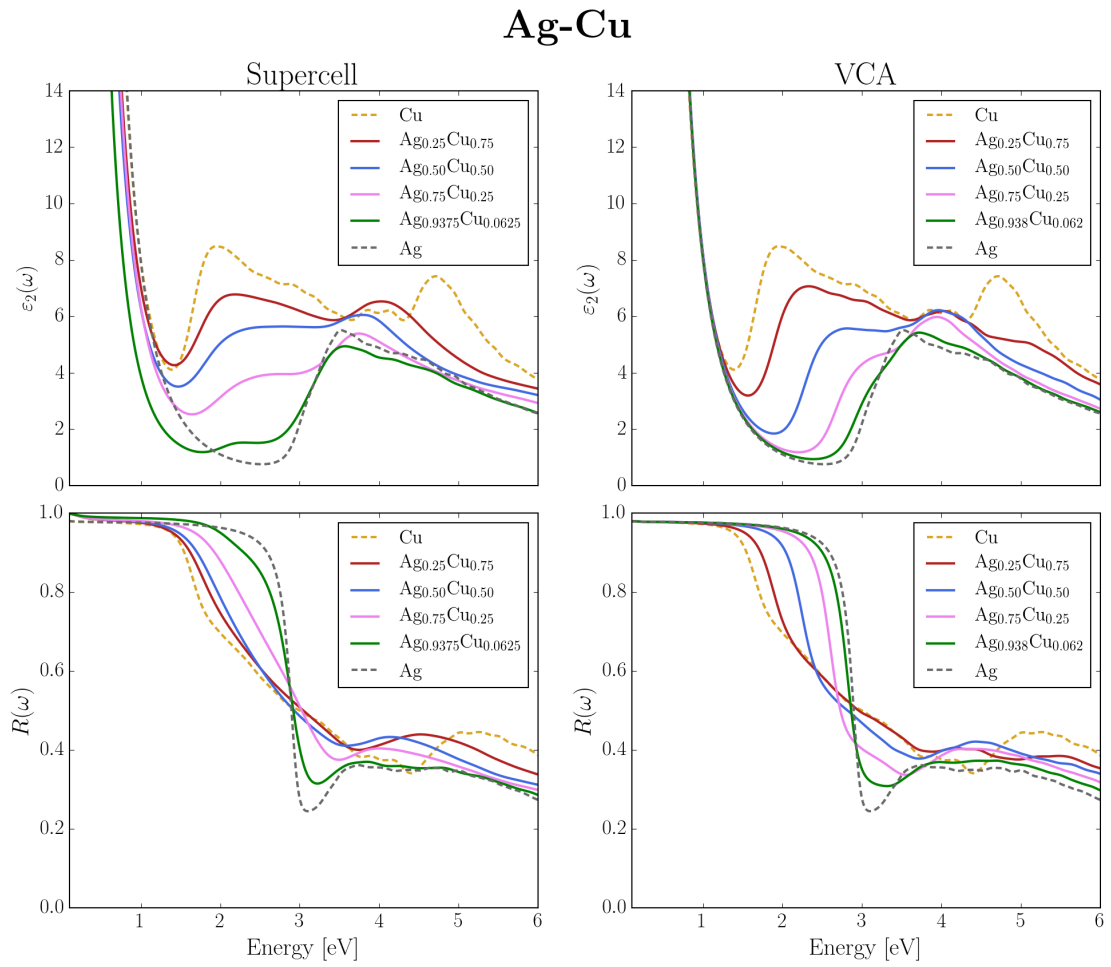


Figure 7.21 – Comparison of the trends in composition of optical absorption and reflectivity for Ag-Cu between supercell and VCA simulations. We report also the results for the elemental constituents, i.e. Ag and Cu (dashed lines).

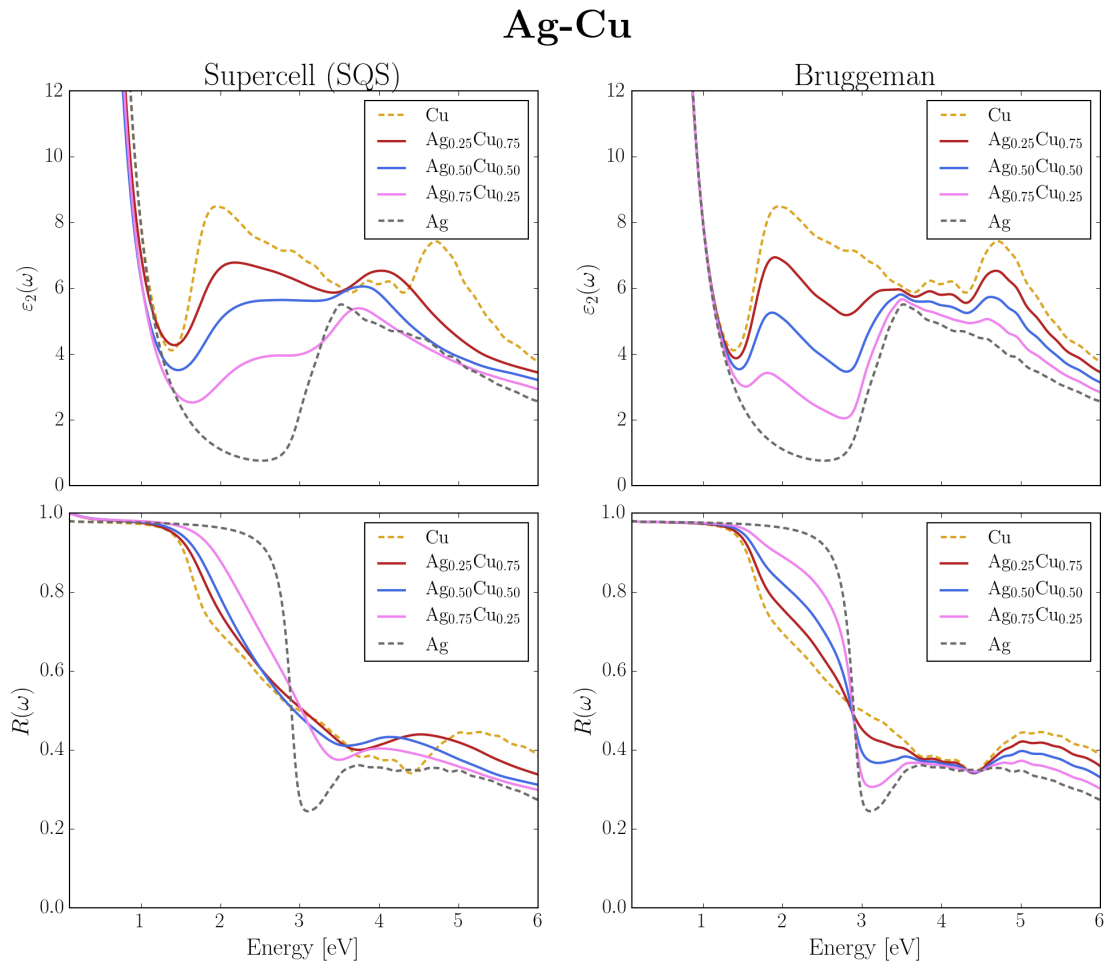


Figure 7.22 – Comparison of the trends in composition of optical absorption and reflectivity for Ag-Cu between supercell simulations and Bruggeman model results applied on elemental Ag and elemental Cu (dashed lines).

### 7.4.3 Au-Pd

For Au-Pd, the supercell and VCA approaches show larger discrepancies in the trends with composition of the optical properties at energies within the visible and infrared spectrum (see Fig. 7.23). Supercell simulations for small Pd concentrations ( $x = 0.0625$ ) show a substantial increase of the optical absorption in the low-energy range that significantly flattens the absorption edge of pure gold. In terms of reflectivity this leads to a smoothing of the reflectivity edge compared to pure gold while the position of the absorption edge is not significantly modified. It should be noted here that the supercell results for  $\text{Au}_{0.9375}\text{Pd}_{0.0625}$  in Fig. 7.23 are almost identical to those for  $\text{Au}_{0.9375}\text{Pt}_{0.0625}$  shown in Fig. 7.13. As already mentioned in Section 7.3.2, supercell simulations give results in qualitative agreement with the trends found in the experiments for Au-Pd solid solutions. In SQS simulations with higher Pd concentrations ( $x = 0.25, 0.50, 0.75$ ) the absorption edge of pure gold in  $\epsilon_2(\omega)$  is not any longer distinguishable and the optical absorption assumes a featureless behaviour more similar to that of elemental Pd, which in turn gives a nearly flat reflectivity curve in the visible range. On the other hand, in VCA simulations for relatively small Pd concentrations ( $\text{Au}_{0.938}\text{Pd}_{0.062}$  and  $\text{Au}_{0.75}\text{Pd}_{0.25}$  in Fig. 7.23), we observe a simple gradual shift of the onset of absorption to lower energies by varying the concentration of the alloy from elemental Au to elemental Pd, which is the same behaviour already encountered in VCA simulations for the Ag-Au and Ag-Cu systems. In this case the trend is significantly different to what observed in supercell simulations of Au-Pd at the same compositions. For larger quantities of Pd instead ( $\text{Au}_{0.50}\text{Pd}_{0.50}$  and  $\text{Au}_{0.25}\text{Pd}_{0.75}$  in Fig. 7.23),  $\epsilon_2(\omega)$  in the visible range assumes a featureless behaviour comparable to the one found in elemental Pd, and SQS and VCA results are, for these compositions, in good agreement. As a consequence, by looking at the VCA reflectivity, we notice first a gradual shift of the reflectivity edge to lower energies by increasing the Pd content in Au ( $x = 0.062, 0.25$ ) which then deforms towards the flat reflectivity curve of elemental Pd ( $x = 0.50, 0.75$ ). The VCA results for Au-Pd can be interpreted within the framework of the simple rigid band model. Indeed, since Pd has one electron less in the valence compared to Au, the Fermi level lowers in energy and moves closer to the  $d$  bands by increasing the Pd content, so that the onset of interband transitions also moves to lower energies. As a confirmation, a band structure analysis shows that the Fermi level gradually moves towards the occupied  $d$ -bands by increasing the Pd content ( $x = 0.062, 0.25$ ). At the composition  $x = 0.50$  the Fermi level moves below the top valence  $d$ -band and the optical properties of Au-Pd then resemble those of elemental Pd for larger Pd content ( $x = 0.75$ ).

As shown by this comparison with experimental data and supercell simulations, the VCA method is not adequate to describe the effects of Pd additions in Au, and more generally, of any transition metal. For this system, the electronic structure of the alloy is not simply a mixture of the electronic structure of the single constituents, as in the case of Ag-Au, because Pd introduces virtual bound states below the Fermi level that increase the optical absorption in the low-energy range. Clearly, this effect cannot be captured by the simple mean-field VCA approach.

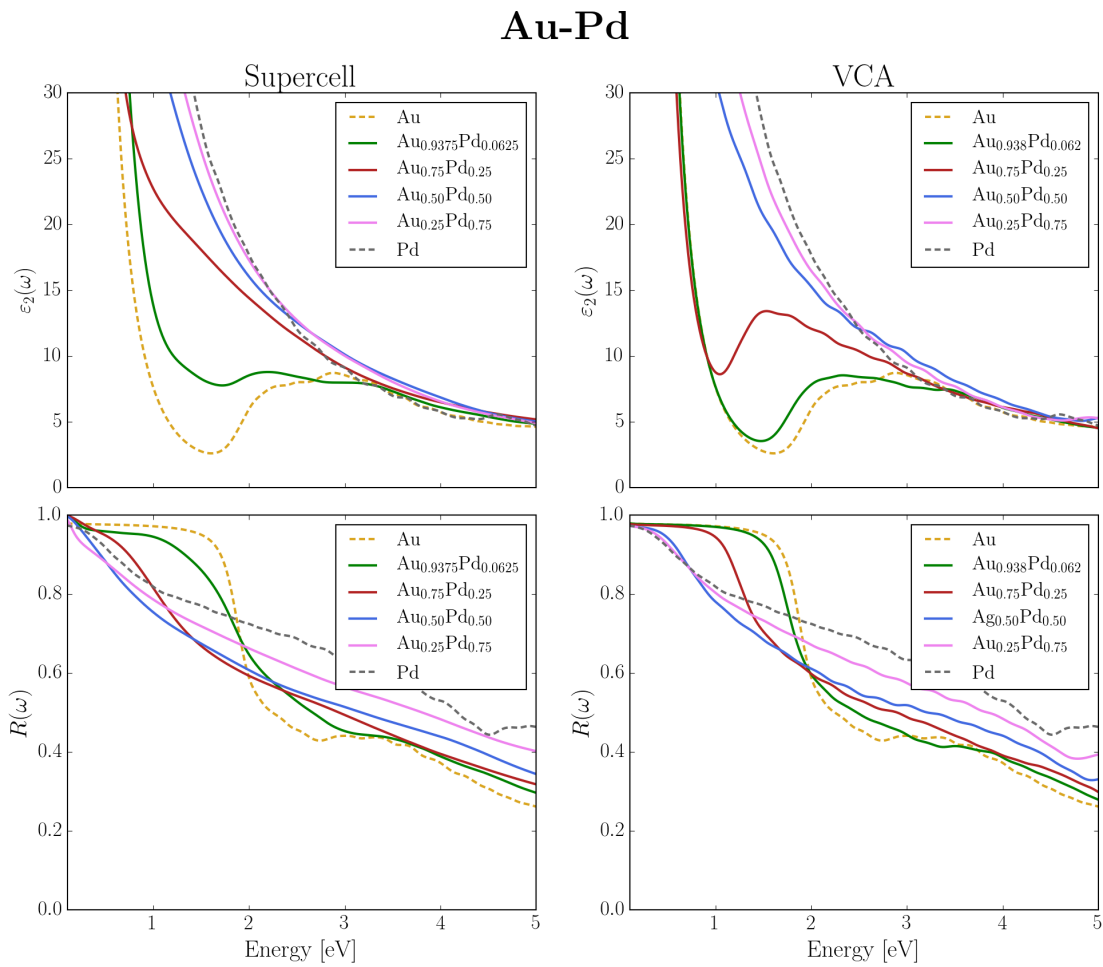


Figure 7.23 – Comparison of the trends in composition of optical absorption and reflectivity for Au-Pd between supercell and VCA simulations. We report also the results for the elemental constituents, i.e. Au and Pd (dashed lines).

#### 7.4.4 Trends in VCA

The comparative studies performed in this Section and in Section 7.3 show that the supercell approach is more predictive than VCA in order to study the optical properties of solid solutions. We have seen that the optical absorption computed with the VCA method for gold alloys give always a simple shift of the absorption onset to lower or higher energies, depending on the alloying element considered, compared to the position of pure gold, which does not often correspond to the experimental situation.

The VCA approach gives the correct trends in gold alloys if the alloying element is an isoelectronic element in the same column of Au in the periodic table, i.e. Cu and Ag. In Ag-Au and Au-Cu solid solutions, the main effect of alloying additions on the electronic structure is a rigid shift of the occupied  $d$ -bands with respect to the Fermi energy which is captured by the VCA model of Eq. 7.1. In Ag-Cu solid solutions instead, since the  $d$ -bands of the constituents elements are more separate in energy, the rigid shift of the  $d$ -bands given by the VCA model is not in agreement with experiments and supercell simulations, because of the presence of localized Cu impurity states in the Ag matrix. For binary alloys of gold with transition-metal elements the disagreement is more significant. Indeed no shift of the onset of absorption is observed in experiments on Au-Pd and Au-Pt alloys; instead the presence of  $d$  impurity states increases the optical absorption in the low-energy range of the spectrum and smoothens the reflectivity edge of pure gold.

We now discuss in more detail the trends in the optical properties with respect to the alloying element for VCA results of binary gold alloys. As already briefly discussed for the case of Au-Pd, the VCA method provides results that can be explained in terms of the simple rigid band model for elements not in the same column of the periodic table. For this purpose we show in Fig 7.24 the VCA optical absorption and reflectivity of the alloys Ag-Au, Au-Pd and Au-Zn, and compare the results with supercell results at the same concentration ( $x = 0.062$ ). In the simple rigid band model the band structures of the two constituent elements are assumed to be equal and the position of the Fermi level is simply given by the following equation

$$\bar{n}_{\text{val}}(E_F) = Z_A(1 - x) + Z_B x, \quad (7.4)$$

where  $\bar{n}_{\text{val}}(E_F)$  is the valence electronic density and the dependence on the Fermi level  $E_F$  is explicitly written, and  $Z_A$  and  $Z_B$  are the number of valence electrons of the A and B element, respectively. Zn has one electron more than Au in the valence, thus the Fermi energy is shifted upwards in energy and, as a consequence, the onset of interband transitions in VCA results is also shifted to higher energies. SQS results provide a qualitative behaviour of the optical spectra similar to the one given by VCA and in agreement with experimental data and first-principles results obtained for the Cu-Zn alloy at small concentrations of Zn [149]. However, similarly to the case of Al-Au, in supercell results there is not only a shift of the absorption edge but also an increase of the optical absorption in the low-energy range, not observed in VCA. On the other hand, Pd has one electron less than Au in the valence, thus the Fermi energy is shifted downwards in energy and, as a consequence, the onset of interband transitions in

## Chapter 7. Reflectivity and colour of alloys

VCA is also shifted to lower energies but, as already discussed in Section 7.2 and Section 7.3, supercell results show a different behaviour. In Ag-Au instead we find a behaviour comparable to the Au-Zn case. But in this case, Ag and Au have the same number of valence electrons and the shift is explained not by the rigid band model of Eq. 7.4 but in terms of a shift of the position of the occupied  $d$ -bands by means of Eq. 7.1.

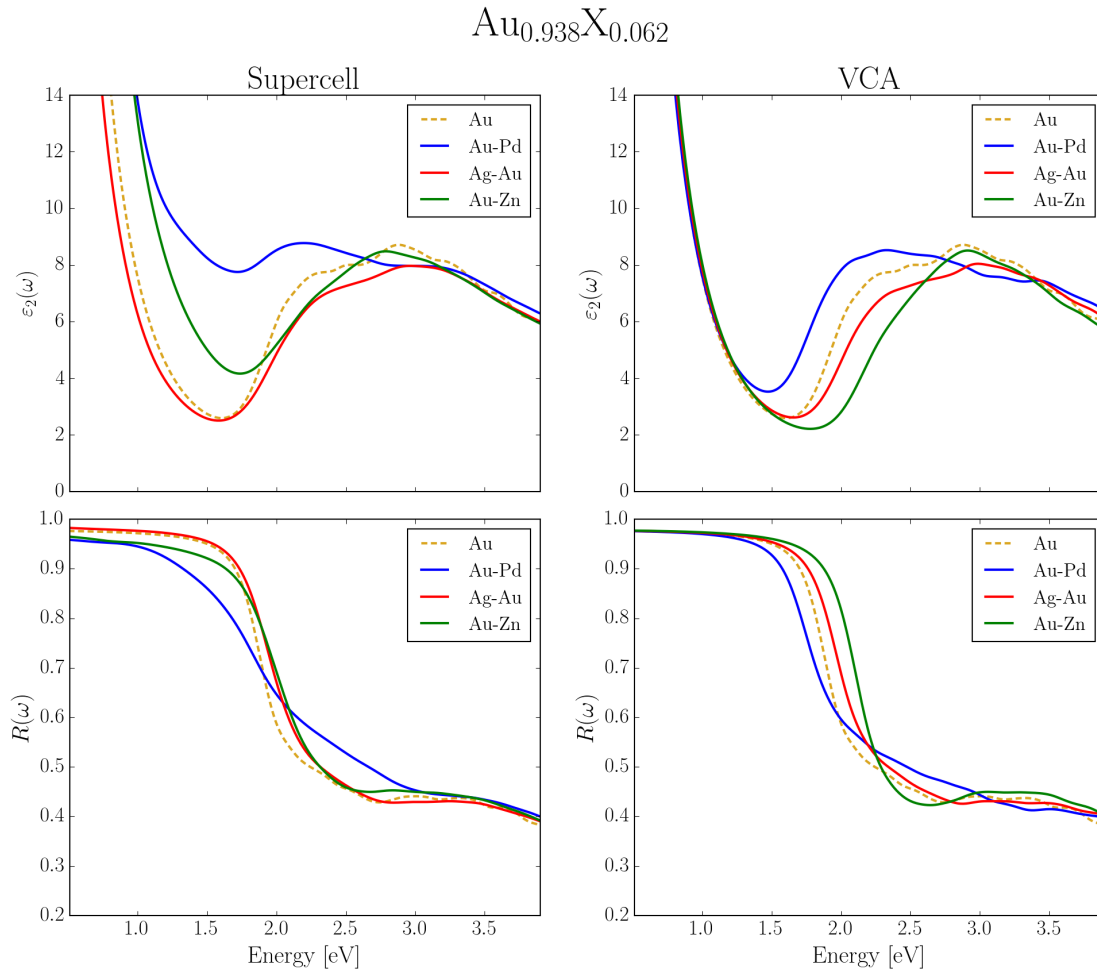


Figure 7.24 – Comparison of the optical absorption and reflectivity of  $\text{Au}_{0.938}\text{X}_{0.062}$ , with  $\text{X} = \text{Pd}$ ,  $\text{Ag}$  and  $\text{Zn}$ , between supercell and VCA simulations. For reference, we report also the results for elemental Au (dashed lines).

### 7.5 Computational screening of gold-based intermetallics

We have used the computational approach described in this thesis in a project in collaboration with industry. The purpose of the project is to identify novel gold alloys with the desired colours by employing, for the screening of possible promising candidate compounds, both experiments and first-principles simulations.

For this project we systematically study the optical properties of experimentally known gold binary intermetallic compounds of gold and the effect of different alloying elements and different compositions on the reflectivity curve in the visible range (and thus on the colour) of gold. In the following we briefly describe the approach followed for the computational screening of binary intermetallics of gold.

We select the experimental crystal structures of binary intermetallic compounds of gold from the Inorganic Crystal Structure Database (ICSD [107]) and from the Crystallography Open Database (COD [108]). In our selection, we neglect structures with more than 20 atoms per cell, compounds containing elements harmful to human health (e.g. Hg, Cd, As, etc.) and compounds containing rare-earth elements. After this preliminary screening we end up with 92 binary intermetallics of gold that are listed in Table 7.3 and Table 7.4. Of these compounds we simulate reflectivity and colour, using the computational approach and workflow described in Chapter 5 and the same computational parameters used for the coloured intermetallics studied in Section 7.3.1.

We show in Fig. 7.25 the resulting CIELAB colour coordinates of the 92 compounds considered. Among these we have identified a few compounds with possibly interesting features in the optical properties within the visible range and that thus could possibly show interesting bulk colours.

## Chapter 7. Reflectivity and colour of alloys

Compound	SG #	Database ID	Compound	SG #	Database ID
Au <sub>16</sub> Al <sub>4</sub>	198	1523317 (COD)	Au <sub>16</sub> Hf <sub>4</sub>	62	611961 (ICSD)
Au <sub>4</sub> Al <sub>4</sub>	11	1523318 (COD)	Au <sub>6</sub> Hf <sub>2</sub>	59	611955 (ICSD)
AuAl	221	57495 (ICSD)	Au <sub>2</sub> Hf	139	611956 (ICSD)
AuAl <sub>2</sub>	225	9008999 (COD)	Au <sub>2</sub> Hf <sub>2</sub>	129	611959 (ICSD)
AuB <sub>2</sub>	191	1510576 (COD)	AuHf <sub>2</sub>	139	1510176 (COD)
Au <sub>5</sub> Ba	191	1510547 (COD)	Au <sub>6</sub> In <sub>2</sub>	59	1510500 (COD)
Au <sub>2</sub> Ba	191	1510358 (COD)	Au <sub>3</sub> In <sub>2</sub>	164	612019 (ICSD)
Au <sub>4</sub> Ba <sub>4</sub>	62	1510584 (COD)	AuIn <sub>2</sub>	225	9009001 (COD)
Au <sub>6</sub> Ba <sub>9</sub>	148	611635 (ICSD)	Au <sub>5</sub> K	191	1510565 (COD)
Au <sub>5</sub> Ca	216	1510549 (COD)	Au <sub>8</sub> K <sub>4</sub>	194	2018869 (COD)
Au <sub>4</sub> Ca <sub>2</sub>	74	1510368 (COD)	Au <sub>3</sub> K <sub>2</sub>	71	7209415 (COD)
Au <sub>8</sub> Ca <sub>6</sub>	148	54547 (ICSD)	Au <sub>3</sub> Li	221	1510505 (COD)
Au <sub>2</sub> Ca <sub>2</sub>	63	54978 (ICSD)	AuLi <sub>3</sub>	225	1510223 (COD)
Au <sub>8</sub> Ca <sub>10</sub>	14	1510534 (COD)	Au <sub>4</sub> Mg <sub>8</sub>	62	1510233 (COD)
Au <sub>6</sub> Ca <sub>10</sub>	140	1510483 (COD)	AuMg	221	1510230 (COD)
Au <sub>4</sub> Ca <sub>10</sub>	15	1510371 (COD)	Au <sub>2</sub> Mg <sub>6</sub>	194	1510237 (COD)
Au <sub>4</sub> Ca <sub>12</sub>	62	1510066 (COD)	Au <sub>4</sub> Mn	87	107998 (ICSD)
Au <sub>4</sub> Cr	87	611737 (ICSD)	Au <sub>5</sub> Mn <sub>2</sub>	12	2310085 (COD)
Au <sub>3</sub> Cu	221	1510492 (COD)	Au <sub>2</sub> Mn	139	2310083 (COD)
AuCu	123	1510113 (COD)	AuMn	221	109348 (ICSD)
AuCu <sub>3</sub>	221	9013496 (COD)	AuMn <sub>2</sub>	139	2310077 (COD)
Au <sub>4</sub> Ga <sub>4</sub>	62	9008926 (COD)	Au <sub>3</sub> Mn <sub>9</sub>	123	150552 (ICSD)
AuGa <sub>2</sub>	225	9009000 (COD)	Au <sub>4</sub> Na <sub>2</sub>	227	1510444 (COD)

Table 7.3 – List of binary intermetallics of gold extracted from ICSD and COD databases (part I). We report chemical formula, space group number (SG #) and database ID.



## 7.5. Computational screening of gold-based intermetallics

Compound	SG #	Database ID	Compound	SG #	Database ID
Au <sub>2</sub> Na <sub>4</sub>	140	1510247 (COD)	Au <sub>4</sub> Ti	87	109132 (ICSD)
Au <sub>2</sub> Nb	191	1510446 (COD)	Au <sub>2</sub> Ti	139	1510471 (COD)
Au <sub>8</sub> Nb <sub>12</sub>	213	612191 (ICSD)	Au <sub>2</sub> Ti <sub>2</sub>	51	612407 (ICSD)
Au <sub>2</sub> Nb <sub>3</sub>	139	1510447 (COD)	Au <sub>2</sub> Ti <sub>2</sub>	129	612415 (ICSD)
Au <sub>2</sub> Nb <sub>6</sub>	223	1510253 (COD)	AuTi	221	1510312 (COD)
Au <sub>4</sub> P <sub>6</sub>	12	2105391 (COD)	Au <sub>2</sub> Ti <sub>6</sub>	223	1510314 (COD)
Au <sub>5</sub> Rb	191	1528238 (COD)	AuTi <sub>3</sub>	221	2310078 (COD)
Au <sub>7</sub> Rb <sub>3</sub>	65	1510588 (COD)	Au <sub>4</sub> V	87	612460 (ICSD)
Au <sub>3</sub> Rb <sub>2</sub>	71	1510510 (COD)	Au <sub>4</sub> V <sub>2</sub>	63	1510476 (COD)
AuRb	221	1517938 (COD)	Au <sub>2</sub> V <sub>6</sub>	223	612459 (ICSD)
Au <sub>4</sub> Sb <sub>8</sub>	205	9016730 (COD)	AuV <sub>3</sub>	221	2310079 (COD)
AuSb <sub>2</sub>	225	9009002 (COD)	Au <sub>6</sub> Y <sub>2</sub>	59	612464 (ICSD)
AuSb <sub>3</sub>	229	1510290 (COD)	Au <sub>2</sub> Y	139	612466 (ICSD)
Au <sub>4</sub> Sc	87	612300 (ICSD)	Au <sub>2</sub> Y <sub>2</sub>	63	169022 (ICSD)
Au <sub>2</sub> Sc	139	612299 (ICSD)	AuY	221	1510318 (COD)
AuSc	221	1510291 (COD)	Au <sub>4</sub> Y <sub>6</sub>	127	2018283 (COD)
Au <sub>5</sub> Sn	155	1510571 (COD)	Au <sub>4</sub> Y <sub>8</sub>	62	2018284 (COD)
Au <sub>2</sub> Sn <sub>2</sub>	194	1510301 (COD)	AuZn	221	1510322 (COD)
Au <sub>2</sub> Sn <sub>8</sub>	41	1510307 (COD)	Au <sub>16</sub> Zr <sub>4</sub>	62	1510543 (COD)
Au <sub>5</sub> Sr	191	1510572 (COD)	Au <sub>6</sub> Zr <sub>2</sub>	59	612509 (ICSD)
Au <sub>4</sub> Sr <sub>2</sub>	74	1510467 (COD)	Au <sub>2</sub> Zr	139	612510 (ICSD)
Au <sub>6</sub> Sr <sub>9</sub>	148	1510468 (COD)	AuZr <sub>2</sub>	139	1510330 (COD)
Au <sub>6</sub> Sr <sub>14</sub>	186	1510514 (COD)	Au <sub>2</sub> Zr <sub>6</sub>	223	1510331 (COD)

Table 7.4 – List of binary intermetallics of gold extracted from ICSD and COD databases (part II). We report chemical formula, space group number (SG #) and database ID.

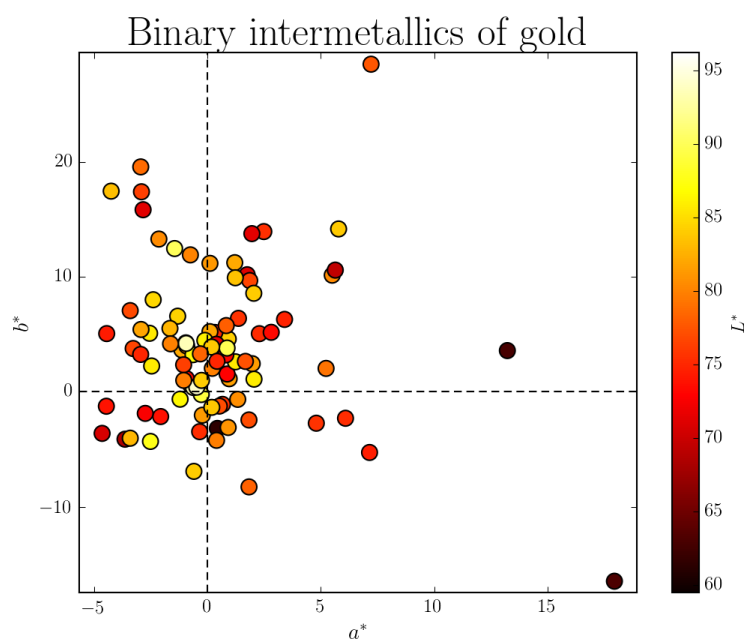


Figure 7.25 – Simulated CIELAB colour coordinates of 92 binary intermetallics of gold extracted from ICSD and COD databases of experimental crystal structures.

## 8 Conclusions

In the course of the thesis we have developed a code, named SIMPLE [89], to calculate optical properties of metals within the independent particle approximation and exploiting Shirley's optimal basis method for interpolations in reciprocal space. The code takes, as starting ingredient, the electronic structure computed solving the Kohn-Sham equations of density-functional theory (considering the semi-local PBE exchange-correlation functional) within the framework of the plane-wave pseudopotential method. SIMPLE computes both interband and intraband contributions to the complex dielectric function. Furthermore the matrix elements of the velocity operator are correctly calculated by including the non-local contribution of the pseudopotentials.

Subsequently, for the purpose of automation of the simulations, all the steps of calculations required to simulate the reflectivity and colour of a material from the initial crystal structure have been implemented as an AiiDA workflow. Thanks to the latter, it is possible, giving as input a generic crystal structure, to obtain directly as output the reflectivity and colour of a given material.

In order to perform efficient and reliable calculations of the dielectric function with SIMPLE, pseudopotentials and wavefunction cutoffs for all the elements of the periodic table considered in this thesis have been selected according to the results of the SSSP protocol developed by us in order to test pseudopotentials for solid-state calculations. The SSSP protocol consists of a verification part, based on the  $\Delta$ -factor test to assess the precision of the pseudopotential equations of state, and an extensive performance-oriented part based on plane-wave convergence tests for phonon frequencies, band structures, cohesive energies and stress tensors. The protocol has been applied to test several pseudopotential libraries available for the Quantum ESPRESSO distribution on 85 elements of the periodic table (the results of this study have been published in Ref. [90]). In particular, by inspecting the data of the SSSP database of tests, we ensure convergence of the band structures with respect to wavefunction cutoff and a good precision of the pseudopotentials used for the simulations of the optical properties of metals.

As a first application and benchmark study we have applied the described computational approach, combining the use of the SIMPLE code, of the AiiDA workflow and of the results of

the SSSP protocol, to systematically compute the reflectivity and colour of 45 elemental metals in their ground-state crystal structure. By means of an extensive comparison with optical experimental data, we have assessed the predictivity of the computational approach used. We have found that, although the colour is not always in quantitative agreement with experiments (e.g. we observe a systematic shift of the reflectivity edge in noble metals), the shape and the main features of the experimental reflectivity curve are reproduced by the simulations together with the trends and main differences among elemental metals. Furthermore, we have verified the consistency of the simulations with the help of the  $f$ -sum rule and we have shown that the inclusion of spin-orbit coupling in heavy elements does not modify significantly the optical properties around the visible range. On the other hand the effect of the inclusion of the non-local contribution to the matrix elements of the velocity operator is, in some cases, important and improves the agreement with experiments. Finally, by a comparison with the results of the empirical Drude model we have concluded that, in order to be predictive in the estimation of the optical properties of metals, both interband and intraband contributions need to be computed *ab initio*.

In the last part of the thesis we have studied the optical properties of different types of metallic alloys, focusing in particular on the simulation of gold-based binary compounds. Disordered solid solutions have been simulated with the supercell approach, based mainly on the use of special quasi random structures, while instead we have employed the Bruggeman model to calculate the dielectric function of macroscopically heterogeneous alloys (ordered intermetallic compounds can be trivially simulated within their unit cell). Before performing a comparison between simulations and experiments, we have studied the interplay between interband and intraband contributions in supercell simulations of disordered alloys. In particular we have numerically analyzed the transfer of spectral weight from intraband contribution (i.e. from the Drude plasma frequency) to interband contribution when increasing the supercell size and the conservation of the total spectral weight by means of the  $f$ -sum rule. Thus we have demonstrated that in the simulation of alloys within the supercell approach only the sum of the two contributions, that is the total dielectric function, is meaningful. Through a comparison with several experimental data, we have then shown that the simulations give accurate results for the coloured intermetallic compounds. Our calculations also reproduce the three main mechanisms by which it is possible to change the bulk colour of gold in alloys (i.e. shift of the reflectivity edge, flattening of the reflectivity edge and new features of the reflectivity curve). Furthermore we manage to describe the main colour trends in the Au-Ag-Cu ternary system if the correct computational methods are used for the different types of compounds. Although, due to the approximations used, we do not have in general quantitative agreement with experiments (with the notable exception of the coloured intermetallic compounds for which the simulations are often in quantitative agreement with experiments), we have instead found the correct qualitative trends with respect to composition and alloying elements. Moreover, we have discussed how the simple virtual crystal approximation is not in general adequate to describe the colour trends in disordered binary alloys of gold and that the more computationally expensive supercell approach is usually necessary in order to find the correct

---

trends in optical properties. Additionally, as a verification test for the computational approach deployed in this thesis, we have compared the optical properties obtained for several elemental metals and coloured intermetallic compounds with previous first-principles simulations available in the literature and we have found good agreement with our results.

We would like to point out here that the work performed in this thesis can be seen as a starting point for more advanced studies that could be built on top of the results discussed here. For example, the systematic study performed on the convergence of band structures obtained at the PBE level can be relevant for further studies going beyond the simple independent particle approximation for the calculation of optical properties and that include many-body effects, such as *GW* band structures and/or optical spectra calculated from the Bethe-Salpeter equation. Furthermore, the systematic validation of the approach performed for elemental metals and binary alloys is an important preliminary step for the simulation of the optical properties of more complex alloys having a larger number of constituent elements, such as ternaries, quaternaries, etc., which are more relevant for technological applications (e.g. superalloys and high-entropy alloys).

In conclusion, we underline that the computational approach discussed can be used in systematic studies on the optical properties of metals in order to predict trends in real metallic systems and to help the search for novel materials with specific optical properties by exploring the composition space through the computational screening of materials. In fact, at the end of the thesis, we have briefly described some of the results obtained from the computational screening of the colour of binary intermetallics of gold extracted from databases of experimental crystal structures.



# A Macroscopic averages in crystals

As discussed in Chapter 3, in order to obtain the macroscopic quantities entering in the macroscopic Maxwell's equations we have to average the corresponding microscopic quantities over distances large compared to the diameter of the primitive cell of the crystal but small compared to the wavelength of light. This is equivalent to perform an average over the primitive cell centered around the Bravais lattice vector  $\mathbf{R}$  and then to consider the discrete variable  $\mathbf{R}$  as the continuous coordinate entering in the macroscopic Maxwell's equations.

In practice, we define the macroscopic average of an arbitrary crystal function  $F(\mathbf{r}, \omega)$  as the average over the primitive cell of the function itself [67]

$$F_M(\mathbf{R}, \omega) \equiv \frac{1}{V_c} \int_{V_c(\mathbf{R})} d\mathbf{r} F(\mathbf{r}, \omega), \quad (\text{A.1})$$

where  $V_c(\mathbf{R})$  is the volume of the primitive cell centered around the Bravais lattice vector  $\mathbf{R}$ . To calculate the integral in Eq. A.1 we expand  $F(\mathbf{r}, \omega)$  in reciprocal space as

$$F(\mathbf{r}, \omega) = \sum_{\mathbf{q}} \sum_{\mathbf{G}} F(\mathbf{q} + \mathbf{G}, \omega) e^{i(\mathbf{q} + \mathbf{G}) \cdot \mathbf{r}}. \quad (\text{A.2})$$

We deal here with the general situation in which we have a sum over the BZ of different wavevectors  $\mathbf{q}$ . For monochromatic perturbations however, as for example for a monochromatic electromagnetic wave, only a single component  $\mathbf{q}$  in the sum over the BZ is different from zero. The assumption that the discrete variable  $\mathbf{R}$  can be considered continuous is appropriate for functions that contain only small Bloch wavevectors in the BZ, i.e. when  $|\mathbf{q}| \ll |\mathbf{G}|$ .

## Appendix A. Macroscopic averages in crystals

---

Indeed the macroscopic average is

$$F_M(\mathbf{R}, \omega) = \frac{1}{V_c} \int_{V_c(\mathbf{R})} d\mathbf{r} F(\mathbf{r}, \omega) \quad (\text{A.3})$$

$$= \frac{1}{V_c} \sum_{\mathbf{q}} \sum_{\mathbf{G}} F(\mathbf{q} + \mathbf{G}, \omega) \int_{V_c(\mathbf{R})} d\mathbf{r} e^{i(\mathbf{q} + \mathbf{G}) \cdot \mathbf{r}} \quad (\text{A.4})$$

$$\simeq \sum_{\mathbf{q}} \sum_{\mathbf{G}} e^{i\mathbf{q} \cdot \mathbf{R}} F(\mathbf{q} + \mathbf{G}, \omega) \delta_{\mathbf{G}, \mathbf{0}} \quad (\text{A.5})$$

$$= \sum_{\mathbf{q}} e^{i\mathbf{q} \cdot \mathbf{R}} F(\mathbf{q} + \mathbf{0}, \omega), \quad (\text{A.6})$$

where we have made use of the approximation that, if  $|\mathbf{q}| \ll |\mathbf{G}|$ , the factor  $e^{i\mathbf{q} \cdot \mathbf{r}}$  in Eq. A.4 can be moved outside the integral over the primitive cell because it is nearly constant and equal to  $e^{i\mathbf{q} \cdot \mathbf{R}}$ . In reciprocal space this reads

$$F_M(\mathbf{q}, \omega) \equiv F_M(\mathbf{q} + \mathbf{G}, \omega) = F(\mathbf{q} + \mathbf{0}, \omega) \delta_{\mathbf{G}, \mathbf{0}}. \quad (\text{A.7})$$

In conclusion, only the Fourier component  $\mathbf{G} = \mathbf{0}$  contributes to the macroscopic average  $F_M(\mathbf{R}, \omega)$ .



## B Derivation of the intraband contribution to the IPA dielectric function

In order to derive the optical limit of the intraband contribution to the IPA dielectric function we follow the treatment of Ref. [66]. It is convenient to start from the real part of the intraband contribution in the limit  $\eta \rightarrow 0$  (see Eq. 3.48), i.e.

$$\epsilon_1^{\text{intra}}(\mathbf{q}, \omega) = -\frac{4\pi}{|\mathbf{q}|^2} \frac{1}{V} \sum_{\mathbf{k}} \sum_n (f_{n\mathbf{k}} - f_{n\mathbf{k}+\mathbf{q}}) \frac{|\langle \psi_{n\mathbf{k}+\mathbf{q}} | e^{i\mathbf{q}\cdot\mathbf{r}} | \psi_{n\mathbf{k}} \rangle|^2}{\omega - (E_{n\mathbf{k}+\mathbf{q}} - E_{n\mathbf{k}})}. \quad (\text{B.1})$$

First of all, we notice that the intraband ( $n' = n$ ) matrix elements in Eq. 3.49 are equal to 1. Then, we rewrite the summation over the KS states as

$$\sum_{\mathbf{k}} \sum_n \frac{f_{n\mathbf{k}} - f_{n\mathbf{k}+\mathbf{q}}}{\omega - (E_{n\mathbf{k}+\mathbf{q}} - E_{n\mathbf{k}})} = \sum_{\mathbf{k}} \sum_n \frac{f_{n\mathbf{k}}}{\omega - (E_{n\mathbf{k}+\mathbf{q}} - E_{n\mathbf{k}})} - \sum_{\mathbf{k}} \sum_n \frac{f_{n\mathbf{k}+\mathbf{q}}}{\omega - (E_{n\mathbf{k}+\mathbf{q}} - E_{n\mathbf{k}})} \quad (\text{B.2})$$

$$= \sum_{\mathbf{k}} \sum_n \frac{f_{n\mathbf{k}}}{\omega - (E_{n\mathbf{k}+\mathbf{q}} - E_{n\mathbf{k}})} - \sum_{\mathbf{k}} \sum_n \frac{f_{n\mathbf{k}}}{\omega - (E_{n\mathbf{k}} - E_{n\mathbf{k}-\mathbf{q}})} \quad (\text{B.3})$$

$$= \sum_{\mathbf{k}} \sum_n f_{n\mathbf{k}} \left[ \frac{1}{\omega - (E_{n\mathbf{k}+\mathbf{q}} - E_{n\mathbf{k}})} - \frac{1}{\omega - (E_{n\mathbf{k}} - E_{n\mathbf{k}-\mathbf{q}})} \right] \quad (\text{B.4})$$

$$= \sum_{\mathbf{k}} \sum_n f_{n\mathbf{k}} \left[ \frac{\omega + (E_{n\mathbf{k}+\mathbf{q}} - E_{n\mathbf{k}})}{\omega^2 - (E_{n\mathbf{k}+\mathbf{q}} - E_{n\mathbf{k}})^2} - \frac{\omega + (E_{n\mathbf{k}} - E_{n\mathbf{k}-\mathbf{q}})}{\omega^2 - (E_{n\mathbf{k}} - E_{n\mathbf{k}-\mathbf{q}})^2} \right] \quad (\text{B.5})$$

where we have performed the substitution  $\mathbf{k} + \mathbf{q} \rightarrow \mathbf{k}$  in the second term of the right-hand side of Eq. B.2. For small  $\mathbf{q}$ ,  $\omega^2 \gg (E_{n\mathbf{k}+\mathbf{q}} - E_{n\mathbf{k}})^2$  and, similarly,  $\omega^2 \gg (E_{n\mathbf{k}} - E_{n\mathbf{k}-\mathbf{q}})^2$ . Moreover we can expand  $E_{n\mathbf{k}+\mathbf{q}}$  and  $E_{n\mathbf{k}-\mathbf{q}}$  around  $\mathbf{k}$  assuming that the transferred momentum is along a generic  $\hat{\mathbf{q}} = \hat{\boldsymbol{\alpha}}$  direction (e.g.  $\hat{\boldsymbol{\alpha}}$  can be one of the three Cartesian directions  $\hat{\mathbf{x}}, \hat{\mathbf{y}}$  or  $\hat{\mathbf{z}}$ ):

$$E_{n\mathbf{k}+\mathbf{q}} \simeq E_{n\mathbf{k}} + |\mathbf{q}| \frac{\partial E_{n\mathbf{k}}}{\partial k_{\alpha}} + \frac{1}{2} |\mathbf{q}|^2 \frac{\partial^2 E_{n\mathbf{k}}}{\partial k_{\alpha}^2}, \quad (\text{B.6})$$

$$E_{n\mathbf{k}-\mathbf{q}} \simeq E_{n\mathbf{k}} - |\mathbf{q}| \frac{\partial E_{n\mathbf{k}}}{\partial k_{\alpha}} + \frac{1}{2} |\mathbf{q}|^2 \frac{\partial^2 E_{n\mathbf{k}}}{\partial k_{\alpha}^2}. \quad (\text{B.7})$$

$$(\text{B.8})$$

## Appendix B. Derivation of the intraband contribution to the IPA dielectric function

---

Thus the summation becomes

$$\sum_{\mathbf{k}} \sum_n \frac{f_{n\mathbf{k}} - f_{n\mathbf{k}+\mathbf{q}}}{\omega - (E_{n\mathbf{k}+\mathbf{q}} - E_{n\mathbf{k}})} = \frac{1}{\omega^2} \sum_{\mathbf{k}} \sum_n f_{n\mathbf{k}} [(E_{n\mathbf{k}+\mathbf{q}} - E_{n\mathbf{k}}) - (E_{n\mathbf{k}} - E_{n\mathbf{k}-\mathbf{q}})] \quad (\text{B.9})$$

$$= \frac{1}{\omega^2} \sum_{\mathbf{k}} \sum_n f_{n\mathbf{k}} |\mathbf{q}|^2 \frac{\partial^2 E_{n\mathbf{k}}}{\partial k_\alpha^2} \quad (\text{B.10})$$

and the real part of the intraband contribution to the dielectric function is therefore

$$\epsilon_1^{\text{intra}}(\hat{\mathbf{q}}, \omega) = -\frac{4\pi}{V\omega^2} \sum_{\mathbf{k}} \sum_n f_{n\mathbf{k}} \frac{\partial^2 E_{n\mathbf{k}}}{\partial k_\alpha^2}. \quad (\text{B.11})$$

In conclusion, we can rewrite  $\epsilon_1^{\text{intra}}(\hat{\mathbf{q}}, \omega)$  in the same form as in the Drude model

$$\epsilon_1^{\text{intra}}(\hat{\mathbf{q}}, \omega) = -\frac{\omega_D^2(\hat{\mathbf{q}})}{\omega^2}, \quad (\text{B.12})$$

by defining the IPA Drude plasma frequency as

$$\omega_D^2(\hat{\mathbf{q}}) = \frac{4\pi}{V} \sum_{\mathbf{k}} \sum_n f_{n\mathbf{k}} \frac{\partial^2 E_{n\mathbf{k}}}{\partial k_\alpha^2}. \quad (\text{B.13})$$

## C Optical data

Here we report the IPA optical properties (computed with the computational approach described in Chapter 5) of the 45 elemental metals studied in Chapter 6 and of the seven coloured intermetallic compounds studied in Section 7.3.1.

We show the full dielectric function  $\varepsilon(\omega) = \varepsilon_1(\omega) + i\varepsilon_2(\omega)$  (real and imaginary parts), the reflectivity  $R(\omega)$ , the interband optical absorption  $\varepsilon_2^{\text{inter}}(\omega)$ , the EELS spectrum  $-\Im[\varepsilon^{-1}(\omega)]$ , and the reflectivity zoomed inside the visible range together with the corresponding CIELAB colour coordinates and colour appearance.

### C.1 Elemental metals

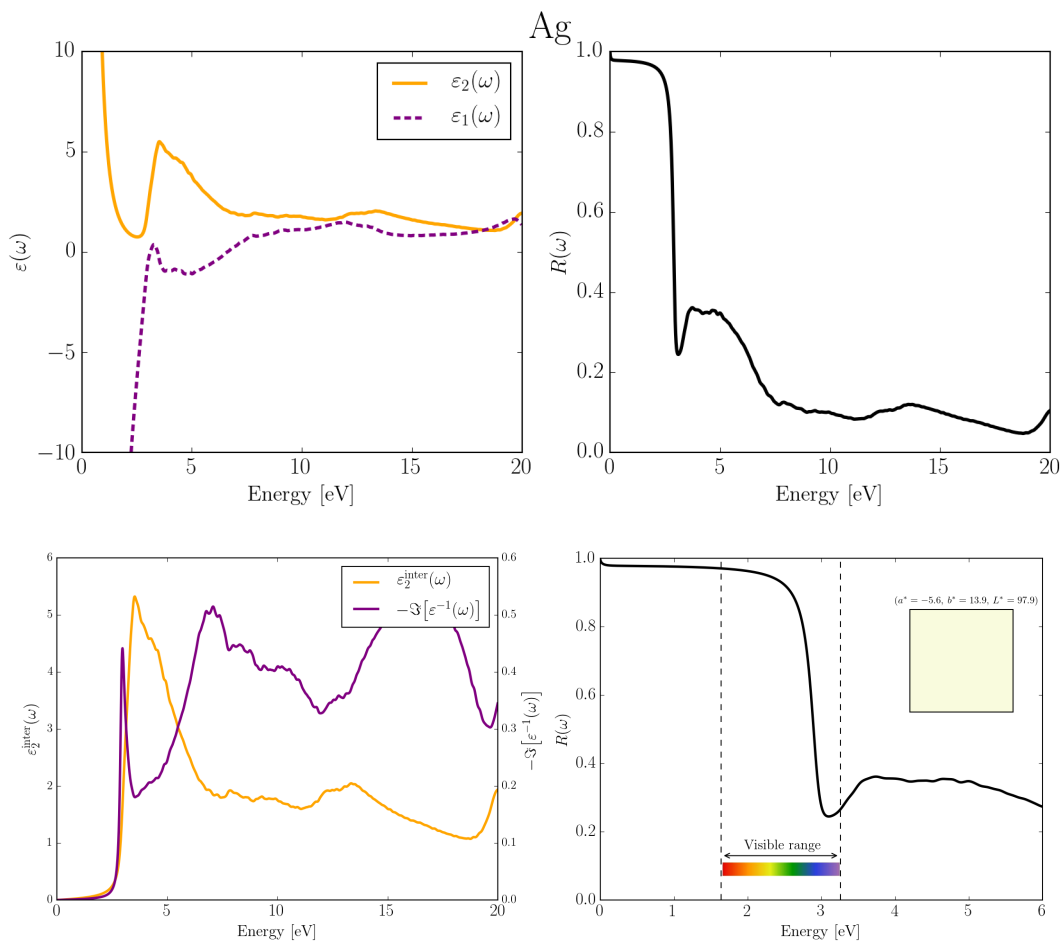


Figure C.1 – Optical properties of Ag simulated at the IPA level starting from the DFT-PBE electronic structure.

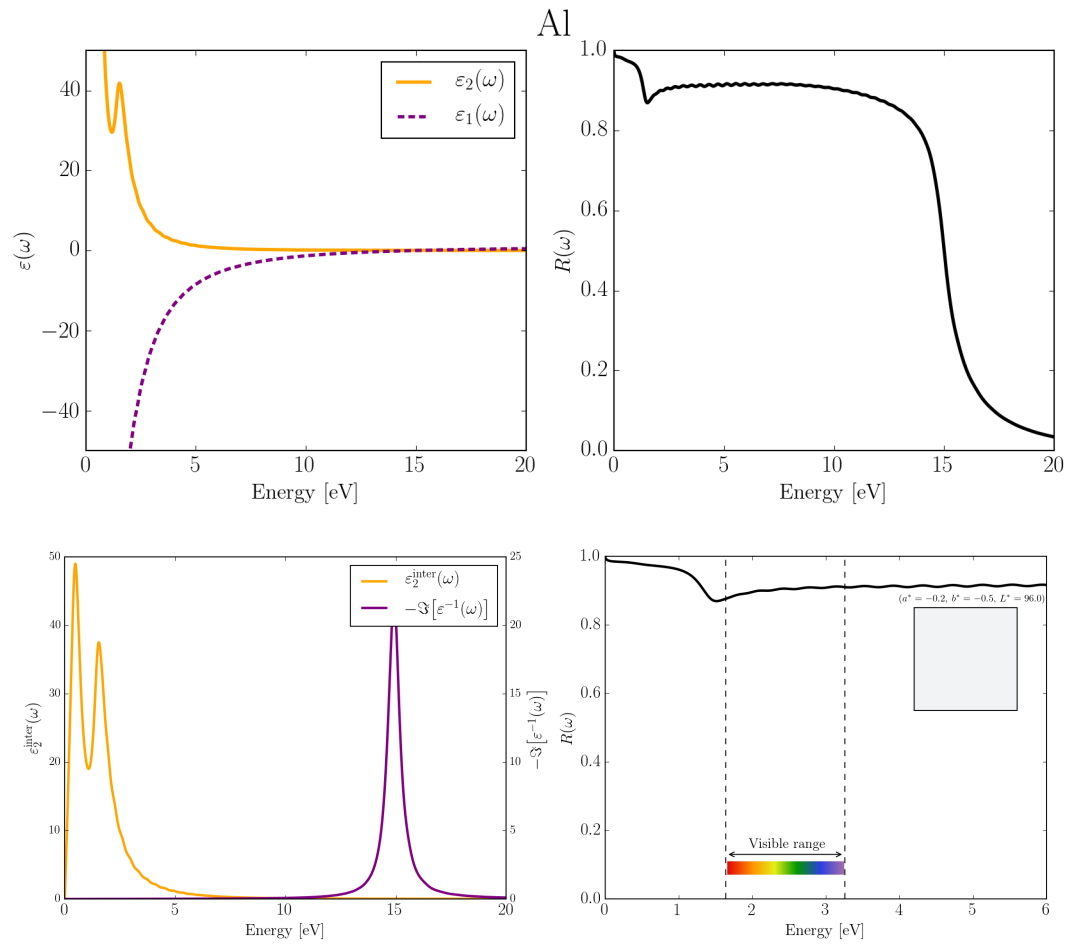


Figure C.2 – Optical properties of Al simulated at the IPA level starting from the DFT-PBE electronic structure.

Appendix C. Optical data

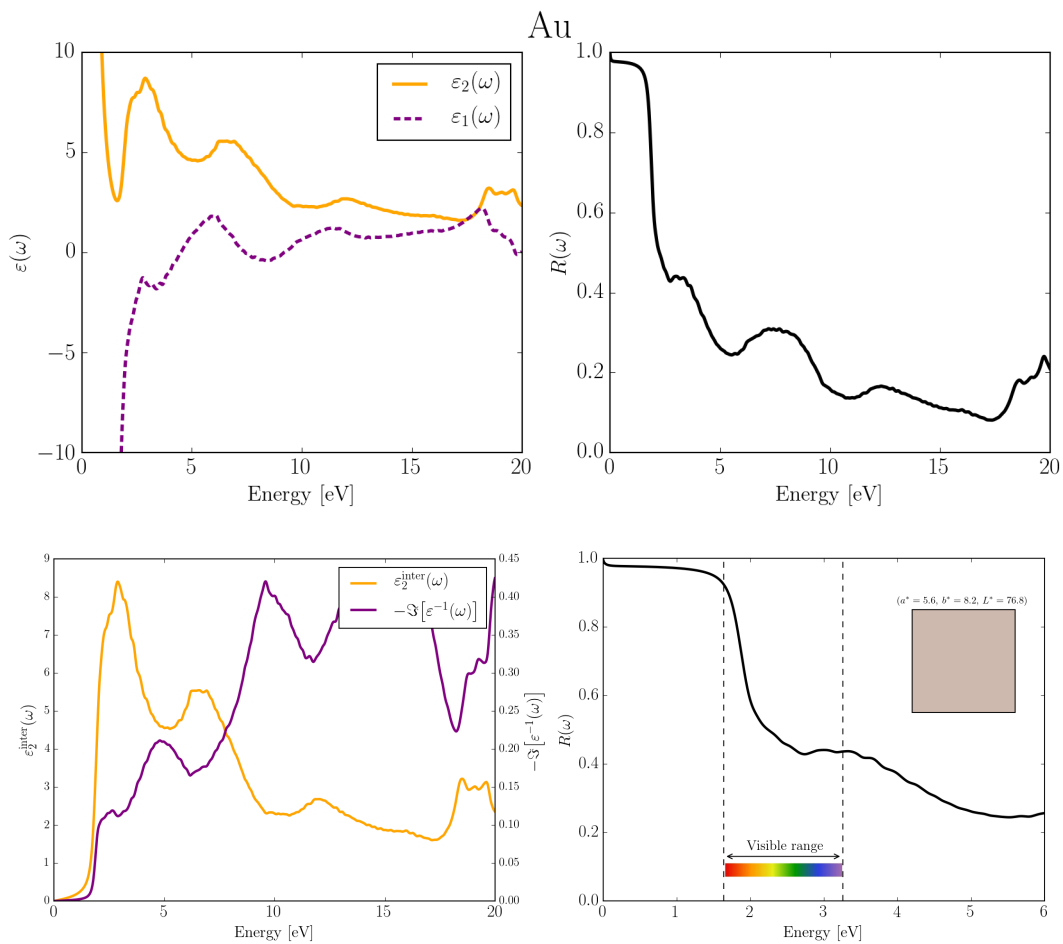


Figure C.3 – Optical properties of Au simulated at the IPA level starting from the DFT-PBE electronic structure.

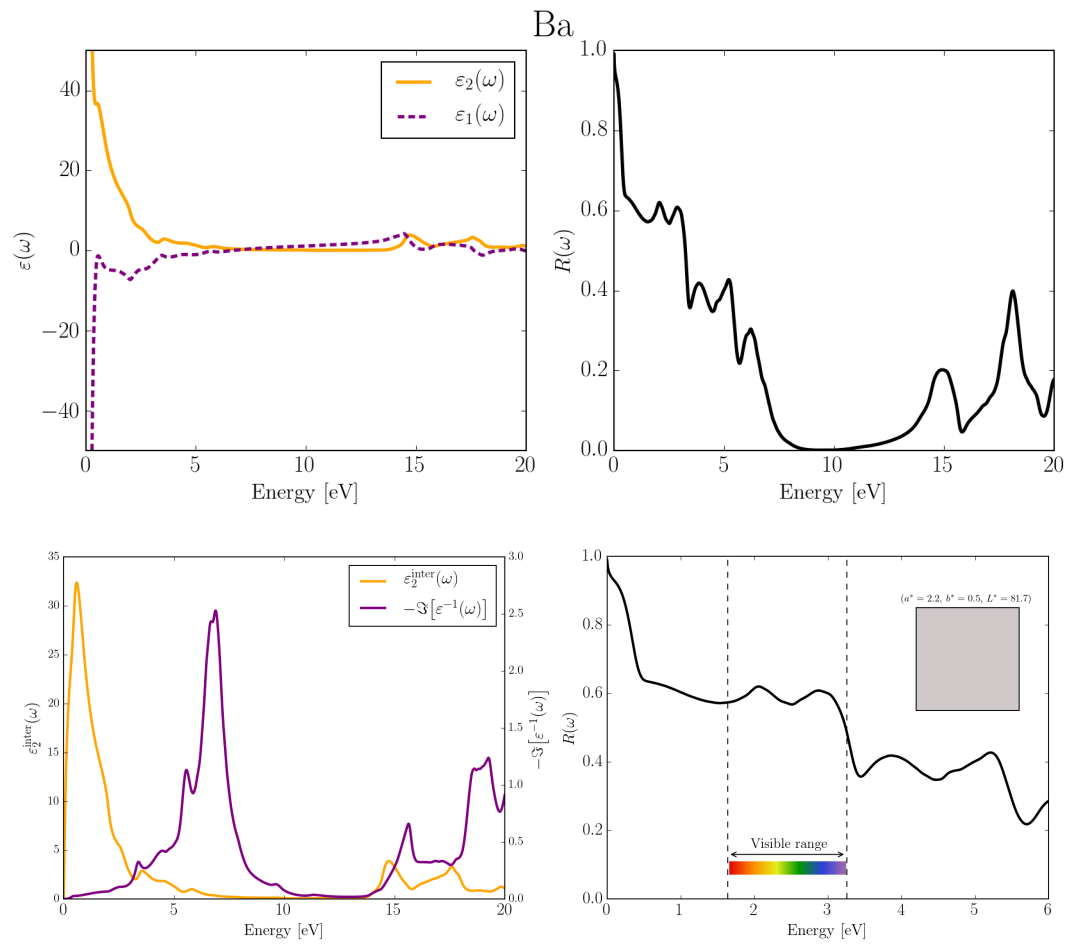


Figure C.4 – Optical properties of Ba simulated at the IPA level starting from the DFT-PBE electronic structure.

Appendix C. Optical data

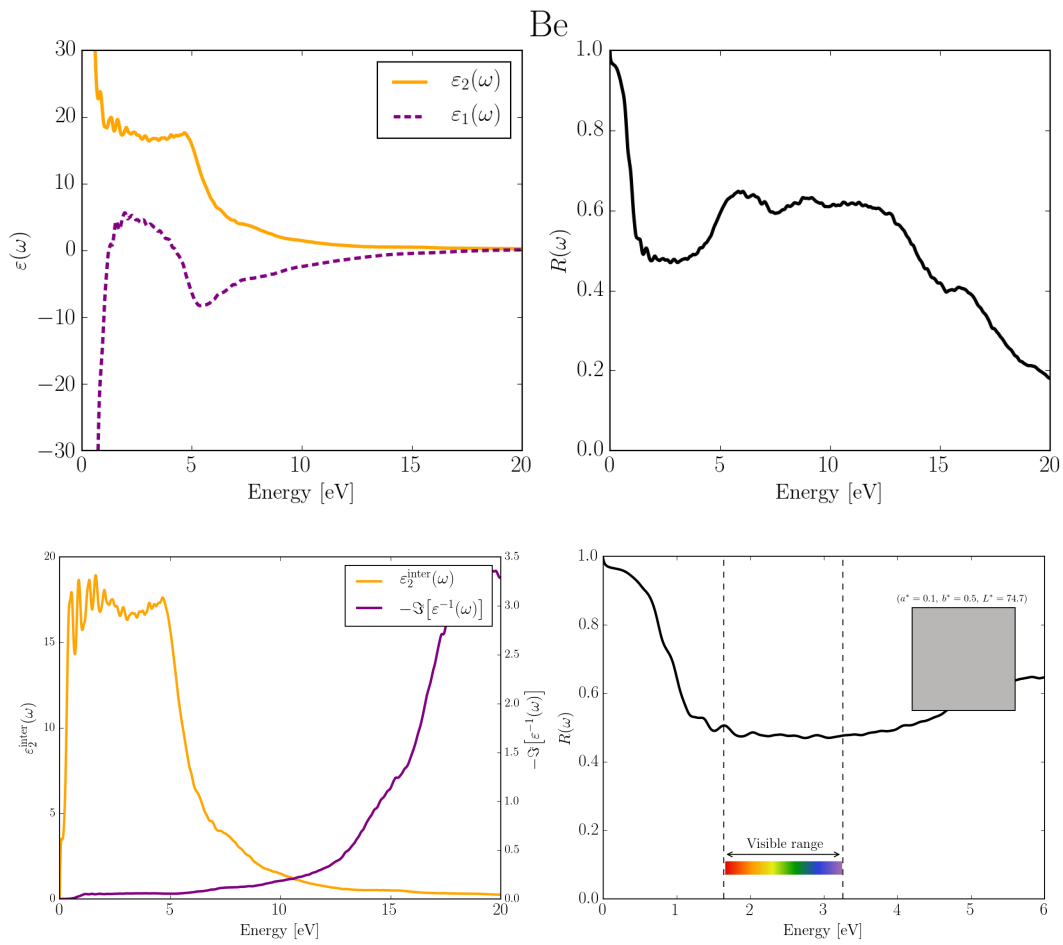


Figure C.5 – Optical properties of Be simulated at the IPA level starting from the DFT-PBE electronic structure.



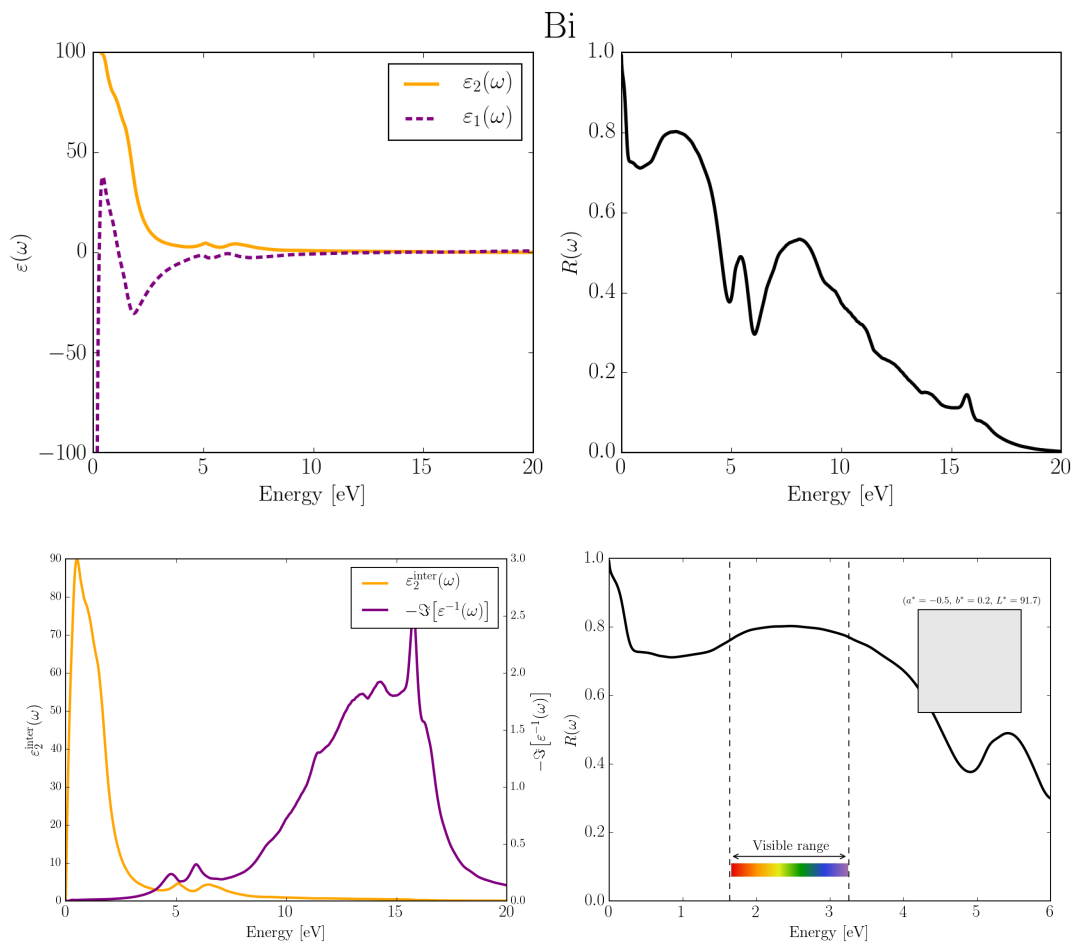


Figure C.6 – Optical properties of Bi simulated at the IPA level starting from the DFT-PBE electronic structure.

Appendix C. Optical data

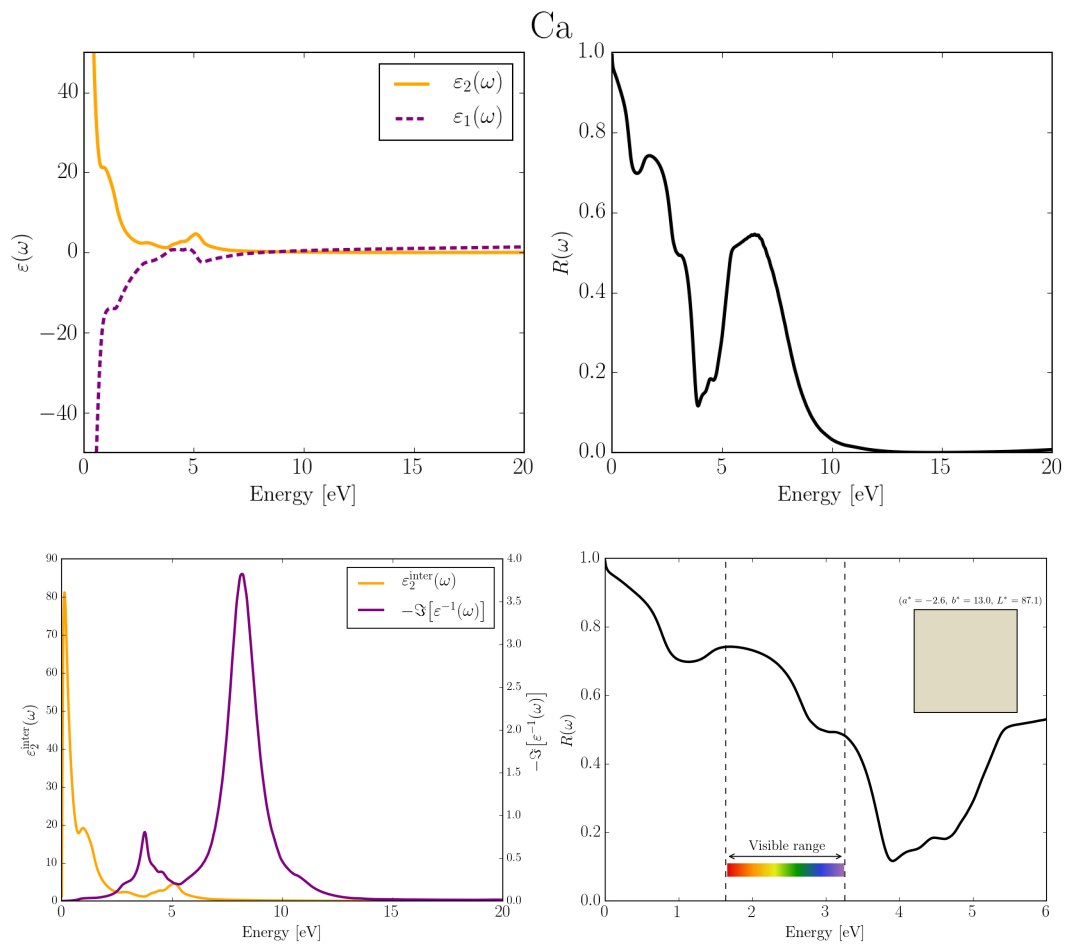


Figure C.7 – Optical properties of Ca simulated at the IPA level starting from the DFT-PBE electronic structure.

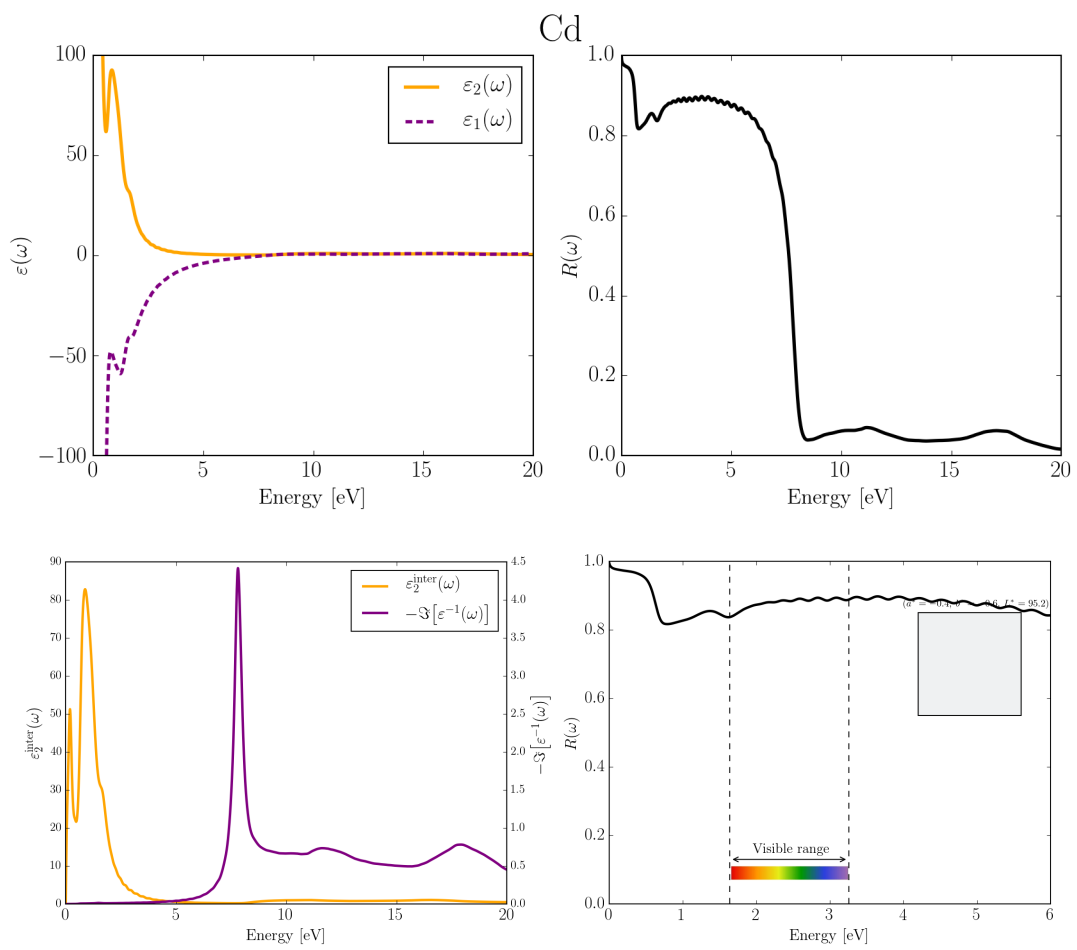


Figure C.8 – Optical properties of Cd simulated at the IPA level starting from the DFT-PBE electronic structure.

## Appendix C. Optical data

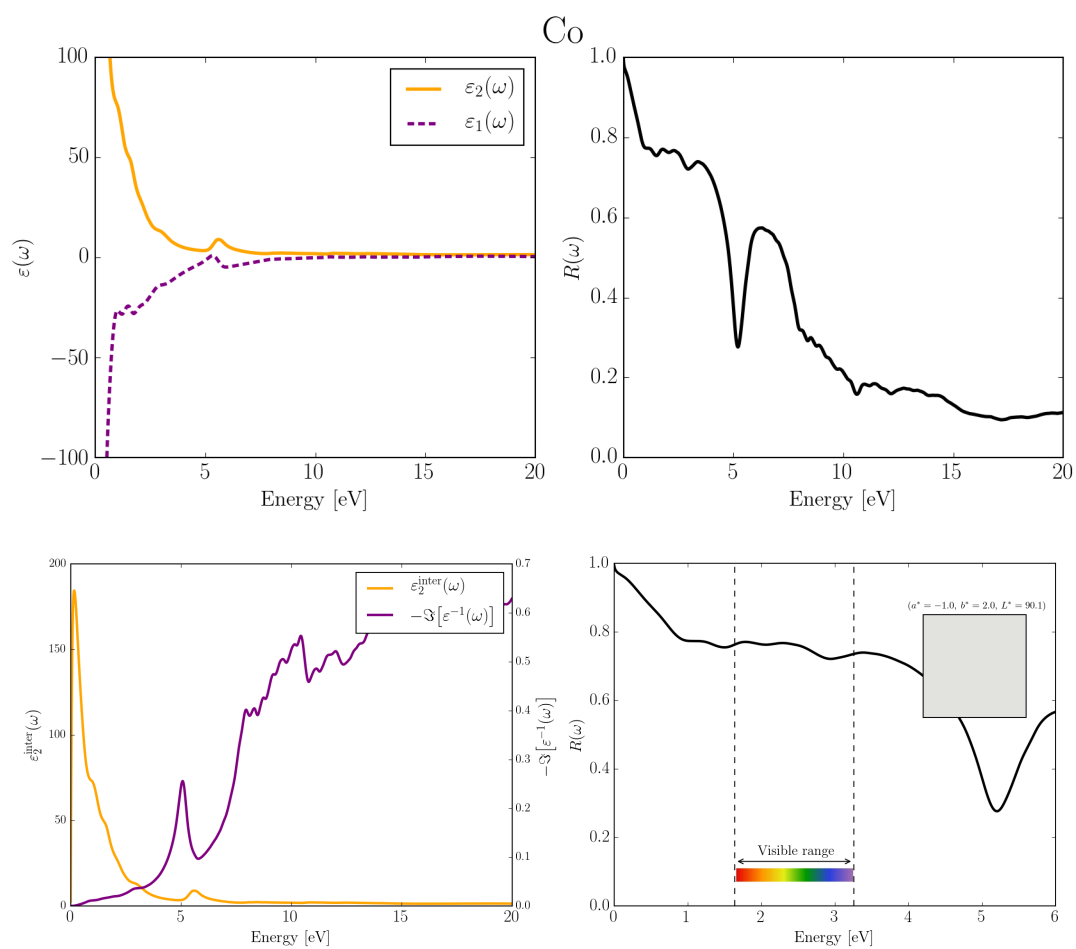


Figure C.9 – Optical properties of Co simulated at the IPA level starting from the DFT-PBE electronic structure.

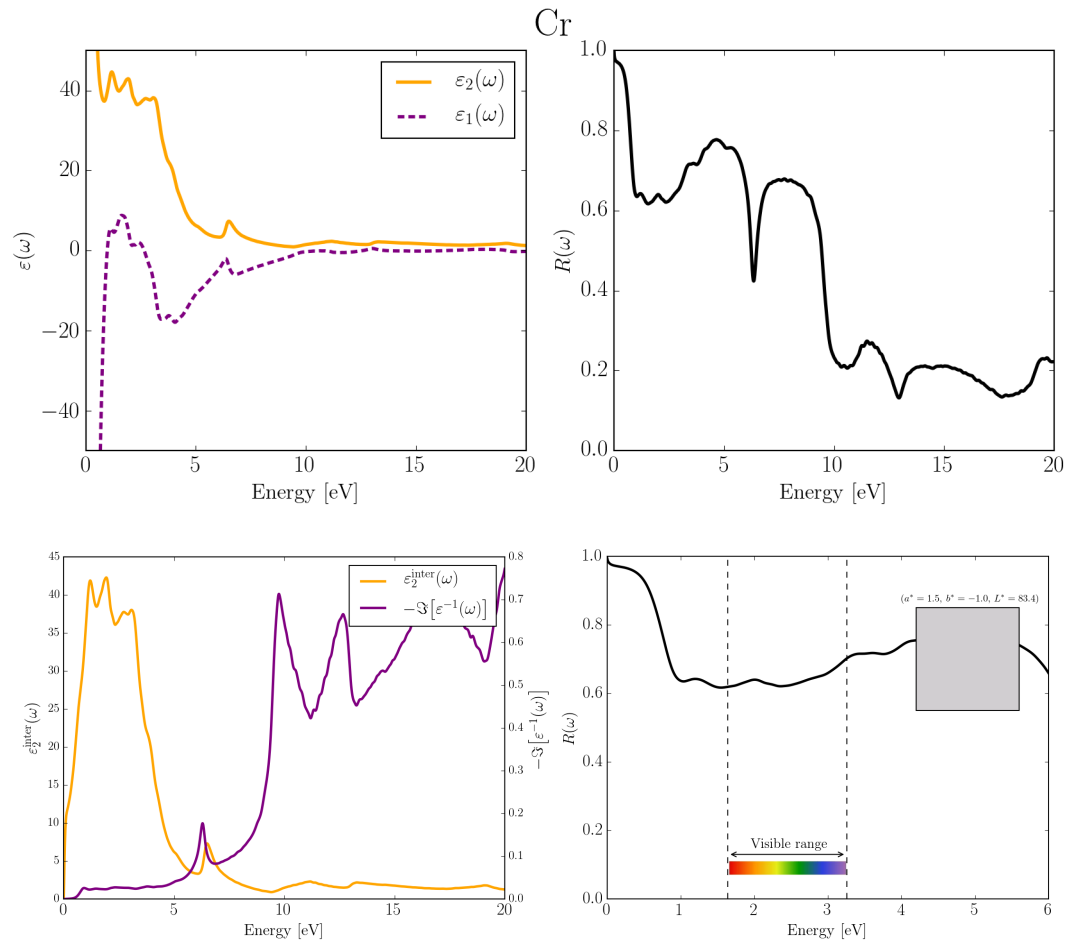


Figure C.10 – Optical properties of Cr simulated at the IPA level starting from the DFT-PBE electronic structure.

## Appendix C. Optical data

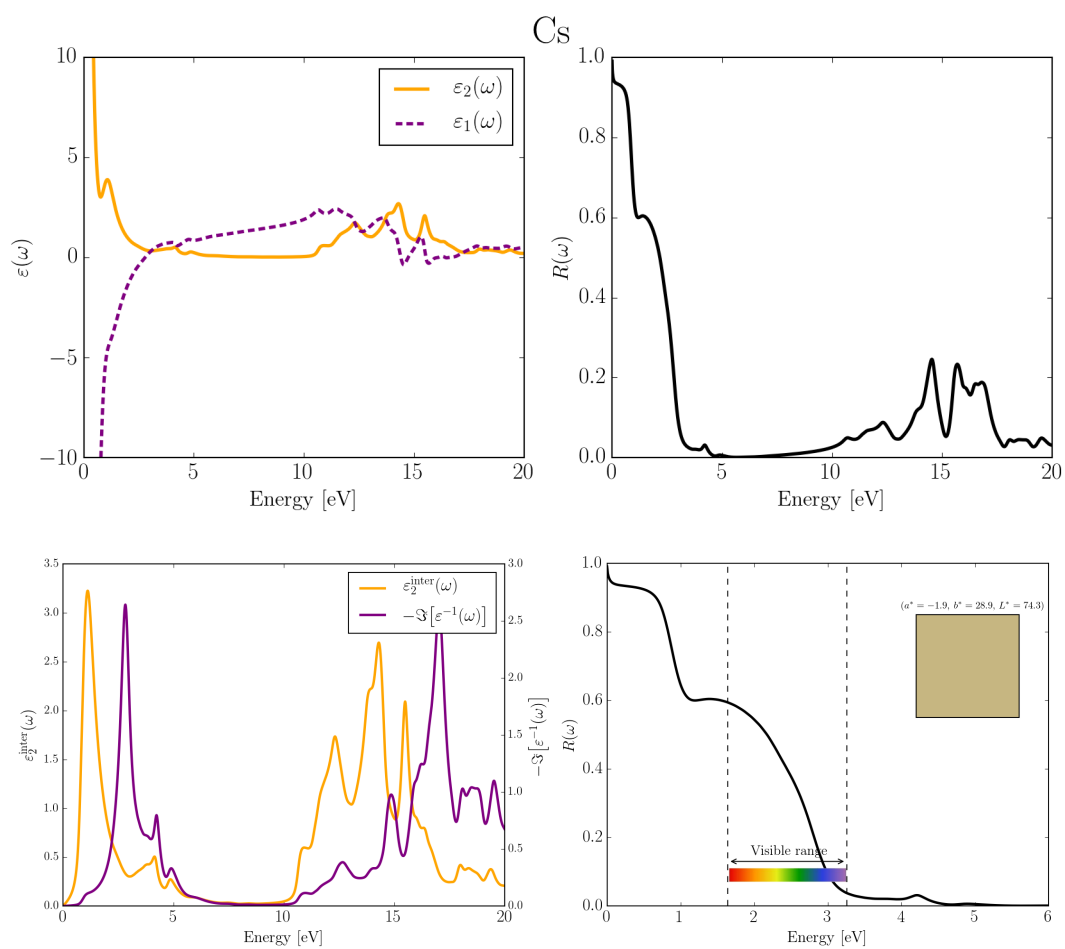


Figure C.11 – Optical properties of Cs simulated at the IPA level starting from the DFT-PBE electronic structure.

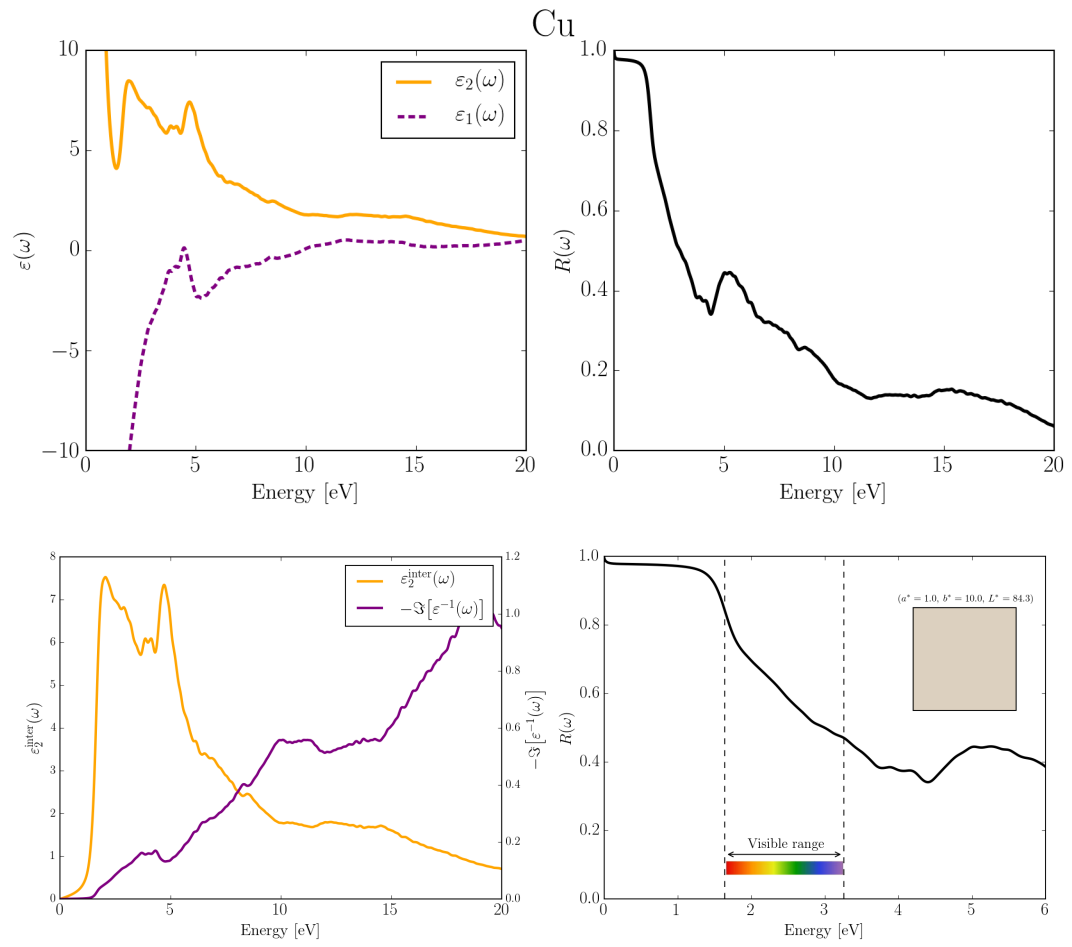


Figure C.12 – Optical properties of Cu simulated at the IPA level starting from the DFT-PBE electronic structure.

Appendix C. Optical data

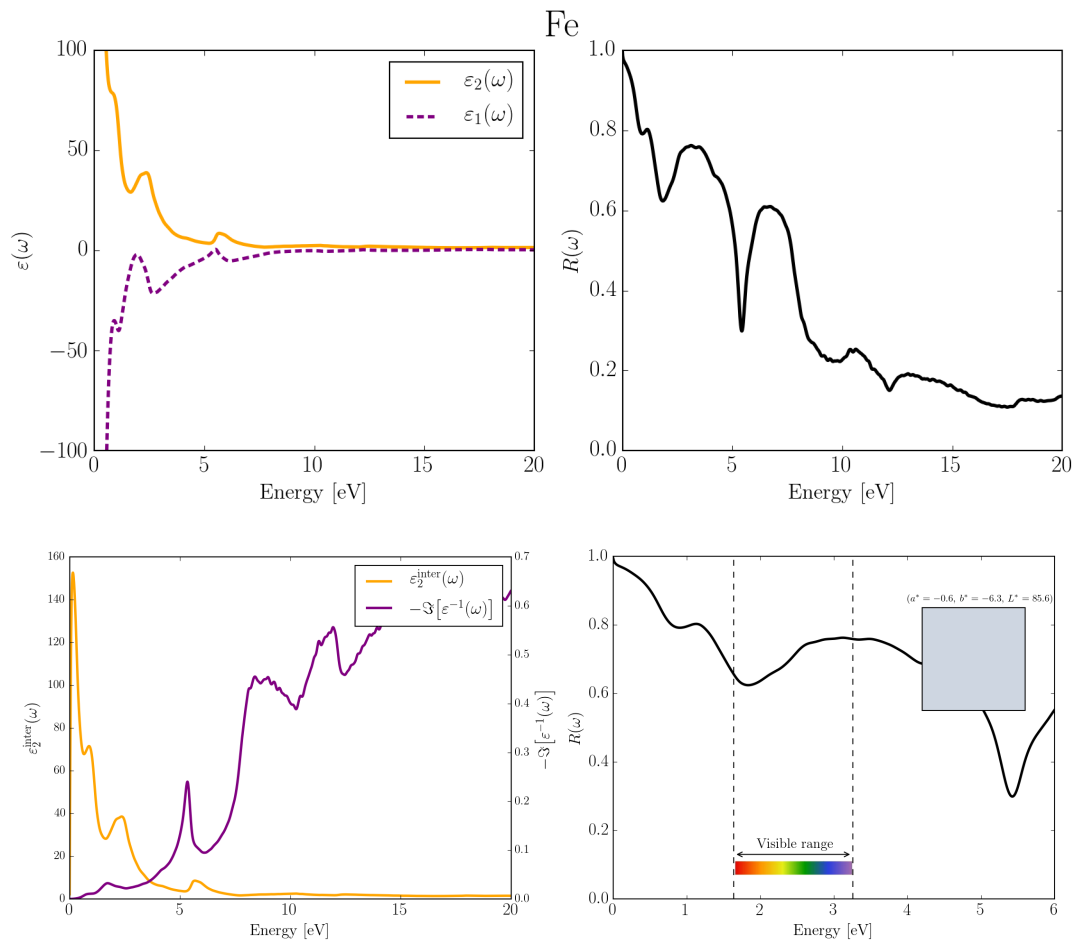


Figure C.13 – Optical properties of Fe simulated at the IPA level starting from the DFT-PBE electronic structure.



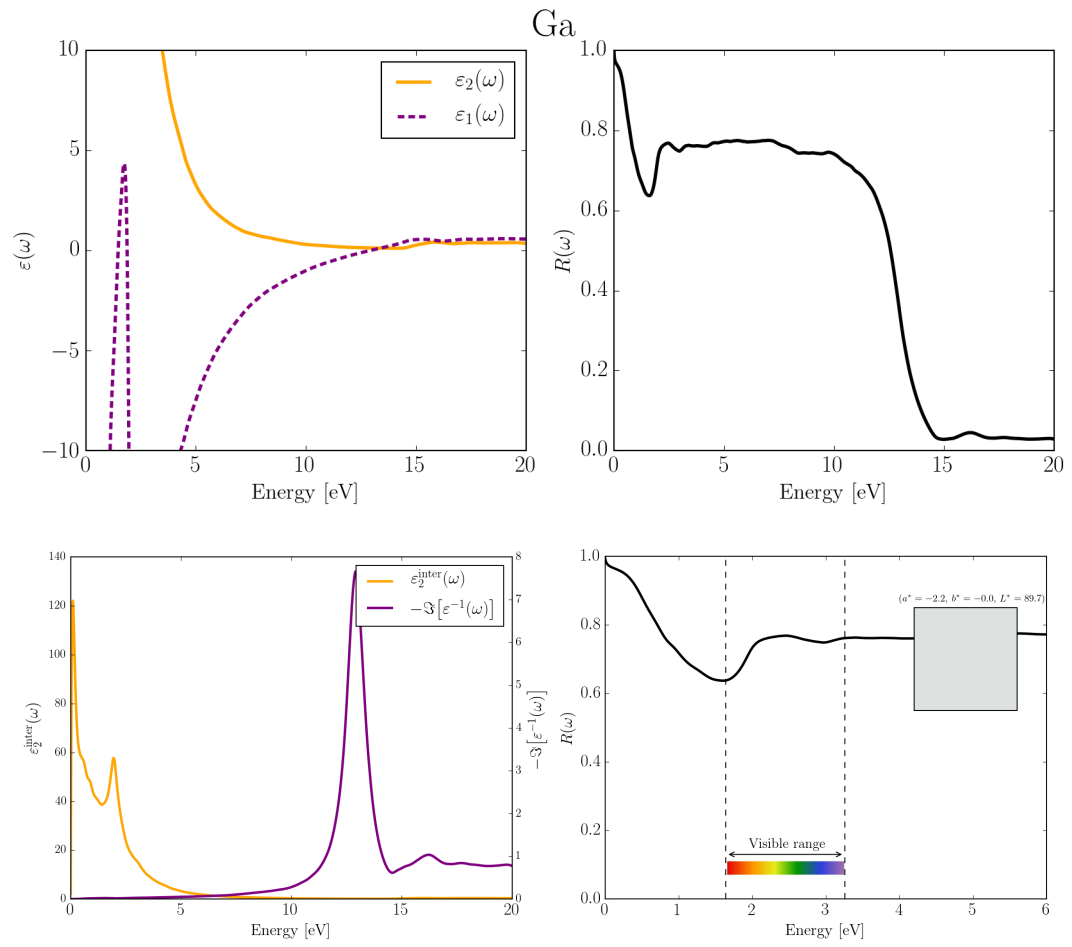


Figure C.14 – Optical properties of Ga simulated at the IPA level starting from the DFT-PBE electronic structure.

Appendix C. Optical data

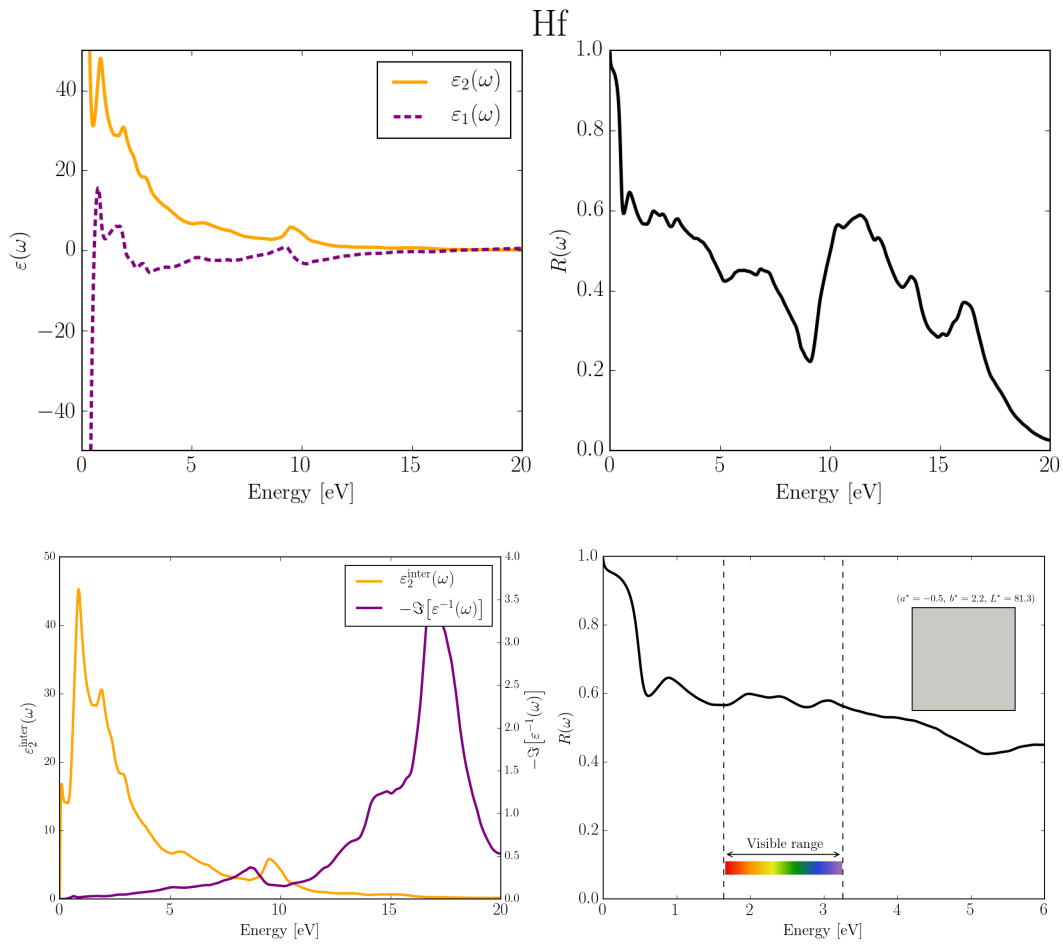


Figure C.15 – Optical properties of Hf simulated at the IPA level starting from the DFT-PBE electronic structure.

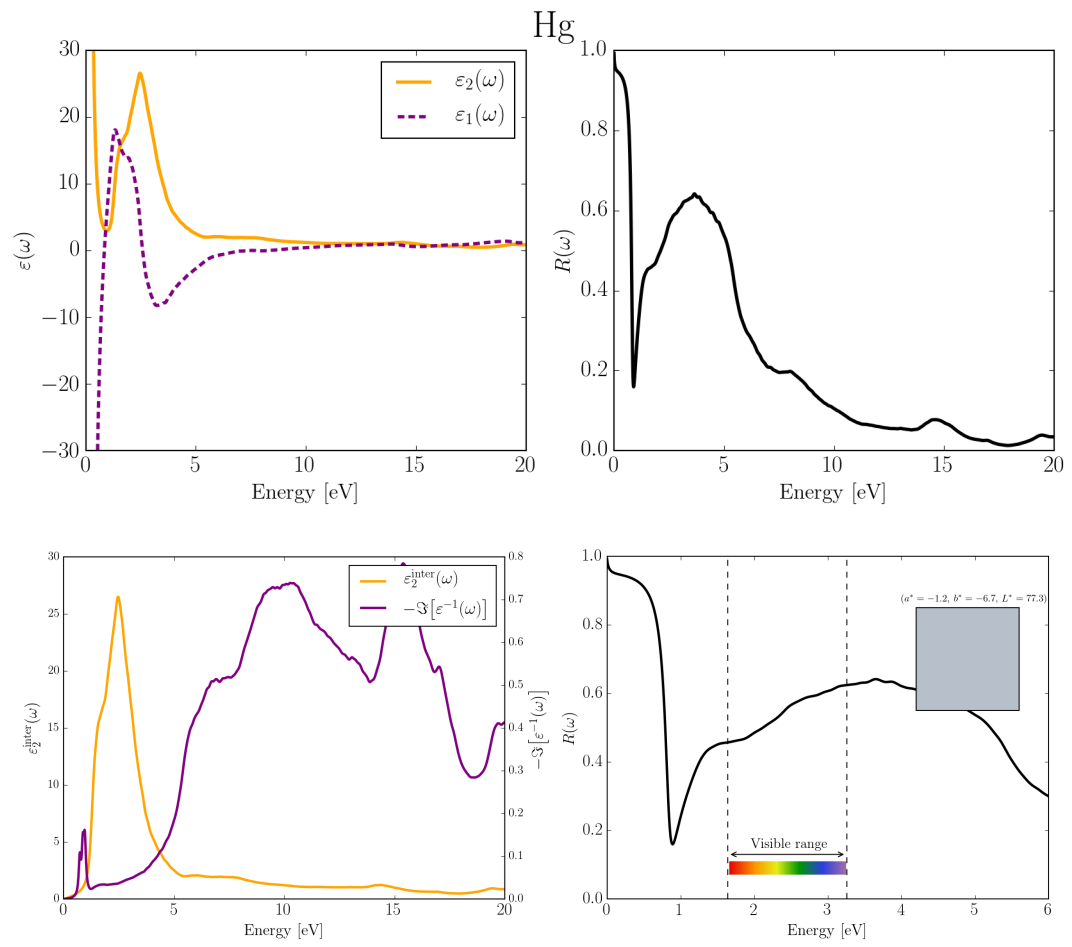


Figure C.16 – Optical properties of Hg simulated at the IPA level starting from the DFT-PBE electronic structure.

Appendix C. Optical data

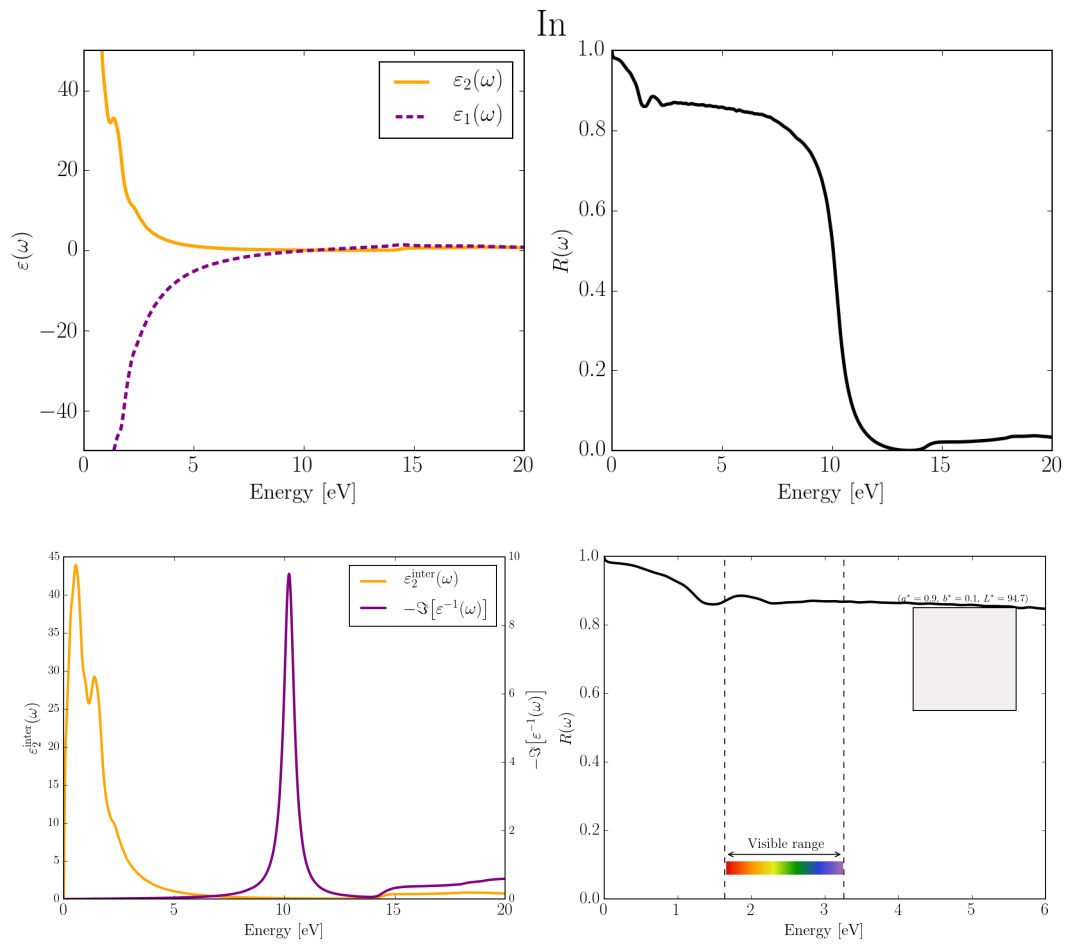


Figure C.17 – Optical properties of In simulated at the IPA level starting from the DFT-PBE electronic structure.

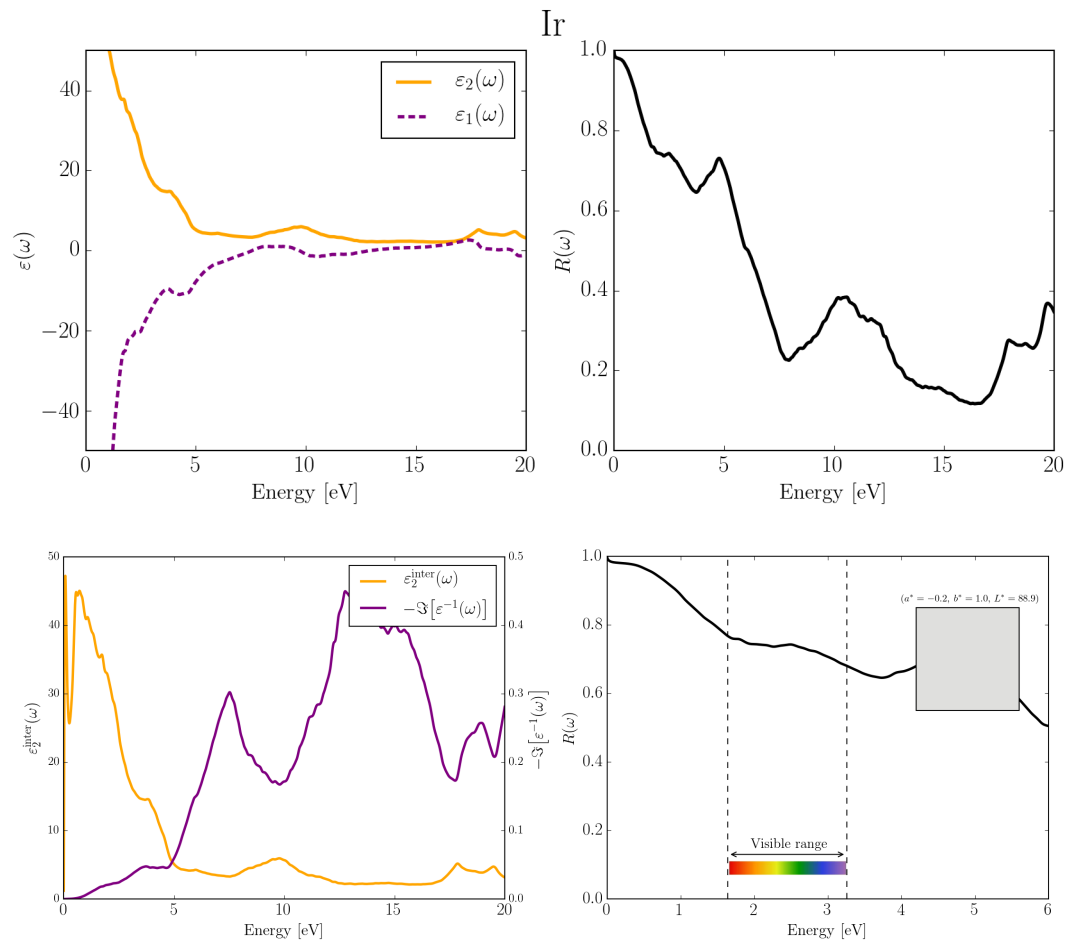


Figure C.18 – Optical properties of Ir simulated at the IPA level starting from the DFT-PBE electronic structure.

Appendix C. Optical data

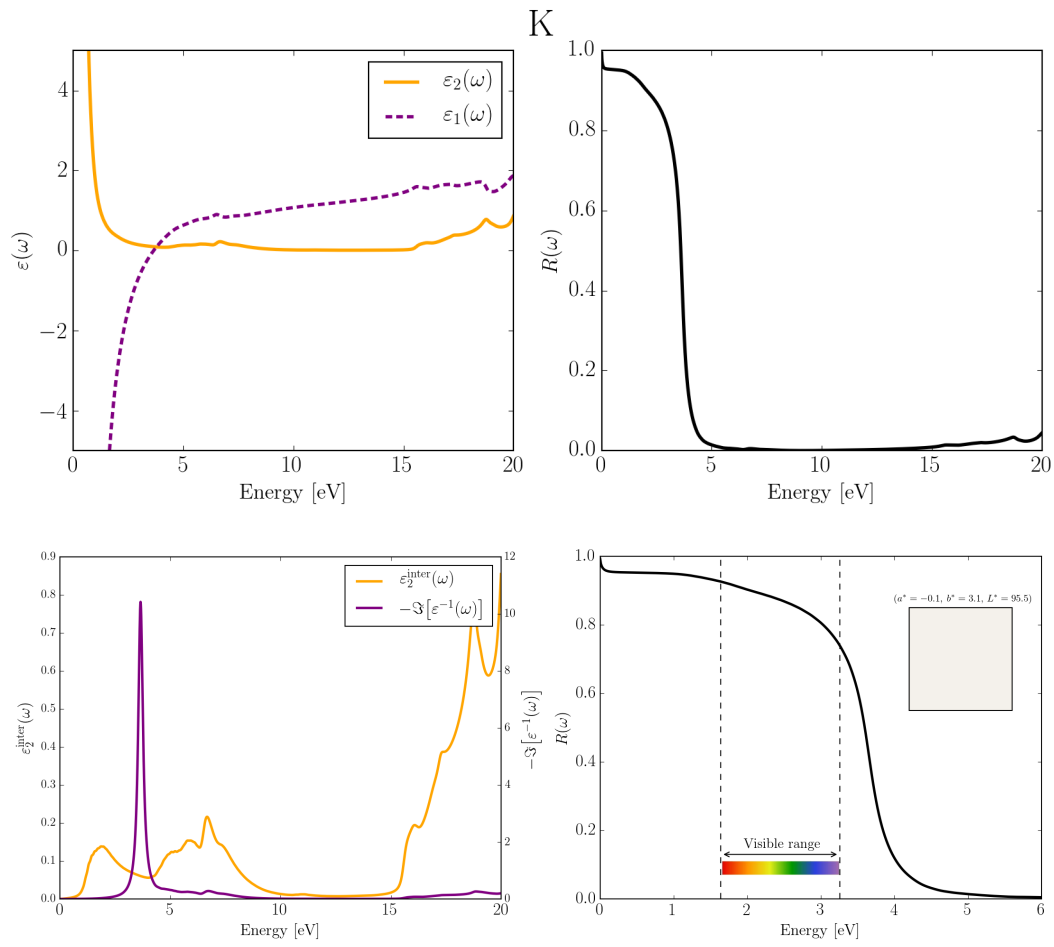


Figure C.19 – Optical properties of K simulated at the IPA level starting from the DFT-PBE electronic structure.

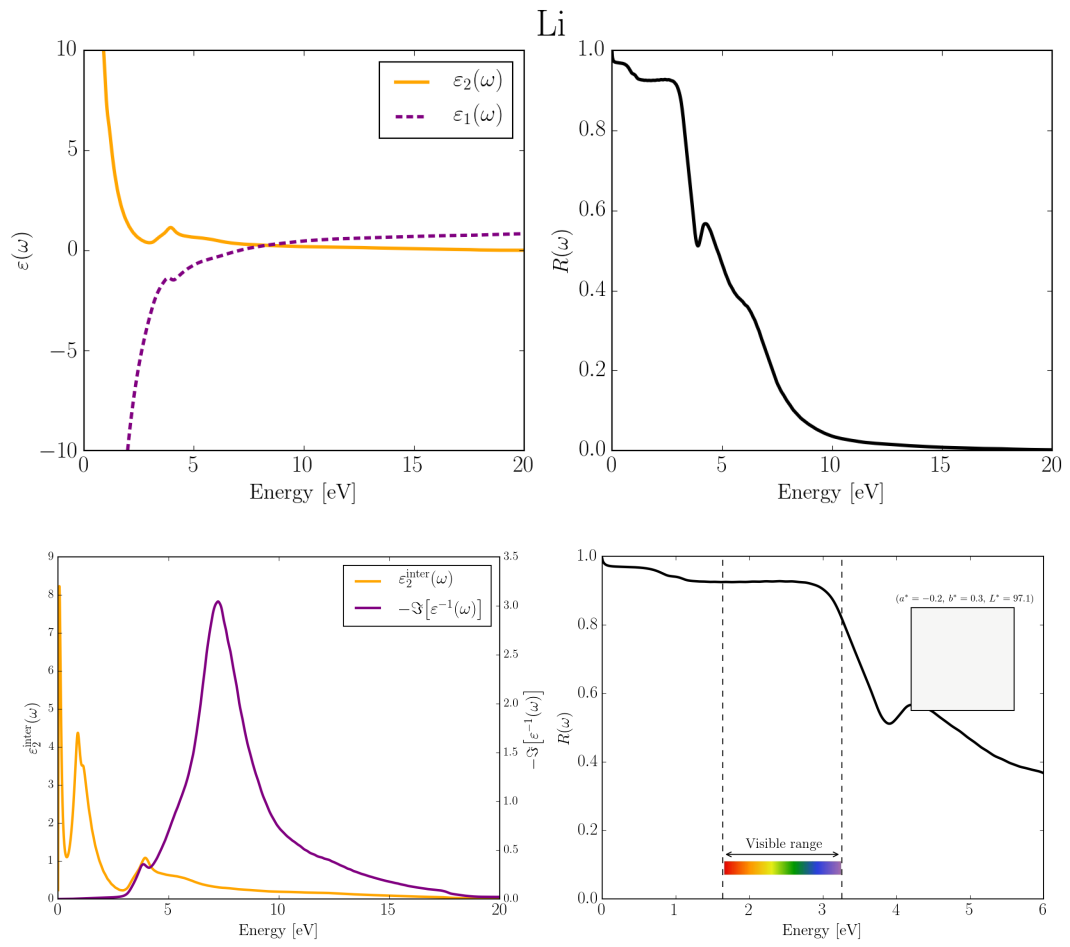


Figure C.20 – Optical properties of Li simulated at the IPA level starting from the DFT-PBE electronic structure.

Appendix C. Optical data

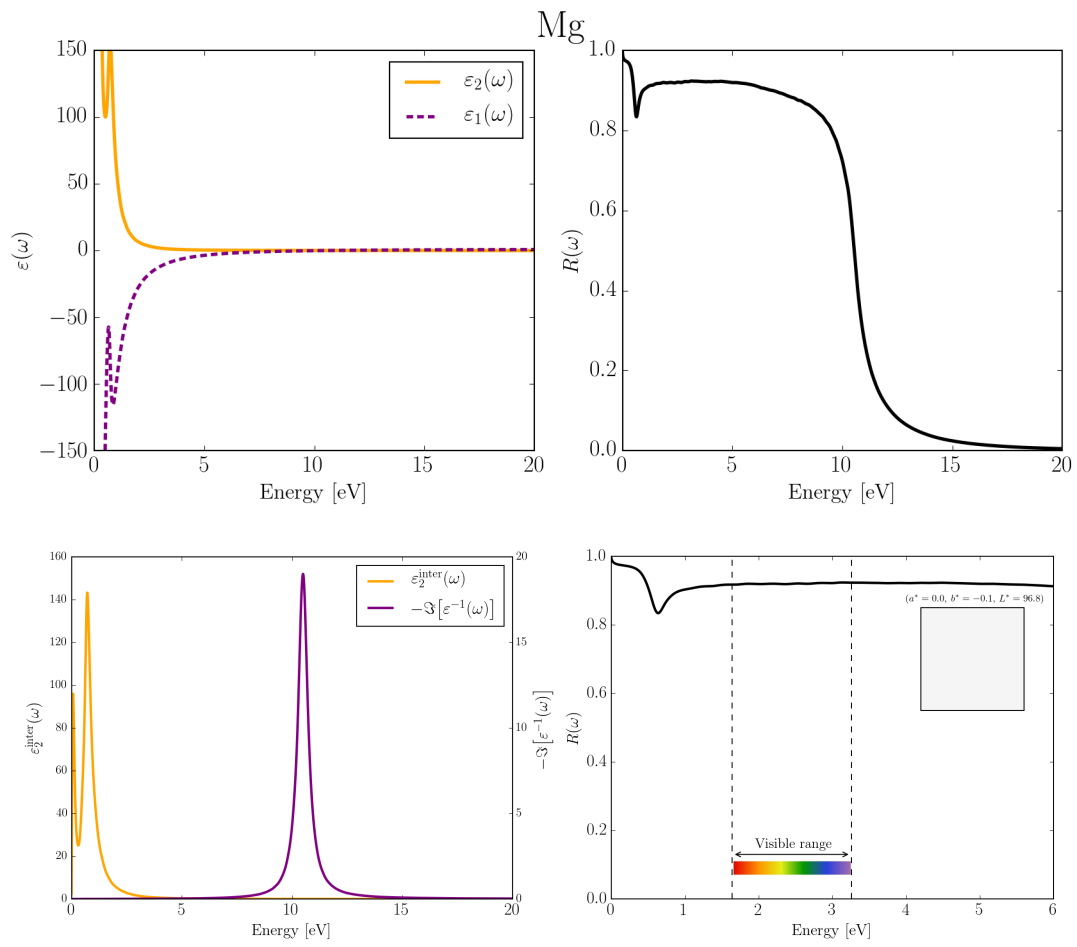


Figure C.21 – Optical properties of Mg simulated at the IPA level starting from the DFT-PBE electronic structure.



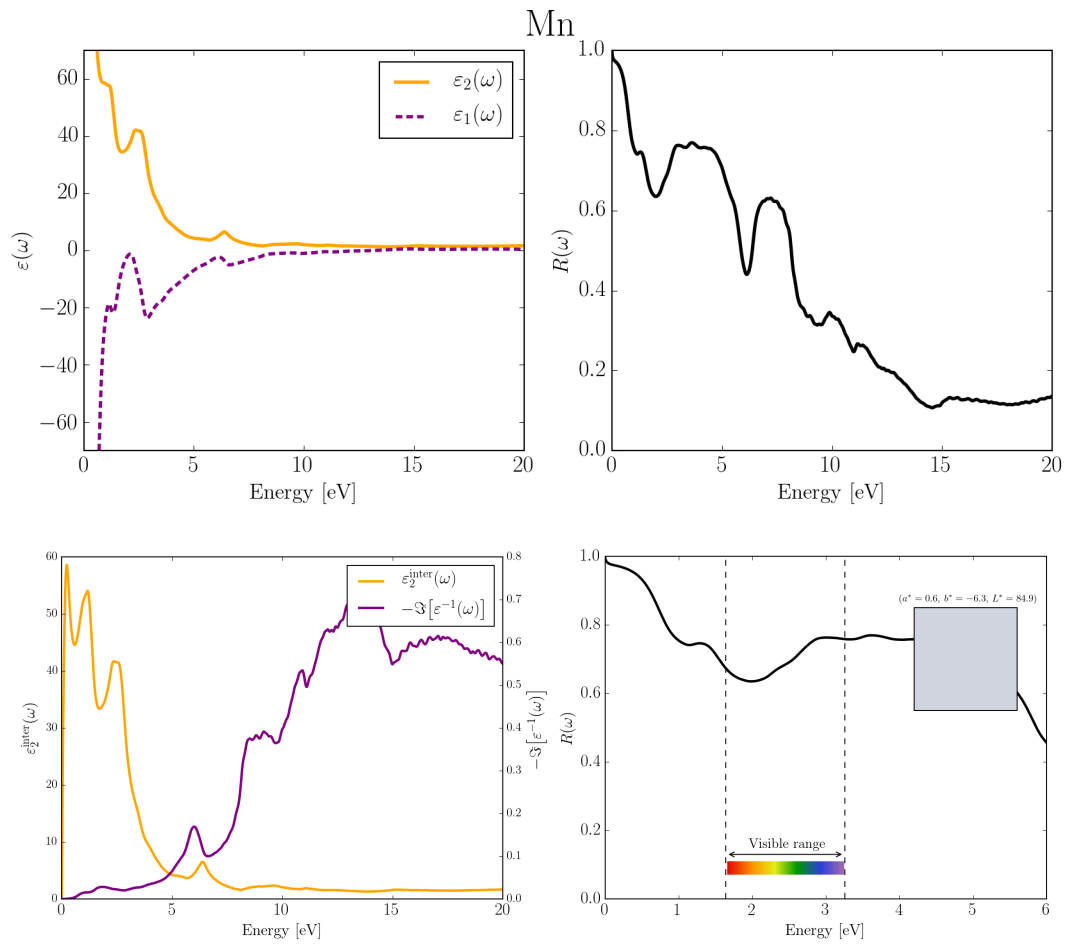


Figure C.22 – Optical properties of Mn simulated at the IPA level starting from the DFT-PBE electronic structure.

Appendix C. Optical data

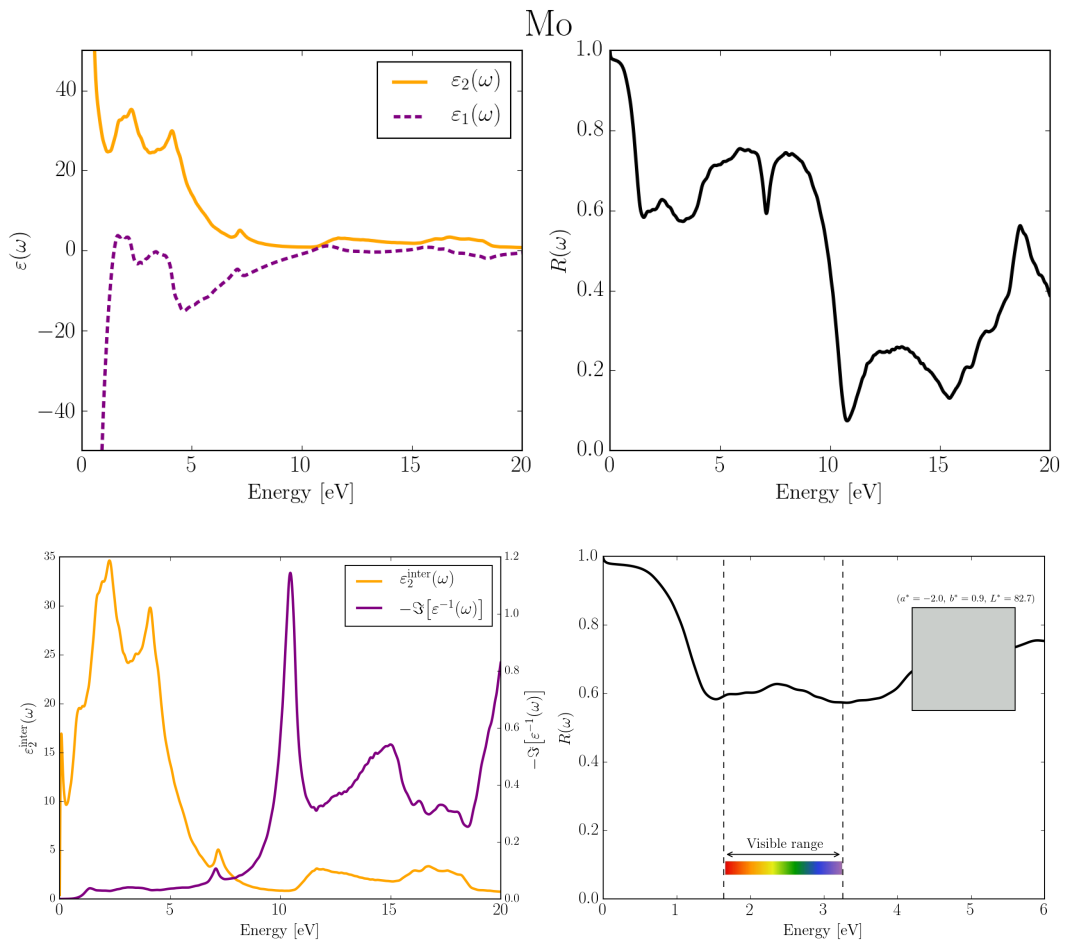


Figure C.23 – Optical properties of Mo simulated at the IPA level starting from the DFT-PBE electronic structure.

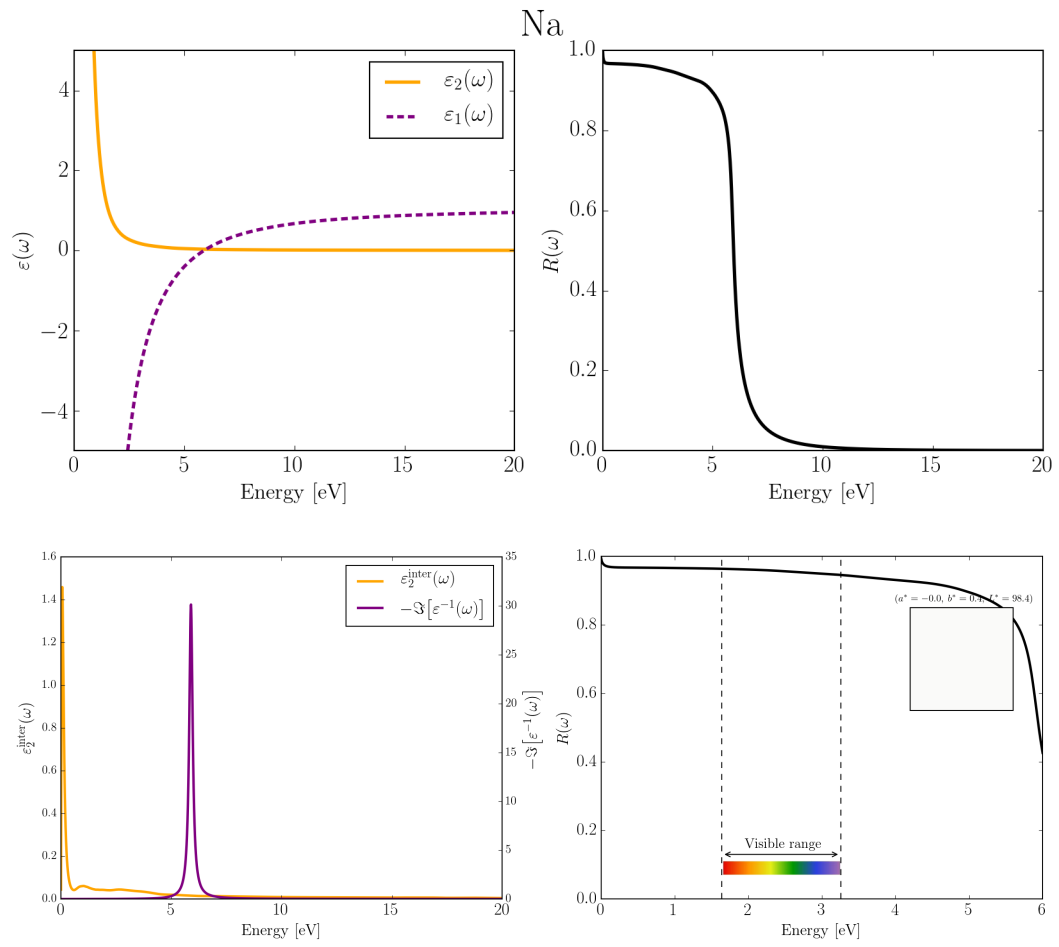


Figure C.24 – Optical properties of Na simulated at the IPA level starting from the DFT-PBE electronic structure.

Appendix C. Optical data

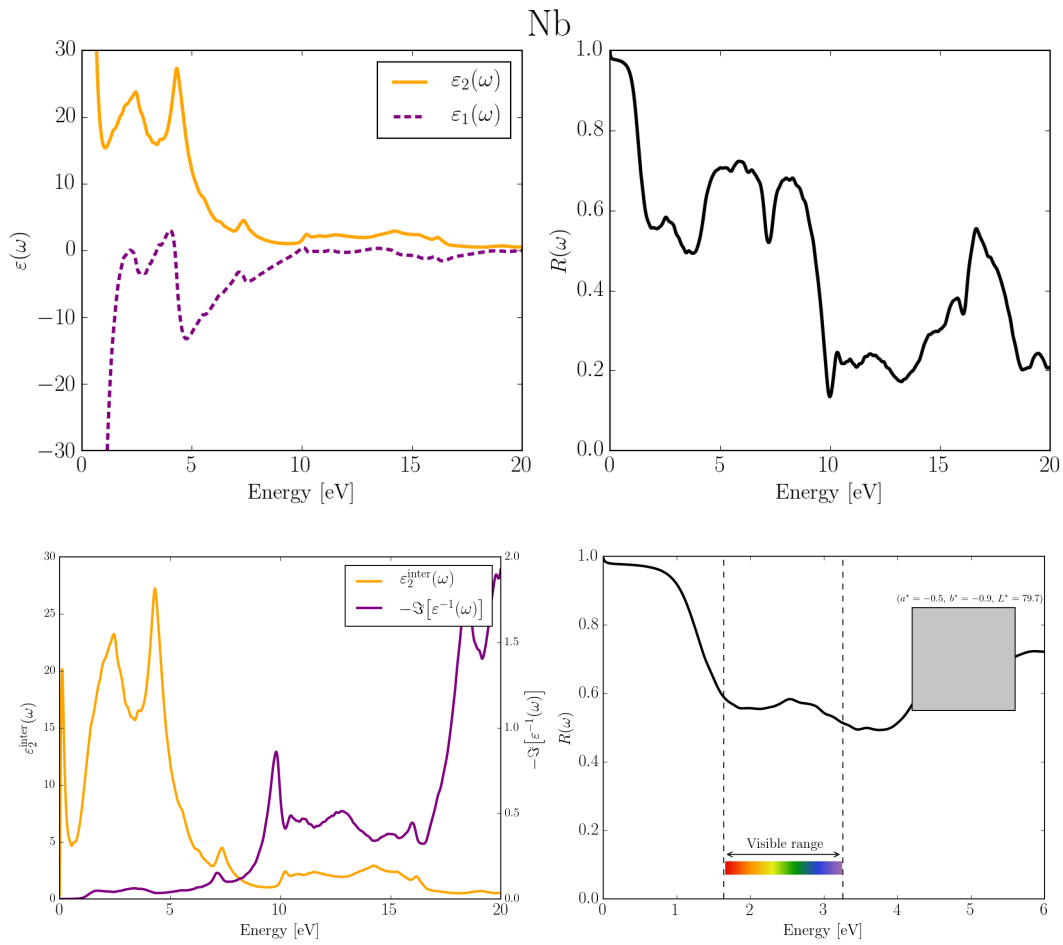


Figure C.25 – Optical properties of Nb simulated at the IPA level starting from the DFT-PBE electronic structure.

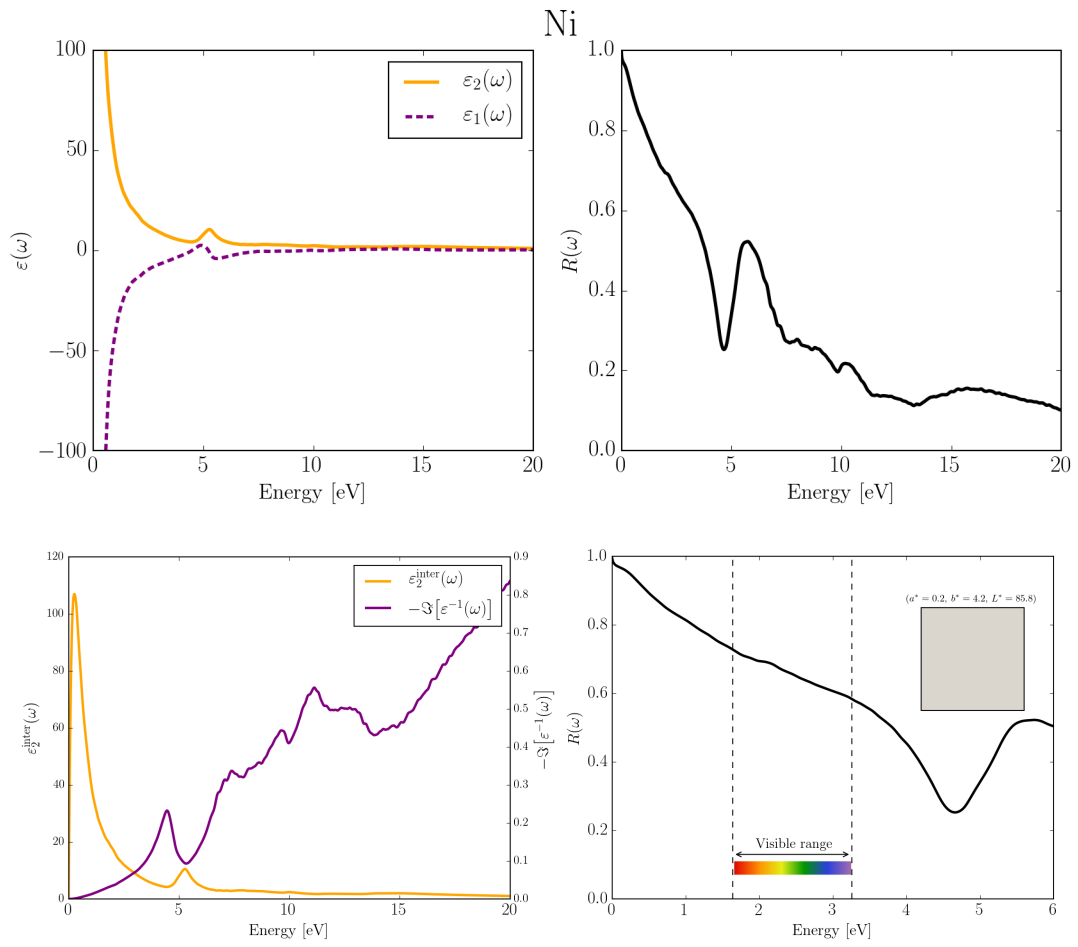


Figure C.26 – Optical properties of Ni simulated at the IPA level starting from the DFT-PBE electronic structure.

Appendix C. Optical data

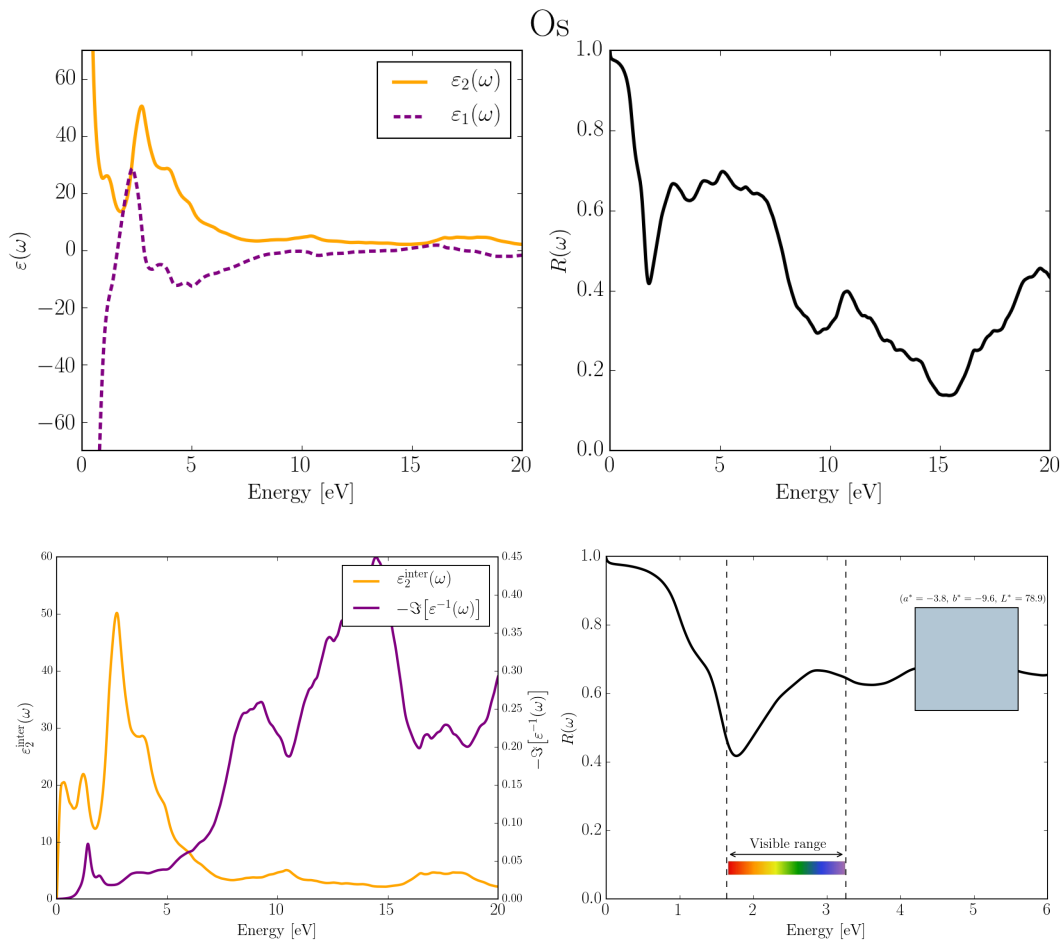


Figure C.27 – Optical properties of Os simulated at the IPA level starting from the DFT-PBE electronic structure.

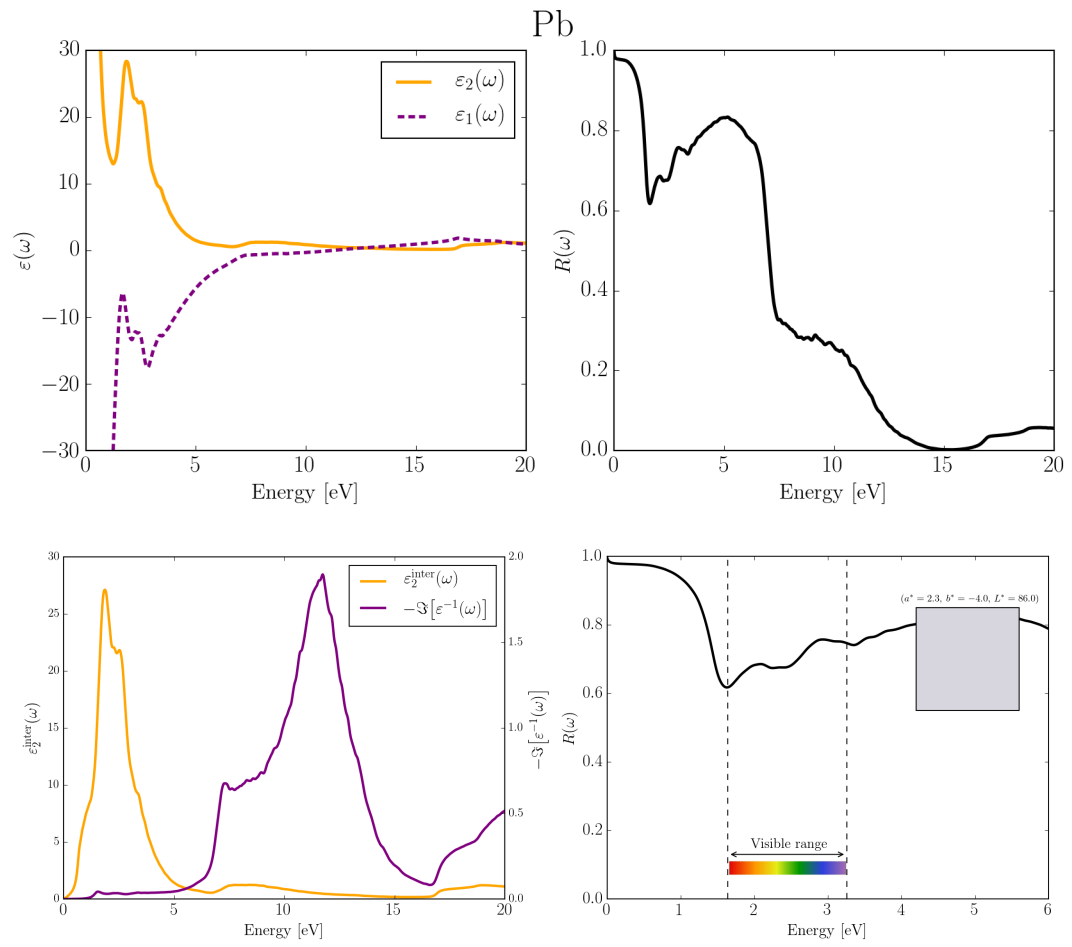


Figure C.28 – Optical properties of Pb simulated at the IPA level starting from the DFT-PBE electronic structure.

Appendix C. Optical data

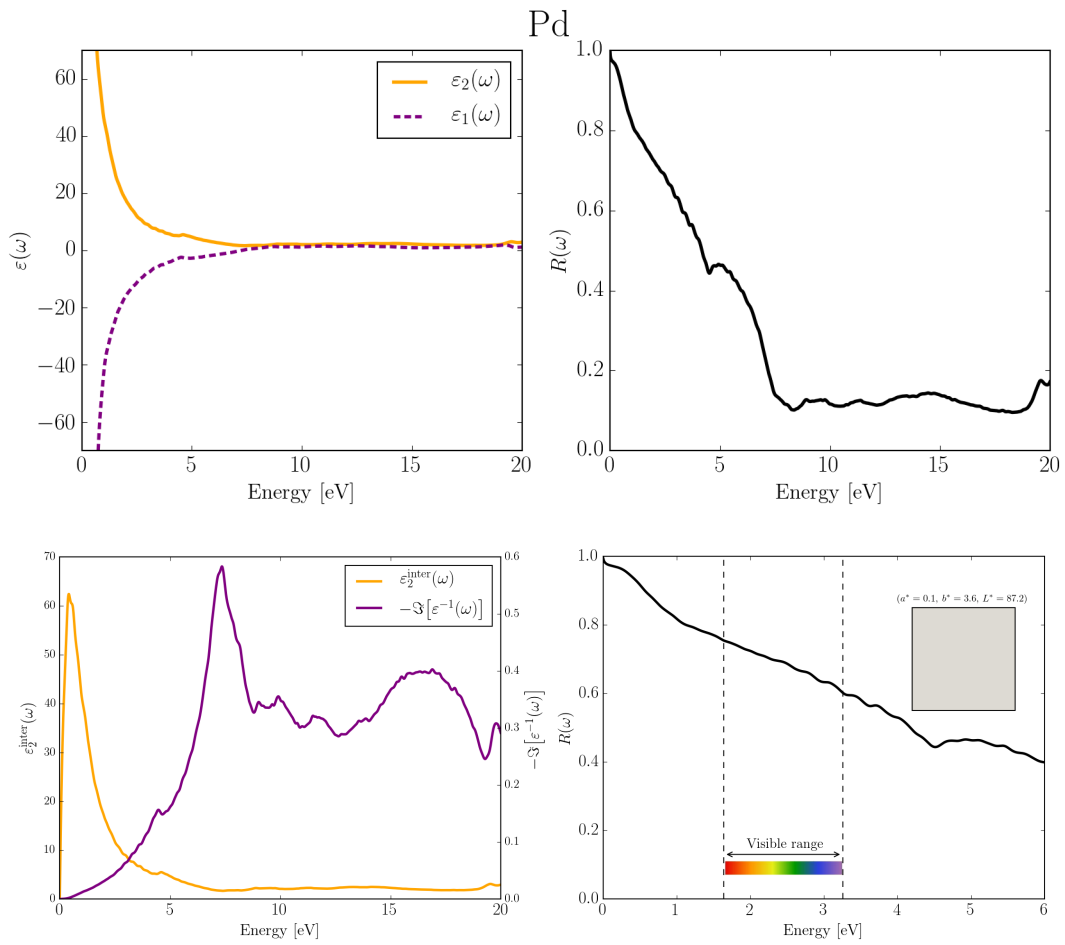


Figure C.29 – Optical properties of Pd simulated at the IPA level starting from the DFT-PBE electronic structure.



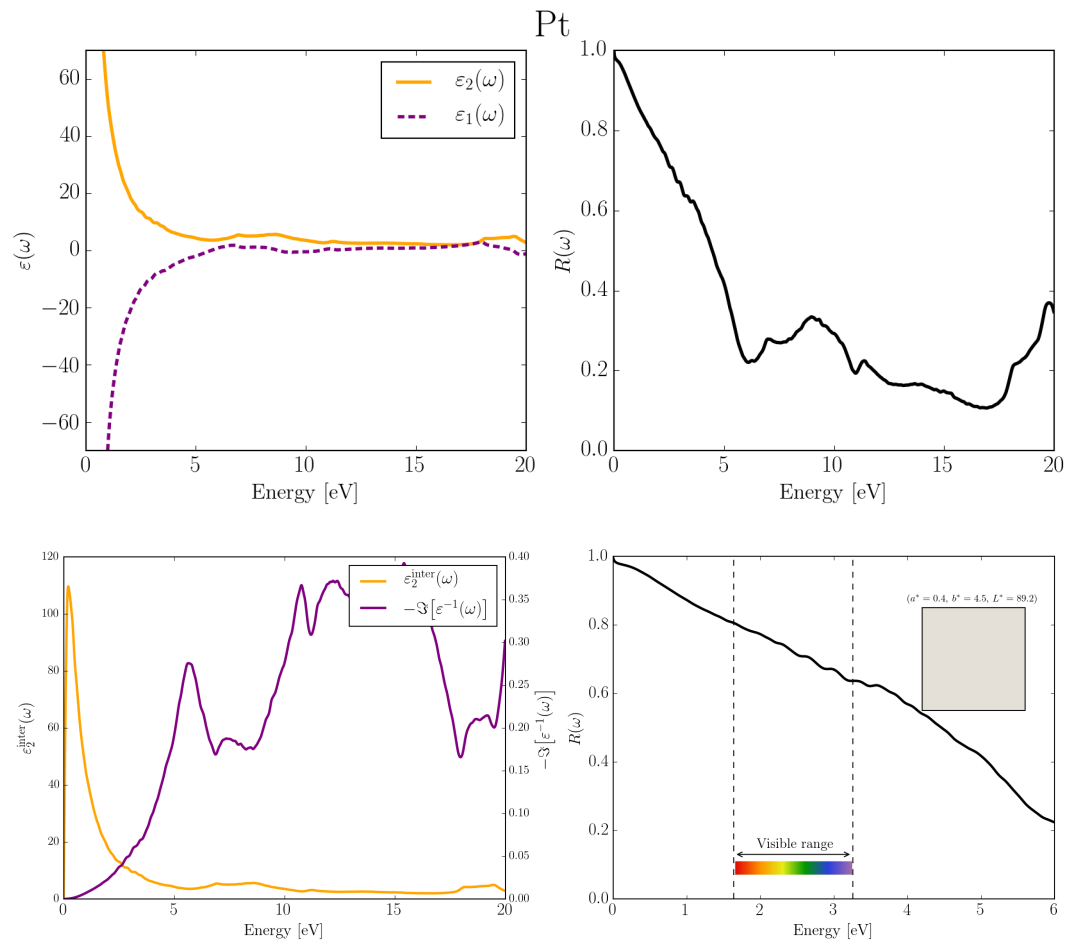


Figure C.30 – Optical properties of Pt simulated at the IPA level starting from the DFT-PBE electronic structure.

Appendix C. Optical data

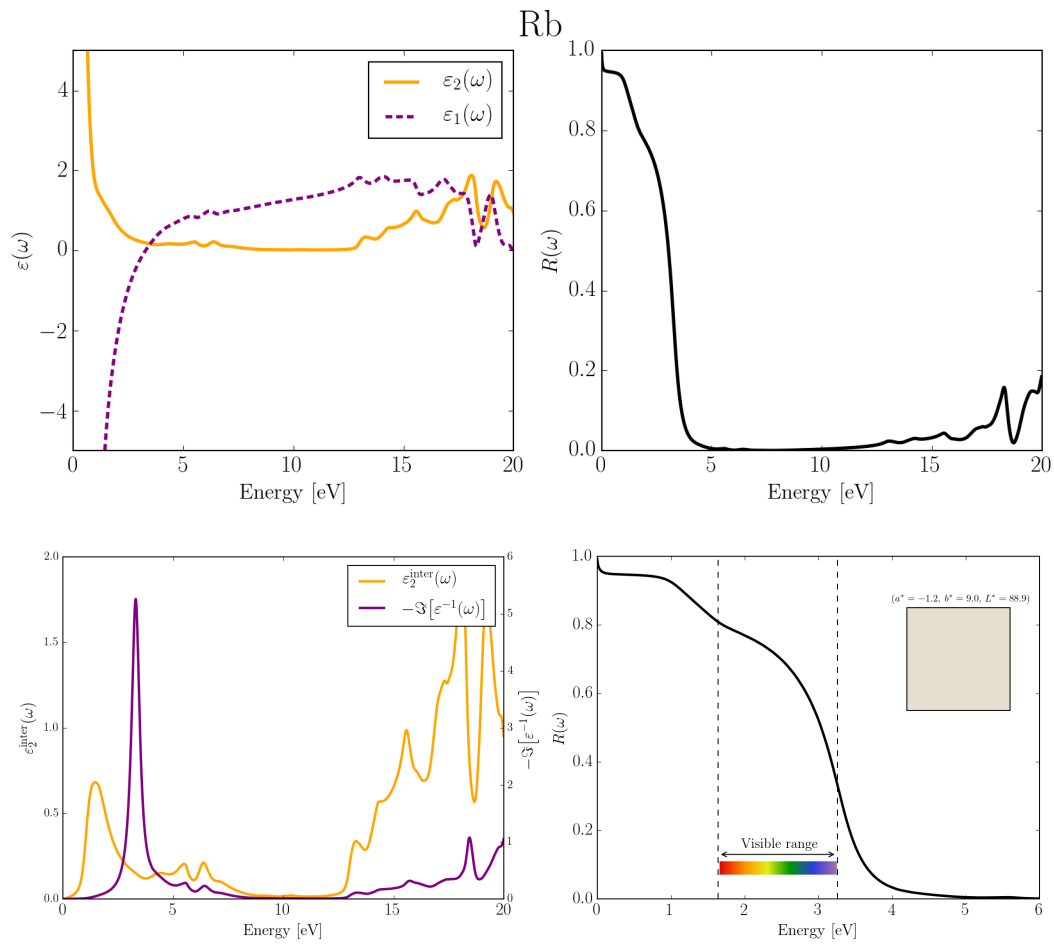


Figure C.31 – Optical properties of Rb simulated at the IPA level starting from the DFT-PBE electronic structure.

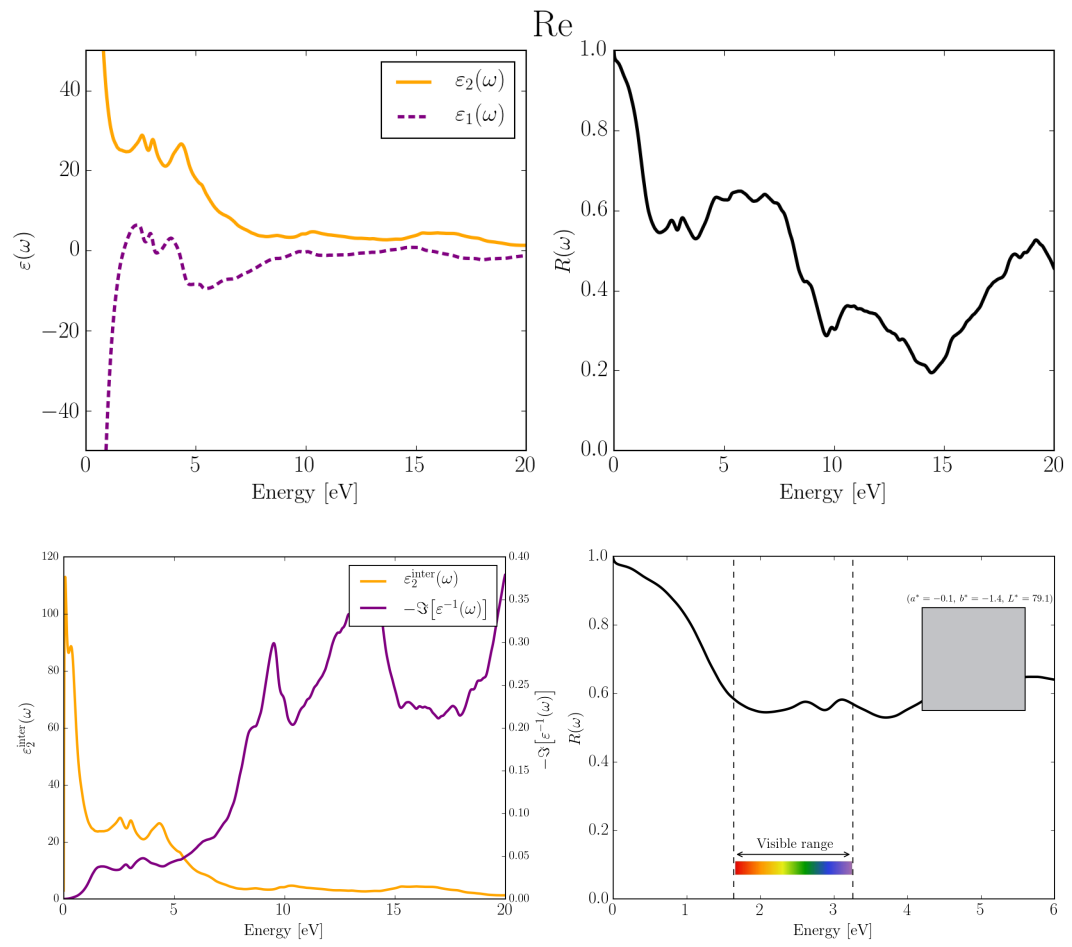


Figure C.32 – Optical properties of Re simulated at the IPA level starting from the DFT-PBE electronic structure.

Appendix C. Optical data

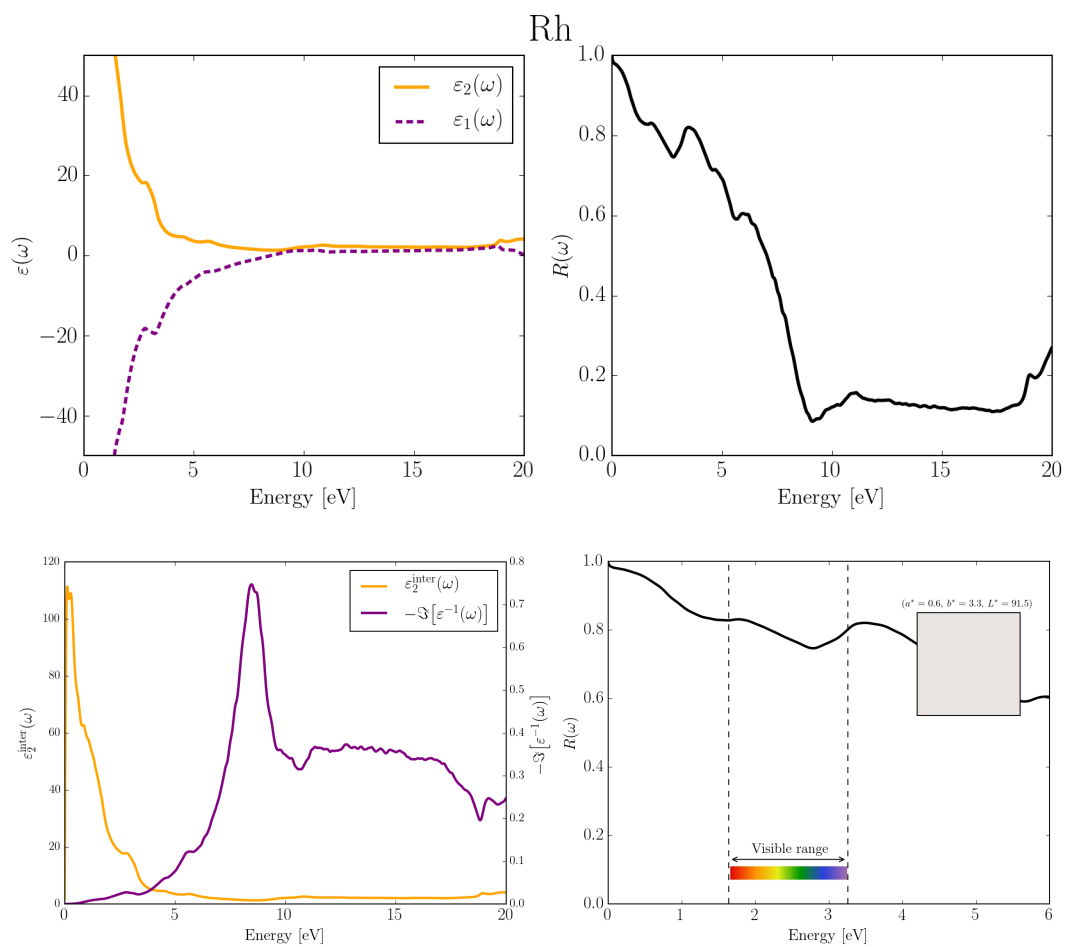


Figure C.33 – Optical properties of Rh simulated at the IPA level starting from the DFT-PBE electronic structure.

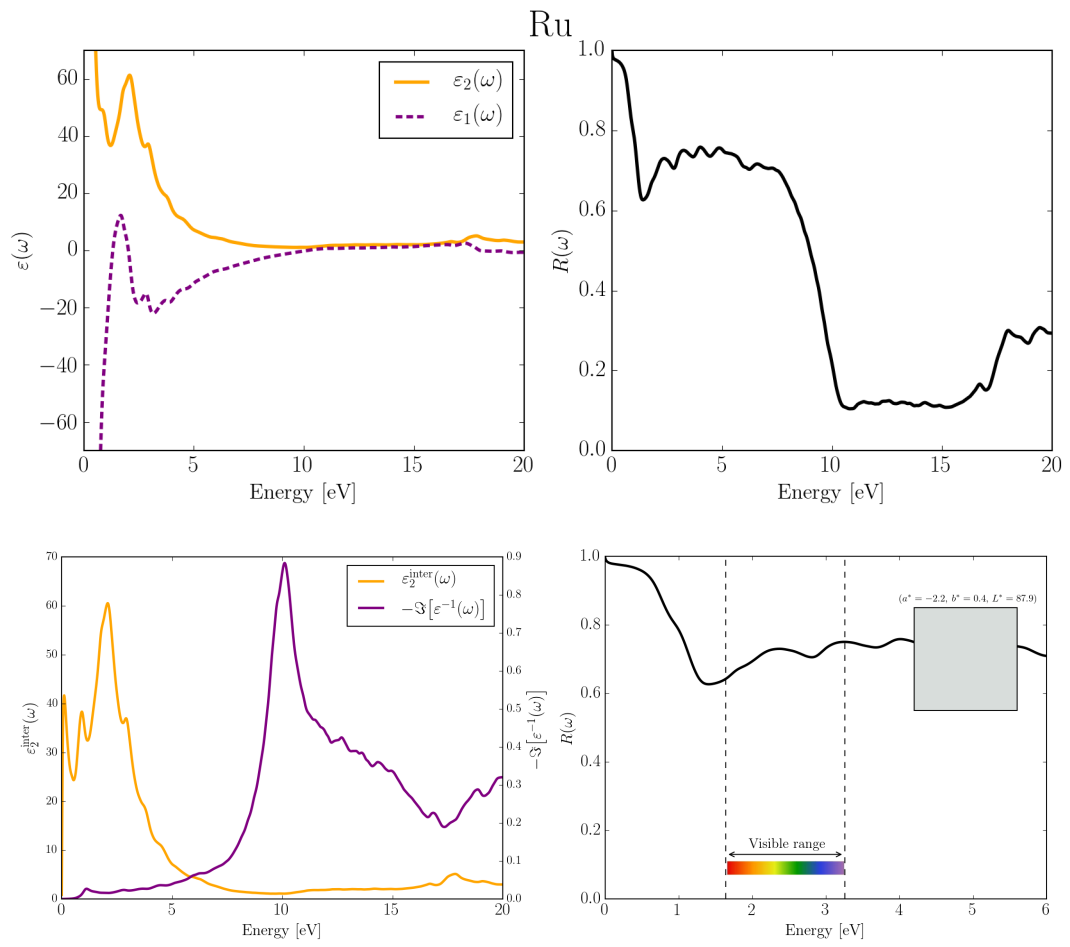


Figure C.34 – Optical properties of Ru simulated at the IPA level starting from the DFT-PBE electronic structure.

Appendix C. Optical data

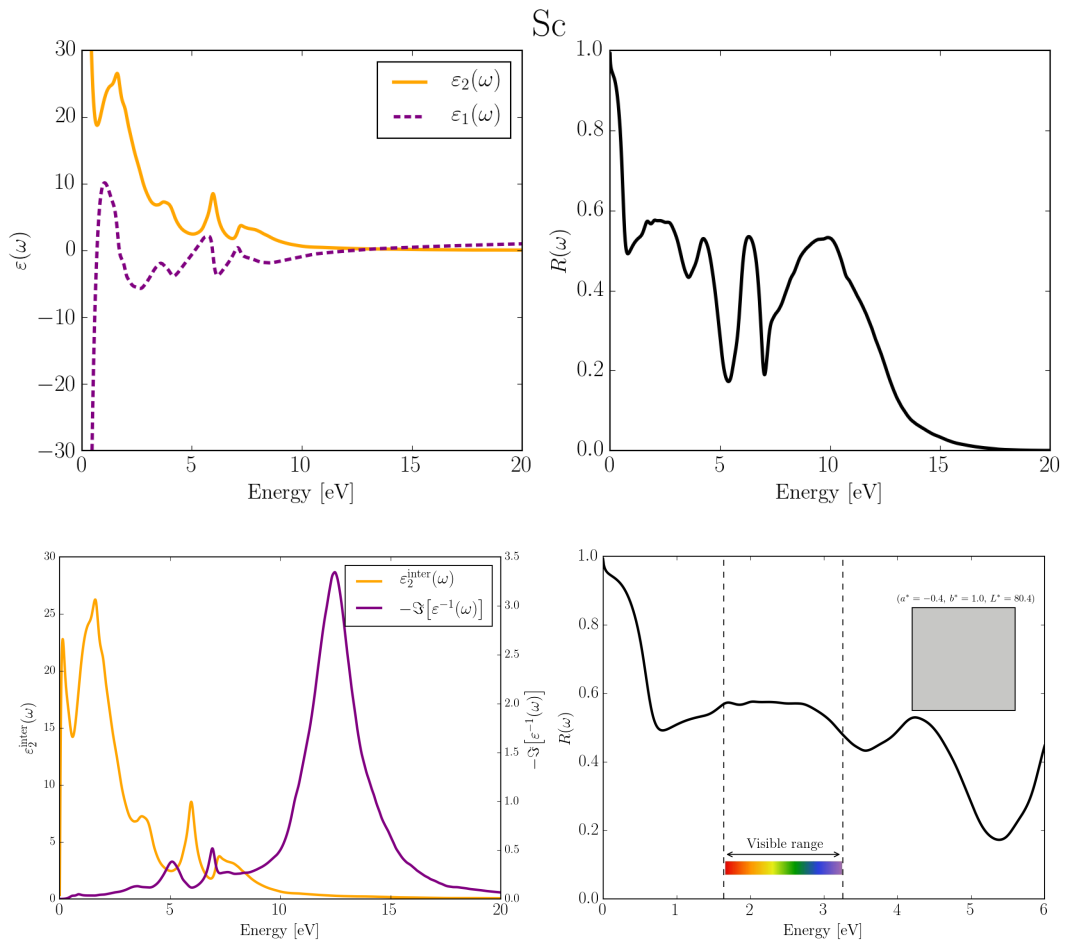


Figure C.35 – Optical properties of Sc simulated at the IPA level starting from the DFT-PBE electronic structure.

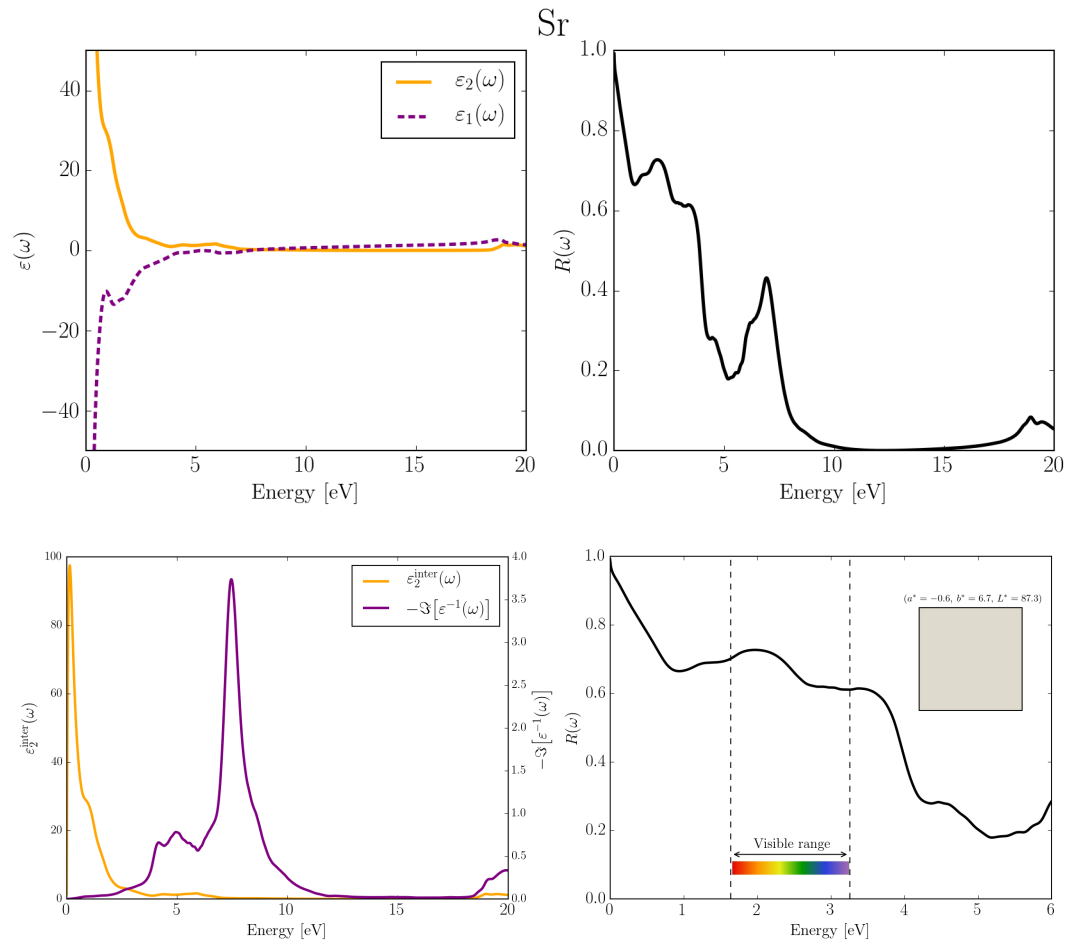


Figure C.36 – Optical properties of Sr simulated at the IPA level starting from the DFT-PBE electronic structure.

Appendix C. Optical data

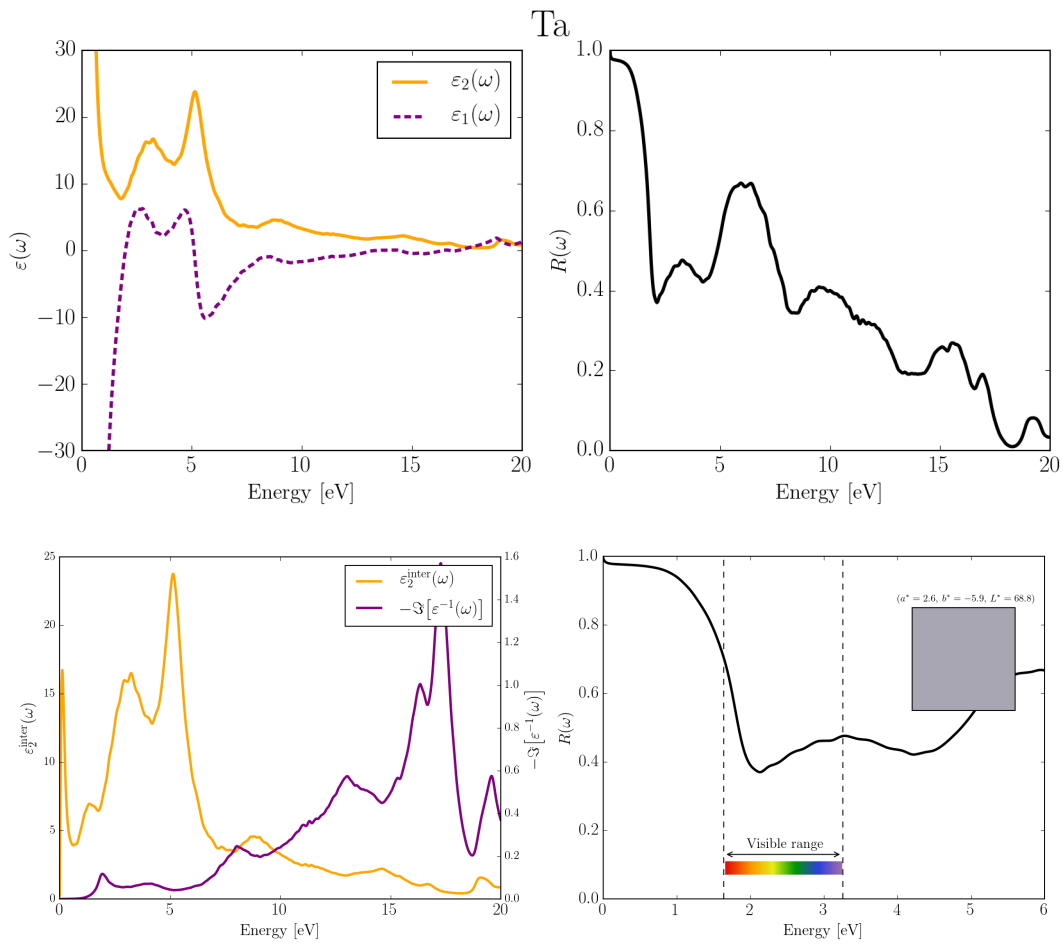


Figure C.37 – Optical properties of Ta simulated at the IPA level starting from the DFT-PBE electronic structure.



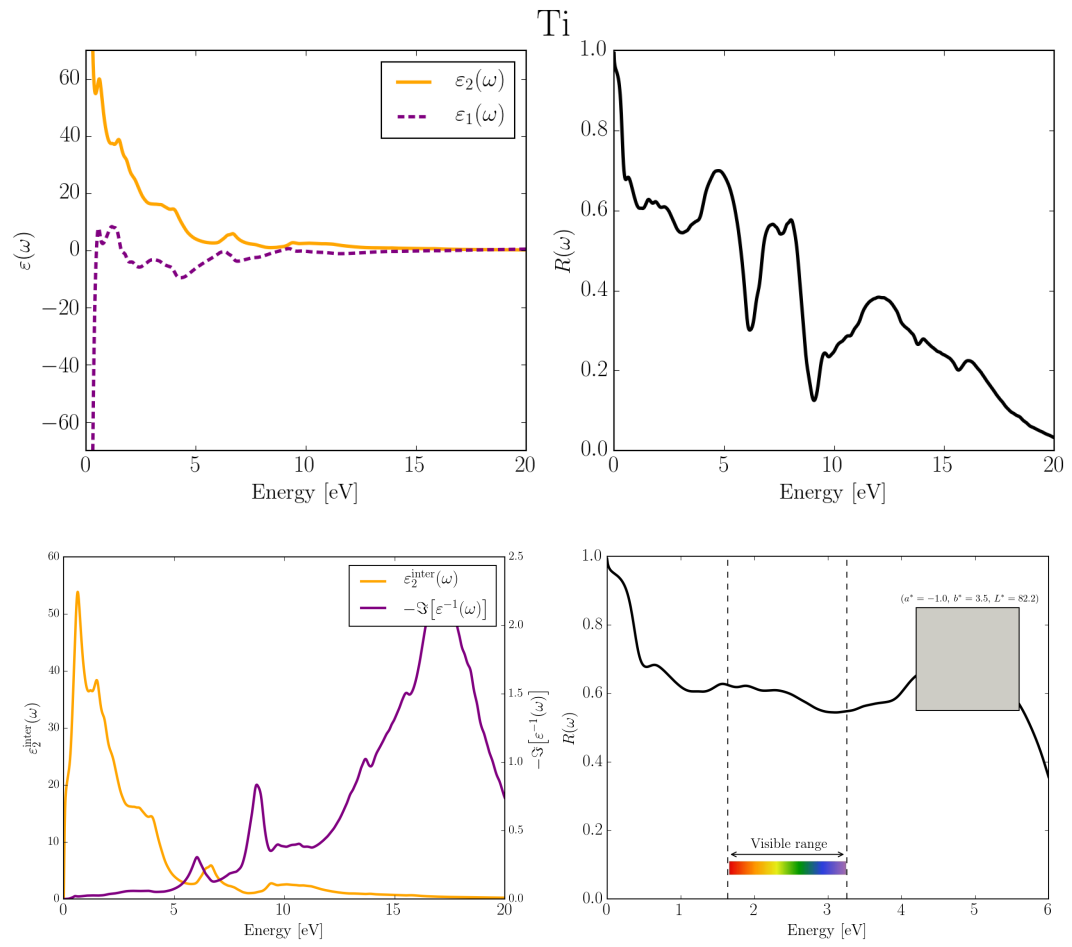


Figure C.38 – Optical properties of Ti simulated at the IPA level starting from the DFT-PBE electronic structure.

Appendix C. Optical data

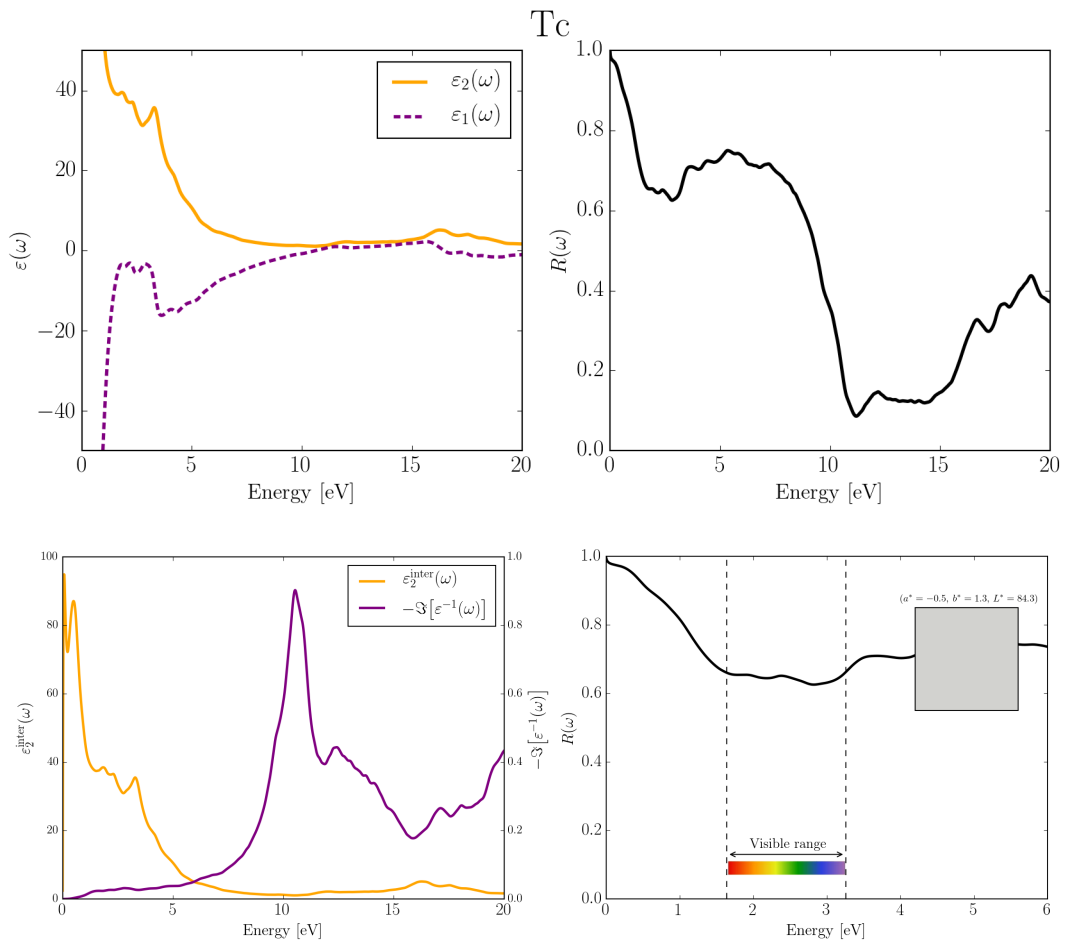


Figure C.39 – Optical properties of Tc simulated at the IPA level starting from the DFT-PBE electronic structure.

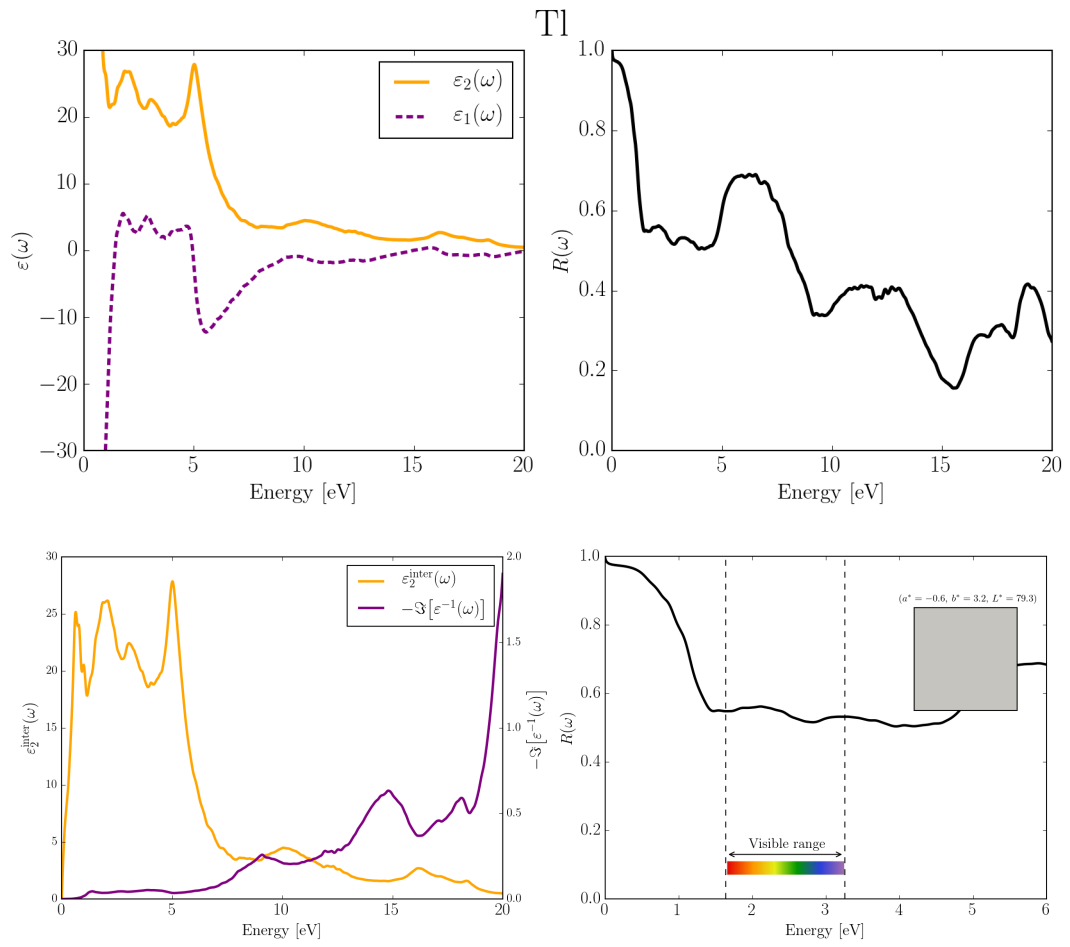


Figure C.40 – Optical properties of Tl simulated at the IPA level starting from the DFT-PBE electronic structure.

Appendix C. Optical data

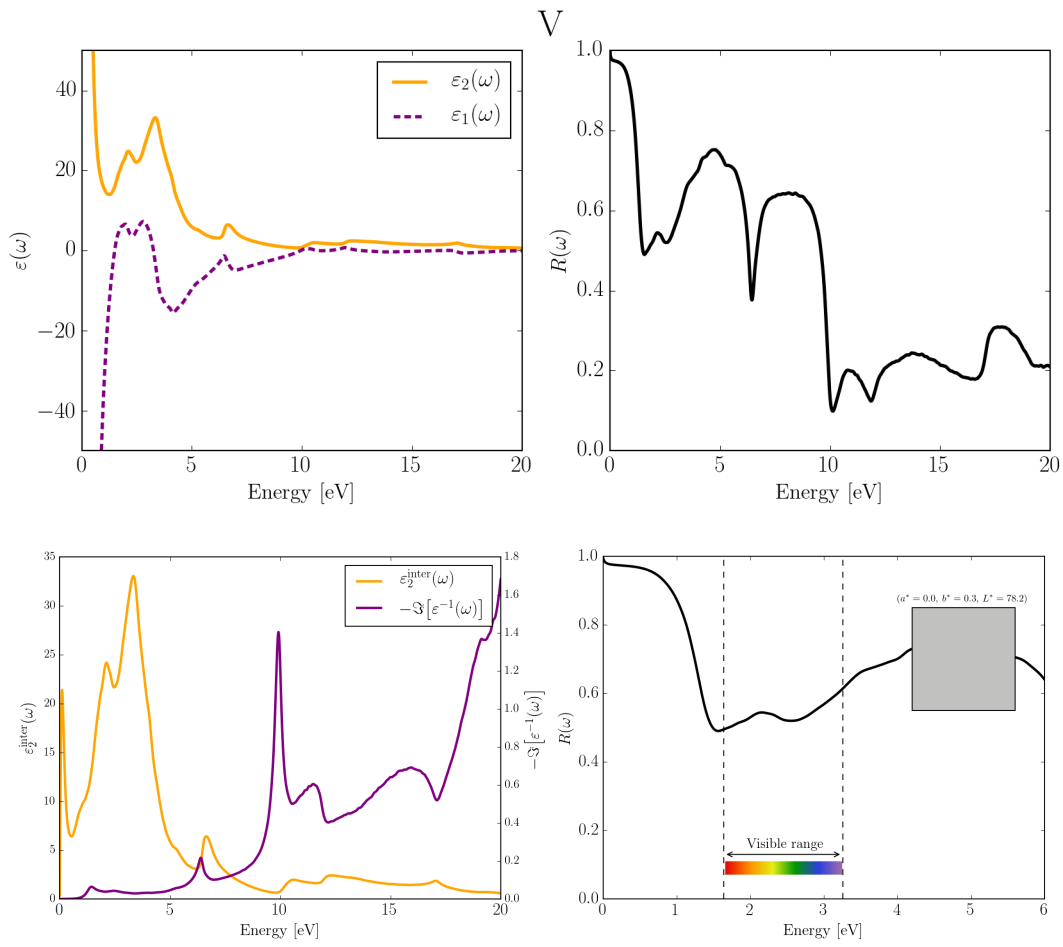


Figure C.41 – Optical properties of V simulated at the IPA level starting from the DFT-PBE electronic structure.

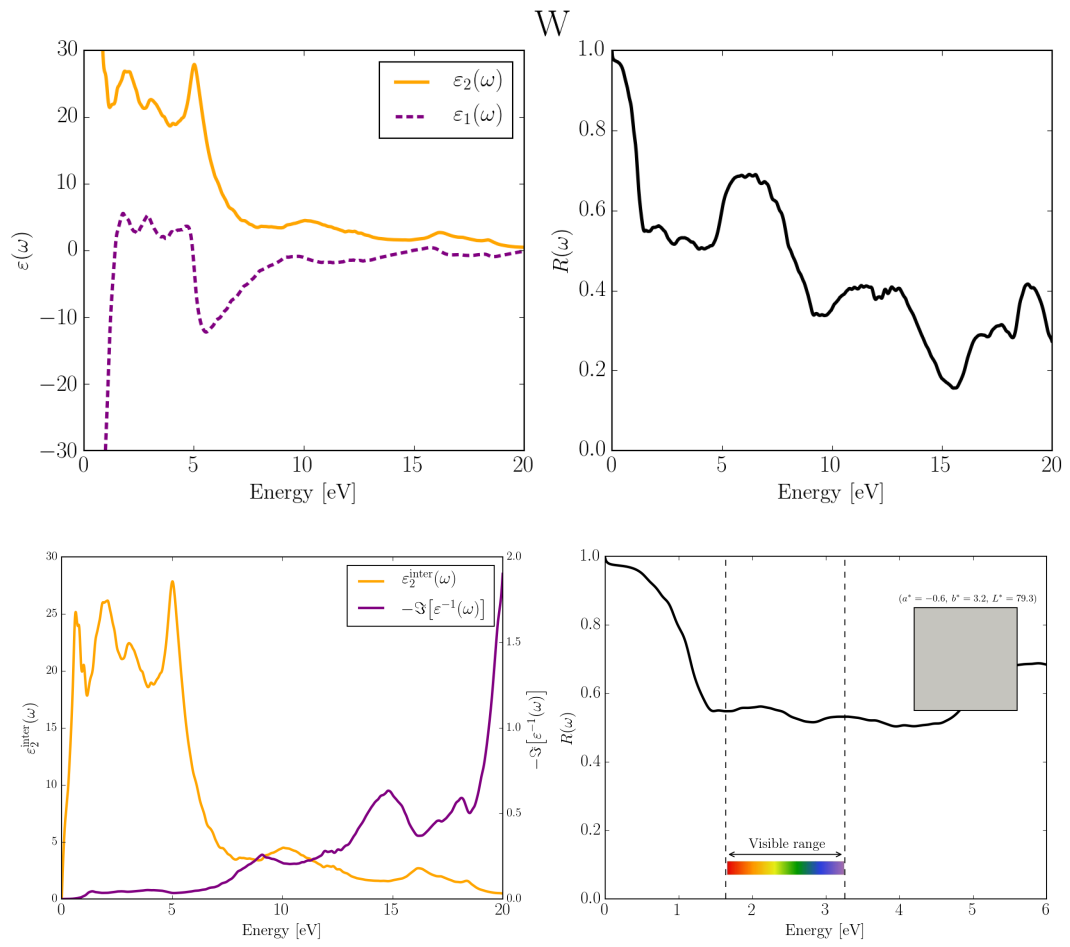


Figure C.42 – Optical properties of W simulated at the IPA level starting from the DFT-PBE electronic structure.

## Appendix C. Optical data

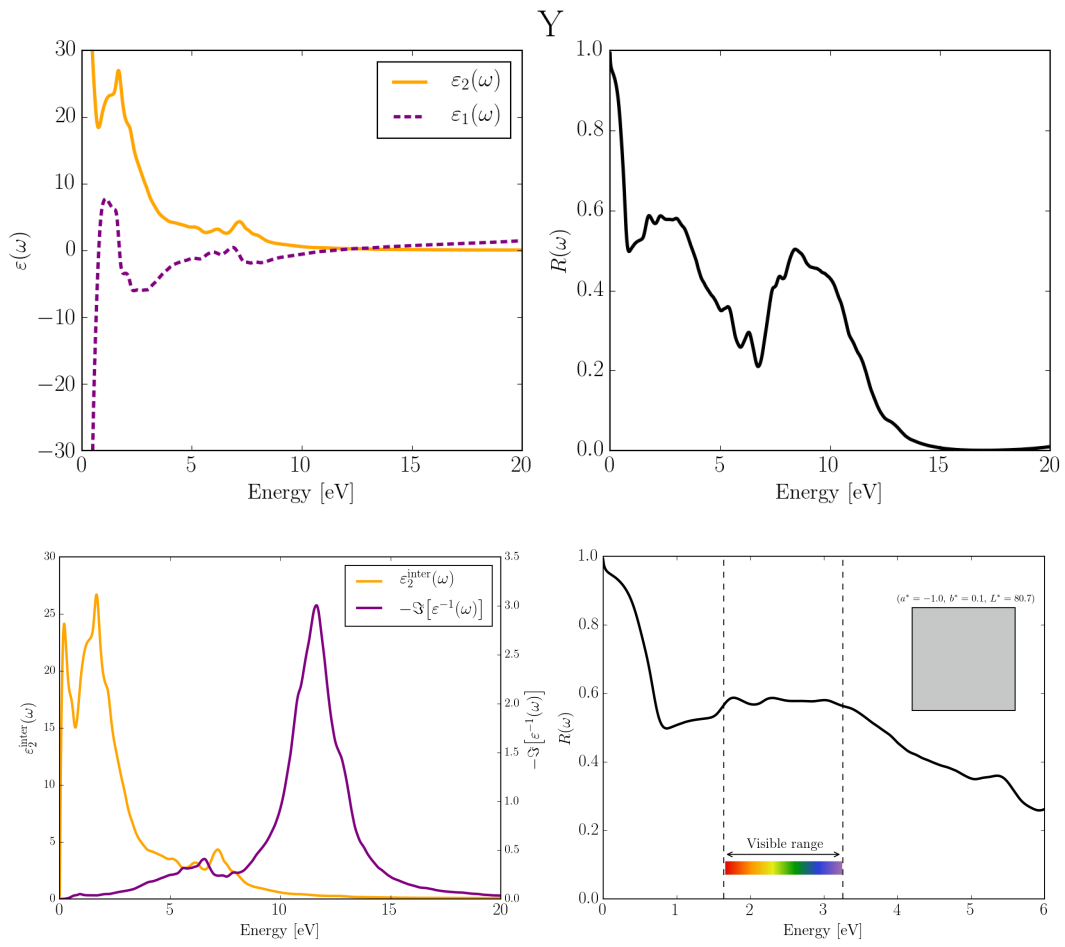


Figure C.43 – Optical properties of Y simulated at the IPA level starting from the DFT-PBE electronic structure.

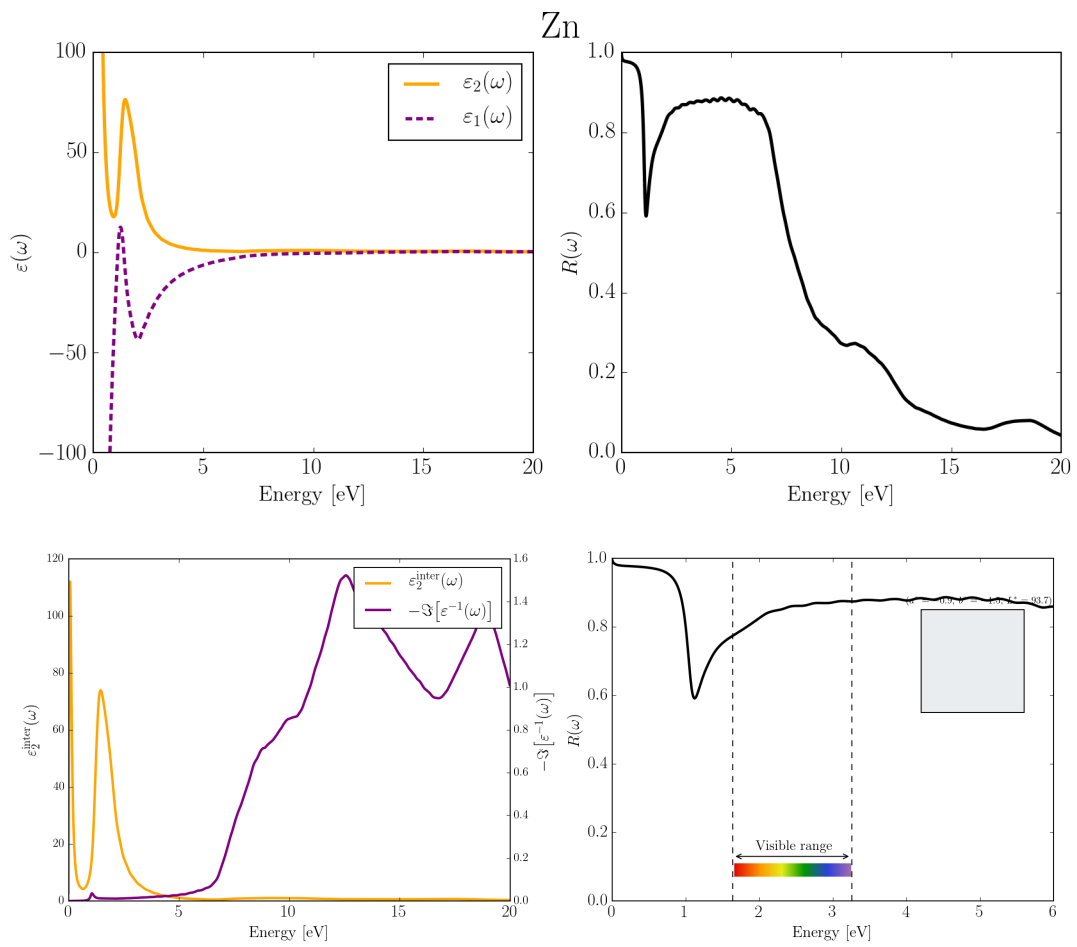


Figure C.44 – Optical properties of Zn simulated at the IPA level starting from the DFT-PBE electronic structure.

Appendix C. Optical data

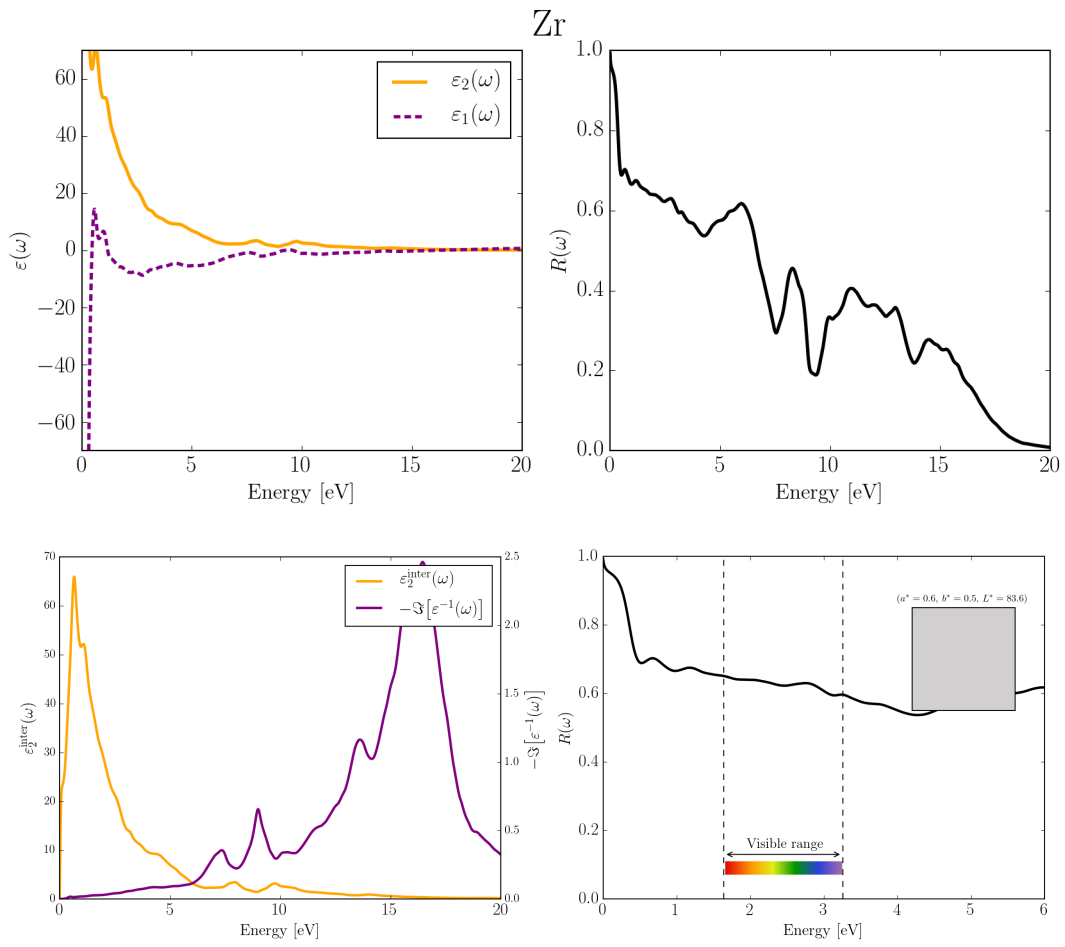


Figure C.45 – Optical properties of Zr simulated at the IPA level starting from the DFT-PBE electronic structure.



## C.2 Coloured intermetallics

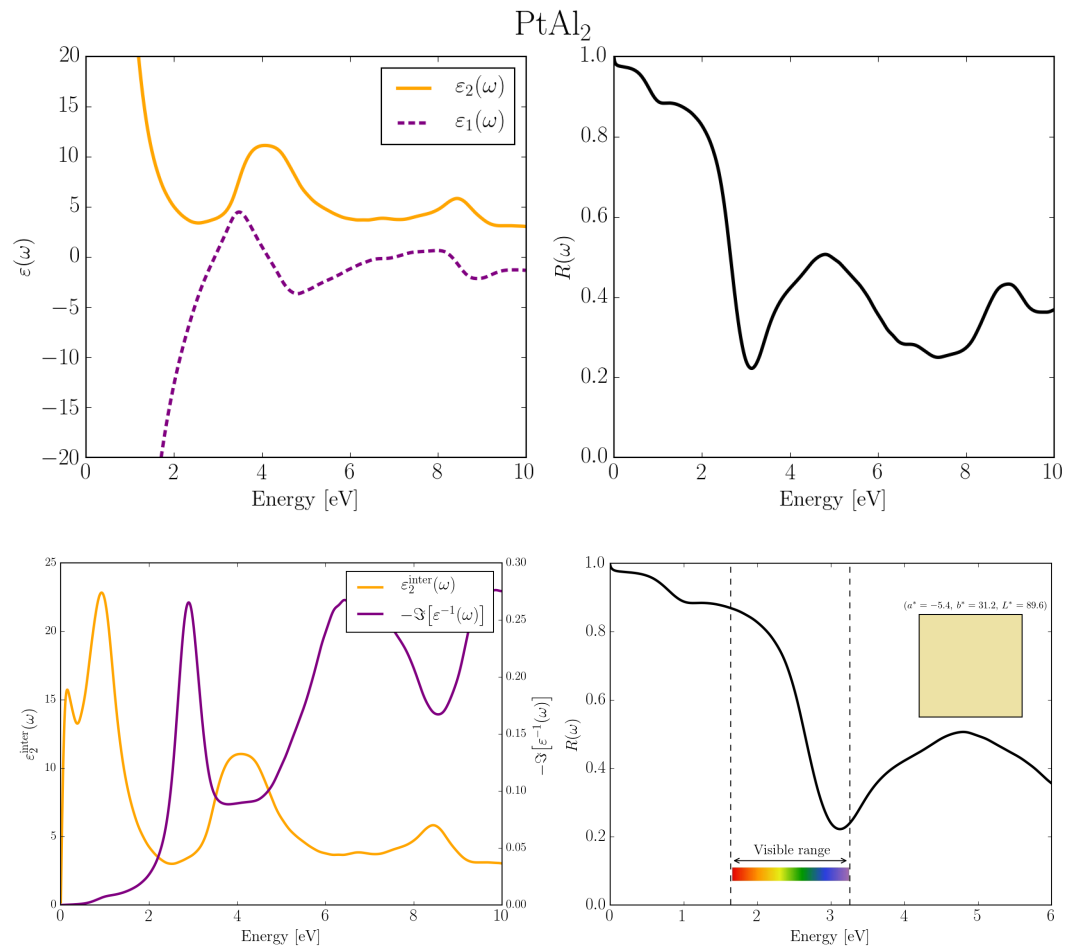


Figure C.46 – Optical properties of PtAl<sub>2</sub> simulated at the IPA level starting from the DFT-PBE electronic structure.

Appendix C. Optical data

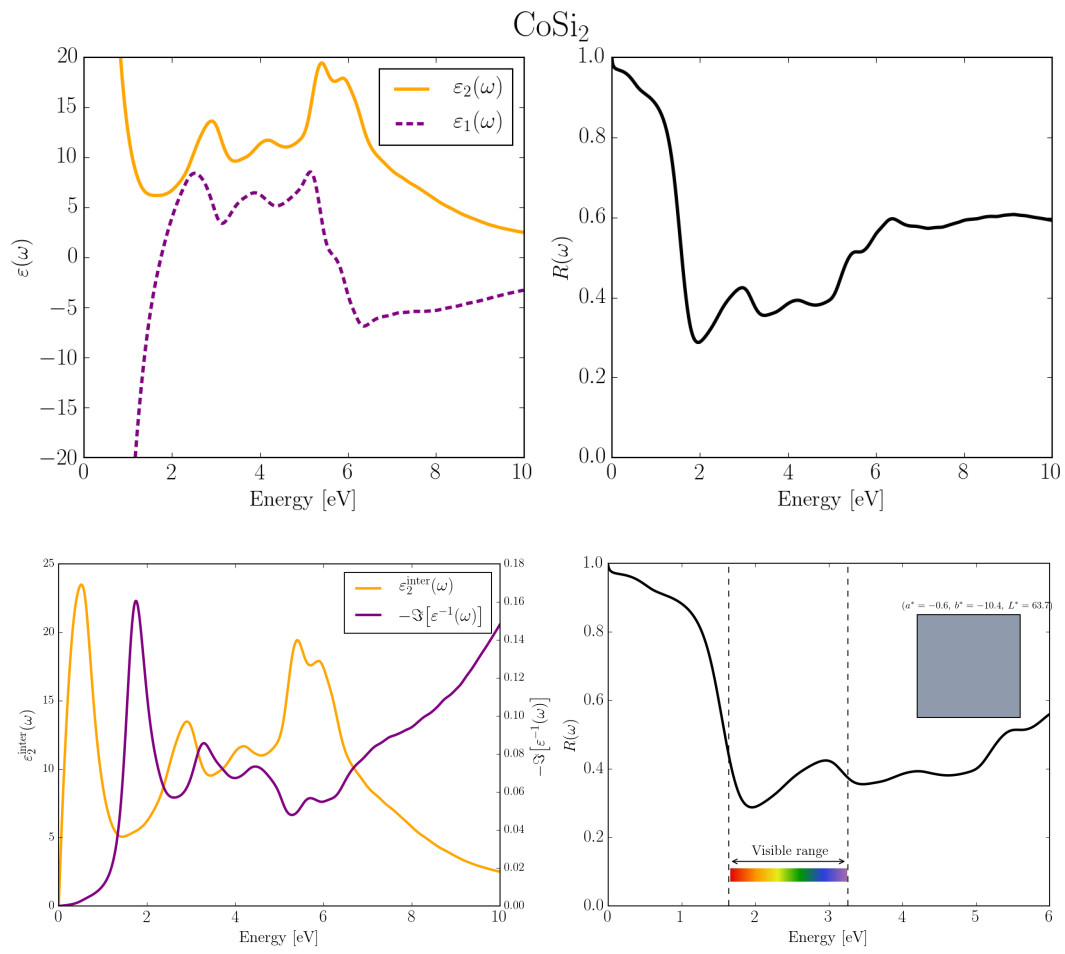


Figure C.47 – Optical properties of  $\text{CoSi}_2$  simulated at the IPA level starting from the DFT-PBE electronic structure.

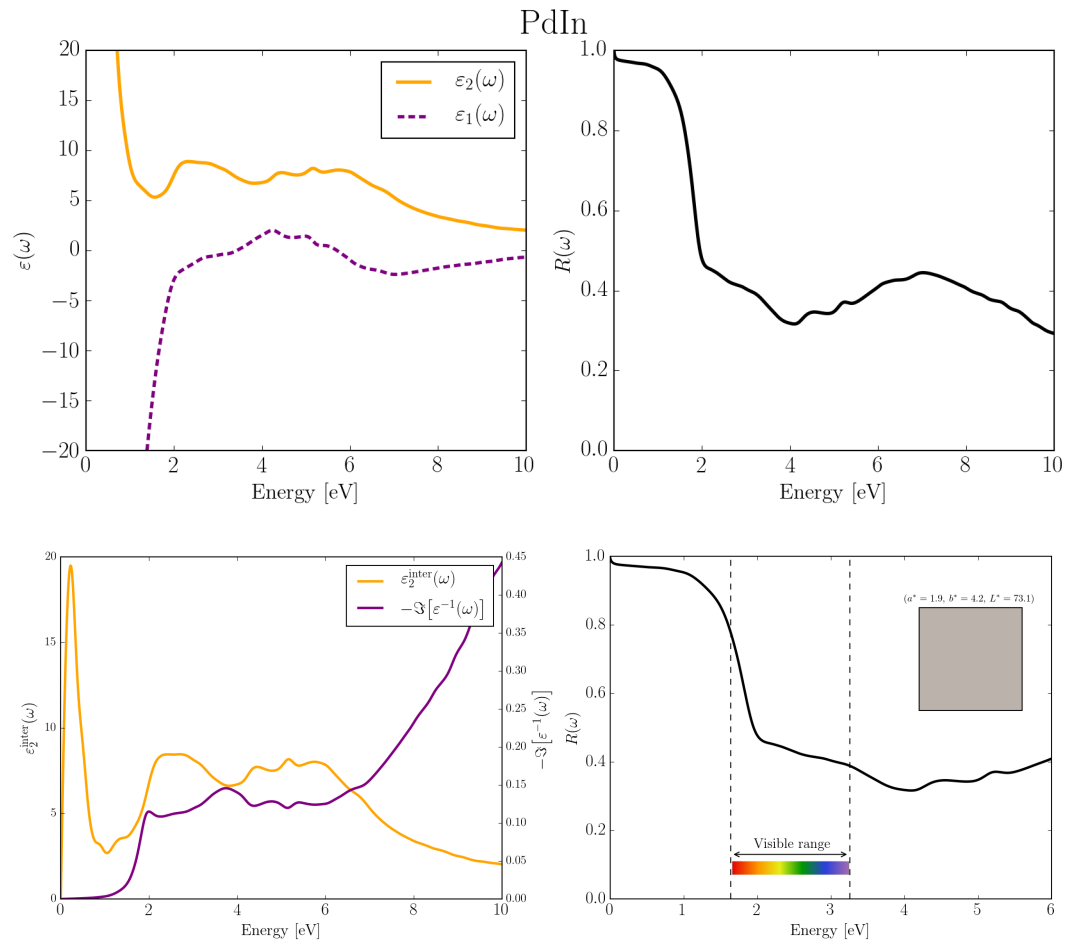


Figure C.48 – Optical properties of PdIn simulated at the IPA level starting from the DFT-PBE electronic structure.

Appendix C. Optical data

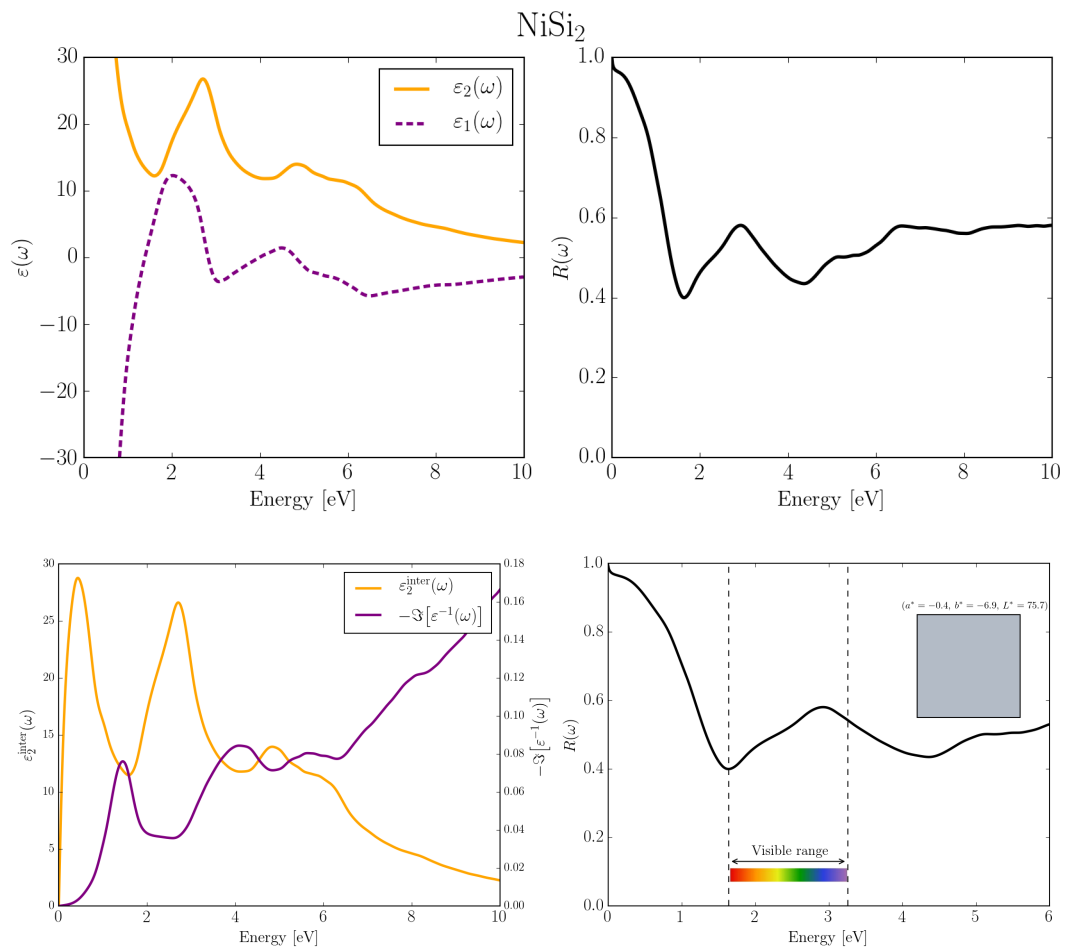


Figure C.49 – Optical properties of NiSi<sub>2</sub> simulated at the IPA level starting from the DFT-PBE electronic structure.

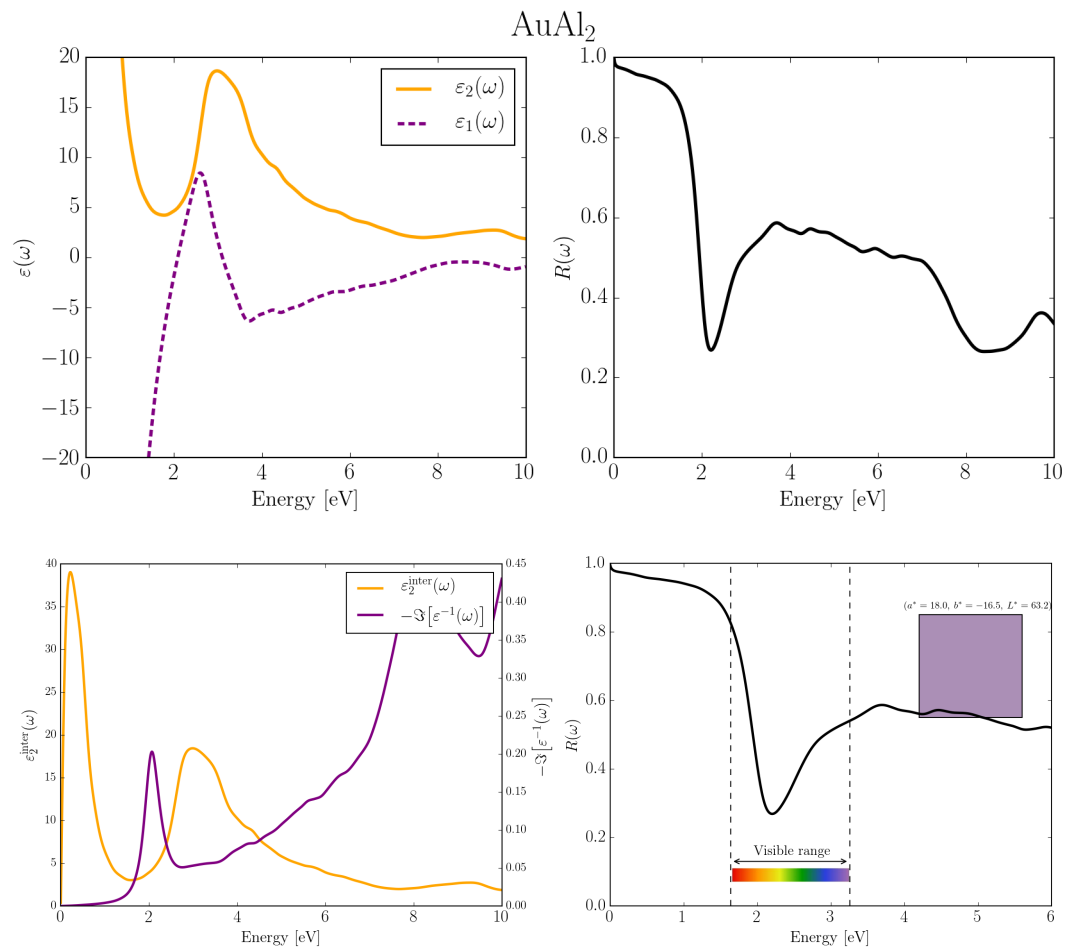


Figure C.50 – Optical properties of AuAl<sub>2</sub> simulated at the IPA level starting from the DFT-PBE electronic structure.

Appendix C. Optical data

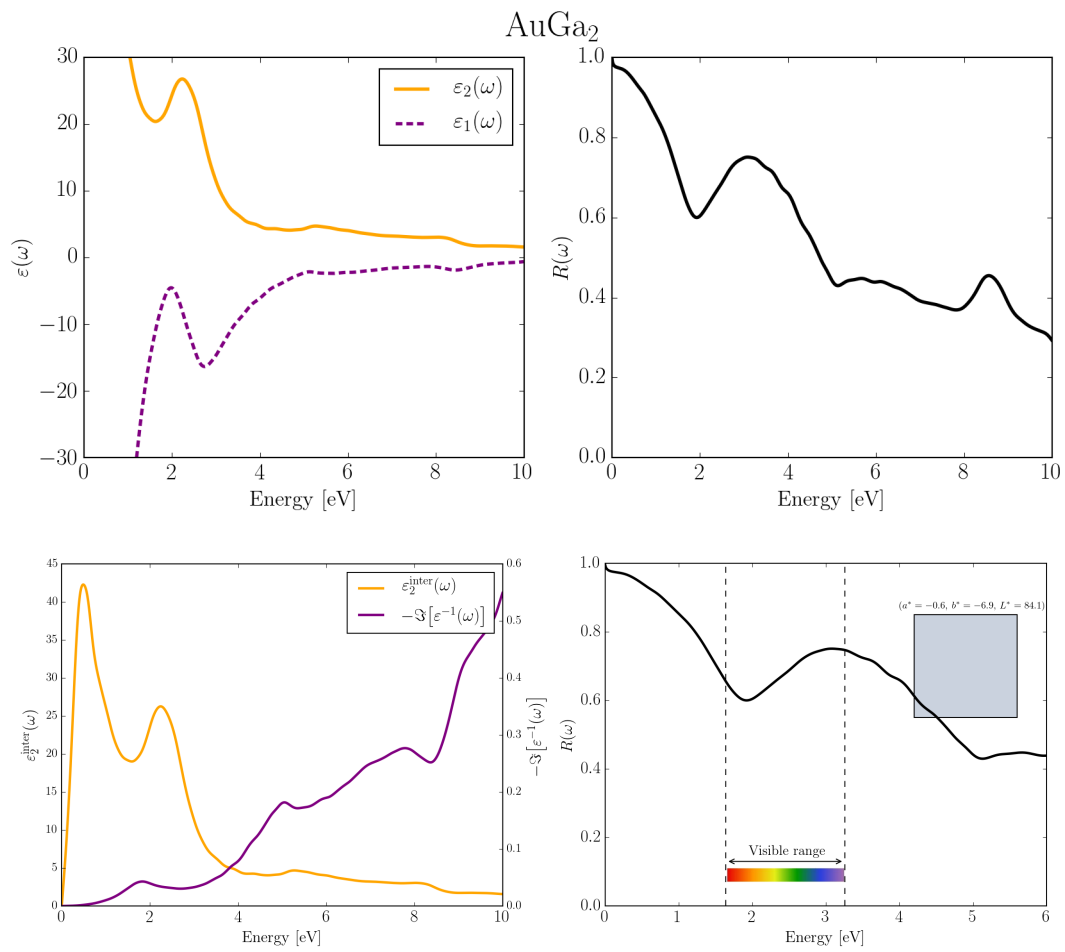


Figure C.51 – Optical properties of AuGa<sub>2</sub> simulated at the IPA level starting from the DFT-PBE electronic structure.

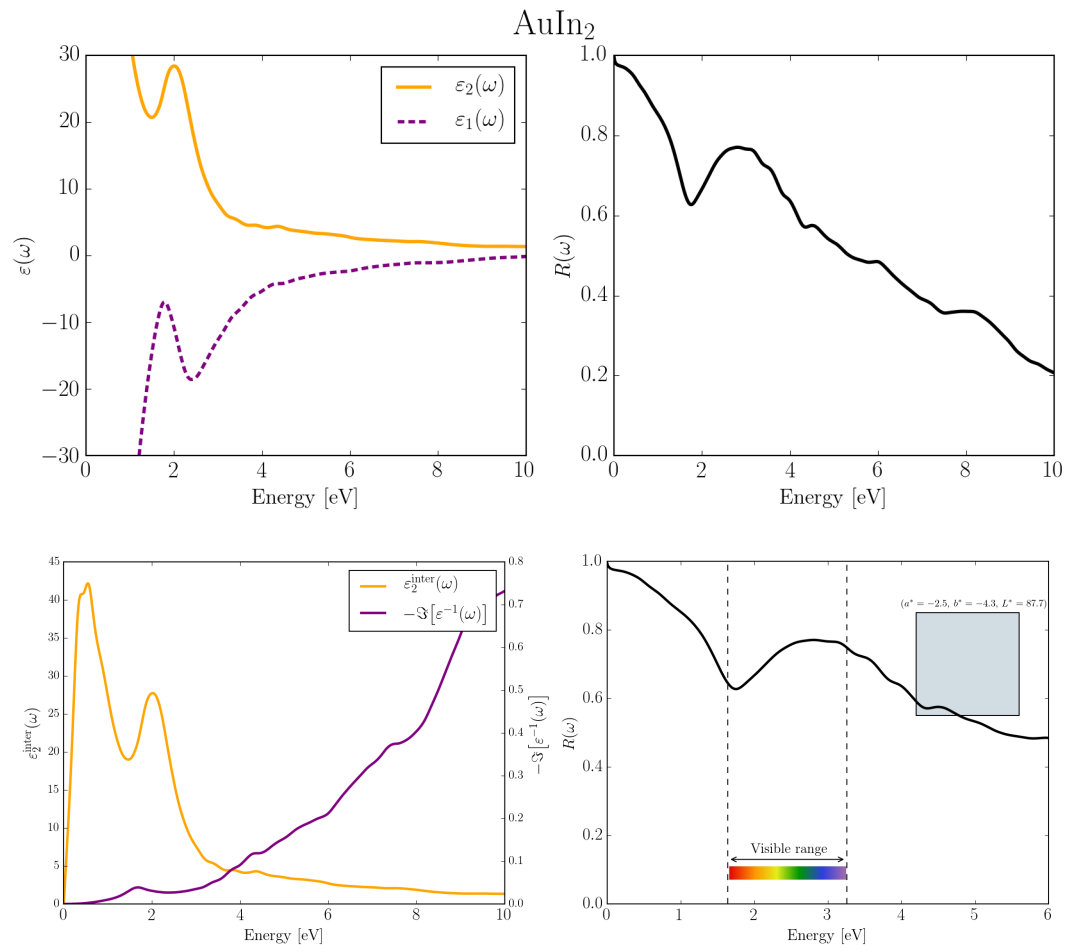


Figure C.52 – Optical properties of AuIn<sub>2</sub> simulated at the IPA level starting from the DFT-PBE electronic structure.





# Bibliography

- [1] R. W. Cahn, A precious stone that isn't, *Nature* 396 (1998) 523.
- [2] A. Furrer, Colours in thin metallic films based on precious metals and their intermetallic phases, Ph.D. thesis, ETH Zurich (2013).
- [3] T. Shiraishi, R. J. D. Tilley, An estimation of the reflectivity of some monophasic binary gold alloys, *Gold Bull.* 47 (2014) 75–82.
- [4] S. S. Vishnubhatla, J. P. Jan, Optical properties of the intermetallic compounds AuAl<sub>2</sub>, AuGa<sub>2</sub> and AuIn<sub>2</sub>, *Philos. Mag.* 16 (139) (1967) 45–50.
- [5] S. Henderson, D. Manchanda, White gold alloys, *Gold Bull.* 38 (2) (2005) 55–67.
- [6] <http://www.mitsuba-renderer.org/>.
- [7] F. Jollet, M. Torrent, N. Holzwarth, Generation of projector augmented-wave atomic data: A 71 element validated table in the xml format, *Comput. Phys. Commun.* 185 (4) (2014) 1246 – 1254.
- [8] <https://www.materialscloud.org/>.
- [9] E. D. Palik, *Handbook of Optical Constants of Solids*, Academic Press handbook series, Elsevier Science, 1998.
- [10] V. Keast, B. Zwan, S. Supansomboon, M. Cortie, P. O. A. Persson, AuAl<sub>2</sub> and PtAl<sub>2</sub> as potential plasmonic materials, *J. Alloy. Comp.* 577 (2013) 581 – 586.
- [11] M. Amiotti, A. Borghesi, G. Guizzetti, F. Nava, Optical properties of polycrystalline nickel silicides, *Phys. Rev. B* 42 (1990) 8939–8946.
- [12] S. G. Steinemann, P. N. B. Anongba, R. Podloucky, Color in Pettifor's Structure Maps: Intermetallic Compounds for a New Use, *J. Phase Equilib.* 18 (6) (1997) 655.
- [13] T. Massalski, H. Okamoto, P. Subramanian, L. Kacprzak, *Binary Alloy Phase Diagrams*, 2nd Edition, ASM International, 1990.
- [14] K. S. B. De Silva, V. Keast, M. Cortie, Effect of Al additions on the optical properties of Au  $\alpha$ -phase, *J. Alloy. Comp.* 679 (2016) 225 – 230.

## Bibliography

---

- [15] J. Rivory, Comparative study of the electronic structure of noble-metal-noble-metal alloys by optical spectroscopy, *Phys. Rev. B* 15 (1977) 3119–3135.
- [16] E. F. I. Roberts, K. M. Clarke, The colour characteristics of gold alloys, *Gold Bull.* 12 (1) (1979) 9–19.
- [17] J. Harl, The linear response function in density functional theory: Optical spectra and improved description of the electron correlation, Ph.D. thesis, Universität Wien (2008).
- [18] M. Bilokur, A. Gentle, M. D. Arnold, M. B. Cortie, G. B. Smith, High Temperature Spectrally Selective Solar Absorbers Using Plasmonic AuAl<sub>2</sub>:AlN Nanoparticle Composites, *Solar RRL* 1 (10) (2017) 1700092.
- [19] C. Guo, T. Sun, F. Cao, Q. Liu, Z. Ren, Metallic nanostructures for light trapping in energy-harvesting devices, *Light Sci. Appl* 3 (e161).
- [20] J. Yun, Ultrathin metal films for transparent electrodes of flexible optoelectronic devices, *Adv. Funct. Mater.* 27 (18) (2017) 1606641.
- [21] X. Ren, X. Li, W. C. Choy, Optically enhanced semi-transparent organic solar cells through hybrid metal/nanoparticle/dielectric nanostructure, *Nano Energy* 17 (2015) 187 – 195.
- [22] T. K. Hatwar, Y. S. Tyan, C. F. Brucker, High-performance Co/Pt multilayer magneto-optical disk using ultrathin seed layers, *J. Appl. Phys* 81 (8) (1997) 3839–3841.
- [23] C. Corti, R. Holliday, *Gold: Science and applications*, CRC Press, 2010.
- [24] C. Cretu, E. van der Lingen, Coloured gold alloys, *Gold Bull.* 32 (September) (1999) 115–126.
- [25] K. E. Saeger, J. Rodies, The colour of gold and its alloys, *Gold Bull.* 10 (1) (1977) 10–14.
- [26] I. B. MacCormack, J. E. Bowers, New white gold alloys, *Gold Bull.* 14 (1) (1981) 19–24.
- [27] G. Normandeau, R. Roeterink, White golds: A question of compromises, *Gold Bull.* 27 (3) (1994) 70–86.
- [28] M. Bassett, D. Beaglehole, Optical studies of dilute AuNi alloys, *J. Phys. F: Metal Phys.* 6 (6) (1976) 1211.
- [29] H. P. Myers, L. Wallden, A. Karlsson, Some optical properties of CuPd, AgPd, AuPd and CuMn, AgMn alloys, *Philos. Mag.* 18 (154) (1968) 725–744.
- [30] D. J. McPherson, S. Supansomboon, B. Zwan, V. J. Keast, D. L. Cortie, A. Gentle, A. Dowd, M. B. Cortie, Strategies to control the spectral properties of Au-Ni thin films, *Thin Solid Films* 551 (2014) 200 – 204.
- [31] J. Friedel, On some electrical and magnetic properties of metallic solid solutions, *Can. J. Phys.* 34 (12A) (1956) 1190–1211.

- [32] P. W. Anderson, Localized Magnetic States in Metals, *Phys. Rev.* 124 (1961) 41–53.
- [33] E. van der Lingen, Aspects of coloured precious metal intermetallic compounds, *J. S. Afr. I. Min. Metall.* 114 (February) (2014) 137.
- [34] V. J. Keast, K. Birt, C. T. Koch, S. Supansomboon, M. B. Cortie, The role of plasmons and interband transitions in the color of AuAl<sub>2</sub>, AuIn<sub>2</sub>, and AuGa<sub>2</sub>, *Appl. Phys. Lett.* 99 (11) (2011) 111908.
- [35] E. G. Maksimov, I. I. Mazin, S. N. Rashkeev, Y. A. Uspenski, First-principles calculations of the optical properties of metals, *J. Phys. F: Metal Phys.* 18 (4) (1988) 833.
- [36] W. S. M. Werner, K. Glantschnig, C. Ambrosch-Draxl, Optical Constants and Inelastic Electron-Scattering Data for 17 Elemental Metals, *J. Phys. Chem. Ref. Data* 38 (2009) 1013–1092.
- [37] M. G. Blaber, M. D. Arnold, M. J. Ford, Optical properties of intermetallic compounds from first principles calculations: a search for the ideal plasmonic material, *J. Phys. Condens. Matter* 21 (14) (2009) 144211.
- [38] V. J. Keast, R. L. Barnett, M. B. Cortie, First principles calculations of the optical and plasmonic response of Au alloys and intermetallic compounds, *J. Phys. Condens. Matter* 26 (30) (2014) 305501.
- [39] D. Kecik, First-principles investigation of the optical properties of gold and its alloys, Ph.D. thesis, EPF Lausanne (2013).
- [40] A. Furrer, R. Spolenak, Colors of thin films of binary and ternary gold- and platinum-based alloys, *Acta Mater.* 66 (2014) 241–250.
- [41] K. S. B. De Silva, V. J. Keast, A. Gentle, M. B. Cortie, Optical properties and oxidation of  $\alpha$ -phase Ag-Al thin films, *Nanotechnology* 28 (2017) 095202.
- [42] N. Shahcheraghi, V. J. Keast, A. Gentle, M. Arnold, M. B. Cortie, Anomalously strong plasmon resonances in aluminium bronze by modification of the electronic density-of-states, *J. Phys. Condens. Matter* 28 (2016) 405501.
- [43] R. Collette, Y. Wu, A. Olafsson, J. P. Camden, P. D. Rack, Combinatorial Thin Film Sputtering Au<sub>x</sub>Al<sub>1-x</sub> Alloys: Correlating Composition and Structure with Optical Properties, *ACS Comb. Sci.* 20 (11) (2018) 633–642.
- [44] Peña-Rodríguez, O. and Caro, M. and Rivera, A. and Olivares, J. and Manuel Perlado, J. and Caro, A., Optical properties of Au-Ag alloys: An ellipsometric study, *Opt. Mater. Express* 4 (2) (2014) 403–410.
- [45] K. S. B. De Silva, A. Gentle, M. Arnold, V. J. Keast, M. B. Cortie, Dielectric function and its predicted effect on localized plasmon resonances of equiatomic Au-Cu, *J. Phys. D: Appl. Phys.* 48 (2015) 215304.

## Bibliography

---

- [46] A. Marini, G. Onida, R. Del Sole, Quasiparticle Electronic Structure of Copper in the *GW* Approximation, *Phys. Rev. Lett.* 88 (1) (2001) 16403.
- [47] A. Marini, R. Del Sole, G. Onida, First-principles calculation of the plasmon resonance and of the reflectance spectrum of silver in the *GW* approximation, *Phys. Rev. B* 66 (11) (2002) 115101.
- [48] T. Rangel, D. Kecik, P. E. Trevisanutto, G.-M. Rignanese, H. Van Swygenhoven, V. Olevano, Band structure of gold from many-body perturbation theory, *Phys. Rev. B* 86 (12) (2012) 125125.
- [49] M. van Schilfgaarde, T. Kotani, S. Faleev, Quasiparticle Self-Consistent *GW* Theory, *Phys. Rev. Lett.* 96 (2006) 226402.
- [50] T. Kotani, M. van Schilfgaarde, S. V. Faleev, Quasiparticle self-consistent *GW* method: A basis for the independent-particle approximation, *Phys. Rev. B* 76 (2007) 165106.
- [51] K. Glantschnig, C. Ambrosch-Draxl, Relativistic effects on the linear optical properties of Au, Pt, Pb and W, *New J. Phys* 12 (10) (2010) 103048.
- [52] P. Romaniello, P. L. de Boeij, The role of relativity in the optical response of gold within the time-dependent current-density-functional theory, *J. Chem. Phys.* 122 (16) (2005) 164303.
- [53] P. Hohenberg, W. Kohn, Inhomogeneous electron gas, *Phys. Rev.* 136 (1964) B864–B871.
- [54] W. Kohn, L. J. Sham, Self-consistent equations including exchange and correlation effects, *Phys. Rev.* 140 (1965) A1133–A1138.
- [55] E. Runge, E. K. U. Gross, Density-functional theory for time-dependent systems, *Phys. Rev. Lett.* 52 (1984) 997–1000.
- [56] D. Hamann, M. Schlüter, C. Chiang, Norm-Conserving Pseudopotentials, *Phys. Rev. Lett.* 43 (20) (1979) 1494–1497.
- [57] D. Vanderbilt, Soft self-consistent pseudopotentials in a generalized eigenvalue formalism, *Phys. Rev. B* 41 (11) (1990) 7892–7895.
- [58] P. E. Blöchl, Projector augmented-wave method, *Phys. Rev. B* 50 (24) (1994) 17953–17979.
- [59] M. Petersilka, U. J. Gossmann, E. K. U. Gross, Excitation energies from time-dependent density-functional theory, *Phys. Rev. Lett.* 76 (1996) 1212–1215.
- [60] S. Botti, A. Schindlmayr, R. D. Sole, L. Reining, Time-dependent density-functional theory for extended systems, *Rep. Prog. Phys.* 70 (3) (2007) 357.
- [61] S. K. Ghosh, A. K. Dhara, Density-functional theory of many-electron systems subjected to time-dependent electric and magnetic fields, *Phys. Rev. A* 38 (1988) 1149–1158.

- 
- [62] G. Vignale, Mapping from current densities to vector potentials in time-dependent current density functional theory, *Phys. Rev. B* 70 (2004) 201102.
- [63] S. L. Adler, Quantum theory of the dielectric constant in real solids, *Phys. Rev.* 126 (1962) 413–420.
- [64] G. Strinati, Application of the green's functions method to the study of the optical properties of semiconductors, *Riv. Nuovo Cimento* 11 (12) (1988) 1–86.
- [65] R. Del Sole, R. Girlanda, Optical properties of semiconductors within the independent-quasiparticle approximation, *Phys. Rev. B* 48 (1993) 11789–11795.
- [66] E. Wooten, *Optical properties of solids*, Academic Press, 1972.
- [67] H. Ehrenreich, *in* *The Optical Properties of Solids: Proceedings of the International School of Physics "Enrico Fermi"* (J. Tauc ed.), Academic Press, New York, 1966.
- [68] G. Giuliani, G. Vignale, *Quantum Theory of the Electron Liquid*, Cambridge University Press, 2005.
- [69] D. Griffiths, *Introduction to Electrodynamics*, 3rd Edition, Pearson Education, 2007.
- [70] M. S. Hybertsen, S. G. Louie, Ab initio static dielectric matrices from the density-functional approach. I. Formulation and application to semiconductors and insulators, *Phys. Rev. B* 35 (1987) 5585–5601.
- [71] G. Onida, L. Reining, A. Rubio, Electronic excitations: density-functional versus many-body green's-function approaches, *Rev. Mod. Phys.* 74 (2002) 601–659.
- [72] A. Marini, G. Onida, R. Del Sole, Plane-wave DFT-LDA calculation of the electronic structure and absorption spectrum of copper, *Phys. Rev. B* 64 (19) (2001) 195125. [arXiv: 0108535](https://arxiv.org/abs/0108535).
- [73] M. G. Blaber, M. D. Arnold, M. J. Ford, Designing materials for plasmonic systems: the alkali-noble intermetallics, *J. Phys.: Condens. Matter* 22 (9) (2010) 095501.
- [74] A. Marini, R. Del Sole, Dynamical excitonic effects in metals and semiconductors, *Phys. Rev. Lett.* 91 (2003) 176402.
- [75] M. S. Hybertsen, S. G. Louie, Electron correlation in semiconductors and insulators: Band gaps and quasiparticle energies, *Phys. Rev. B* 34 (1986) 5390–5413.
- [76] L. Reining, The GW approximation: content, successes and limitations, *Wiley Interdiscip. Rev.: Comput. Mol. Sci.* 8 (3) (2017) e1344.
- [77] F. Bassani, G. P. Parravicini, *Electronic states and optical transitions in solids*, Pergamon Press, 1975.
- [78] N. Ashcroft, N. Mermin, *Solid State Physics*, Cengage Learning, 1976.

## Bibliography

---

- [79] W. Kohn, Theory of the Insulating State, *Phys. Rev.* 133 (1964) A171–A181.
- [80] R. Resta, Theory of the insulating state, *Riv. Nuovo Cimento* 41 (9) (2018) 463–512.
- [81] C. J. Pickard, M. C. Payne, Second-order  $\mathbf{k} \cdot \mathbf{p}$  perturbation theory with Vanderbilt pseudopotentials and plane waves, *Phys. Rev. B* 62 (2000) 4383–4388.
- [82] M. Gajdoš, K. Hummer, G. Kresse, J. Furthmüller, F. Bechstedt, Linear optical properties in the projector-augmented wave methodology, *Phys. Rev. B* 73 (2006) 045112.
- [83] P. Alippi, P. La Rocca, G. B. Bachelet, Alkali-metal plasmons, pseudopotentials, and optical sum rules, *Phys. Rev. B* 55 (1997) 13835–13841.
- [84] A. F. Starace, Length and velocity formulas in approximate oscillator-strength calculations, *Phys. Rev. A* 3 (1971) 1242–1245.
- [85] B. Adolph, V. I. Gavrilenko, K. Tenelsen, F. Bechstedt, R. Del Sole, Nonlocality and many-body effects in the optical properties of semiconductors, *Phys. Rev. B* 53 (1996) 9797–9808.
- [86] <http://www.cie.co.at/>.
- [87] J. Schanda, *Colorimetry: Understanding the CIE system*, Wiley-Interscience, 2007.
- [88] J. T. Kajiya, The rendering equation, *SIGGRAPH Comput. Graph.* 20 (4) (1986) 143–150.
- [89] G. Prandini, M. Galante, N. Marzari, P. Umari, SIMPLE code: optical properties with optimal basis functions, submitted.
- [90] G. Prandini, A. Marrazzo, I. E. Castelli, N. Mounet, N. Marzari, Precision and efficiency in solid-state pseudopotential calculations, *npj Comput. Mater.* 4 (2018) 72.
- [91] E. L. Shirley, Optimal basis sets for detailed Brillouin-zone integrations, *Phys. Rev. B* 54 (1996) 16464–16469.
- [92] N. Marzari, D. Vanderbilt, Maximally localized generalized Wannier functions for composite energy bands, *Phys. Rev. B* 56 (1997) 12847–12865.
- [93] J. R. Yates, X. Wang, D. Vanderbilt, I. Souza, Spectral and Fermi surface properties from Wannier interpolation, *Phys. Rev. B* 75 (2007) 195121.
- [94] I. Souza, N. Marzari, D. Vanderbilt, Maximally localized Wannier functions for entangled energy bands, *Phys. Rev. B* 65 (2001) 035109.
- [95] A. Damle, L. Lin, L. Ying, SCDM-k: Localized orbitals for solids via selected columns of the density matrix, *J. Comput. Phys.* 334 (2017) 1–15.
- [96] A. Damle, L. Lin, Disentanglement via Entanglement: A Unified Method for Wannier Localization, *Multiscale Model. Simul.* 16 (3) (2018) 1392–1410.

- 
- [97] D. Prendergast, S. G. Louie, Bloch-state-based interpolation: An efficient generalization of the Shirley approach to interpolating electronic structure, *Phys. Rev. B* 80 (2009) 235126.
- [98] P. Giannozzi, S. Baroni, N. Bonini, M. Calandra, R. Car, C. Cavazzoni, D. Ceresoli, G. L. Chiarotti, M. Cococcioni, I. Dabo, A. Dal Corso, S. de Gironcoli, S. Fabris, G. Fratesi, R. Gebauer, U. Gerstmann, C. Gougoussis, A. Kokalj, M. Lazzeri, L. Martin-Samos, N. Marzari, F. Mauri, R. Mazzarello, S. Paolini, A. Pasquarello, L. Paulatto, C. Sbraccia, S. Scandolo, G. Sclauzero, A. P. Seitsonen, A. Smogunov, P. Umari, R. M. Wentzcovitch, QUANTUM ESPRESSO: a modular and open-source software project for quantum simulations of materials., *J. Phys. Condens. Matter* 21 (39) (2009) 395502.
- [99] J. Perdew, K. Burke, M. Ernzerhof, Generalized Gradient Approximation Made Simple., *Phys. Rev. Lett.* 77 (18) (1996) 3865–3868.
- [100] M. Schlipf, F. Gygi, Optimization algorithm for the generation of ONCV pseudopotentials, *Comput. Phys. Commun.* 196 (2015) 36–44.
- [101] H. J. Monkhorst, J. D. Pack, Special points for Brillouin-zone integrations, *Phys. Rev. B* 13 (1976) 5188–5192.
- [102] A. Marini, C. Hogan, M. Grüning, D. Varsano, yambo: An *ab initio* tool for excited state calculations, *Comput. Phys. Commun.* 180 (8) (2009) 1392 – 1403.
- [103] G. Pizzi, D. Volja, B. Kozinsky, M. Fornari, N. Marzari, An updated version of BOLTZWANN: A code for the evaluation of thermoelectric and electronic transport properties with a maximally-localized Wannier functions basis, *Comput. Phys. Commun.* 185 (8) (2014) 2311–2312.
- [104] A. A. Mostofi, J. R. Yates, Y.-S. Lee, I. Souza, D. Vanderbilt, N. Marzari, wannier90: A tool for obtaining maximally-localised Wannier functions, *Comput. Phys. Commun.* 178 (9) (2008) 685–699.
- [105] N. Marzari, A. A. Mostofi, J. R. Yates, I. Souza, D. Vanderbilt, Maximally localized Wannier functions: Theory and applications, *Rev. Mod. Phys.* 84 (2012) 1419–1475.
- [106] G. Pizzi, A. Cepellotti, R. Sabatini, N. Marzari, B. Kozinsky, AiiDA: automated interactive infrastructure and database for computational science, *Comput. Mater. Sci.* 111 (2016) 218–230.
- [107] [http://www2.fiz-karlsruhe.de/icsd\\_home.html/](http://www2.fiz-karlsruhe.de/icsd_home.html/).
- [108] <http://www.crystallography.net/cod/>.
- [109] <http://paulingfile.com/>.

## Bibliography

---

- [110] Lejaeghere, K. and Van Speybroeck, V. and Van Oost, G. and Cottenier, S., Error estimates for solid-state density-functional theory predictions: An overview by means of the ground-state elemental crystals, *Crit. Rev. Solid State Mater. Sci.* 39 (1) (2014) 1–24.
- [111] K. Lejaeghere, G. Bihlmayer, T. Bjorkman, P. Blaha, S. Blugel, V. Blum, D. Caliste, I. E. Castelli, S. J. Clark, A. Dal Corso, S. de Gironcoli, T. Deutsch, J. K. Dewhurst, I. Di Marco, C. Draxl, M. Duak, O. Eriksson, J. A. Flores-Livas, K. F. Garrity, L. Genovese, P. Gianozzi, M. Giantomassi, S. Goedecker, X. Gonze, O. Granas, E. K. U. Gross, A. Gulans, F. Gygi, D. R. Hamann, P. J. Hasnip, N. A. W. Holzwarth, D. Iuan, D. B. Jochym, F. Jollet, D. Jones, G. Kresse, K. Koepernik, E. Kucukbenli, Y. O. Kvashnin, I. L. M. Locht, S. Lubeck, M. Marsman, N. Marzari, U. Nitzsche, L. Nordstrom, T. Ozaki, L. Paulatto, C. J. Pickard, W. Poelmans, M. I. J. Probert, K. Refson, M. Richter, G.-M. Rignanese, S. Saha, M. Scheffler, M. Schlipf, K. Schwarz, S. Sharma, F. Tavazza, P. Thunstrom, A. Tkatchenko, M. Torrent, D. Vanderbilt, M. J. van Setten, V. Van Speybroeck, J. M. Wills, J. R. Yates, G.-X. Zhang, S. Cottenier, Reproducibility in density functional theory calculations of solids, *Science* 351 (6280) (2016) aad3000.
- [112] E. Kucukbenli, M. Monni, B. I. Adetunji, X. Ge, G. A. Adebayo, N. Marzari, S. de Gironcoli, A. D. Corso, Projector augmented-wave and all-electron calculations across the periodic table: a comparison of structural and energetic properties, arXiv:1404.3015.
- [113] A. Dal Corso, Pseudopotentials periodic table: From H to Pu, *Comput. Mater. Sci.* 95 (2014) 337–350.
- [114] K. F. Garrity, J. W. Bennett, K. M. Rabe, D. Vanderbilt, Pseudopotentials for high-throughput DFT calculations, *Comput. Mater. Sci.* 81 (2014) 446–452.
- [115] M. Topsakal, R. Wentzcovitch, Accurate projected augmented wave (PAW) datasets for rare-earth elements (RE=La-Lu), *Comput. Mater. Sci.* 95 (2014) 263–270.
- [116] A. Willand, Y. O. Kvashnin, L. Genovese, Á. Vázquez-Mayagoitia, A. K. Deb, A. Sadeghi, T. Deutsch, S. Goedecker, Norm-conserving pseudopotentials with chemical accuracy compared to all-electron calculations, *J. Chem. Phys.* 138 (10).
- [117] M. van Setten, M. Giantomassi, E. Bousquet, M. Verstraete, D. Hamann, X. Gonze, G.-M. Rignanese, The pseudodojo: Training and grading a 85 element optimized norm-conserving pseudopotential table, *Comput. Phys. Commun.* 226 (2018) 39 – 54.
- [118] P. Blaha, K. Schwarz, P. Sorantin, S. Trickey, Full-potential, linearized augmented plane wave programs for crystalline systems, *Comput. Phys. Commun.* 59 (2) (1990) 399 – 415.
- [119] N. Marzari, D. Vanderbilt, A. De Vita, M. C. Payne, Thermal contraction and disordering of the al(110) surface, *Phys. Rev. Lett.* 82 (1999) 3296–3299.
- [120] <http://molmod.ugent.be/deltacodesdft/>.



- 
- [121] A. Georges, G. Kotliar, W. Krauth, M. J. Rozenberg, Dynamical mean-field theory of strongly correlated fermion systems and the limit of infinite dimensions, *Rev. Mod. Phys.* 68 (1996) 13–125.
- [122] W. P. Huhn, V. Blum, One-hundred-three compound band-structure benchmark of post-self-consistent spin-orbit coupling treatments in density functional theory, *Phys. Rev. Materials* 1 (2017) 033803.
- [123] Y. Hinuma, G. Pizzi, Y. Kumagai, F. Oba, I. Tanaka, Band structure diagram paths based on crystallography, *Comput. Mater. Sci.* 128 (Supplement C) (2017) 140 – 184.
- [124] W. Setyawan, S. Curtarolo, High-throughput electronic band structure calculations: Challenges and tools, *Comput. Mater. Sci.* 49 (2) (2010) 299 – 312.
- [125] S.-Y. Xu, I. Belopolski, N. Alidoust, M. Neupane, G. Bian, C. Zhang, R. Sankar, G. Chang, Z. Yuan, C.-C. Lee, S.-M. Huang, H. Zheng, J. Ma, D. S. Sanchez, B. Wang, A. Bansil, F. Chou, P. P. Shibayev, H. Lin, S. Jia, M. Z. Hasan, Discovery of a Weyl fermion semimetal and topological Fermi arcs, *Science* 349 (6248) (2015) 613–617.
- [126] A. A. Soluyanov, D. Gresch, Z. Wang, Q. Wu, M. Troyer, X. Dai, B. A. Bernevig, Type-II Weyl semimetals, *Nature* 527 (7579) (2015) 495–498.
- [127] E. Prodan, W. Kohn, Nearsightedness of electronic matter, *Proc. Natl. Acad. Sci. U.S.A.* 102 (33) (2005) 11635–11638.
- [128] X. Gonze, R. Stumpf, M. Scheffler, Analysis of separable potentials, *Phys. Rev. B* 44 (1991) 8503–8513.
- [129] <https://atztogo.github.io/spglib/>.
- [130] H. U. Yang, J. D’Archangel, M. L. Sundheimer, E. Tucker, G. D. Boreman, M. B. Raschke, Optical dielectric function of silver, *Phys. Rev. B* 91 (2015) 235137.
- [131] R. L. Olmon, B. Slovick, T. W. Johnson, D. Shelton, S.-H. Oh, G. D. Boreman, M. B. Raschke, Optical dielectric function of gold, *Phys. Rev. B* 86 (2012) 235147.
- [132] D. Y. Smith, E. Shiles, Finite-energy  $f$ -sum rules for valence electrons, *Phys. Rev. B* 17 (1978) 4689–4694.
- [133] A. Zunger, S.-H. Wei, L. G. Ferreira, J. E. Bernard, Special quasirandom structures, *Phys. Rev. Lett.* 65 (1990) 353–356.
- [134] S.-H. Wei, L. G. Ferreira, J. E. Bernard, A. Zunger, Electronic properties of random alloys: Special quasirandom structures, *Phys. Rev. B* 42 (1990) 9622–9649.
- [135] P. Soven, Coherent-potential model of substitutional disordered alloys, *Phys. Rev.* 156 (1967) 809–813.

## Bibliography

---

- [136] S. de Gironcoli, P. Giannozzi, S. Baroni, Structure and thermodynamics of  $\text{Si}_x\text{Ge}_{1-x}$  alloys from ab initio Monte Carlo simulations, *Phys. Rev. Lett.* 66 (1991) 2116–2119.
- [137] J. Sanchez, F. Ducastelle, D. Gratias, Generalized cluster description of multicomponent systems, *Physica A* 128 (1-2) (1984) 334–350.
- [138] C. Jiang, C. Wolverton, J. Sofo, L.-Q. Chen, Z.-K. Liu, First-principles study of binary bcc alloys using special quasirandom structures, *Phys. Rev. B* 69 (2004) 214202.
- [139] V. Popescu, A. Zunger, Effective band structure of random alloys, *Phys. Rev. Lett.* 104 (2010) 236403.
- [140] G. A. Niklasson, C. G. Granqvist, O. Hunderi, Effective medium models for the optical properties of inhomogeneous materials, *Appl. Opt.* 20 (1) (1981) 26–30.
- [141] S. Laref, J. Cao, A. Asaduzzaman, K. Runge, P. Deymier, R. W. Ziolkowski, M. Miyawaki, K. Muralidharan, Size-dependent permittivity and intrinsic optical anisotropy of nanometric gold thin films: a density functional theory study, *Opt. Express* 21 (10) (2013) 11827–11838.
- [142] W. Ming, S. Blair, F. Liu, Quantum size effect on dielectric function of ultrathin metal film: a first-principles study of  $\text{Al}(111)$ , *J. Phys. Condens. Matter* 26 (50) (2014) 505302.
- [143] A. van de Walle, M. D. Asta, G. Ceder, The Alloy Theoretic Automated Toolkit: A user guide, *Calphad* 26 (2002) 539–553.
- [144] A. van de Walle, P. Tiwary, M. M. de Jong, D. L. Olmsted, M. D. Asta, A. Dick, D. Shin, Y. Wang, L.-Q. Chen, Z.-K. Liu, Efficient stochastic generation of special quasirandom structures, *Calphad* 42 (2013) 13–18.
- [145] J. Harl, G. Kresse, L. D. Sun, M. Hohage, P. Zeppenfeld, Ab initio reflectance difference spectra of the bare and adsorbate covered  $\text{Cu}(110)$  surfaces, *Phys. Rev. B* 76 (2007) 035436.
- [146] V. J. Keast, J. W. Wallace, C. J. Wrightson, M. Tai, A. Gentle, M. D. Arnold, M. B. Cortie, The effect of vacancies on the optical properties of  $\text{AuAl}_2$ , *J. Phys. Condens. Matter* 27 (50) (2015) 505501.
- [147] L. Bellaiche, D. Vanderbilt, Virtual crystal approximation revisited: Application to dielectric and piezoelectric properties of perovskites, *Phys. Rev. B* 61 (2000) 7877–7882.
- [148] Y. Nishijima, S. Akiyama, Unusual optical properties of the Au/Ag alloy at the matching mole fraction, *Opt. Mater. Express* 2 (9) (2012) 1226–1235.
- [149] V.J. Keast and J. Ewald and K.S.B. De Silva and M.B. Cortie and B. Monnier and D. Cuskelly and E.H. Kisi, Optical properties and electronic structure of the Cu-Zn brasses, *J. Alloy. Comp.* 647 (2015) 129 – 135.

---

# Gianluca Prandini

Avenue de Longemalle 7  
Renens, 1020  
+41 079 930 81 19  
[gianluca.prandini.90@gmail.com](mailto:gianluca.prandini.90@gmail.com)

Birth date: 13/04/1990  
Nationality: Italian

## EDUCATION

<b>Ph.D. candidate in Materials Science and Engineering</b> , EPFL	2015 - present
<b>Master Degree in Condensed Matter Physics</b> , Università degli Studi di Trieste Grade: 110 / 110 e lode ( <i>summa cum laude</i> )	2012 - 2014
<b>Bachelor Degree in Physics</b> , Università degli Studi di Trieste	2009 - 2012
<b>High School Diploma</b> , Liceo Classico Dante Alighieri, Trieste	2009

## PUBLICATIONS

G. Prandini<sup>\*</sup>, A. Marrazzo<sup>\*</sup>, I. E. Castelli<sup>\*</sup>, N. Mounet, and N. Marzari, *Precision and efficiency in solid-state pseudopotential calculations*, npj Computational Materials, 4, 72 (2018)

G. Prandini, M. Galante, N. Marzari, and P. Umari, *SIMPLE code: optical properties with optimal basis functions*, submitted

G. Prandini, G. Rignanese, and N. Marzari, *Photorealistic simulation of metals from first principles, in preparation*

D. Sangalli, A. Ferretti, H. Miranda, C. Attaccalite, I. Marri, E. Cannuccia, P. Melo, M. Marsili, F. Paleari, A. Marrazzo, G. Prandini, P. Bonfa, M. O. Atambo, F. Affinito, M. Palumbo, A. Molina-Sanchez, C. Hogan, M. Gruning, D. Varsano and A. Marini, *Many-Body perturbation theory calculations using the yambo code*, submitted

V. Carnevali, L. L. Patera, G. Prandini, M. Jugovac, G. Comelli, M. Peressi, and C. Africh, *Doping of epitaxial graphene by direct incorporation of nickel adatoms*, submitted

\*: equally contributed

---

## INVITED TALKS

CCMX - NCCR MARVEL Materials Science Day 2018, Bern, Switzerland, 4 October 2018, *White and Bright 18k Gold* (with Dr. Fanny Lalire)

## CONTRIBUTED TALKS

German Physical Society (DPG) spring meeting, Regensburg, Germany, 6 - 11 March 2016, *First-principles study of the colour and reflectivity of metals*

## POSTERS

The COMDI 2018 International Workshop on Computational Design and Discovery of Novel Materials, Lausanne, Switzerland, 10 - 12 September 2018

CECAM school, Advanced computing of excited state properties in solids and nanostructures with Yambo, Lausanne, Switzerland, 24 - 28 April 2017

18th International Workshop on Computational Physics and Materials Science: Total Energy and Force Methods, Trieste, Italy, 12 - 14 January 2017

The 2016 CAMD Summer School on Electronic Structure Theory and Materials Design, Copenhagen, Denmark, 14 - 19 August 2016

HoW exciting! 2016 International Workshop and Hands-on Tutorial, Berlin, Germany, 3 - 11 August 2016

CECAM school, Theoretical Spectroscopy Lectures, Lausanne, Switzerland, 18 - 22 May 2015

CECAM school, Excitations in Realistic Materials using Yambo on Massively Parallel Architectures, Lausanne, Switzerland, 13 - 17 April 2015



